DEVELOPING CARBON NANOTUBE OPTICAL SENSORS FOR *IN VITRO*

AND *IN VIVO* DETECTION OF BIOMARKERS AND DRUGS

A Dissertation

Presented to the Faculty of the Weill Cornell Graduate School

Of Medical Sciences

In Partial Fulfillment of the Requirements for the Degree of

Doctor of Philosophy

By

Jackson Harvey

December 2017

DEVELOPING CARBON NANOTUBE OPTICAL SENSORS FOR *IN VITRO*
AND *IN VIVO* DETECTION OF BIOMARKERS AND DRUGS

Jackson Harvey, Ph.D.

Cornell University 2017

Diseases such as cancer can develop asymptomatically, preventing
opportunities for early detection. The drive for "liquid biopsies" that can detect
biomarkers in a rapid, point-of-care setting has spurred innovation in nanoparticle-
based sensing schemes. One biomarker, cell-free circulating microRNA, has been a
major target due to its diagnostic potential and difficulties in detecting it with standard
assays. If cancer is detected, chemotherapy is often administered; unfortunately,
chemotherapy can greatly decrease patient quality of life due to toxicity. Some side
effects can be permanent and cumulative, as in the case of the drug doxorubicin.
Sensors that can detect chemotherapy drugs *in vivo* would be useful as a research tool
to better assess drug distribution in the organism and in cells. Clinically, an
implantable cumulative sensor for doxorubicin could provide a record of lifetime
exposure, minimizing chances of adverse effects.

A potential nanomaterial for developing implantable sensors for biomarkers
and chemotherapy drugs are single-walled carbon nanotubes. Carbon nanotubes are
fluorescent in the near-infrared range, which is highly penetrant to tissue, and report
their local environment *via* changes in their emission energy and intensity. Here, we
have developed DNA-functionalized carbon nanotubes for the detection of
oligonucleotide biomarkers, alkylating agents, and DNA-intercalating drugs like
doxorubicin. We have discovered a method by which optical changes due to

hybridization on the nanotube can be greatly enhanced, and applied it to the detection of microRNA in biofluids and *in vivo*. By adapting our understanding of this enhancement we were able to show directional control of nanotube solvatochromism to alkylating agents, which enabled control of sensing output signal. Mechanistic experiments allowed us to obtain new insight about the interaction of DNA-suspended nanotubes with anionic analytes, including oligonucleotides, to provide better selectivity. In detecting oligonucleotides in serum, we discovered that serum proteins can be denatured to selectively interact with nanotubes after hybridization to enhance sensing, and used this to detect viral RNA. Finally we developed a cumulative, implantable sensor for doxorubicin and other intercalating agents that enabled real-time sensing in live mice.

BIOGRAPHICAL SKETCH

Jackson Dean Harvey, son of Dean Harvey and Donna Harvey, was born in Fitchburg, MA and raised in Cortland, NY. He graduated from Cortland Jr. Sr. High School and attended SUNY Binghamton for his undergraduate work. While at Binghamton, he was a dual major in Biochemistry and Philosophy, and inducted into the Phi Beta Kappa society. He graduated in December 2009 earning a Bachelor of Science, Magna Cum Laude. Upon graduation he worked as a research technician at the New England Primate Research Center in the laboratory of David T. Evans, under the mentorship of Michael Alpert, studying the role of antibody-dependent cell-mediated cytotoxicity in HIV immunization. While here he attended night classes in statistics and portfolio theory at the Harvard Extension School.

In 2011 he became a graduate student at Weill Cornell Graduate School of Medical Sciences. His first rotation was with David Scheinberg, where he worked with Justin Mulvey on a project covalently functionalizing carbon nanotubes for the delivery of alpha-emitting payloads to pre-targeted tumors. Captivated by this nanomaterial, he later joined the laboratory of Daniel Heller in 2012 to continue working with it. In the Heller lab, he was focused on utilizing their optical properties rather than their pharmacokinetic properties. Surrounded by an interdisciplinary team of scientists, Jackson was able to develop several collaborative projects, including a very productive relationship with Jeetain Mittal and Gül Zerze at Lehigh University. He has given oral presentations at meetings of the Electrochemical Society and presented work at the Gordon Research Conference. He is a founding member of the Weill Cornell Biotech Club and has served as the director of finance for three years. He is also a founding member of GRO-Biotech, a coalition of industry-minded graduate students around New York City.

This work is dedicated to:

My parents, Dean and Donna Harvey.

My grandparents, Lawrence and Eleanor Harvey.

My wife, Soyeon Kate Kim.

And the rest of my wonderful family.

My mentor and advisor, Daniel Heller.

With sincerest thanks to the leadership of the pharmacology program:

David Scheinberg, Lorraine Gudas, and Yueming Li.

And to my students:

Lexi Sun, Xinghuo Li, Hanan Baker,

Corrin Pimentel, Deeksha Deep, and Kathryn Tully.

Docendo discimus.

ACKNOWLEDGMENTS

TABLE OF CONTENTS

LIST OF FIGURES

xiii

xiv

LIST OF TABLES

CHAPTER 1: UNDERSTANDING CARBON NANOTUBE OPTICAL SENSORS FOR APPLICATIONS IN BIOLOGY

1.1 Abstract

This doctoral dissertation is organized as largely independent chapters consisting of papers that have been published, submitted, or close to submission. Each chapter contains an introduction relating to the specific material contained within the chapter, sufficient for each chapter to be read and understood on its own. Overall, *the thesis is unified by the use of carbon nanotubes as biological sensors*. As will be described, they change their fluorescent emission wavelength and intensity in response to analytes. While carbon nanotube sensors have been demonstrated to be useful for biological sensing, they are also under intense study by physical scientists interested in one-dimensional materials. Their findings have important implications for developing and improving nanotube-based sensors for biology, in particular for understanding why and how an analyte of a given character produces an observed optical change. This understanding is essential for the rational design of sensors and the proper interpretation of optical changes. However, the different vocabulary and assumed set of requisite knowledge in the nanotube physical science literature makes it difficult to access. Additionally, the theory for how nanotube optical properties change in different environments is a work in progress in some respects, adding to the difficulty. The purpose of this introductory chapter is to provide pertinent fundamental information about carbon nanotubes in an accessible manner, and summarize the current understanding in how analytes elicit optical changes in nanotubes.

1.2 Carbon and carbon nanotubes

Known since ancient times, carbon is truly an element that has changed the world[1]. Carbon is absolutely central to life as we know it, in both a fundamental biological sense and in a more abstract societal sense. Some forms of carbon have taken key roles in powering humanity, from industrial growth to transportation[2]. Other forms of carbon are hung ornately around necks and fingers, studded in ears or as part of hair accessories, incorporated into blades for cutting[3], and have been presented countless times as tokens of love[4]. Carbon has made some people extremely wealthy, and dictated the policies of entire regions[5]. Carbon has also brought out the worst of humanity, fueling greed-based violence and being made into explosive compounds for propelling objects at high speed into other humans[6]. Carbon in a particular gaseous form has been especially problematic as of late[7]. Carbon has seen an entire field of science grown around her, organic chemistry, that has sullied the dreams of countless pre-med undergraduates[8] but enabled others to synthesize new material to improve human health and convenience.

But even more fundamental than organic chemistry, some forms of pure carbon have proven fascinating for their unusual properties. One such allotrope, carbon nanotubes, have been the subject of intense research[9], and sometimes hype[10], due to their potentially useful properties. The excitement surrounding carbon nanotubes was so great that they have entered the public lexicon through lay-person science articles. A carbon nanotube was even featured on the cover of the organic chemistry textbook I studied[11] as an undergraduate.

The electronic and optical properties of carbon nanotubes are truly remarkable. Carbon nanotubes consist of an ensemble of closely related structures, but small

differences in diameter and other geometry impart some with metallic properties and some with semi-conductor properties. Nanotubes can also be found inside of other nanotubes, like Russian nesting dolls, as so-called multi-walled carbon nanotubes. While multi-walled carbon nanotubes have some interesting applications[12], what follows will be focused solely on single-walled carbon nanotubes (SWNT, SWCNT, carbon nanotubes, or nanotubes).

In some iterations (as will be described), carbon nanotubes fluoresce in the near-infrared spectral range. This is especially important for some biomedical applications, as the near-infrared red range falls in the "window of transparency[13]" where tissue can be maximally penetrated for deep imaging. Carbon nanotubes do not photobleach, but their emission intensity can be quenched or enhanced reversibly in some cases[14]. The emission wavelength of carbon nanotubes can also change in response to their environment. Tissue penetrant emission, resistance to photobleaching, and sensitivity to the local environment make nanotubes an exciting option for developing *in vivo* sensors based completely on optical excitation and emission—no batteries or wires required.

A holistic view of the advantages of using carbon nanotubes to address biological problems are hidden somewhat behind nomenclature and models developed by physicists. Solid state physicists talk about wave vectors and reciprocal space in the way cancer biologists talk about c-Myc and transcriptomes—equally bewildering from each other's point of view. What follows is an attempt to explain the electronic origins of the properties of carbon nanotubes in a qualitative way (more detailed explanations may be found elsewhere[15-17]). This is not meant to disparage the excellent work of many brilliant physicists and chemists, who have pieced together exact quantitative

3

relationships of all the variables and physical forces to describe the electronic states with great understanding[18]. Indeed, I am enamored of this work and rely on it *via* collaborators who have made fantastic progress in computationally simulating carbon nanotubes interacting with other molecules[19]. Rather, my goal is to establish a qualitative foundation for understanding one aspect of carbon nanotubes, their optical properties, in the context of sensing small molecule analytes. For this purpose, the level of quantitative detail that is known can become counterproductive. The following sections aim to explain, qualitatively and admittedly superficially, the electronic origins of the optical properties of nanotubes. This is important background for understanding the basis of nanotube-based sensor responses, and therefore correct usage and interpretation of sensing events.

1.3 The origin and naming of carbon nanotubes

Carbon nanotubes are composed of sp^2 hybridized carbon that curls around into cylinders of diameters ranging from about 0.8 to 1.2 nm (depending on their synthesis) and can be of variable length. They are best conceptualized as a piece of 2-dimensional graphene (an atomic layer of graphite) that has been rolled up into a tube. This is not how carbon nanotubes are made. They are typically "grown" around an iron metal nanoparticle catalyst under high pressure conditions using carbon monoxide (high pressure carbon monoxide, HiPco) or around a or Co-Mo catalyst under carbon vapor deposition (Co-Mo catalysis, CoMoCAT)[20]. Envisioning nanotubes as rolled-up graphene is useful for understanding nanotube nomenclature. The graphene may be folded in a number of ways to create nanotubes with different diameters and pitch. Indeed, carbon nanotubes are named according to vectors built on a hypothetical graphene grid. Any particular nanotube can be geometrically described by "rolling up" a single graphene strip along a chiral vector that can connect any two

crystallographically identical points. This chiral vector is defined by two component vectors, called the chiral index (n,m), that uniquely describes any particular carbon nanotube. From the chiral index, one can calculate the chiral vector, the nanotube diameter, the chiral angle, and the number of carbon atoms per unit cell by simple geometric arguments. Even more conveniently, the metallic or semiconductor character of any nanotube can be determined from the chiral index; a nanotube is metallic if (2n+m) is a multiple of 3. All other nanotubes are semiconductors. The armchair nanotubes, (n,n) are always metallic, while zigzag (n,0) nanotubes are only metallic when n=3. For example, the (4,1) nanotube is metallic, while the (8,3) nanotube is a semiconductor. Figure 1.1 contains a selected set of semiconducting nanotubes.

(8,3) (6,5) (7,5) (10,2) (9,4) (8,4) (7,6) (12,1) (8,6) (11,3) (10,3) (10,5) (8,7)
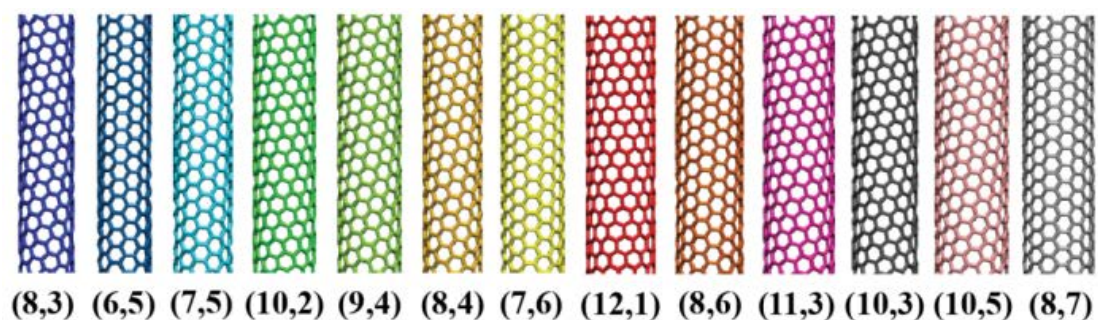
Figure 1.1 Selected semiconducting nanotubes named by their chiral index in (n,m) notation.

While metallic carbon nanotubes are useful for some applications, it is only the semiconducting nanotubes that have near-infrared fluorescence. At first glance, it seems incredible that pure carbon materials that differ in seemingly small ways, such

as diameter, can have such diverse physical properties. It is insightful to understand the origin of these differences in electronic, and thus optical, properties.

1.4 Electronic properties of carbon nanotubes: the basics

Carbon is at the top of column IV on the periodic table, and each atom contains six electrons occupying $1s^2$, $2s^2$, and $2p^2$ atomic orbitals. The two electrons occupying $1s^2$ are strongly bound core electrons, and do not appreciably affect any solid state properties. The four electrons occupying $2s^2$ and $2p^2$ atomic orbitals are the weakly bound valence electrons responsible for forming covalent bonds. The energy difference between the lower 2s and upper 2p levels is relatively small; a consequence of this is that the wave functions of these four electrons can mix and produce hybridization states, enhancing binding energy to adjacent atoms. Three possible hybridization states are allowed: sp, sp^2, and sp^3. Graphite, fullerenes, and carbon nanotubes consist entirely of sp^2 hybridized carbon, resulting in delocalized π orbitals perpendicular to the plane of the sigma bonds. These π electrons are ultimately responsible for the metallic or semiconductor properties of carbon nanotubes.

Although the first experimental observation of carbon nanotubes was reported by Sumio Iijima in 1991[21], the theoretical framework of carbon nanotubes was already being pieced together based on the recent discovery of fullerenes by Harry Kroto, Richard Smalley, and Robert Curl (with the assistance of three graduate students, James Heath, Sean O'Brien, and Yuan Liu)[22]. Part of the theoretical framework had predicted that more than one "type" of carbon nanotube was possible. That is, carbon nanotubes with different diameters and pitch were possible, and would have different electronic properties. It was predicted that 1/3 of possible carbon nanotube structures would have a metallic electronic structure, and 2/3 would be semiconductors[23, 24].

6

These predictions were based on the electronic structure of graphite[23, 25] and the recently discovered fullerene[26]. The explanation for how this can be predicted will be the subject of the next few subsections.

In our analysis, we will move from molecular orbital theory to a theory from solid state physics called band theory. Molecular orbital theory is powerful for small molecules, but for larger molecules a better understanding can emerge using the language and models from solid state physics. In considering carbon nanotubes, they have several convenient features that make this transition relatively painless. First, they are pseudo-1 dimensional. It's easier to deal with electrons in one dimension rather than three. Second, it is only the π electrons that must considered. Third, they are qualitatively similar to graphite, with only some additional geometric considerations, meaning that the electronic structure of graphite can serve as a convenient foundation for the electronic structure of carbon nanotubes.

1.4.1 From wave functions to density of states

The advent of quantum mechanics introduced us to the wave function. The wave function contains all the information that can be known about a particle. It is from the wave function that atomic orbitals are calculated, and from atomic orbitals covalent bonds are described—this is, based on the probability density of the electron[27]. An interesting feature of the wave function is that two distinct wave functions can yield the same probability density. This becomes significant when two atomic orbitals must be considered interacting with each other. The wave function of the two atoms can combine to form a composite wave, where there is a nonzero probability of an electron between the two atoms (in phase), or can combine in a destructive way, where the wave functions subtract, leading to a point of zero probability for an electron (a node)

between the two atoms (out of phase). These two possible combinations correspond to the bonding orbital, which is lower energy, and the anti-bonding orbital, which is higher energy (Figure 1.2).
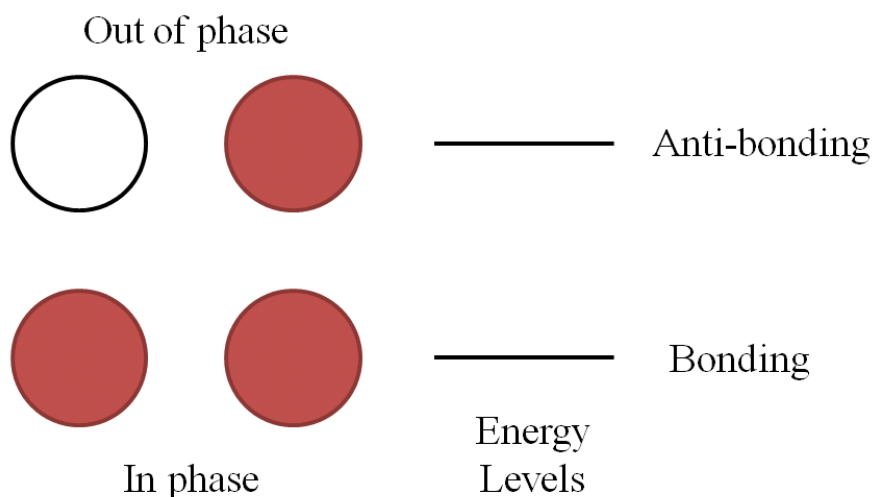
Figure 1.2 In phase and out of phase wave functions combine to produce bonding and anti-bonding energy levels.

As more atoms are added to this system, more combinations of states with varying degrees of in-phase and out-of-phase mixtures become available, producing a greater number of intermediate energy states (Figure 1.3a and b). The most stable combination, which is node-less, demarcates the lowest possible energy, while the least stable combination, with the maximum number of nodes (Figure 1.3, a), defines the highest possible energy. In solids, where the number of atoms approaches a huge number (10^{23}) per microscopic unit, the number of discrete states between the most stable and least stable combination of wave functions becomes tremendous, and can be represented as a continuous band of energies (Figure 1.3, imagine energy states being added to b until it looks like c). Solid state physics treats the wave function in this

situation slightly differently. If all the atoms are the same, as in some simple crystals, then the translational symmetry can be used to make symmetry-adapted linear combinations of the wave function[28]. Symmetry adaptation in solids like this is called "forming a Bloch function." If we use the letter k as an index (wavenumber) for the combination state that the wave function combines into, it's possible to correspond the lowest energy wave function composite (no nodes) and the highest energy wave function composite (maximal number of nodes) within a certain range, called the first Brillouin zone[29]. Outside this range, the values simply repeat due to the translational symmetry of the solid. The number of values that k can take is equal to the number of translations in the crystal, which is approximately 10^{23}. The formation of bands occurs for each quantum state, and are referred to as the 1s band, 2s band, etc. For most quantum states, there exists a gap between the energy bands, which are forbidden energies; however, some bands have energies that disperse so much they overlap with other bands.
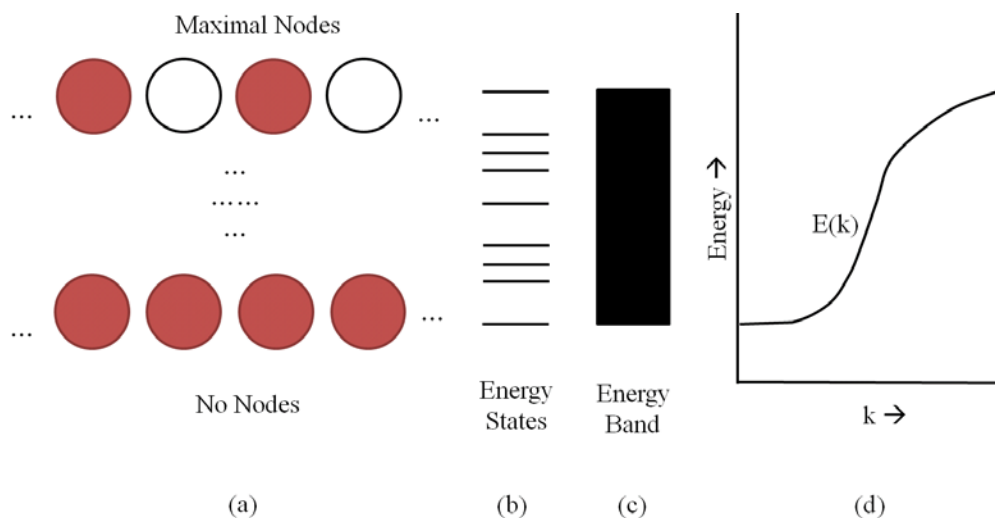
Figure 1.3 How many wave functions produce nearly continuous energy states that can be represented as a band. a, orbital representation of the lowest energy and highest energy combinations. Dotted lines between these combinations represent all other intermediate energy combinations. b, a small set of the energy states. As more combinations are considered, more lines will be added until it is no longer to distinguish individual states by eye. c, the energy band representation of the energy states, treating it as if it were continuous. d, The energy of different wave function combinations E(k), indexed by k.

This so called band theory of solids is the ideal framework for understanding the origins of metallic and semiconducting behavior[30] in carbon nanotubes. In general, one must only consider the two outermost energy bands of a material. The lower, filled band (analogous to the HOMO) is called the valence band, and the upper, empty band (analogous to the LUMO) is called the conduction band. The separation of these two bands (if they don't overlap) is called the energy gap. A generic metal would have an overlap of the valence and conduction band (Figure 1.4). If a potential difference is applied to the metal, only a small amount of energy is needed for electrons to reach empty energy states above it, allowing the electron to be mobile (and explaining why

metals are good conductors of electricity). In the case of a semi-conductor, there is an energy gap between the valence and conduction band. Because of the band gap, more energy must be applied to enable an electron to "jump" the forbidden energy levels in the band gap to enter the conduction band. In traditional semiconducting material, thermal energy can allow electrons to enter the conduction band, which explains why the conductivity of semiconductors increases with temperature. Insulating materials have a large band gap, meaning only very few electrons can enter the conduction band with added energy.
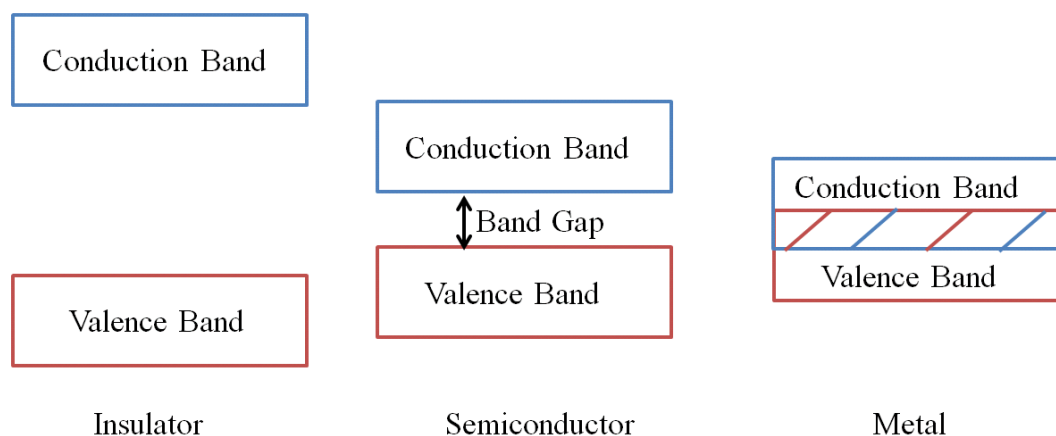
Figure 1.4: Schematic of an insulator, semiconductor, and metal according to band theory.

With this simplified framework, we can begin to partially understanding the electronic properties of carbon nanotubes. Conceptually, a carbon nanotube is simply a rolled up piece of graphene. Thus, the electronic properties will be that of graphene, with additional boundary conditions introduced by this rolling. In considering graphene, we only have to focus on the behavior of π energy bands, as these are the most important

electrons in determining physical properties. Graphene is technically a semi-metal, which according to the band theory of solids mean that their valence band and conduction band touch with an energy-gap of zero—not quite overlapping, but not quite a semiconductor either. For all intents and purposes though, we can consider the electronic behavior to be that of a metal.

The electronic structure of graphene will form the basis for the electronic structure of nanotubes, so we begin by considering all the wave functions combinations that comprise the range of k, and subsequently defines the first Brillouin zone of graphene. In considering the Brillouin zone of graphene, it is useful to point out here the Brillouin zone is actually an abstraction. It results from a mathematical transformation from real space to "reciprocal space," which makes a lot of sense due to a relationship between waves and energy that isn't essential to explain in great detail. ***What is important to remember is that this abstraction contains the all the relevant composite wave function information that is used to define the electronic bands for the π electrons in graphene***. And being a space, although abstract, it can be treated as a coordinate system. It turns out that in the Brillouin zone of graphene, there are locations where the dispersions of energy that define the bands "touch" (shown in Figure 1.5 as vertices of a hexagon), and render graphene with metallic properties. There are actually two inequivalent points, K and K', but the distinction here is not essential. To calculate the band structure of carbon nanotubes, the idea is to "fold" the graphene into a tube and by doing so we introduce boundary conditions (quantized circumferential momentum) to the wave functions. This results in a set of discrete energy sub-bands that are essentially "slices" of the energy bands in graphene. To aid in this abstraction, these discrete sub-bands can be superimposed onto the original Brillouin zone of graphene to yield a series of parallel lines whose length, number, and

orientation depend on the particular geometry that the graphene has been folded into.
These differences in folding correspond to the creation of different (n,m) type
nanotubes. Thus, each (n,m) nanotube will have the electronic properties contained in
the "slices" of the graphene band structure. Whenever the resulting allowed sub-bands
includes a K or K' point, and therefore has a band structure where the valence and
conduction band touch, the nanotube will behave as a metal. When the K point is not
included due to the particular boundary condition introduced by folding, the nanotube
is a semiconductor with a small band gap that depends on the diameter. The valence
band and conduction band energy gap will be defined by the sub-bands located closest
to the K point.

(a)   (b)
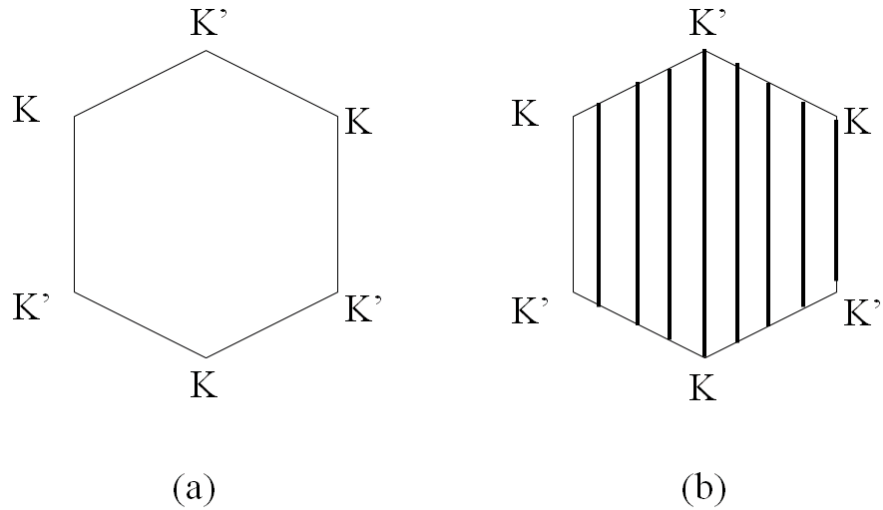
Figure 1.5 Deriving electronic properties of nanotubes. **a**, First Brillouin zone of
graphene. K and K' represent points where the valence and conduction band touch. **b**,
First Brillouin zone of graphene with allowed (5,5) nanotube sub-bands due to folding
(dark vertical lines). The sub-bands include the K point, making this nanotube a metal.

Understanding the electronic properties of carbon nanotubes as allowed "slices" of the graphene band structure using the first Brillouin zone is insightful but requires a high level of abstraction. A more intuitive understanding is to plot the band dispersions instead as density of states (DOS). The DOS plot is convenient because it does not require reciprocal space; the DOS is an average of the Brillouin zone over all k that give a molecular orbital at the specified energy level. In general, the DOS is highly dependent on the dimensionality of the material. Carbon nanotubes, being one dimensional, have large spikes in their density of states close the ends of bands, referred to as van Hove singularities. Inspection of the density of states for a particular nanotube type can also reveal if it is metallic or semiconducting. Metallic nanotubes have states that exist at every energy level, with no gaps. Semiconducting nanotubes have a gap were no electronic states exist; this is the band gap introduced earlier that defines semiconductors (Figure 1.6). These spikes, called Van Hove singularities, have been observed directly[31] and have significant consequences in considering the optical properties of carbon nanotubes.

1.4.2 Electronic properties: summary

We have considered how the wave function, which contains all the information of a particle, can be applied to an electron involved in bonding. The wave function can combine with other wave functions to produce a bonding and anti-bonding orbital with different energies. For large systems approaching 10^{23} atoms, the combinations of wave functions can be described as a dispersion of wave function composites of nearly continuous energies delineated by a perfectly in-phase combination at the lowest energy extreme, and by a perfectly out-of-phase combination at the high energy extreme. This dispersion can be treated as an energy band for a quantum state. Because it is the π electrons that determine the properties of graphene, and thus carbon

nanotubes, we considered the dispersion of possible wave functions for the π electrons of graphene. In a convenient abstraction, we considered the possible wave functions of graphene in reciprocal space, called the first Brillouin zone. Here the extremes of the valence and conduction band touch at points of high symmetry, the K and K' points, giving graphene (semi)metallic properties. We then saw that introducing circumferential constraints to the electronic structure of graphene when folding it into a one-dimensional tube results in a set of sub-band "slices" of graphene that, when superimposed on the original Brillouin zone of graphene, can predict if the particular nanotube will be metallic or semiconducting based on whether the sub-band slice contains the point where the valence and conduction bands touch. Different circumferential constraints from folding graphene into tubes with different diameter and pitch change the boundary conditions used to compute wave functions, and thus the allowed sub-bands of graphene that comprise the nanotube's electronic structure. This is how the metallic or semiconducting character of a nanotube can be predicted. We also saw that nanotube electronic properties can also be conveniently described by density of states diagrams, which also show metallic or semiconducting behavior. These DOS diagram contain sharp van Hove singularities, which dominate the optical properties of nanotubes.

1.5 Optical properties of carbon nanotubes

The optical properties of nanotubes include absorption, fluorescence, and Raman scattering. For our application of carbon nanotubes as sensors, we will not be dealing with their Raman properties, although excellent reviews on this property exist[32, 33]. Absorbance and fluorescence phenomena from carbon nanotubes are best understood in terms of the density of states diagrams introduced earlier. We will consider both metallic and semi-conducting type nanotubes for this purpose. Figure 1.6 contains the

DOS for a generic metallic and semi-conducting nanotube. The valence band has been colored in red, while the conduction band is colored in blue. The van Hove singularities for both the valence band and the conduction band can be indexed by numbers starting in the center and moving downward or upward.

Energy transitions happen between van Hove singularities. For example, light with energy equal to the gap between two van Hove singularities of matched numbers is able to promote an electron from the valence band van Hove singularity to the conduction band van Hove singularity. Transitions can happen from 1 to 1, 2 to 2, etc. but not from 1 to 2, 1 to 3, etc. Each type of transition is said to be E_{11}, E_{22}, etc. (read as "E-one-one, E-two-two", and so forth). In the case of a metal, we may imagine light with energy equal to E_{11} promoting an electron to the conduction band. Spectroscopically, light will be absorbed maximally at this energy. However, because states exist contiguous with the valence band, the electron can non-radiatively decay back to the valence band (indicated by dotted arrow). An absorption event would also be detected with light equivalent to the energy of the E_{22}; again, there will be a route to non-radiative decay, so no fluorescence will be observed.

In considering a semi-conducting nanotube, the absorption will be detected similarly as the metallic tube. However, now there is an energy gap between the valence band and conduction band, with no path for non-radiative decay. Because of this band gap, the electron will release a photon with energy equal to the E_{11} to return to the valence band. An interesting case arises with excitation of a semi-conducting nanotube at the E_{22} transition. The excited electron now has a path to non-radiatively decay to the E_{11}. Thus, excitation at the E_{22} will still only produce fluorescence at the E_{11} energy.
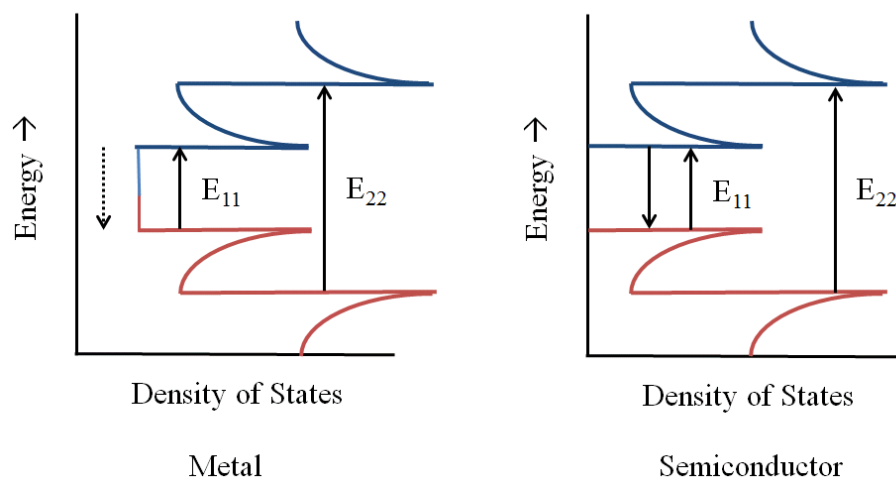
Figure 1.6: Density of states with van Hove singularities for metallic nanotubes and semiconducting nanotubes. Valence band is colored red, while the conduction band s blue. Non-radiative decay is represented by the dotted arrow. Absorption of a photon is represented by arrow point up, while emission of a photon is an arrow pointing down.

The fluorescence of semiconducting nanotubes was predicted before they could be measured; indeed, it took nearly a decade after the discovery of carbon nanotubes to measure their fluorescence. The key step in enabling observation of nanotube fluorescence was to create a colloidally stable solution of single nanotubes. As produced, carbon nanotubes form large aggregates as parallel bundles, with a van der Waals binding energy of approximately 500 eV per micron of tube contact[34]. This strong bundling interferes with the electronic structure provides non-radiative decay pathways to quench electronic excitation and prevent fluorescence. Metallic nanotubes in contact with semiconducting nanotubes can provide non-radiative pathways, masking fluorescence[35, 36]. Getting a solution of single nanotubes was no easy task, especially considering that covalent modifications could not be used, as too many sp3 defects on the nanotube surface will also quench fluorescence[37]. Suspension of single

nanotubes was finally achieved by vigorous sonication of nanotubes in the presence of surfactant; the sonication physically debundled the nanotubes, while the surfactant coated the hydrophobic surface and prevented re-aggregation through electrostatic repulsion. Bundles of tubes that were suspended in surfactant micelles could be removed by centrifugation, leaving mostly single nanotubes in the supernatant.

With this preparation of nanotubes, better absorption spectra could be obtained, and the nanotubes were found to have fluorescence from 800-1600 nm (the near-infrared spectral range). It was found that the wavelength of the absorbance peak in the spectral region of the first van Hove band gap, E_{11}, was nearly identical to the wavelength of the emission peak, making it possible to assign the emission to semiconducting nanotubes[34]. Shortly thereafter, it became possible to identify (n,m) species based on their excitation and emission[38].

The optical properties of carbon nanotubes became a scientific pursuit in its own right as a one-dimensional system[39]. It was confirmed experimentally that the optical resonances in carbon nanotubes arise from excitons[40], as was predicted by theory[41], and many photophysical studies were performed to better understand this system[42]. Excitons are quasi-particles consisting of an electron associated with a positively charged hole. When the electron is excited to the conduction band, the "hole" it leaves in the valence band can be considered a particle with a positive charge whose magnitude is equivalent to the electron. The electron-hole pair stays associated *via* a Coulombic interaction, and is mobile along the nanotube surface. The excitonic origin of nanotube fluorescence has important ramifications[15, 43, 44], including for their applications as sensors[45], which will be examined in the next section. Because it is mobile on the nanotube surface, the exciton can often find defect sites on the surface that allow for non-radiative decay[46]. For understanding changes in carbon nanotube

18

emission wavelength and intensity as a result of analyte binding, the excitonic nature will provide an important framework.

1.6 Carbon nanotubes as optical sensors

Concurrent to the basic photophysical studies, exploration of carbon nanotube fluorescence in response to various perturbations was already underway. In the original report of nanotube fluorescence, it was observed that lowering pH quenched fluorescence, but could be reversed by restoring the pH toward neutral. Follow-up work implicated a critical role for molecular oxygen pre-adsorbing to the nanotube side wall[47]. Metallic nanotubes reacted first near neutral pH, followed by protonation of nanotubes with increasing band gap as the solution continued to drop in pH[47]. Further redox studies with organic acceptors found that nanotubes could act as an electron donor, bleaching the nanotube fluorescence and absorbance. This was selective, based on differences in electronic structure related to diameter and chirality[48]. Reversible quenching in a nanotube chirality-dependent manner suggested that nanotubes could become sensors for redox events.

The use of carbon nanotubes as optical sensors has become a rich field, beginning with the detection of pH and redox changes. However, the use of carbon nanotubes as optical sensors is complicated by the inability to use covalent chemistry for functionalization, as too many sp3 defects along the nanotube sidewall will quench fluorescence due to non-radiative decay at the defect site. Thus, non-covalent functionalization schemes are required for their application as biosensors. Using such strategies, sensors have been developed for Beta-D-glucose[30], DNA hybridization[29], microRNA hybridization[49], divalent metal cations[31], assorted genotoxins[32], nitroaromatics[33], nitric oxide[34], pH[26], and the protein avidin[35]. More recently, specific

19

recognition of target analytes using changes in the corona phase of an adsorbed polymer has been developed[36,37]. A major challenge in developing non-covalent, colloidally stable sensors for use in biological systems is imparting appropriate specificity for the target analyte while resisting non-specific interactions with other biological material.

In all cases, analyte binding induces a change in the nanotube fluorescence, either a shift in emission wavelength, change in emission intensity, or some combination thereof. The possible sensing mechanisms are often reported to be solvatochromism, charge-transfer, or doping and redox reactions.

1.6.1 Solvatochromism

Of the sensing mechanisms, solvatochromism is the most robust for sensing, especially in considering *in vivo* situations, due to the fact that changes in emission wavelength is an absolute measurement (in energy) while intensity is in arbitrary units. Solvatochromism in general refers to a change in color as a result from the dielectric environment due to solvation. Several theoretical treatments of solvatochromism in carbon nanotubes have been explored[50-52]. The situation that arises with carbon nanotubes can become complicated, as the suspending agent provides a microenvironment around the nanotube that is different from the bulk solvent (almost always water). However, experiments have been conducted with uncoated nanotubes suspended over a pillar, surrounded only by air[53]. Compared to surfactant suspended nanotubes, the emission peaks were blue-shifted by 28 meV on average[54]. Similarly, nanotubes grown over trenches were directly immersed in different solvents[55]. A potential confounding factor in these studies relates to mechanical strain and substrate contact, which could impact the nanotube fluorescence[56]. Other studies using

surfactant coated nanotubes have been conducted by changing the bulk solvent to liquids with different relative dielectric constants, such as hexane and o-Dichlorobenzene[57]. Although organic solvents can affect the surfactant around the nanotube and thus the emission[58], the authors found that the use of SDBS has minimal rearrangements and could be used for reasonable comparisons. The nanotubes showed significant sensitivity to the solvent dielectric environment; a change of the dielectric constant from 2 to 5 resulted in a drop of emission intensity of more than 50%. It was found that the peak position was most impacted though. Comparative studies between different surfactants have also proven insightful in establishing the effect of the solvent dielectric on nanotube emission wavelength[59-61].

There additionally is a strong chirality dependence on the degree and sensitivity to solvatochromism[62-65]. Even small, micro-dielectric environmental effects are sufficient to produce change in many cases[66]. In general, carbon nanotube emission peaks exhibit a red-shift and broadening with increasing solvent dielectric constants. The effect of increasing dielectric constant of the solvent causes the electron-electron and electron-hole exciton interactions to decrease in energy. The reduction in the exciton binding energy is expected to cause a blue-shift in the optical transition energy, while the reduction of electron-electron repulsion is expected to cause a red-shift. Experimentally, a red-shift is observed, because the repulsion energy of the electrons is larger than that of the exciton binding energy[67].

1.6.2 Charge-transfer and redox reactions

The theory and experimental data relating the dielectric environment of the nanotube with the energy of the optical emission is an important framework for understanding the optical changes as sensing events for applied nanotube sensors. However, one

aspect that is not well explained is the photoluminescent intensity changes due to the solvent. Intensity changes in nanotubes have been best described so far by charge-transfer events and redox reactions.

In charge-transfer events, the analyte orbital overlaps with the nanotube or suspending agent's orbital. Electron transfer leads to altered rates of exciton quenching due to changes in the ground or excited states[48]. Spectral evidence for this came from experiments with nitric oxide interacting with carbon nanotubes that suggest electron transfer from the valence band of the nanotube to the LUMO of the nitric oxide radical[68]. Evidence for transfer from an excited state came from experiments with dye-ligand conjugates that quench the nanotube, but have a LUMO in the band gap of the nanotube, making a ground-state charge transfer impossible[69].

Redox reactions are thought to occur when the analyte changes the electron availability on the nanotube lattice, which could prevent or enhance exciton decay. Enhancement of intensity was shown with reducing agents such as dithiothreitol[70], a vitamin E analog called Trolox, and β-mercaptoethanol. Remarkably, the nanotubes were nearly 10 times brighter in some cases. It was concluded that the enhancement was due to passivation of defects or oxygen adsorption on the nanotube surface by the reducing agents, which acted as electron donors at these sites. The role in mitigating the effect of pre-adsorbed oxygen was strengthened by the finding that the reducing agents restored fluorescence in nanotubes that were oxidized with methyl viologen[70]. Conversely, protonation of the nanotube side wall from acidic species [34, 47, 71, 72] creates a non-radiative recombination site by withdrawing electron density from the side wall[73].

Recently, new insight in the impact of another quality of the solvent beside the dielectric constant has been found to play an important role in the nanotube optical response[74]. Using a novel polymer that suspends nanotubes stably in a range of solvents, the impact of solvent dielectric was better able to be assessed. Like other studies, it was found that the solvent dielectric greatly affects the wavelength of emission, and found that emission intensity was also affected. However, some irregularities suggested that the dielectric of the solvent alone was not sufficient in explaining the observed effects on emission intensity. For example, two solvent conditions that had only a small difference in their dielectric constant ($D_20 = 80$ vs. 9:1 ratio D_20: DMF = 76) showed a large difference in emission intensity. One potential factor could be the electrophilicity of the solvent. It was hypothesized that strongly electrophilic solvents could behave like acidic protons in pulling away electron density and making a site for non-radiative decay of the exciton. The solvents were ranked by acceptor number, which is a relative measure of the electrophilic character of the solvent determined by the ^{31}P NMR chemical shift induced by electron-withdrawing interactions of the solvent with the triethylphosphine oxide oxygen lone pair. A plot of the emission intensity with AN showed a monotonic trend. Conversely, a plot of the solvent donor number (DN), which measures the electron donating character of a solvent, showed the opposite effect on nanotube intensity. Solvents better able to donate electrons produced brighter emission intensity.

1.6.3 An integrated view

An integrated view of how nanotubes will respond to a given analyte from an excitonic perspective is beginning to emerge. The recent discovery that the solvent electrophilicity or donor ability can quench or enhance nanotube intensity according to similar mechanisms as protonation and reducing agents seemingly unites solvent

solvatochromism and redox reactions. It also resolves irregularities that have been observed in the past relating the dielectric environment with nanotube optical changes. Ultimately, we would like to be able to completely explain how the optical changes (emission wavelength and intensity) that arise upon analyte interaction with a nanotube results. An understanding of these forces may allow us to better predict how analytes will impact nanotube fluorescence, and aid in the design of better nanotube-based sensors. So far, the prediction of how a given analyte will affect the nanotube emission must be based on how the dielectric environment will change, if there will be electron withdrawing or donating forces, and if the analyte's orbital can overlap with the nanotube's orbital to provide transfer to lower energy states for electrons.

An added layer of difficulty toward this goal stems from the variety of materials that can be used to suspend carbon nanotubes. Interaction of analytes with the suspending material to change conformation, destabilize, or covalently modify are all expected to have large effects on the nanotube emission, and may complement or oppose the optical changes the analytes induces from direct interaction with the nanotube. To help reduce this complexity, this thesis has focused primarily on one type of suspending agent, single-stranded DNA, which has several favorable properties as explained in the following section.

1.7 DNA-suspended carbon nanotubes as sensors

The original report of nanotube suspension used a detergent called sodium dodecyl sulfate (SDS), a commonly used anionic detergent in molecular biology. Other surfactants and amphiphiles with different characters were also characterized in an attempt to improve dispersion efficiencies and explore new systems for study[61]. With an eye toward biological application, relatively "biocompatible" surfactants such as

the Pluronic series were also tested. Of all the things that can be used to make fluorescent suspensions of carbon nanotubes[61, 75, 76], single-strand DNA was also considered. Using water soluble polymers such as single-strand DNA to disperse nanotubes was proposed early on[77], and experimental success was obtained soon after[78]. Surprisingly, it has proven highly effective in nanotube chirality purification[79]. Using single-strand DNA to disperse nanotubes had many important implications for potential biomedical sensing applications. Being a biological molecule, single-strand DNA is inherently biocompatible in a way surfactants aren't. Single-strand DNA is also relatively cheap and easy to produce, with nearly limitless combinations of four bases available. The sequence of DNA also carries biological information and inherent selectivity based on Watson-Crick base-pairing. Suspension of nanotubes with DNA often produces solutions with higher efficiency than other surfactants[78]. The suspensions are observed to be stable for months or longer at room temperature. DNA-dispersed nanotubes quickly received the attention of many researchers for these reasons.

Single-strand DNA has several characteristics that make it exceptionally well suited for suspending nanotubes. Single-strand DNA is a flexible polymer with a negatively charged phosphate backbone. The DNA bases are rich in π electrons and relatively hydrophobic[80]. This enables effective π-π stacking on the nanotube surface, directing the negatively charged phosphate backbone into the solvent. π-π interactions are caused by intermolecular overlap of p-orbitals in π-conjugated systems[81]. A loss of entropy upon confinement on the nanotube also plays a notable role[82]. Wrapping around the tube was confirmed in high-resolution AFM imaging that shows periodic bulges[83]. Many experiments were conducted to examine the role of the sequence in dispersion, and from this it was appreciated that polymers with alternating G and T

bases were well-suited for dispersion and separation[60, 78, 79]. Compared to other surfactants such as SDS and SDBS, nanotubes suspended with DNA are red-shifted by 10-20 meV[60, 84]. This is due to incomplete coverage of the nanotube by DNA compared to surfactants, allowing more contact to the strong dielectric environment provided by water[52]. This free space has important implications as a sensor, because it is interaction with the nanotube surface that causes optical changes. High-resolution, tip-enhanced near-field optical microscopy was used to study the optical properties of single nanotubes with a spatial resolution of 15 nm. Doing this, it was possible to resolve photoluminescence variation along DNA-wrapped nanotubes. Two distinct emission bands were found, corresponding to DNA covered and uncovered portions. The shift between these two regions for the (6,5) nanotube was 18 meV[85].

Some of the first demonstrations of the sensing ability of DNA-suspended nanotubes came with the discovery that divalent ions can lead to greatly red-shifted emission from DNA-suspended nanotubes[86]. Other work from the Strano group demonstrated detection of specific oligonucleotides using DNA-suspended nanotubes[87, 88]. However, this approach failed to be generalizable to any target sequence[89]. Using DNA-suspended nanotubes, it was later shown that multi-modal detection of analytes (genotoxins and reactive oxygen species) inside of cells could also be obtained[90]. A sensor for nitric oxide was also developed using $(AT)_{15}$ suspended nanotubes[91, 92]. Another sequence, $(AAAT)_7$, was used for detection of nitric oxide in an inflamed mouse liver[93]. Even some neurotransmitters could be detected with some DNA-sequences[94]. Aptamers, which are conformations of DNA that can specifically recognize analytes, have also been used as part of carbon nanotube-based sensing schemes for insulin[95].

1.8 Realizing the potential of carbon nanotube-based sensors: the challenges

In the work that follows, great effort has been put forth in developing carbon-nanotube based sensors for clinical applications. A potential biomarker for disease, microRNA, and chemotherapy drugs were chosen as targets of detection due to the clinical utility of having implantable sensors for such analytes. A major challenge in building such sensors was imparting the appropriate specificity for target analytes, even in highly complex biological environments.

A key step forward as will be described in great detail was the combination of DNA-suspended nanotubes with another amphiphile. This combination enabled greatly enhanced and robust detection of target microRNA, even in complex biological environments and in vivo. At a more fundamental level, this helped clarify how changes at the nanotube surface translate into observed optical changes.

1.9 References

1.   Browne, J. Seven elements that have changed the world: an adventure of ingenuity and discovery. (Weidenfeld & Nicolson, London; 2013).

2.   Ashton, T.S. & Sykes, J. The coal industry of the eighteenth century, Edn. 2d. (Manchester UP, Manchester,; 1964).

3.   Owers, C. Industrial diamond: applications, economics and a view to the future. *Ind Diamond Rev* **60**, 176-+ (2000).

4.   Brinig, M.F. Rings and Promises. *Journal of Law, Economics, & Organization* **6**, 203-215 (1990).

5.   Ross, M. The oil curse : how petroleum wealth shapes the development of nations. (Princeton University Press, Princeton, NJ; 2012).

6.   Andrade, T. Gunpowder Age: China, Military Innovation, and the Rise of the West in World History. *Gunpowder Age: China, Military Innovation, and the Rise of the West in World History*, 1-432 (2016).

7.   Cox, P.M., Betts, R.A., Jones, C.D., Spall, S.A. & Totterdell, I.J. Acceleration of global warming due to carbon-cycle feedbacks in a coupled climate model (vol 408, pg 184, 2000). *Nature* **408**, 750-750 (2000).

8.   Lovecchio, K. & Dundes, L. Premed survival: Understanding the culling process in premedical undergraduate education. *Acad Med* **77**, 719-724 (2002).

9.   Baughman, R.H., Zakhidov, A.A. & de Heer, W.A. Carbon nanotubes--the route toward applications. *Science* **297**, 787-792 (2002).

10.   Davenport, M. in C&EN Chemical&Engineering News, Vol. 93 5 (American Chemical Society, 2015).

11.   Carey, F.A. Organic chemistry, Edn. 7th. (McGraw-Hill, Boston; 2007).

12.   Andrews, R., Jacques, D., Qian, D.L. & Rantell, T. Multiwall carbon nanotubes: Synthesis and application. *Accounts of Chemical Research* **35**, 1008-1017 (2002).

13.   Cheong, W.F., Prahl, S.A. & Welch, A.J. A review of the optical properties of biological tissues. *IEEE Journal of Quantum Electronics* **26**, 2166-2185 (1990).

14.   Carlson, L.J. & Krauss, T.D. Photophysics of individual single-walled carbon nanotubes. *Accounts of Chemical Research* **41**, 235-243 (2008).

15.   Dresselhaus, M.S., Dresselhaus, G., Saito, R. & Jorio, A. Exciton photophysics of carbon nanotubes. *Annual review of physical chemistry* **58**, 719-747 (2007).

16.   Saito, R. & Dresselhaus, M.S. Optical Properties of Carbon Nanotubes. *Carbon Nanotubes and Graphene, 2nd Edition*, 77-98 (2014).

17.   Saito, R., Nugraha, A.R.T., Hasdeo, E.H., Hung, N.T. & Izumida, W. Electronic and Optical Properties of Single Wall Carbon Nanotubes. *Topics in current chemistry* **375** (2017).

18.   Saito, R., Dresselhaus, G. & Dresselhaus, M.S. Physical Properties of Carbon Nanotubes. (Imperial College Press,World Scientific Publishing Company, London; 1998).

19.   Song, M., Snyder, M.A. & Mittal, J. Effect of molecular structure on fluid transport through carbon nanotubes. *Molecular Physics* **112**, 2658-2664 (2014).

20.   Prasek, J., Drbohlavova, J., Chomoucka, J. et al. Methods for carbon nanotubes synthesis-review. *Journal of Materials Chemistry* **21**, 15872-15884 (2011).

21.   Iijima, S. Helical Microtubules of Graphitic Carbon. *Nature* **354**, 56-58 (1991).

22.   O'Brien, S.C. The discovery of the fullerenes. *Pan Stanf Ser Nanoma* **1**, 73-85 (2016).

23.   Saito, R., Fujita, M., Dresselhaus, G. & Dresselhaus, M.S. Electronic-Structure of Graphene Tubules Based on C-60. *Physical Review B* **46**, 1804-1811 (1992).

24. Saito, R., Fujita, M., Dresselhaus, G. & Dresselhaus, M.S. Electronic-Structure of Chiral Graphene Tubules. *Applied Physics Letters* **60**, 2204-2206 (1992).

25. Wallace, P.R. The Band Theory of Graphite. *Phys Rev* **71**, 622-634 (1947).

26. Harigaya, K. From C-60 to a Fullerene Tube - Systematic Analysis of Lattice and Electronic-Structures by the Extended Su-Schrieffer-Heeger Model. *Physical Review B* **45**, 12071-12076 (1992).

27. Atkins, P.W. & De Paula, J. Physical chemistry, Edn. 7th. (W.H. Freeman, New York; 2002).

28. Ashcroft, N.W. & Mermin, N.D. Solid state physics. (Holt, New York,; 1976).

29. Hoffmann, R. How Chemistry and Physics Meet in the Solid-State. *Angewandte Chemie-International Edition in English* **26**, 846-878 (1987).

30. Serway, R.A. Physics for scientists & engineers, Edn. 2nd. (Saunders College Pub., Philadelphia; 1987).

31. Wildoer, J.W.G., Venema, L.C., Rinzler, A.G., Smalley, R.E. & Dekker, C. Electronic structure of atomically resolved carbon nanotubes. *Nature* **391**, 59-62 (1998).

32. Dresselhaus, M.S., Jorio, A. & Saito, R. Characterizing Graphene, Graphite, and Carbon Nanotubes by Raman Spectroscopy. *Annu Rev Conden Ma P* **1**, 89-108 (2010).

33. Dresselhaus, M.S., Dresselhaus, G., Saito, R. & Jorio, A. Raman Spectroscopy of Carbon Nanotubes. *Cont Concept Condens*, 83-108 (2008).

34. O'Connell, M.J., Bachilo, S.M., Huffman, C.B. et al. Band gap fluorescence from individual single-walled carbon nanotubes. *Science* **297**, 593-596 (2002).

35. Ma, Y.Z., Stenger, J., Zimmermann, J. et al. Ultrafast carrier dynamics in single-walled carbon nanotubes probed by femtosecond spectroscopy. *The Journal of chemical physics* **120**, 3368-3373 (2004).

36. Hertel, T., Fasel, R. & Moos, G. Charge-carrier dynamics in single-wall carbon nanotube bundles: a time-domain study. *Appl Phys a-Mater* **75**, 449-465 (2002).

37. Riggs, J.E., Guo, Z.X., Carroll, D.L. & Sun, Y.P. Strong luminescence of solubilized carbon nanotubes. *Journal of the American Chemical Society* **122**, 5879-5880 (2000).

38. Bachilo, S.M., Strano, M.S., Kittrell, C. et al. Structure-assigned optical spectra of single-walled carbon nanotubes. *Science* **298**, 2361-2366 (2002).

39. Weisman, R.B. & Bachilo, S.M. Dependence of optical transition energies on structure for single-walled carbon nanotubes in aqueous suspension: An empirical Kataura plot. *Nano letters* **3**, 1235-1238 (2003).

40. Wang, F., Dukovic, G., Brus, L.E. & Heinz, T.F. The optical resonances in carbon nanotubes arise from excitons. *Science* **308**, 838-841 (2005).

41. Ando, T. Excitons in carbon nanotubes. *Journal of the Physical Society of Japan* **66**, 1066-1073 (1997).

42. Avouris, P., Freitag, M. & Perebeinos, V. Carbon-nanotube photonics and optoelectronics. *Nature Photonics* **2**, 341-350 (2008).

43. Spataru, C.D., Ismail-Beigi, S., Capaz, R.B. & Louie, S.G. Quasiparticle and excitonic effects in the optical response of nanotubes and nanoribbons. *Top Appl Phys* **111**, 195-227 (2008).

44. Perebeinos, V., Tersoff, J. & Avouris, P. Scaling of excitons in carbon nanotubes. *Physical review letters* **92**, 257402 (2004).

45. Ohno, Y., Maruyama, S. & Mizutani, T. Environmental effects on photoluminescence of single-walled carbon nanotubes. *Carbon Nanotubes*, 109-121 (2010).

46.   Cognet, L., Tsyboulski, D.A., Rocha, J.D. et al. Stepwise quenching of exciton fluorescence in carbon nanotubes by single-molecule reactions. *Science* **316**, 1465-1468 (2007).

47.   Strano, M.S., Huffman, C.B., Moore, V.C. et al. Reversible, band-gap-selective protonation of single-walled carbon nanotubes in solution. *Journal of Physical Chemistry B* **107**, 6979-6985 (2003).

48.   MJ, O.C., Eibergen, E.E. & Doorn, S.K. Chiral selectivity in the charge-transfer bleaching of single-walled carbon-nanotube spectra. *Nature materials* **4**, 412-418 (2005).

49.   Harvey, J.D., Jena, P.V., Baker, H.A. et al. A carbon nanotube reporter of microRNA hybridization events in vivo. *Nature Biomedical Engineering* **1**, 0041 (2017).

50.   Choi, J.H. & Strano, M.S. Solvatochromism in single-walled carbon nanotubes. *Applied Physics Letters* **90**, 223114 (2007).

51.   Brown, M.S., Shan, J.W., Lin, C. & Zimmermann, F.M. Electrical polarizability of carbon nanotubes in liquid suspension. *Applied Physics Letters* **90** (2007).

52.   Miyauchi, Y., Saito, R., Sato, K. et al. Dependence of exciton transition energy of single-walled carbon nanotubes on surrounding dielectric materials. *Chemical Physics Letters* **442**, 394-399 (2007).

53.   Walsh, A.G., Vamivakas, A.N., Yin, Y. et al. Screening of excitons in single, suspended carbon nanotubes. *Nano letters* **7**, 1485-1488 (2007).

54.   Lefebvre, J., Fraser, J.M., Homma, Y. & Finnie, P. Photoluminescence from single-walled carbon nanotubes: a comparison between suspended and micelle-encapsulated nanotubes. *Appl Phys a-Mater* **78**, 1107-1110 (2004).

55.   Ohno, Y., Iwasaki, S., Murakami, Y. et al. Excitonic transition energies in single-walled carbon nanotubes: Dependence on environmental dielectric constant. *physica status solidi (b)* **244**, 4002-4005 (2007).

56.   Maki, H., Sato, T. & Ishibashi, K. Direct observation of the deformation and the band gap change from an individual single-walled carbon nanotube under uniaxial strain. *Nano letters* **7**, 890-895 (2007).

57.   Silvera-Batista, C.A., Wang, R.K., Weinberg, P. & Ziegler, K.J. Solvatochromic shifts of single-walled carbon nanotubes in nonpolar microenvironments. *Physical chemistry chemical physics : PCCP* **12**, 6990-6998 (2010).

58.   Wang, R.K., Chen, W.C., Campos, D.K. & Ziegler, K.J. Swelling the Micelle Core Surrounding Single-Walled Carbon Nanotubes with Water-immiscible Organic Solvents. *Journal of the American Chemical Society* **130**, 16330-16337 (2008).

59.   Fantini, C., Cassimiro, J., Peressinotto, V.S.T. et al. Investigation of the light emission efficiency of single-wall carbon nanotubes wrapped with different surfactants. *Chemical Physics Letters* **473**, 96-101 (2009).

60.   Haggenmueller, R., Rahatekar, S.S., Fagan, J.A. et al. Comparison of the quality of aqueous dispersions of single wall carbon nanotubes using surfactants and biomolecules. *Langmuir : the ACS journal of surfaces and colloids* **24**, 5070-5078 (2008).

61.   Moore, V.C., Strano, M.S., Haroz, E.H. et al. Individually suspended single-walled carbon nanotubes in various surfactants. *Nano letters* **3**, 1379-1382 (2003).

62. Ohno, Y., Iwasaki, S., Murakami, Y. et al. Chirality-dependent environmental effects in photoluminescence of single-walled carbon nanotubes. *Physical Review B* **73** (2006).

63. Jiang, J., Saito, R., Samsonidze, G.G. et al. Chirality dependence of exciton effects in single-wall carbon nanotubes: Tight-binding model. *Physical Review B* **75** (2007).

64. Nugraha, A.R.T., Saito, R., Sato, K. et al. Dielectric constant model for environmental effects on the exciton energies of single wall carbon nanotubes. *Applied Physics Letters* **97**, 091905 (2010).

65. Araujo, P.T., Jorio, A., Dresselhaus, M.S., Sato, K. & Saito, R. Diameter dependence of the dielectric constant for the excitonic transition energy of single-wall carbon nanotubes. *Physical review letters* **103**, 146802 (2009).

66. Hirana, Y., Tanaka, Y., Niidome, Y. & Nakashima, N. Strong Micro-Dielectric Environment Effect on the Band Gaps of (n,m)Single-Walled Carbon Nanotubes. *Journal of the American Chemical Society* **132**, 13072-13077 (2010).

67. Spataru, C.D., Ismail-Beigi, S., Benedict, L.X. & Louie, S.G. Excitonic effects and optical spectra of single-walled carbon nanotubes. *Physical review letters* **92**, 077402 (2004).

68. Kim, J.H., Heller, D.A., Jin, H. et al. The rational design of nitric oxide selectivity in single-walled carbon nanotube near-infrared fluorescence sensors for biological detection. *Nature chemistry* **1**, 473-481 (2009).

69. Satishkumar, B.C., Brown, L.O., Gao, Y. et al. Reversible fluorescence quenching in carbon nanotubes for biomolecular sensing. *Nature nanotechnology* **2**, 560-564 (2007).

70. Lee, A.J., Wang, X., Carlson, L.J. et al. Bright fluorescence from individual single-walled carbon nanotubes. *Nano letters* **11**, 1636-1640 (2011).

71. Blackburn, J.L., McDonald, T.J., Metzger, W.K. et al. Protonation effects on the branching ratio in photoexcited single-walled carbon nanotube dispersions. *Nano letters* **8**, 1047-1054 (2008).

72. Dukovic, G., White, B.E., Zhou, Z.Y. et al. Reversible surface oxidation and efficient luminescence quenching in semiconductor single-wall carbon nanotubes. *Journal of the American Chemical Society* **126**, 15269-15276 (2004).

73. Wang, F., Dukovic, G., Knoesel, E., Brus, L.E. & Heinz, T.F. Observation of rapid Auger recombination in optically excited semiconducting carbon nanotubes. *Physical Review B* **70** (2004).

74. Larsen, B.A., Deria, P., Holt, J.M. et al. Effect of solvent polarity and electrophilicity on quantum yields and solvatochromic shifts of single-walled carbon nanotube photoluminescence. *Journal of the American Chemical Society* **134**, 12485-12491 (2012).

75. Rastogi, R., Kaushal, R., Tripathi, S.K. et al. Comparative study of carbon nanotube dispersion using surfactants. *Journal of colloid and interface science* **328**, 421-428 (2008).

76. Vaisman, L., Wagner, H.D. & Marom, G. The role of surfactants in dispersion of carbon nanotubes. *Advances in colloid and interface science* **128-130**, 37-46 (2006).

77. O'Connell, M.J., Boul, P., Ericson, L.M. et al. Reversible water-solubilization of single-walled carbon nanotubes by polymer wrapping. *Chemical Physics Letters* **342**, 265-271 (2001).

78. Zheng, M., Jagota, A., Semke, E.D. et al. DNA-assisted dispersion and separation of carbon nanotubes. *Nature materials* **2**, 338-342 (2003).

79. Zheng, M., Jagota, A., Strano, M.S. et al. Structure-based carbon nanotube sorting by sequence-dependent DNA assembly. *Science* **302**, 1545-1548 (2003).

80. Gao, H. & Kong, Y. Simulation of DNA-Nanotube Interactions. *Annual Review of Materials Research* **34**, 123-150 (2004).

81. Anslyn, E.V. & Dougherty, D.A. Modern physical organic chemistry. (University Science, Sausalito, CA; 2006).

82. Manohar, S., Tang, T. & Jagota, A. Structure of homopolymer DNA-CNT hybrids. *J Phys Chem C* **111**, 17835-17845 (2007).

83. Campbell, J.F., Tessmer, I., Thorp, H.H. & Erie, D.A. Atomic force microscopy studies of DNA-wrapped carbon nanotube structure and binding to quantum dots. *Journal of the American Chemical Society* **130**, 10648-10655 (2008).

84. Hughes, M.E., Brandin, E. & Golovchenko, J.A. Optical absorption of DNA-carbon nanotube structures. *Nano letters* **7**, 1191-1194 (2007).

85. Qian, H., Araujo, P.T., Georgi, C. et al. Visualizing the local optical response of semiconducting carbon nanotubes to DNA-wrapping. *Nano letters* **8**, 2706-2711 (2008).

86. Heller, D.A., Jeng, E.S., Yeung, T.K. et al. Optical detection of DNA conformational polymorphism on single-walled carbon nanotubes. *Science* **311**, 508-511 (2006).

87. Jeng, E.S., Moll, A.E., Roy, A.C., Gastala, J.B. & Strano, M.S. Detection of DNA hybridization using the near-infrared band-gap fluorescence of single-walled carbon nanotubes. *Nano letters* **6**, 371-375 (2006).

88. Jeng, E.S., Barone, P.W., Nelson, J.D. & Strano, M.S. Hybridization kinetics and thermodynamics of DNA adsorbed to individually dispersed single-walled carbon nanotubes. *Small* **3**, 1602-1609 (2007).

89. Jeng, E.S., Nelson, J.D., Prather, K.L. & Strano, M.S. Detection of a single nucleotide polymorphism using single-walled carbon-nanotube near-infrared fluorescence. *Small* **6**, 40-43 (2010).

90. Heller, D.A., Jin, H., Martinez, B.M. et al. Multimodal optical sensing and analyte specificity using single-walled carbon nanotubes. *Nature nanotechnology* **4**, 114-120 (2009).

91. Zhang, J.Q., Boghossian, A.A., Barone, P.W. et al. Single Molecule Detection of Nitric Oxide Enabled by d(AT)(15) DNA Adsorbed to Near Infrared Fluorescent Single-Walled Carbon Nanotubes. *Journal of the American Chemical Society* **133**, 567-581 (2011).

92. Boghossian, A.A., Zhang, J.Q., Le Floch-Yin, F.T. et al. The chemical dynamics of nanosensors capable of single-molecule detection. *Journal of Chemical Physics* **135** (2011).

93. Iverson, N.M., Barone, P.W., Shandell, M. et al. In vivo biosensing via tissue-localizable near-infrared-fluorescent single-walled carbon nanotubes. *Nature nanotechnology* **8**, 873-880 (2013).

94. Kruss, S., Landry, M.P., Vander Ende, E. et al. Neurotransmitter detection using corona phase molecular recognition on fluorescent single-walled carbon nanotube sensors. *Journal of the American Chemical Society* **136**, 713-724 (2014).

95. Cha, T.G., Baker, B.A., Sauffer, M.D. et al. Optical Nanosensor Architecture for Cell-Signaling Molecules Using DNA Aptamer-Coated Carbon Nanotubes. *ACS nano* **5**, 4236-4244 (2011).

CHAPTER 2: A CARBON NANOTUBE REPORTER OF MIRNA HYBRIDIZATION EVENTS IN VIVO[*]

2.1 Abstract

MicroRNAs and other small oligonucleotides in biofluids are promising disease biomarkers, yet conventional assays require complex processing steps that are unsuitable for point-of-care testing or for implantable or wearable sensors. Single-walled carbon nanotubes are an ideal material for implantable sensors, owing to their emission in the near-infrared spectral region, photostability and exquisite sensitivity. Here, we report an engineered carbon-nanotube-based sensor capable of real-time optical quantification of hybridization events of microRNA and other oligonucleotides. The mechanism of the sensor arises from competitive effects between displacement of both oligonucleotide charge groups and water from the nanotube surface, which result in a solvatochromism-like response. The sensor, which allows for detection via single-molecule sensor elements and for multiplexing by using multiple nanotube chiralities, can monitor toehold-based strand-displacement events, which reverse the sensor response and regenerate the sensor complex. We also show that the sensor functions in whole urine and serum, and can non-invasively measure DNA and microRNA after implantation in live mice.

---

[*] Harvey et al. A Carbon nanotube reporter of miRNA hybridization events *in vivo.* Nature Biomedical Engineering (2017) **1**, 0041

2.2 Introduction

The detection of oligonucleotide hybridization is important for a broad range of applications, from devices based on dynamic DNA nanotechnology to clinical point-of-care diagnostics. Oligonucleotides in biofluids such as serum, urine, and peritoneal fluid[1, 2] are a promising source of biomarkers for a variety of pathologies, including cancer[3, 4]. Of potential biomarker oligonucleotides[5-7], microRNA (miRNA) was found to be highly stable in body fluids, as many studies to date identify specific patterns of miRNA expression indicative of disease states[3, 8-13]. Devices that can measure changes in biomarker miRNA[14] or cell-free DNA[15] concentrations in biofluids such as urine, serum, or ascites in patients with risk factors for a disease or its relapse may improve early detection and treatment. Implantable or wearable devices that enable minimally-invasive continuous biomarker monitoring may extend this strategy to detect biomarkers at the earliest possible stages of disease.

The current standard for miRNA measurement, with limits of detection ranging from aM to fM[16], is quantitative PCR (qPCR)[17], but this method requires purification and amplification of miRNA that can introduce biases and variability[18]. Commercially available techniques that do not involve amplification, such as microarrays, suffer from poorer sensitivity (pM to nM) and high false positive rates[16, 18]. Detection strategies that avoid amplification, labeling, and purification from biofluids are under investigation[19, 20], but in vivo detection strategies are sparse. The detection of nucleic acid biomarkers in real-time and in situ within living tissues and organisms remains an important challenge.

Of potential materials for detecting nucleic acids, individually-dispersed semiconducting single-walled carbon nanotubes (SWCNTs) exhibit exciting properties

for use as optical biomedical sensors[21, 22]. Semiconducting carbon nanotubes are fluorescent in the near-infrared spectral region[23], a wavelength range penetrant to tissue[24], and they do not photobleach[25]. Their emission wavelength[26] and intensity[27] are sensitive to the local environment, allowing perturbations at the nanotube surface to be transduced via modulation of their emission, with up to single-molecule sensitivity[28]. Up to 17 distinct nanotube (n,m) species (chiralities) with unique and resolvable emission wavelengths can be measured, potentiating multiplexed detection schemes[29].

Herein, we describe a label-free approach to detect hybridization events of miRNA and other oligonucleotides transiently and in vivo. We designed a sensor which transduces the hybridization of small DNA and RNA oligonucleotides into spectral changes of carbon nanotube photoluminescence, and we determined its mechanism of action via experiments and molecular dynamics simulations to be a competitive response to local dielectric and electrostatic factors. Using this understanding, we designed a scheme wherein amphiphilic moieties undergo triggered assembly on the nanotube surface upon binding of target miRNA, resulting in a markedly enhanced spectral response. We showed that the sensor enables multiplexed detection using different nanotube chiralities and real-time monitoring of toehold-mediated DNA-strand displacement, which caused a reversal of the signal response. The sensor was highly resistant to non-specific interactions with biological molecules, allowing for direct detection in urine and serum. Finally, we showed the first in vivo optical detection of target DNA and miRNA by encasing the sensor within an implantable device through which we detected hybridization non-invasively via near-infrared fluorescence in live mice.

2.3 Results and Discussion

2.3.1 Development of sensor

We synthesized a DNA-nanotube complex consisting of a single oligonucleotide sequence with two domains—one to impart nanotube colloidal stability (nanotube-binding sequence) and a second with a complementary sequence to a target oligonucleotide (miRNA capture sequence). For the miRNA capture sequence, we chose a specific 23-mer miRNA (miR-19) as a model target due to its role in oncogenesis[30]. Figure 2.1 shows the synthesis scheme. A screen of potential nanotube-binding sequences found $(GT)_{15}$, known to efficiently encapsulate nanotubes[31], to provide superior resistance to non-complementary oligonucleotides (Figure 2.2). The purified DNA-nanotube construct was found to be highly photoluminescent and is herein referred to as the GT15mir19 sensor.
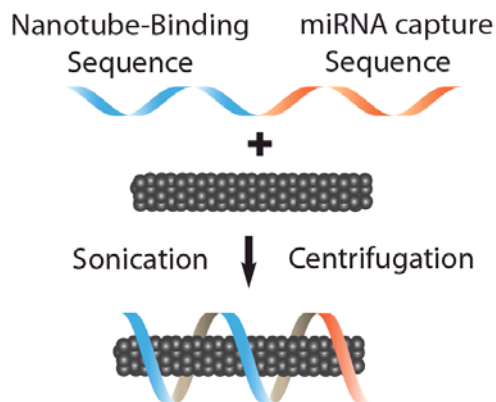
Figure 2.1 Construction scheme of the miRNA sensor complex. A single DNA oligonucleotide containing a nanotube-binding sequence (blue) and miRNA capture sequence (orange) which is non-covalently bound to the carbon nanotube surface.
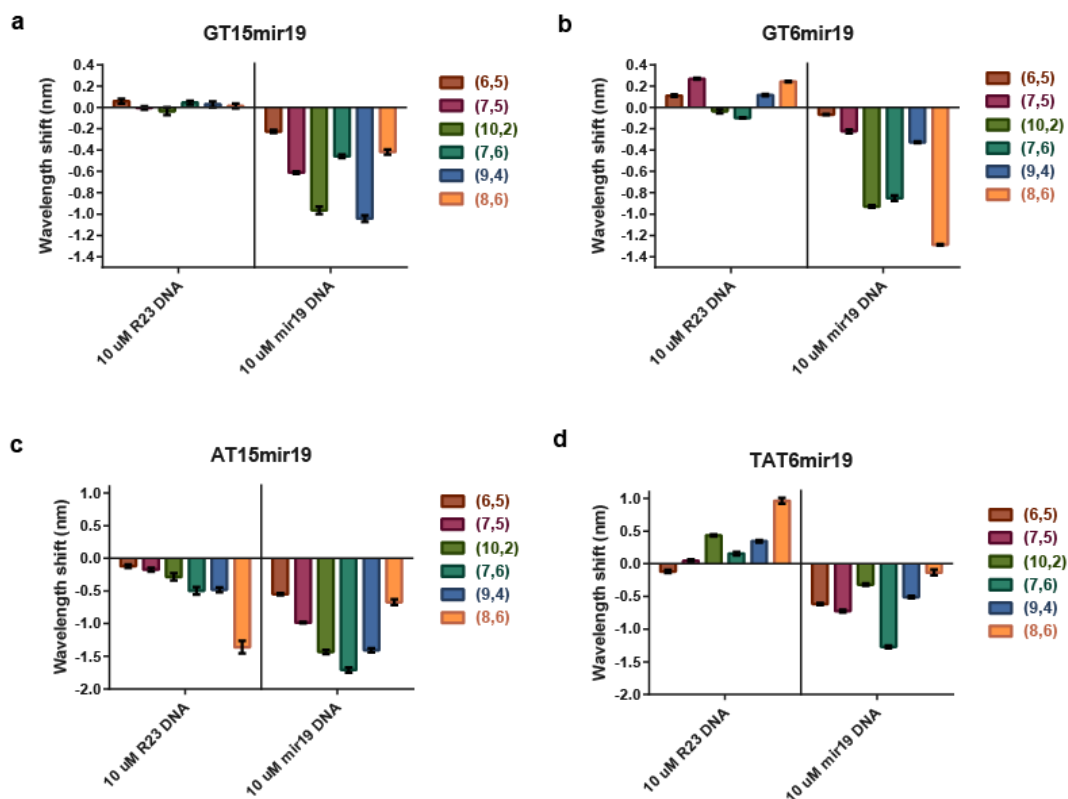
Figure 2.2 Selectivity assessment of different nanotube binding domains.
Wavelength shift of modified sensors after addition of non-complementary control
(R23) or miR-19 DNA. **a,** Sensor composed of the $(GT)_{15}$ nanotube binding sequence
(GT15mir19). **b,** Sensor composed of the $(GT)_6$ nanotube binding sequence
(GT6mir19). **c,** Sensor composed of the $(AT)_{15}$ nanotube binding sequence
(AT15mir19). **d,** Sensor composed of the $(TAT)_6$ nanotube binding sequence
(TAT6mir19). Error bars represent standard deviation for $n = 3$ technical replicates.

The optical response of the GT15mir19 sensor was then tested using both a DNA-
based and RNA-based analyte miR-19 sequence, as well as a length-matched,
randomly generated, non-complementary control (R23). After incubation with miR-19
or R23, eleven different nanotube chiralities were measured via two-dimensional
excitation/emission photoluminescence spectroscopy[32] ("PL plots", Figure 2.3). Each
nanotube emission peak exhibited a shift in wavelength which was specific to the
miR-19 target sequence over the R23 control (Figure 2.4). In general, nanotube
emission peak wavelengths blue-shifted and intensity increased upon introduction of

the target oligonucleotide (Figure 2.5); excitation peaks (E_{22} transitions) also blue-shifted (Figure 2.6).
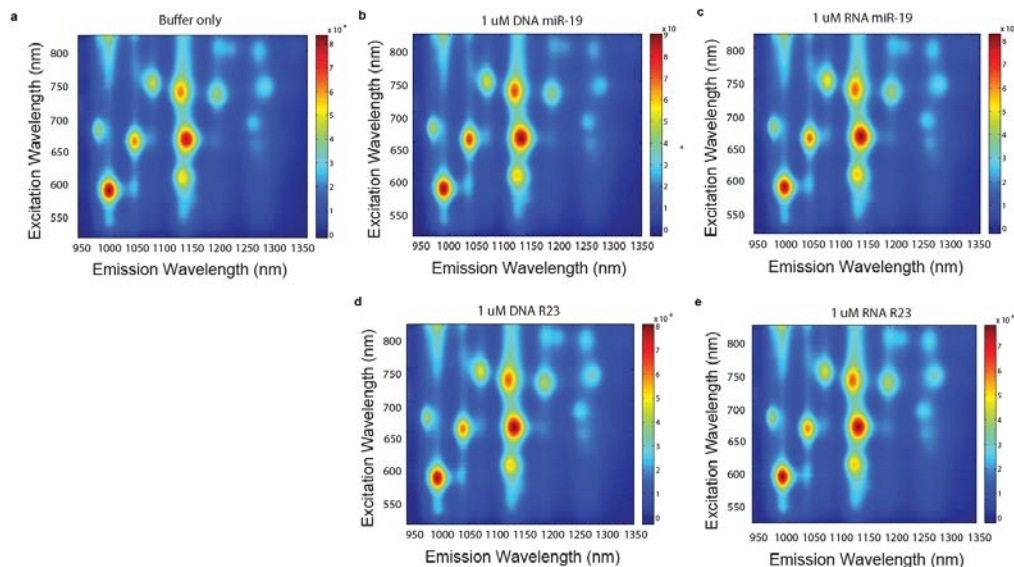
***Figure 2.3. Photoluminescence excitation/emission plots of the GT15mir19 sensor* a,** in buffer only, **b,** after interrogation with miR-19 DNA, **c,** after interrogation with miR-19 RNA, **d,** after interrogation with R23 DNA, **e,** after interrogation with R23 RNA.
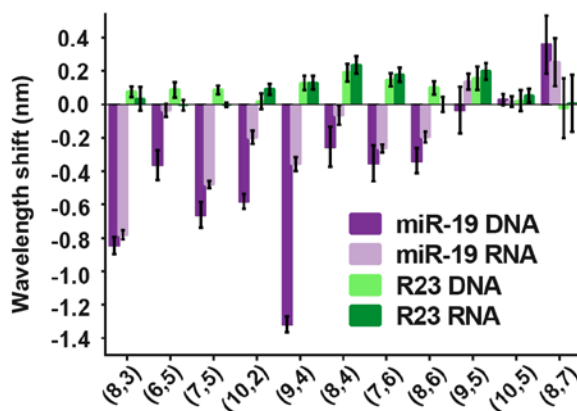
Figure 2.4 Response of the GT15mir19 sensor to analyte DNA or RNA with the miR-19 sequence, or a control sequence (R23). Response of nanotube emission is shown for each nanotube chirality. Positive wavelength shift denotes a red-shift in the emission peak, and negative numbers denote a blue-shift
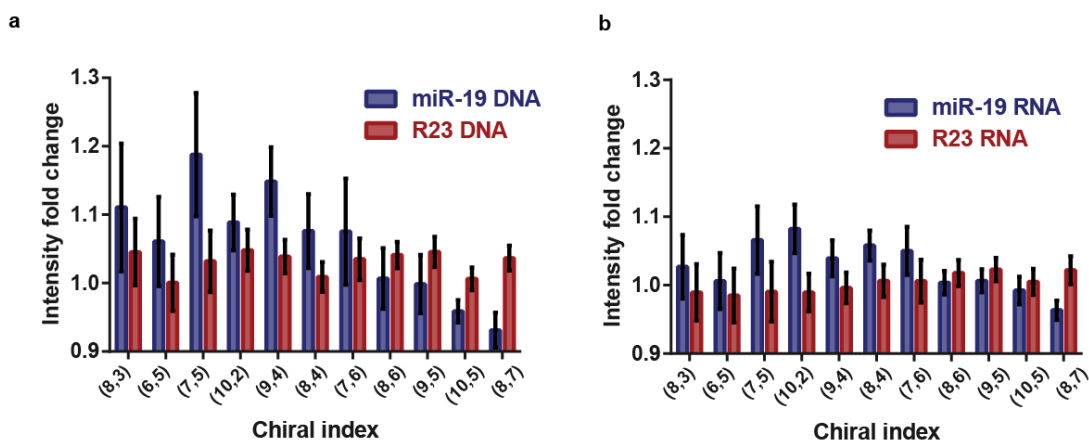
***Figure 2.5. Intensity response of the GT15mir19 sensor.* a,** Response after addition of miR-19 DNA analogue or random sequence DNA control. **b,** Response after addition of miR-19 RNA or random sequence RNA control. Error bars represent standard deviation for n = 3 technical replicates.
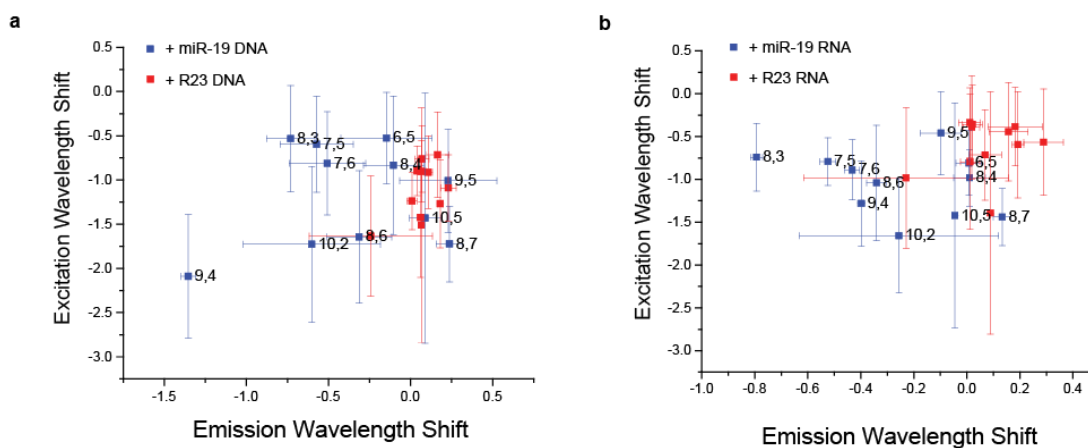
***Figure 2.6. Plots of excitation and emission wavelength shifts calculated from photoluminescence plots.* a,** Responses to miR-19 DNA analogue and random sequence DNA control (R23). **b,** Responses to miR-19 RNA and random sequence RNA control (R23). Error bars represent standard deviation for n = 3 technical replicates.

To verify that hybridization to the GT15mir19 sensor occurred upon introduction of the target, we designed a hairpin oligonucleotide which would make binding of the target more apparent by atomic force microscopy (AFM). The oligonucleotide was composed of the miR-19 or R23 sequence, a short spacer, and a 52-nucleotide hairpin region (diagram in Figure 2.7). After incubation with the miR-19-hairpin, the average height of the sample increased by ~0.6 nm, as measured by AFM in dry conditions (Figure 2.7). Upon imaging in aqueous conditions, we observed distinct protrusions from the nanotubes which were absent in the R23 hairpin-treated sample and buffer controls (Figure 2.8). Based on this pattern and other AFM studies[33], we estimate that the GT15mir19 sensor presents 5-10 binding sites per 100 nm of nanotube. Our preparation method yielded nanotubes with a mean length of 166 nm (SD 149nm)[34]; thus we calculate that an average single nanotube could potentially bind approximately 8-17 copies of miRNA.

a miR-19HP

A T T A T
T
T ᵀ ᴬ ᵀ ᴬ ᵀ
TAACAACTACGAACTACTGATTTTTGTGCAAATCTATGCAAAACTGA
ATTGTTGATGCTTGATGACT

b R23HP

A T T A T
T
T ᵀ ᴬ ᵀ ᴬ ᵀ
TAACAACTACGAACTACTGATTTTTGATCGTTACTGGGTGACTGGCT
ATTGTTGATGCTTGATGACT

c miR-19HP R23HP

d
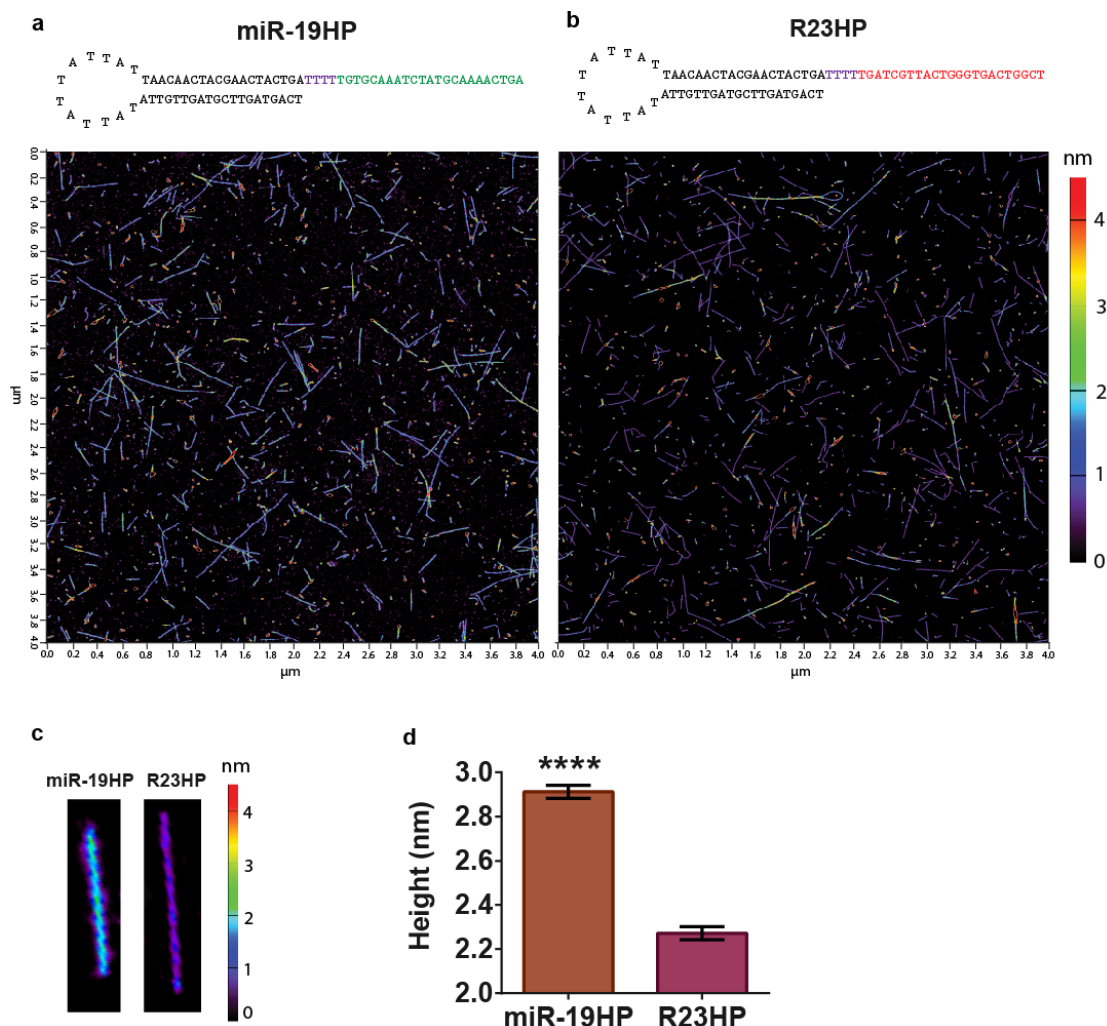
Figure 2.7. Atomic force microscopy of the GT15mir19 complex under dry conditions. **a** and **b**, Sequences of the hairpin RNAs miR-19HP and R23HP, respectively, and AFM height profiles after incubation. Green bases are complementary to the GT15mir19 capture sequence, red bases are random sequence control, and purple bases are thymine spacers. **c,** Images of single nanotubes from miR-19HP and R23HP images. **d**, Average height of nanotubes after addition of miR-19HP or R23HP, calculated from n = 1332 nanotubes. Error bars represent standard error of the mean.
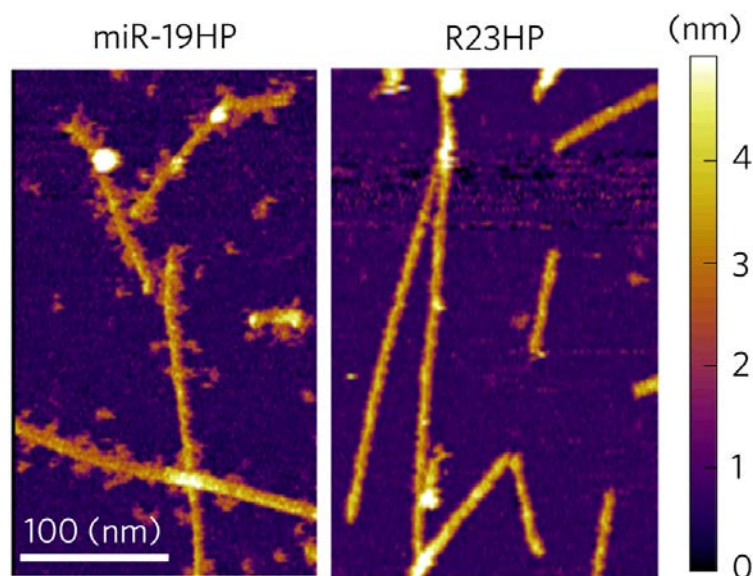
Figure 2.8 Atomic force microscopy images in aqueous conditions of the sensor complex upon incubation with non-complementary (R23HP) or complementary (miR-19HP) hairpin DNA.

Because the mechanism of nanotube spectral changes induced by oligonucleotide hybridization is poorly understood, we designed a set of experiments to better understand the structural changes of the sensor induced by hybridization. We first investigated whether the hybridized duplex remained near the nanotube surface after the binding of target miRNA. We developed an assay using an organic fluorophore conjugated to the miRNA capture sequence under the premise that the fluorophore intensity would increase upon hybridization if the fluorophore desorbed from the nanotube surface, as organic fluorophores are known to quench upon interaction with the nanotube surface via an energy transfer mechanism[35]. We suspended nanotubes with the sequence GT6mir19, (shortened due to synthesis constraints) containing the Cy5 dye conjugated to the 3' end of the miR-19-binding domain. Upon addition of miR-19 to the modified complex, we found that Cy5 fluorescence increased over time, while the R23 sequence caused no change in Cy5 fluorescence (Figure 2.9). To validate GT6mir19-Cy5 as a proxy for the GT15mir19 sequence, we measured the

47

nanotube emission upon introduction of the miR-19 sequence to the fluorophore-labeled complex. Again, we saw blue-shifting upon hybridization with the target oligonucleotide, suggesting the same sensor function despite the shortened nanotube-binding domain (Figure 2.10). In agreement with the Cy5 fluorescence change, we found nanotube fluorescence emission to blue-shift at a slower rate compared to GT6mir19 without Cy5 (Figure 2.10). We interpret this relatively slow rate as a result of the affinity of Cy5 for the nanotube surface, based on π stacking interactions between the Cy5 dye, which is rich with π electrons, and the graphitic π electrons of the nanotube. The fluorophore de-quenching and AFM together suggest a final hybridized structure consisting of a partial duplex dissociating from the nanotube surface.
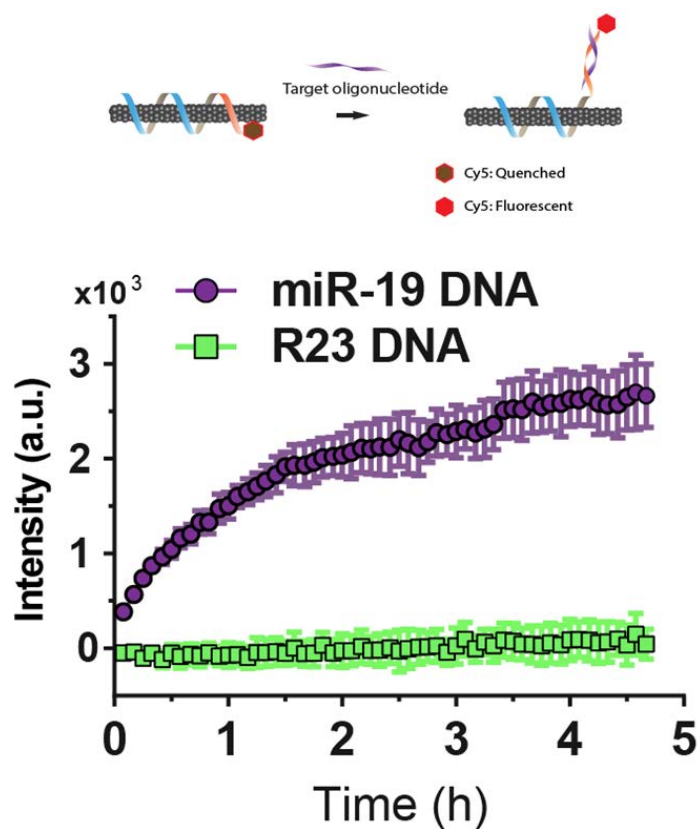
Figure 2.9 Intensity of Cy5 emission from the GT15mir19-Cy5-nanotube complex after introducing miR-19 DNA or R23 DNA.
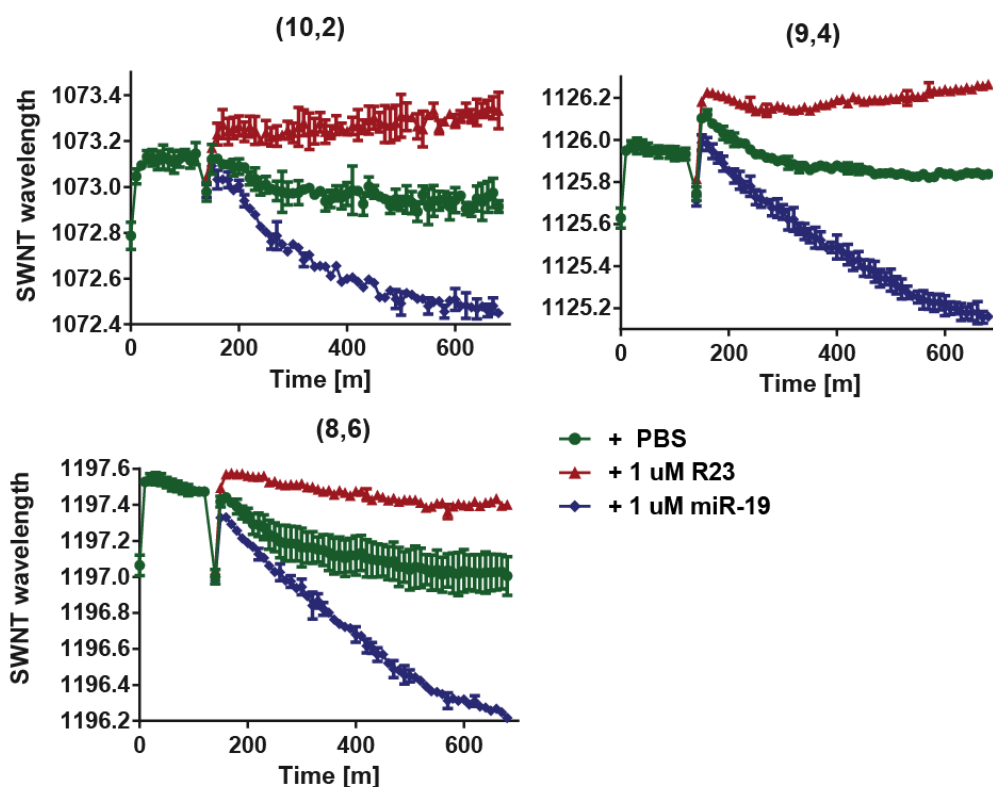
Figure 2.10 Near-infrared emission wavelength response of the modified sensor complex, GT6mir19-Cy5, used for the fluorophore dequenching experiment. The sensor was interrogated with miR-19 (blue), R23 (red), or buffer only (green). The emission wavelength response of three nanotube chiralities, (10,2), (9,4), and (8,6), are shown. Error bars represent standard error of the mean for n = 3 technical replicates.

Using all-atom molecular dynamics simulations, we assessed whether the GT15mir19 sequence could remain stable on the nanotube upon partial hybridization. The pre-hybridized sequence was placed in the vicinity of the (9,4) nanotube with explicit water and counterions, and a simulation was run for 250 ns (details in methods). The single-stranded portion of the oligomer bound to the nanotube and the hybridized construct remained stable on the nanotube surface for the remainder of the simulation (Figure 2.11 "Hyb"). A second simulation was run in absence of the hybridization strand. During the simulation, the entire oligomer bound to the surface and wrapped

the nanotube, with the nucleobases orienting closely to the nanotube surface in a

parallel orientation (Figure 2.11, "Unhyb").
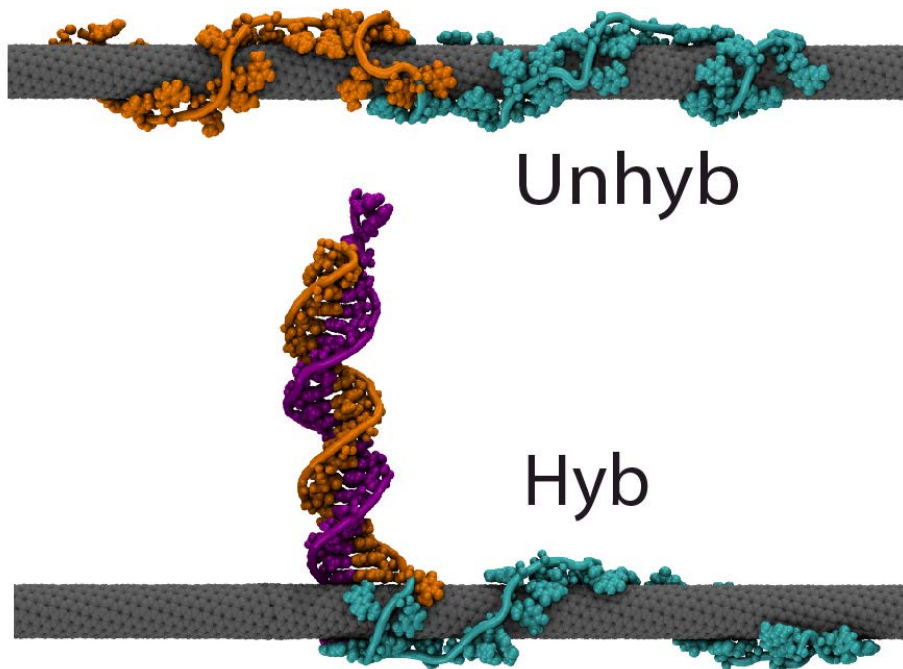
Figure 2.11 Snapshot images of molecular dynamics simulations of the GT15mir19 sensor (Unhyb) and GT15mir19 sensor hybridized with miR-19 (Hyb) after equilibrating for 250 ns. Teal color denotes the $(GT)_{15}$, nanotube-binding sequence, and orange denotes the miR-19 capture sequence. The purple strand denotes miR-19.

The simulations allowed the quantification of nucleobase adsorption to the nanotube

surface. We measured the radial distance of the nucleobases from the nanotube surface

and their stacking angles relative to the nanotube surface (Figure 2.12). We observed

that all bases of the $(GT)_{15}$ nanotube-binding domain remained adsorbed on the

nanotube surface, whereas only 1-2 terminal bases of the double-stranded miR-

19/miRNA capture sequence adsorbed to the nanotube surface. In the simulation

without the complementary strand, all bases of the $(GT)_{15}$ nanotube binding domain

adsorbed to the nanotube surface, as well as most of the bases of the miR-19 miRNA

capture sequence (Figure 2.12).
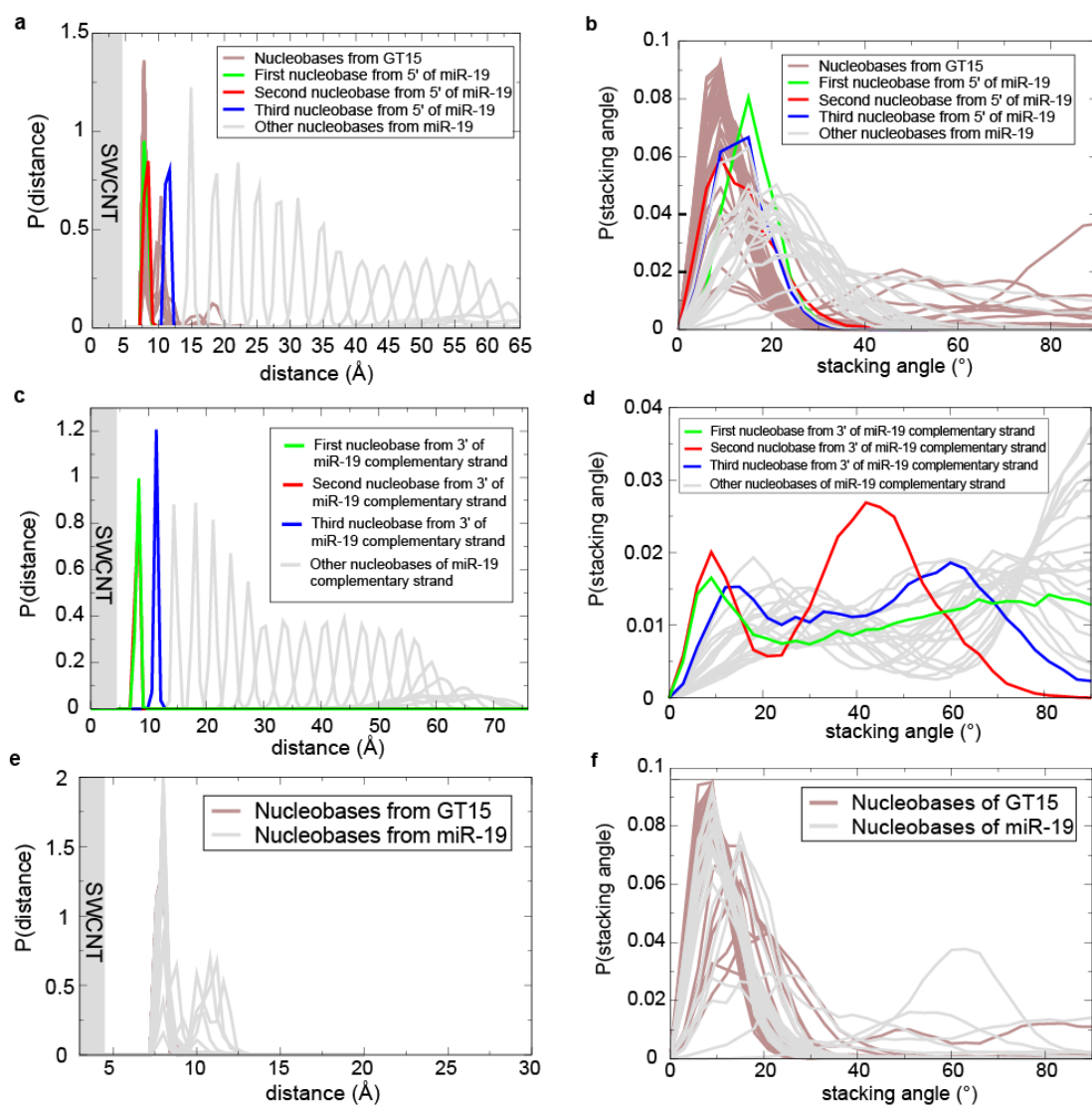
Figure 2.12. Structural parameters of the GT15mir19 sensor complex computed for the (9,4) nanotube via molecular dynamics simulations. **a**, Distribution of radial distance and **b**, stacking angle relative the nanotube for nucleobases from the GT15 nanotube binding domain and miR-19 miRNA capture sequence domain when hybridized to target miR-19. **c**, Distribution of radial distance and **d**, stacking angle relative to the nanotube for nucleobases from the hybridized target miR-19 when hybridized with the miRNA capture sequence. **e** Distributions of radial distance from the nanotube of the miR-19 miRNA capture sequence when target miR-19 is not hybridized. **f**, Stacking angle of miR-19 miRNA capture sequence when target miR-19 is not hybridized.

51

We assessed the thermodynamic concerns regarding the stability of the hybridized duplex in the presence of the nanotube. Molecular dynamics simulations of hybridized miR-19, without the $(GT)_{15}$ nanotube binding domain, in the presence of the nanotube were run using several different initial conditions (Figure 2.13). In all simulations, no de-hybridization of the duplex was observed, suggesting that the nanotube would not destabilize the hybridized duplex. To understand how the partial hybridized state of the DNA is stable on the nanotube (or preferred over single strand adsorption on the nanotube), we conducted a free energy analysis. We used the two schemes shown in Figure 2.14 to estimate the difference in free energy of ssDNA adsorption and dsDNA hybridization at the nanotube surface. As parameters needed for such a calculation are available from Jung et al.[36] for a 17-mer duplex strand, we focus our analysis for this particular DNA length and sequence. For case A, one ssDNA is already adsorbed on the nanotube surface and its complementary partner ssDNA is introduced in the solution like the experimental setup reported in this paper. The change in free energy upon hybridization is approximately -135 kcal/mol (at (300 K, 1 bar), which clearly indicates that hybridization is preferred over adsorption. Similar analysis for case B, where both strands are initially adsorbed on the nanotube surface, the change in free energy upon hybridization (again using values reported by Jung et al.) is approximately +9 kcal/mol. This indicates that when both strands are initially adsorbed (Figure 2.14 Case B), ssDNA adsorption is slightly more favorable than dsDNA hybridization. In our experimental setup of miR-19 hybridization on the nanotube, we expect the case A to be the relevant one as complementary strand is introduced after ssDNA and surfactant are allowed to adsorb on the nanotube surface. Thus, our analysis findings are consistent with the observed hybridization leading to the function of biosensor / reporter.

The analysis suggests that hybridization of the dsDNA is favored if the analyte strand is not initially adsorbed on the nanotube surface, as is the case in our experiments.
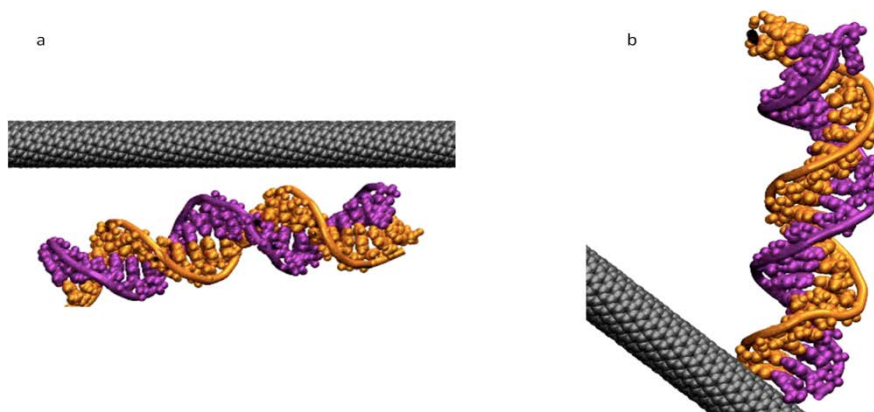
Figure 2.13 Starting configurations of molecular dynamics simulations involving the duplex miRNA capture sequence + miR-19 without the GT$_{15}$ nanotube binding domain. **a**, miRNA capture sequence/miR-19 duplex initially configured parallel to the axial vector of the nanotube **b**, miRNA capture sequence/miR-19 duplex initially configured perpendicular to the axial vector of the nanotube.

$$\Delta G_{\text{hyb on SWCNT}} = G_{\text{dsDNA+SWCNT}} - (G_{\text{ssDNA+SWCNT}} + G_{\text{cDNA}}) = -135 \text{ kcal/mol}$$

$$\Delta G_{\text{hyb on SWCNT}} = (G_{\text{dsDNA+SWCNT}} + G_{\text{SWCNT}}) - (G_{\text{ssDNA+SWCNT}} + G_{\text{cDNA}}) = 9 \text{ kcal/mol}$$
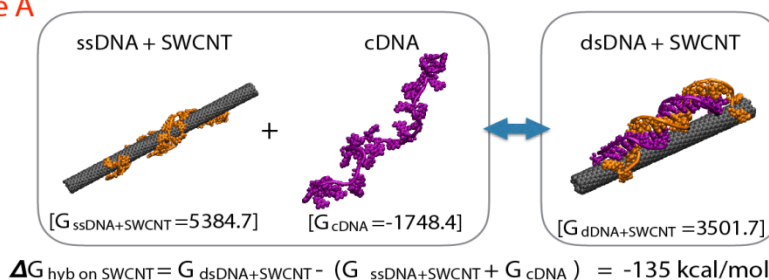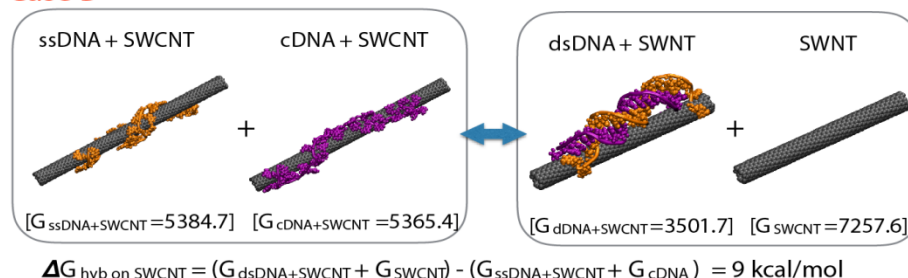
Figure 2.14 Two calculations of hybridization free energy of DNA on the nanotube surface. Graphics are illustrative examples of the reference states and G_{binding} values are taken the work by Jung et al.[36] **Case A** depicts the scenario where single stranded DNA on a nanotube hybridizes with complementary DNA in solution. **Case B** depicts the scenario were both strands are first adsorbed to the nanotube surface.

We also analyzed the molecular dynamics simulations to gain a quantitative understanding of the carbon nanotube spectral response upon hybridization. On comparing the water density as a function of distance at the end of the two simulations, we found a slight increase in the water concentration near the nanotube in the hybridized structure (Figure 2.15a). In addition, we found that the density of phosphate ions as a function of distance from the nanotube decreased upon hybridization (Figure 2.15b). While an increase in local water density is known to cause red-shifting[37] of the nanotube emission wavelength, a decrease in local anionic charge density in the local environment of the nanotube was found to cause a blue-shifting response, according to recent work[34]. As the nanotube emission exhibited a net blue-shift upon hybridization, we thus conclude that the effect of the removal of phosphate charges from the nanotube surface out-competed the effects of increased local water density.
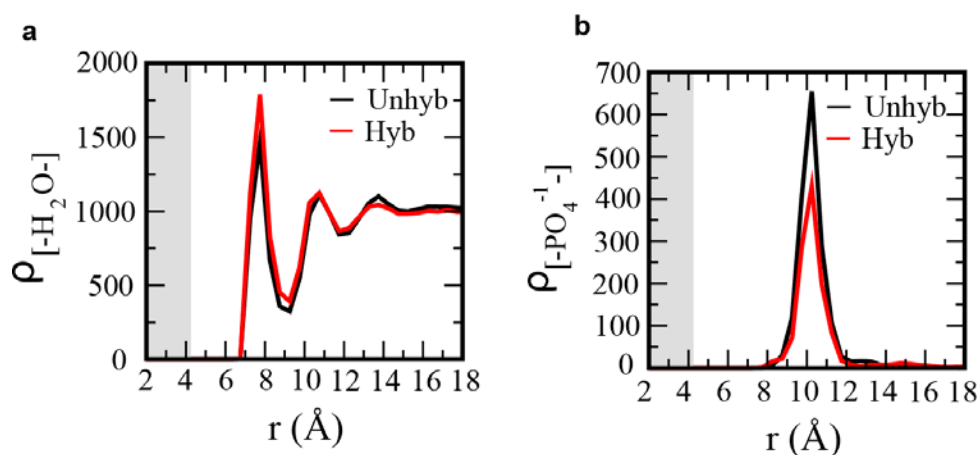
Figure 2.15 Water and phosphate density from the nanotube surface. **a**, Density of water as a function of radial distance from the nanotube, calculated for both simulations. **b**, Density of phosphate groups as a function of radial distance from the nanotube, calculated for the final frame of both simulations.

2.3.2 Effects of amphipathic molecules on sensor response

As the simulations showed an increase in available nanotube surface area upon hybridization, we hypothesized that additional small amphipathic molecules might assemble on this newly exposed nanotube surface to enhance the optical response. Low concentrations of several candidate surfactants (Table 2.1) were tested to determine whether they changed the optical response of the GT15mir19 sensor. Several classes of amphipathic molecules were introduced to the GT15mir19 sensor to assess their potential to modulate the optical response to hybridization. Selected molecules included ionic surfactants, non-ionic triblock copolymers, non-ionic surfactants, PEG-functionalized lipid, and BSA due to their variety of steric and electrostatic properties (Table 2.1). After treatment for 4 hours with each amphipathic molecule, but before addition of target oligonucleotide, emission spectra were measured to assess the effect of each molecule in the absence of target miRNA. The impact on center wavelength and intensity are shown for the (7,5) nanotube, which was similar to the responses of other chiralities (Figure 2.16). All molecules either elicited a blue-shift to varying degrees or had no apparent effect. SDC was an outlier in that the intensity was enhanced 2-3 fold. While other molecules were found to also enhance intensity to different degrees, none matched the effect of SDC.

Table 2.1 Panel of amphipathic molecules tested.

Name	Abbreviation	Class of amphipathic molecule
Sodium deoxycholate	SDC	ionic surfactant
Sodium dodecyl sulfate	SDS	ionic surfactant
Sodium dodecylbenenesulfonate	SDBS	ionic surfactant
Pluronic F-68	Pluronic	non-ionic triblock copolymers
Triton X-100	n/a	non-ionic surfactant
IGEPAL CO-530	IGEPAL	non-ionic surfactant
Span 80	n/a	non-ionic surfactant
Brij 52	n/a	non-ionic surfactant
D-α-Tocopherol polyethylene glycol 1000 succinate	TPGS	non-ionic surfactant (vitamin E)
1,2-distearoyl-sn-glycero-3-phosphoethanolamine-N-[methoxy(polyethylene glycol)-1000] (ammonium salt))	Lipid-PEG	PEGylated lipid
Bovine serum albumin	BSA	protein

Figure 2.16 Baseline response to amphipathic molecules. **a**, Mean peak wavelength and **b**, intensity values of the GT15mir19 complex after incubation with amphipathic molecules. Data is shown for the (7,5) nanotube species. Error bars represent standard deviation from three technical replicates.

For each set of surfactant-treated nanotubes, complementary and non-complementary target oligonucleotides were introduced and incubated for 4 hours. Each amphipathic molecule was tested at a final concentration of 0.2% wt/vol with 2 mg/L of GT15mir19. Endpoint data showed that SDBS and IGEPAL provided the greatest enhancement of target miRNA-induced blue-shifting, followed by SDS, Brij52, and lipid-PEG to a smaller extent (Figure 2.17). The presence of Pluronic, SDC, and Triton X-100 resulted in no apparent blue-shift of the sensor upon introduction of target miRNA, although we note that SDC and Triton X-100 substantially blue-shifted the nanotube before target oligonucleotides were added. The initial blue-shift suggests that these amphiphiles likely coated the nanotube so efficiently as to displace water from the nanotube surface and prevent the capture sequence of the GT15mir19 oligonucleotide from interacting with the nanotube surface prior to hybridization. There are no obvious patterns relating the structure of the amphiphiles to the modulation of the response to miRNA, although there are certain factors that can be

noted. It is not surprising that SDC caused an initial blue-shift and prevented the response to miRNA, for example, because it is a very strong surfactant that is known to efficiently suspend nanotubes and enhance nanotube emission. Pluronic and Triton X-100 are fairly large/bulky surfactant molecules which may have similarly prevented interactions of the capture sequence with the nanotube surface. We also note the structural similarity between SDBS and IGEPAL, the two surfactants that resulted in the largest hybridization-induced enhancements. The supramolecular interactions of the surfactant molecules with each other and the nanotube surface are complex and warrant further study in this context.
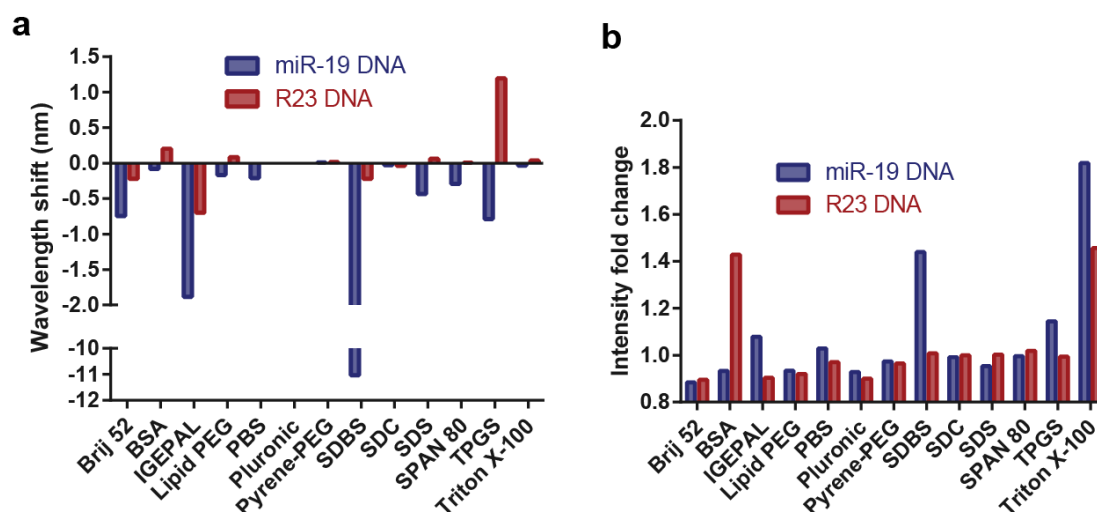
Figure 2.17 Change of the GT15mir19 sensor response to miRNA upon interrogation with a panel of amphiphilic molecules. **a,**Wavelength shift from buffer control and **b,** intensity fold enhancement over buffer control are shown following incubation with the target oligonucleotide or non-complementary control after 4 hours.

The study found that a low concentration (0.2% wt/vol, or 5.7 mM) of sodium dodecylbenzenesulfonate (SDBS), a mild surfactant known to associate with nanotubes[38], resulted in an increase in the degree of hybridization-dependent blue-shifting and intensity enhancement by an order of magnitude (Figure 2.18). In the SDBS-supplemented buffer-only condition and in the presence of the R23 control, the

emission bands broadened slightly but did not increase or shift appreciably. Upon hybridization in the presence of SDBS, all nanotube chiralities exhibited a greatly enhanced blue-shift (Figure 2.19), even those that that did not blue-shift in the absence of SDBS (Figure 2.4). A significant blue-shift in the excitation wavelength was also observed (Figure 2.20). The magnitude of blue-shifting and intensity enhancement (Figure 2.21) upon hybridization of DNA and RNA were identical. In the absence of the target oligonucleotide, the GT15mir19 sensor emission remained stable over a wide-range of SDBS concentrations (Figure 2.22). To further assess the specificity of the sensor response, we introduced an ensemble of randomly generated oligonucleotides. A random library of 23 nt oligonucleotides, with a diversity of approximately 4^{23} different sequences, was introduced to the GT15mir19 sensor, resulting in no response (Figure 2.23). In the presence of the random library, the GT15mir19 sensor maintained sensitivity to miR-19.
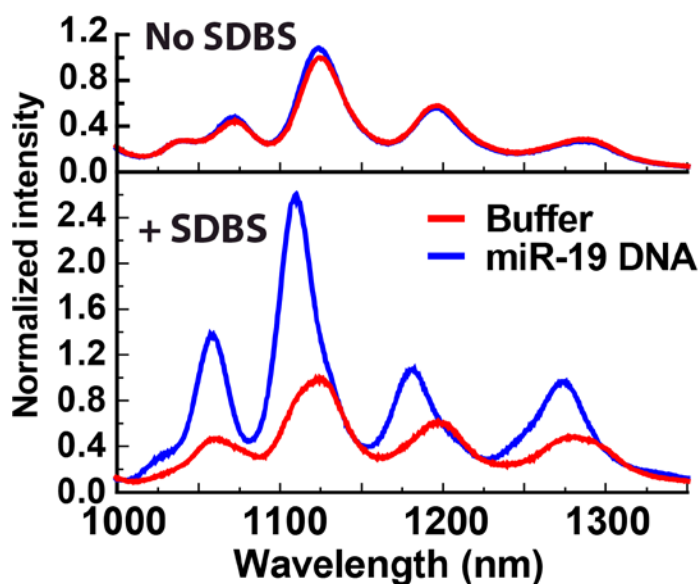
Figure 2.18 Photoluminescence spectra of the GT15mir19 sensor on hybridization with miR-19 in the absence (Top) or presence (Bottom) of SDBS, normalized to the buffer condition .
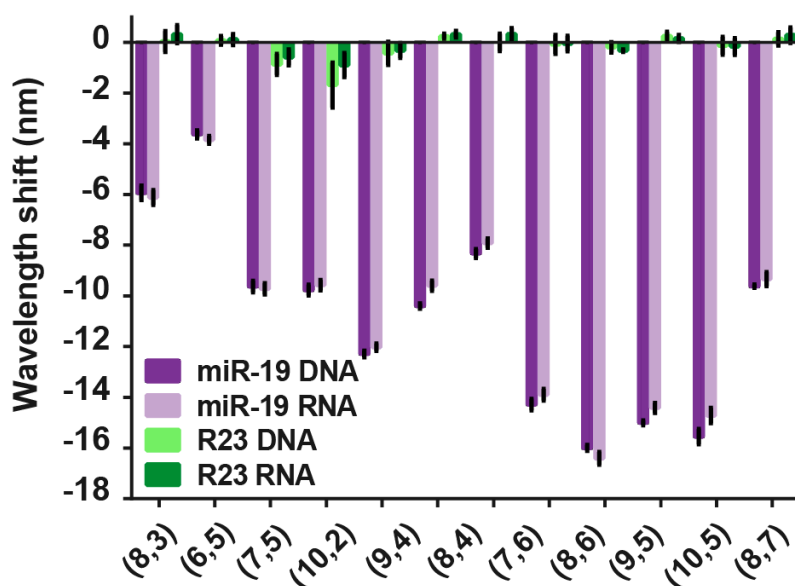
Figure 2.19 Response of the sensor complex to analyte DNA or RNA with the miR-19 sequence, or a control sequence (R23), in the presence of SDBS, for each nanotube chirality.
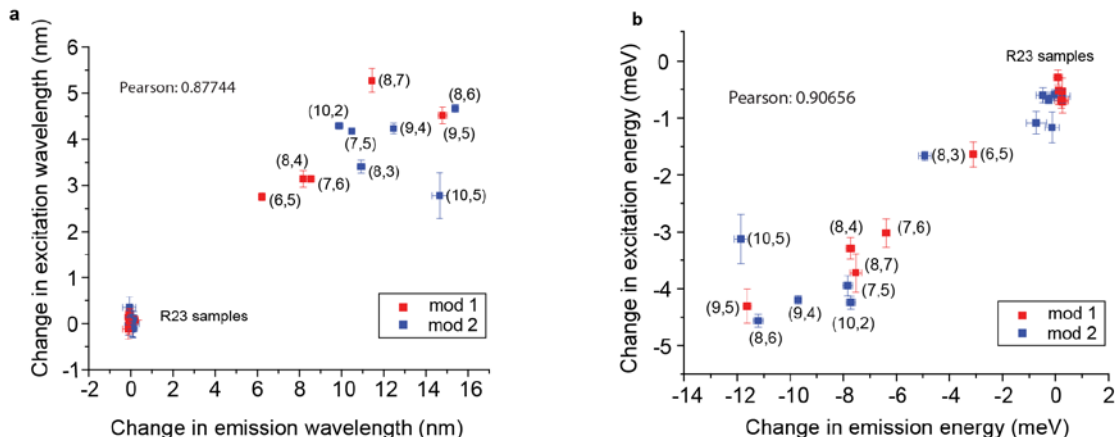
Figure 2.20 Excitation and emission wavelength shifts of the GT15mir19 sensor, calculated from photoluminescence excitation/emission (PL) plots. **a,** Absolute wavelength shifts of the sensor upon introduction of miR-19 RNA or random sequence RNA control (R23). **b,** Change in excitation and emission energy in response to miR-19 RNA or random sequence RNA control (R23). Red = nanotube chiralities that satisfy (2n+m) mod 3 = 1 (mod 1). Blue = nanotube chiralities that satisfy (2n + m) mod3 = 2 (mod2). The Pearson correlation coefficient for the x vs. y values of each graph is indicated. Error bars represent standard error of the mean for n = 3 technical replicates.

59
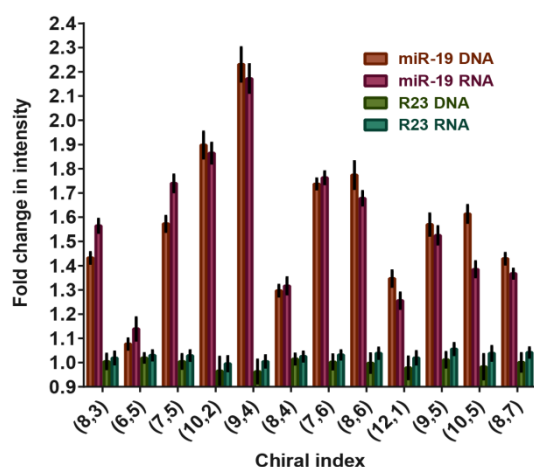
***Figure 2.21 Change in intensity of the GT15mir19 sensor in the presence of 0.2%
SDBS***. Intensity was calculated from photoluminescence excitation/emission plots and
normalized to buffer only control. Error bars represent standard error of the mean for n
= 3 technical replicates.
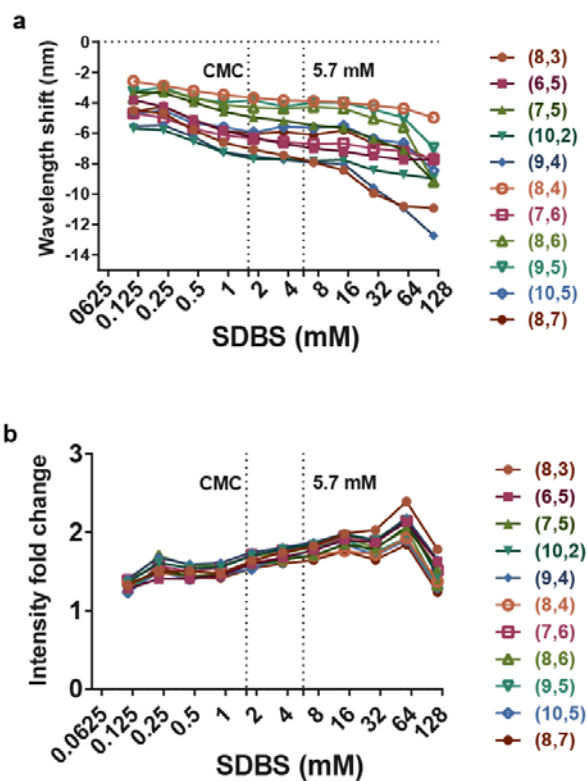
***Figure 2.22 Emission response of the GT15mir19 sensor to different SDBS
concentrations, in the absence of analyte***. **a**, Emission wavelengths of 11 nanotube
chiralities after an overnight incubation with SDBS. **b**, Intensity change in response to
SDBS. Dotted lines indicate critical micelle concentration (CMC, 1.6 mM), and the
concentration of SDBS used in most experiments of this work (5.7 mM, 0.2% w/v).

60
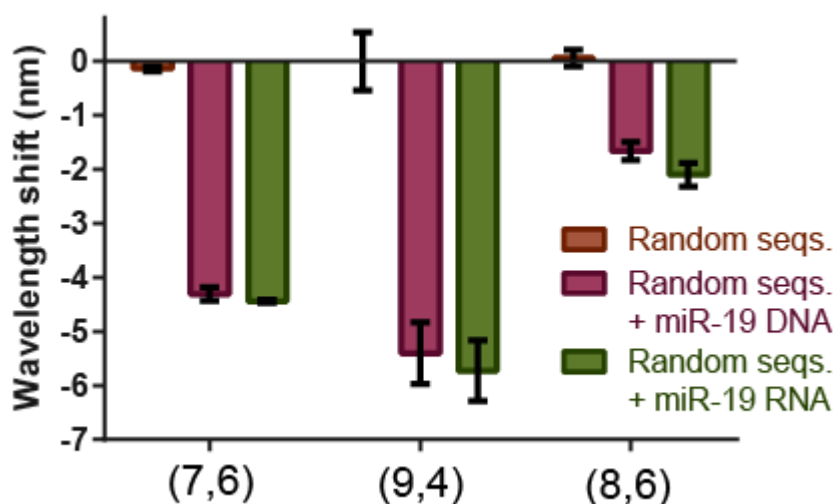
Figure 2.23 Response to random sequence controls. Wavelength response of the GT15mir19 sensor in the presence of random permutations of DNA 23 nucleotides in length (random seqs.) alone, random seqs. with miR-19 DNA, and random seqs. with miR-19 RNA. The responses of three different nanotube chiralities are shown. Error bars represent standard error of the mean for n = 3 technical replicates.

2.3.3 SDBS-induced spectroscopic changes

Previous work has shown that the optical transition energies for DNA-wrapped nanotubes are red-shifted by 10-20 meV (14-22 nm, depending on chirality) and quenched as compared to nanotubes suspended entirely with small molecule anionic surfactants like SDS or SDBS[39-41]. A proposed mechanism has attributed this finding to incomplete coverage of the nanotube surface by DNA, which allows for greater accessibility of water, resulting in an increased polarity of the local solvent environment (higher local dielectric constant) in the immediate vicinity of the nanotube[41]. In the current work, we observed a blue-shifted shoulder in the spectrum of the GTmir19 sensor in the absence of the complementary miR-19 strand upon introduction of SDBS. In light of previous findings, this spectral change suggests that SDBS binds to the exposed surfaces on the DNA-suspended nanotube, causing the displacement of water from the nanotube surface, which produces a slight blue-shift in

the emission. When target RNA or DNA hybridizes and the duplex dissociates from the surface, bare nanotube surface is exposed, allowing SDBS to bind and become the dominant factor determining of the nanotube emission peak wavelength, and intensity. The net effect was a dramatic blue-shift (4-17 nm, depending on the nanotube chirality) and intensity increase (1.3 -2.2 fold) from the assembly of supramolecular complexes of SDBS, triggered by the introduction of target RNA or DNA.

From spectroscopic studies of the GT15mir19 sensor response, we observed a blue shift in nanotube excitation wavelengths, suggesting that the binding of miR-19 RNA and DNA affects the ground state absorption energies in addition to the excited state. Figure 2.20a shows the correlation between the excitation wavelength shift and the emission wavelength shift for the ensemble of chiralities, yielding a Pearson correlation coefficient of 0.87744 (p=0.00188). When plotted as change in energy (Figure 2.20b), the Pearson correlation coefficient is similar 0.90656 (p=0.0007). The environmental effects on nanotube optical properties have been shown to depend at least in part on the mod type of the nanotube[42]. On stratifying the nanotubes by mod type, defined for any nanotube as mod(n-m,3), we found that mod2 nanotubes exhibited an emission energy modulation that increased nearly linearly (R^2=0.9272) with nanotube diameter (Figure 2.24a). Interestingly, for the mod2 nanotubes, the intensity enhancement did not show the same linear relationship with nanotube diameter, although all nanotubes increased in intensity. A maximum was found for nanotubes ~0.9 nm in diameter (Figure 2.24b). A slight difference also became apparent between the responses to target DNA and RNA, with RNA eliciting a slightly enhanced intensity increase for small diameter nanotubes and a slightly dampened enhancement for larger diameter nanotubes. This small, diameter-dependent difference

may be related to the difference in binding strength and hydration between DNA-DNA hybrids and DNA-RNA hybrids[43, 44].
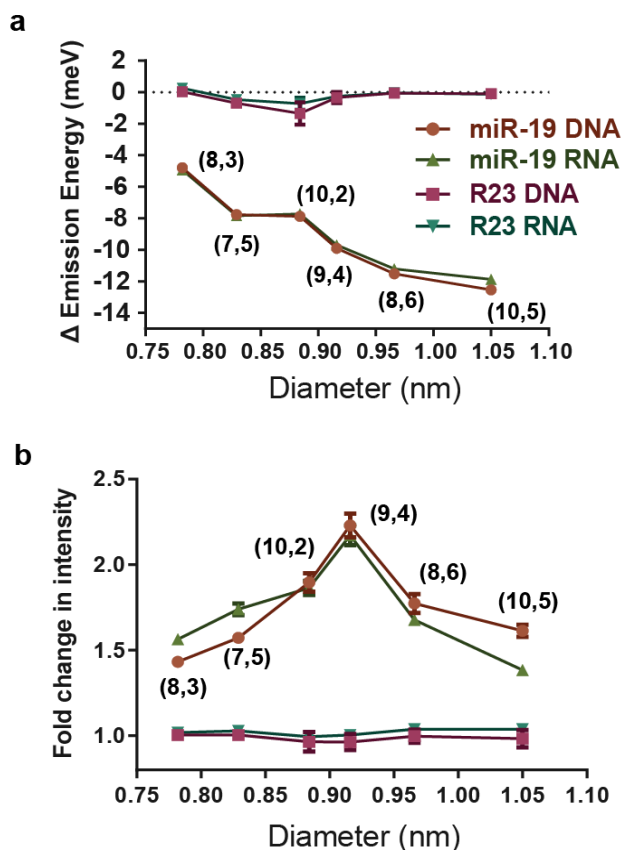
Figure 2.24 Diameter dependence of emission energy change and intensity change.
a, Change in emission energy of the GT15mir19 sensor as a function of nanotube diameter, for mod2 nanotubes. b, Change in GT15mir19 sensor emission intensity, as a function of nanotube diameter, for mod 2 nanotubes. Error bars represent standard error of the mean for n = 3 technical replicates

We present our model of SDBS-mediated hybridization-dependent signal enhancement in Figure 2.25, wherein hybridization triggers SDBS assembly on the newly-exposed nanotube surface.
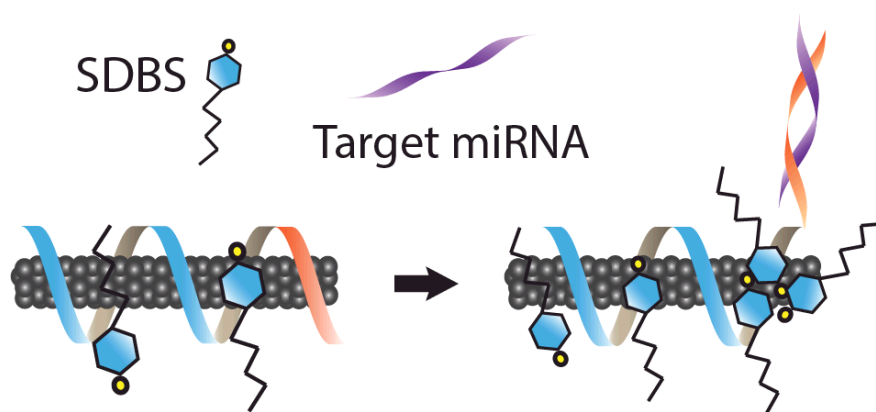
Figure 2.25 Cartoon depicting the proposed mechanism of SDBS-mediated enhancement of the blue shifting response upon hybridization.

2.3.4 Detection limit, kinetics, and breadth of applicability

Given the variety of potential miRNA biomarkers, we sought to assess the modularly of the sensor. The miRNA capture sequence was substituted with several sequences specific to 9 different serum or urine miRNA biomarkers, as well as a sequence not found in humans (*C. elegans* miR-39) used for standardization in clinical applications[45] (Table 2.2). Each GT15mirX sensor was treated with SDBS and interrogated with its respective miRNA target sequence, resulting in a wavelength shift which was comparable to that of the original miR-19 sensor, with slight sequence-to-sequence variations (Figure 2.26 and Figure 2.27). Intensity was similarly enhanced (Figure 2.28). In all of the sensors, no appreciable responses from the control sequence (R23) were observed.

Table 2.2 Disease-relevant miRNA biomarkers

Name	Disease relevance	Biofluid	Ref
miR-21	Diffuse large B-cell lymphoma	serum	9
miR-96	Urothelial carcinoma	urine sediment	10
miR-183	Urothelial carcinoma	urine sediment	10
miR-126	Urinary bladder cancer	voided urine	11
miR-182	Urinary bladder cancer	voided urine	12
miR-152	Healthy control	voided urine	11
miR-494	Acute kidney injury	voided urine	13
miR-509	Healthy control, highly expressed	voided urine	8
miR-39	Found only in C. elegans; spike-in control	N/A	3
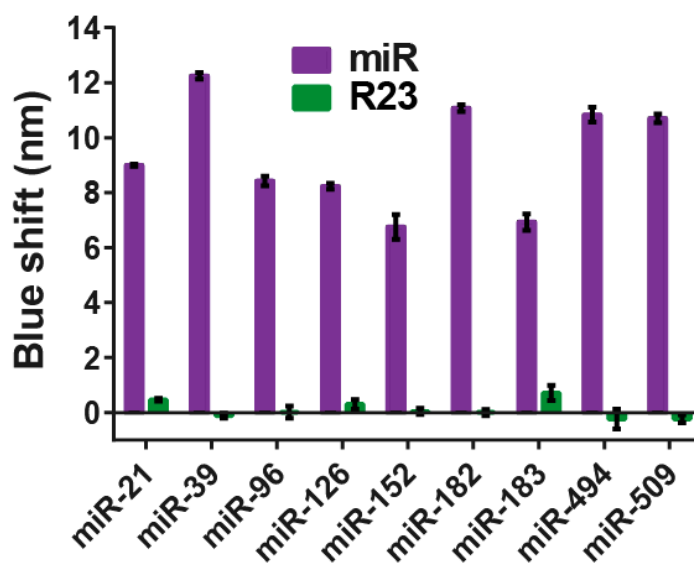
Figure 2.26 Optical responses of the sensor composed of different capture sequences to recognize the specified miRNA sequences (DNA analogues), shown for the (7,5) chirality.
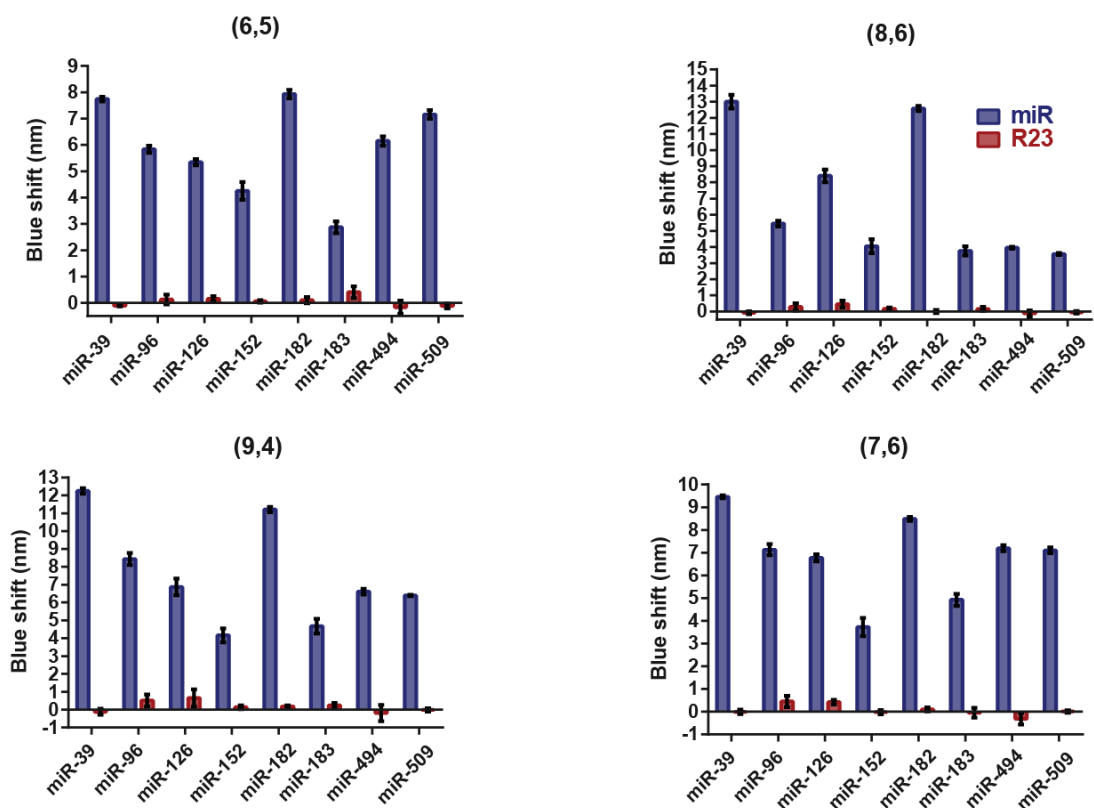
Figure 2.27 Emission wavelength response of GT15mirX sensors to their complementary miR biomarker sequence or R23 non-complementary control (DNA). The responses of four nanotube chiralities are shown. Error bars represent standard error of the mean for n = 3 technical replicates.
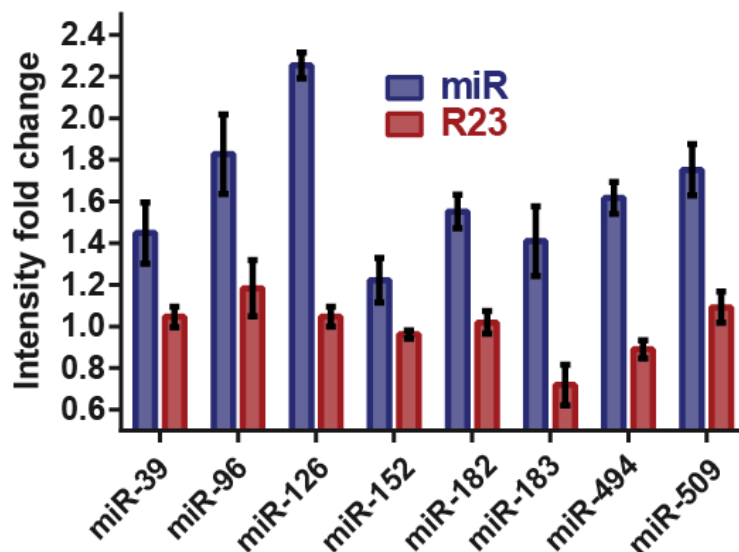
Figure 2.28 Intensity response of the GT15mirX sensors after the introduction of target miR sequences or R23 non-complementary control. The response of the (7,5) nanotube is shown, normalized to the buffer only control. Error bars represent standard error of the mean for n = 3 technical replicates.

To determine if the SDBS-GT15mirX sensor could discriminate among similar sequences, three related sequences from the miR-200 family were selected. The miR-200 family plays an essential role in the epithelial-to-mesenchymal transition (EMT)[46] in cancer. Focusing on the wavelength response of the (9,4) nanotube chirality, we observed a high degree of discrimination between the three sequences after one hour of incubation (Figure 2.29). Complete time-course data for both the (9,4) and (8,6) nanotubes (Figure 2.30 and 2.31, respectively) revealed that the intensity increase provided near-perfect discrimination in most cases. Although the SDBS-GT15mirX sensor responded to target miRNA via both wavelength shifting and intensity changes, we assessed detection limits, kinetics, and other sensor characteristics using the wavelength response, due to the inherent quantifiability and internal standard provided by this mode.
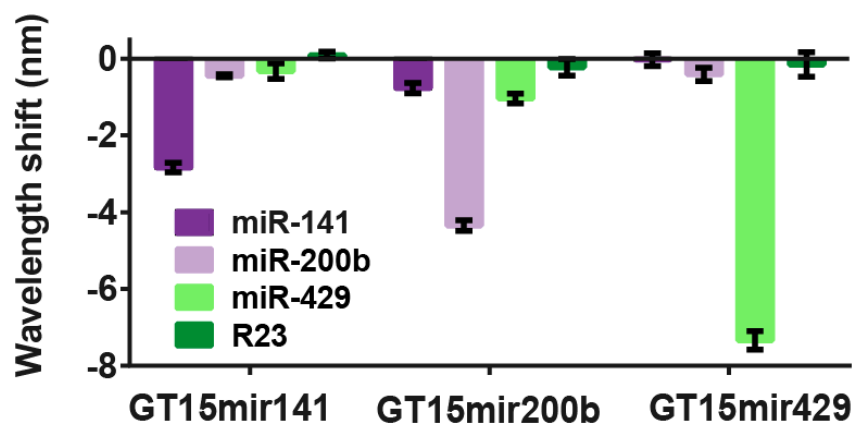
Name	Sequence
miR-141	5'-TAACACTGTCTGGTAAAGATGG-3'
miR-200b	5'-TAATACTGCCTGGTAATGATGA-3'
miR-429	5'-TAATACTGTCTGGTAAAACCGT-3'

Figure 2.29 Intensity response of the GT15mirX sensors after the introduction of target miR sequences or R23 non-complementary control. The response of the (7,5) nanotube is shown, normalized to the buffer only control. Error bars represent standard error of the mean for n = 3 technical replicates
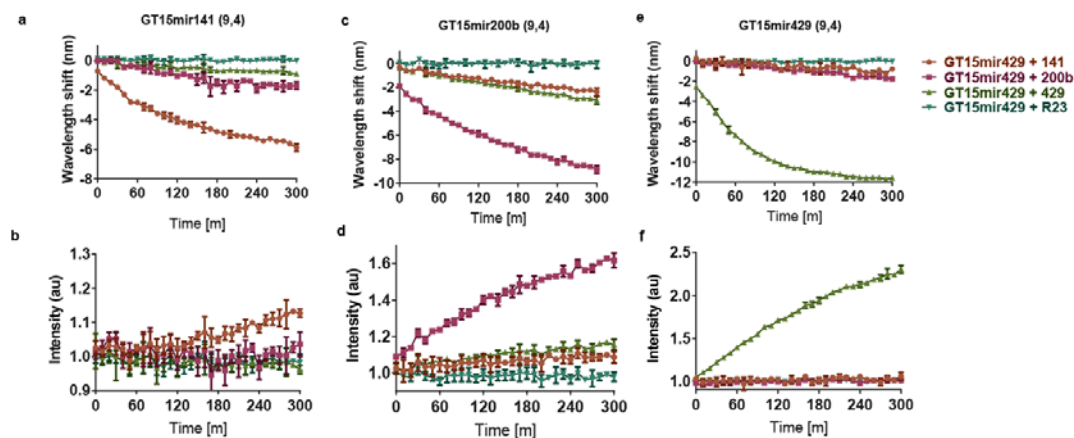
Figure 2.30 Kinetic response of the GT15mirX sensor to three closely-related sequences for the (9,4). The response of the (9,4) chirality is shown. a and b, wavelength shift and intensity change of the sensor specific for miR-141 (GT15mir141). c and d, wavelength shift and intensity change over time for sensor specific for miR-200b (GT15mir200b). e and f, wavelength shift and intensity fold change over time for sensor specific for miR-429 (GT15mir429). Error bars represent standard error of the mean for n = 3 technical replicates.
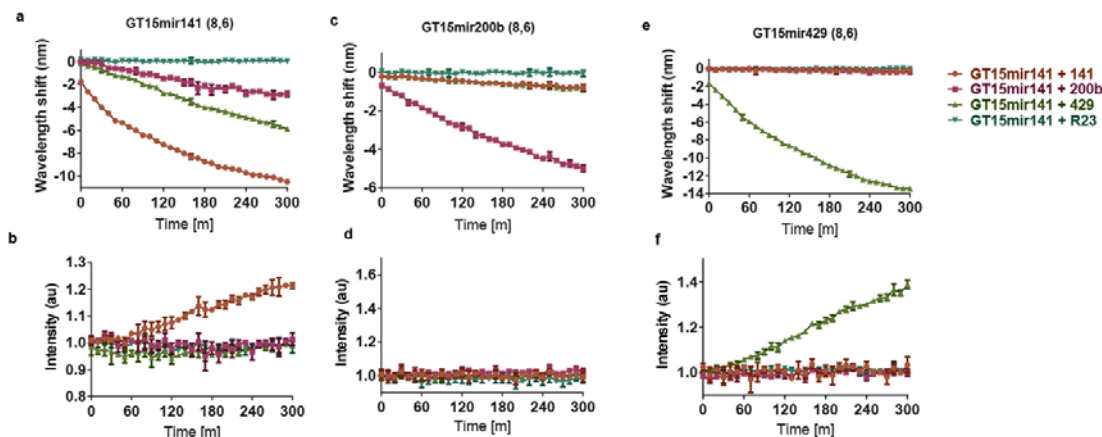
Figure 2.31 Kinetic response of the GT15mirX sensor to three closely-related sequences for the (8,6). The response of the (8,6) chirality is shown. **a** and **b**, wavelength shift and intensity fold change over time for sensor specific for miR-141 (GT15mir141). **c** and **d**, wavelength shift and intensity fold change over time for sensor specific for miR-200b (GT15mir200b). **e** and **f**, wavelength shift and intensity fold change over time for sensor specific for miR-429 (GT15mir429). Error bars represent standard error of the mean for n = 3 technical replicates.

To determine the limit and range of detection, a dose-response curve of the sensor was constructed over several orders of magnitude of miR-19 concentrations. At a minimal sensor concentration of 0.02 mg/L, the limit of detection of miRNA was between 10 and 100 pM (500 attomoles to 5 femtomoles) (Figure 2.32). Signal saturation occurred at a high concentration between 1 and 10 nM. The dynamic range was tuned by adjusting the concentration of the GT15mir19 sensor to cover at least 5 orders of magnitude, from 10 pM to 1 uM (Figure 2.33). We calculated the number of binding sites using the mass of DNA used to suspend 1 mg of nanotubes (see Methods). We estimated that 2.117 nM of miR-19 binding sites were available in a solution of 0.02 mg/L of the GT15mir19 sensor, consistent with the observed saturating range of concentrations (between 1 and 10 nM).
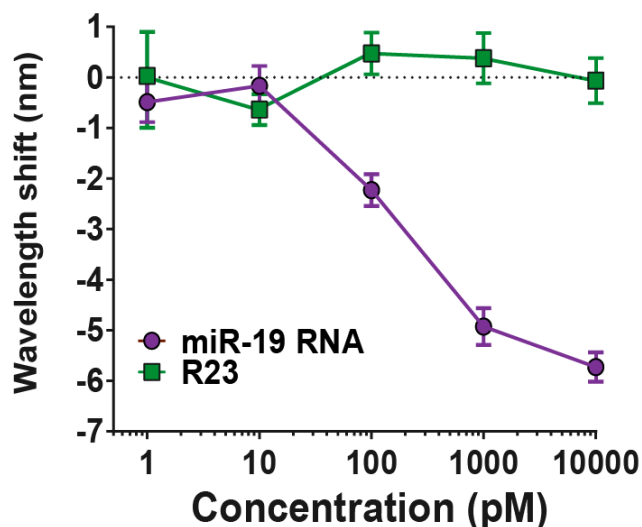
Figure 2.32 Dose-response curve of the GT15mir19 sensor, shown for the (7,6) nanotube species.
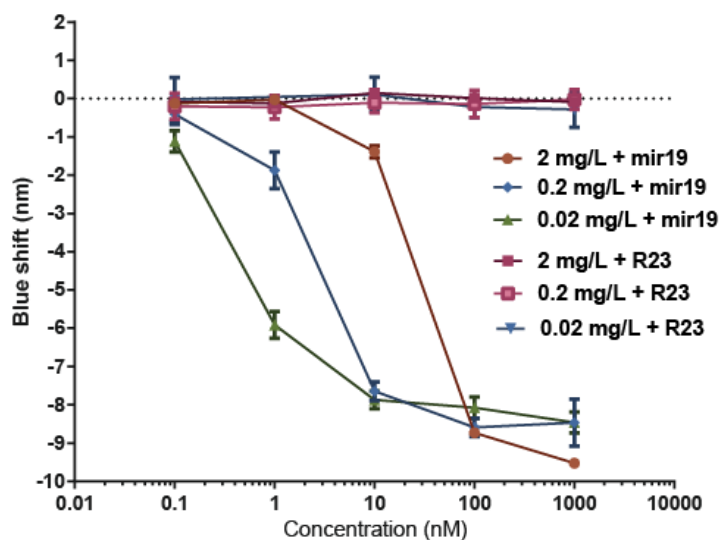
SWCNT conc.	LOD	Binding sites	Saturating range
2 mg/L	1 nM to 10 nM	211.7 nM	100-1000 nM
0.2 mg/L	100 pM to 10 nM	21.17 nM	10-100 nM
0.02 mg/L	10 pM to 100 pM	2.117 nM	1-10 nM

Figure 2.33 Dose-response curves of the GT15mir19 sensor response, using three different sensor concentrations. Table indicates observed limit of detection (LOD), calculated number of binding sites, and measured saturating range of the sensor. Error bars represent standard error of the mean for n = 3 technical replicates.

The kinetics of both DNA and miRNA detection were assessed via transient measurements. The kinetics of eleven different nanotube chiralities were measured by excitation/emission spectroscopy (Figure 2.34). Within 10 minutes of introducing the analyte to the sensor, significant blue-shifting was discerned. The rate of blue-shifting behaved with pseudo-first order kinetics and showed no obvious dependence on nanotube structure (Figure 2.35). The sensor kinetics were consistently faster for DNA (1.8x on average), as compared to RNA (Figure 2.36). We ascribe this difference to the longer persistence length and higher rigidity of single-stranded RNA as compared to single-strand DNA[47].
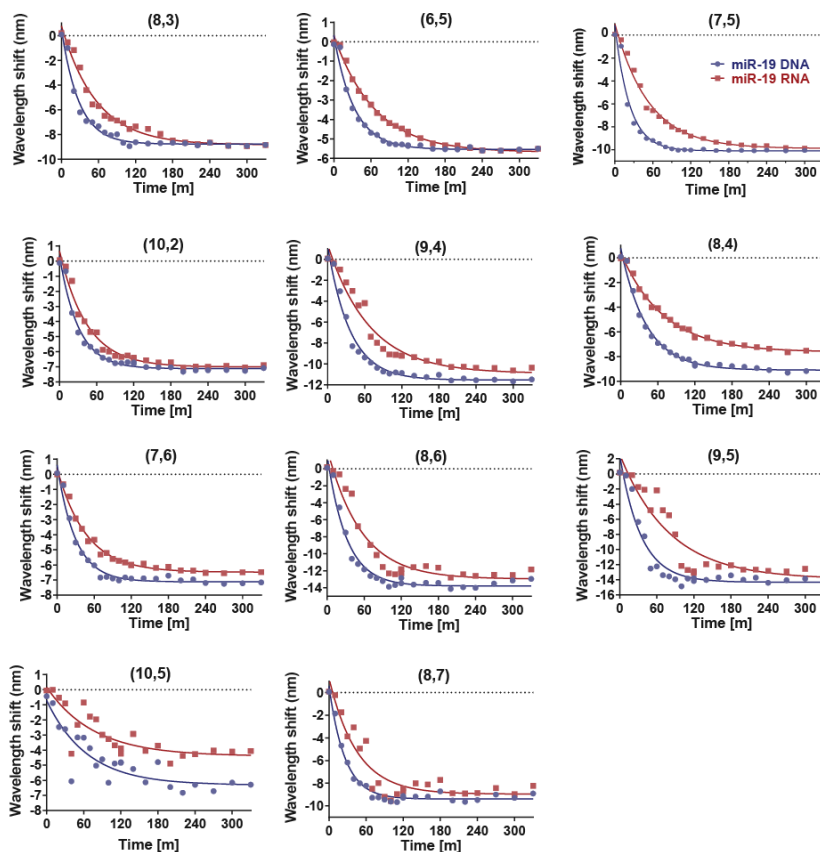
Figure 2.34 Kinetic data for all measured chiralities of the GT15mir19 sensor after addition of miR-19 DNA or miR-19 RNA. Data was acquired in 10-minute intervals. All data is fitted to an exponential decay, $y = y_0\, e^{-kt}$.
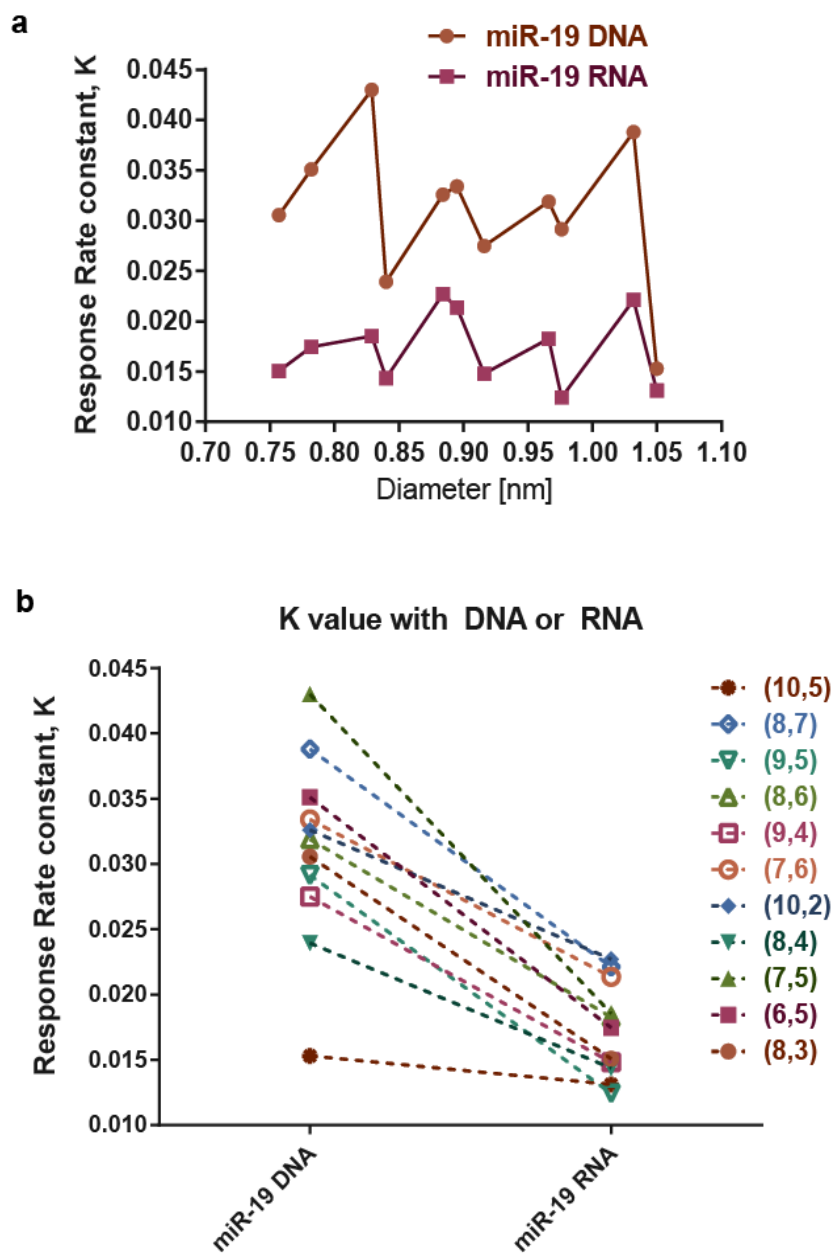
Figure 2.35 Comparison of the response rate of the GT15mir19 sensor to DNA or RNA versions of the target, for eleven different nanotube chiralities. **a**, Rate constant K of the GT15mir19 wavelength response after addition of miR-19 DNA or RNA, arranged according to nanotube diameter. **b**, Comparison of rate constants of each nanotube chirality, in response to miR-19 DNA and miR-19 RNA.

72
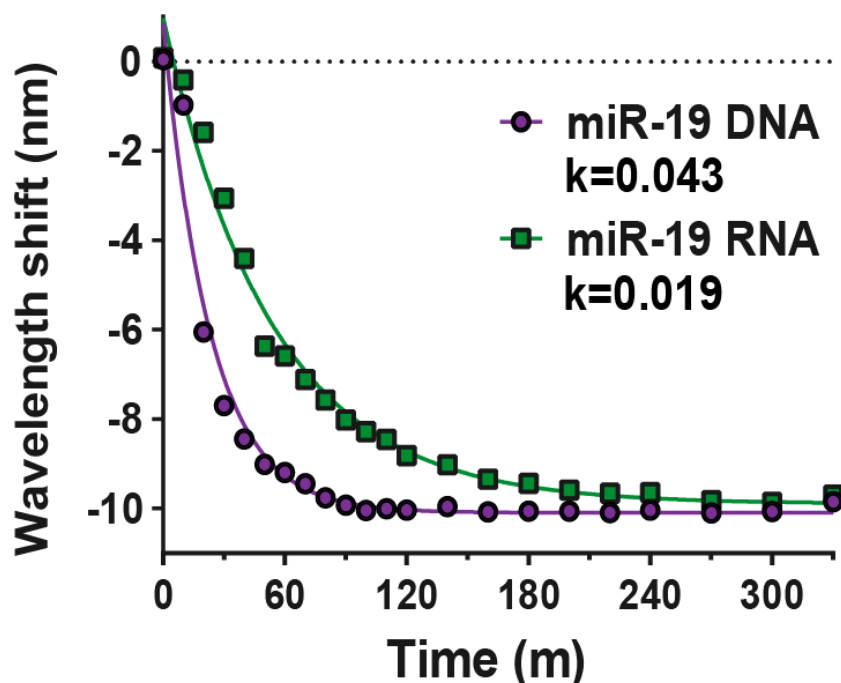
Figure 2.36 Kinetics of the sensor response upon interrogating with miR-19 RNA or the DNA analogue, fitted with the exponential function, $y = y_0 \, e^{-kt}$*.* R^2=0.97 and 0.99 for DNA and RNA, respectively.

To test if the composition of the miRNA capture sequence influenced sensor kinetics, we compared the response rates for the sensor using 8 different miRNA capture sequences (Figure 2.37). On comparing the sensor kinetics as a function of guanine content, we found a significant correlation, with Pearson coefficients of -0.74195 (p=0.035) for the (9,4) nanotube and -0.77215 (p=0.0248) for the (8,6) nanotube (Figure 2.38). This result may be explained by the high affinity of guanine for the nanotube surface, which was determined previously via both molecular dynamics and *ab initio* calculations[48] to fall in the order: G > A > T > C. Thus, the affinity of guanine to the nanotube surface may slow the hybridization process. The content of other nucleotide bases, as well as the overall ΔG of hybridization, did not show any statistically significant correlations (Figure 2.39 and 2.40).

73
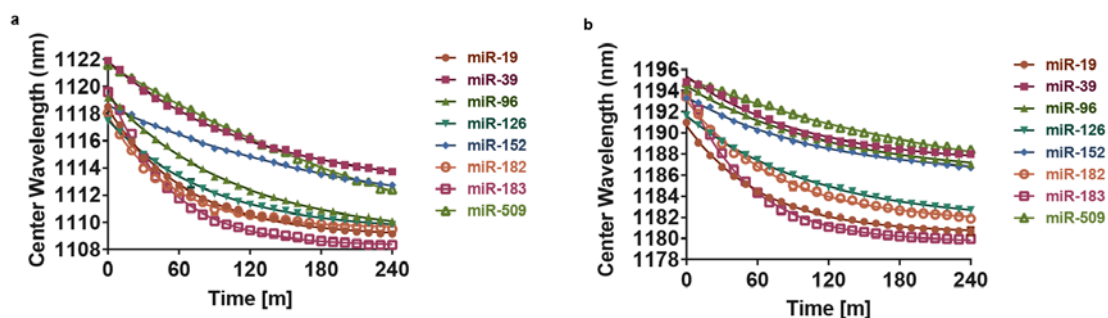
Figure 2.37 Kinetics of the wavelength response of GT15mirX sensors after addition of target miR biomarker sequences. **a**, Response of the (9,4) nanotube chirality. **b**, Response of the (8,6) nanotube chirality. Smooth curves are fitted exponential decays, $y = y_0\, e^{-kt}$.
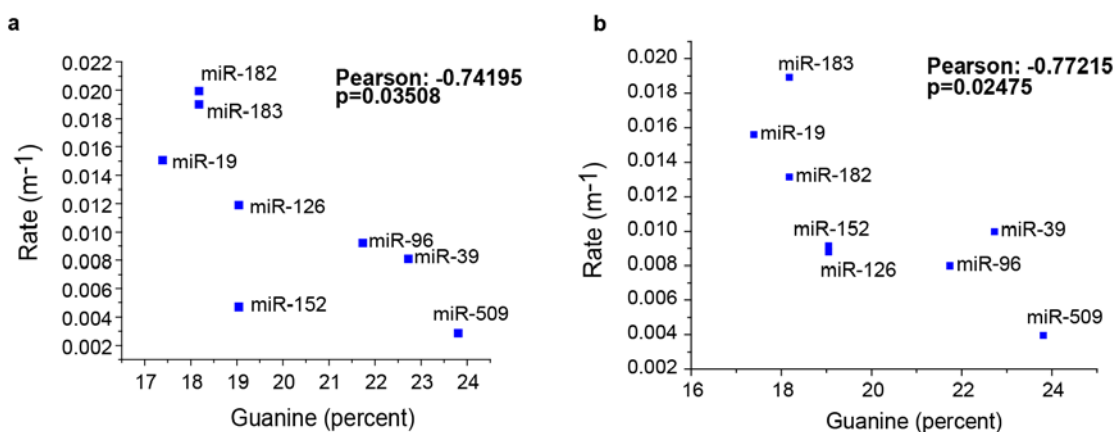
Figure 2.38 GT15mirX sensor response rates vs. guanine content of the miRNA capture sequences. **a**, Response of the (9,4) nanotube chirality. **b**, Response of the (8,6) nanotube chirality. Pearson correlation coefficients are indicated.
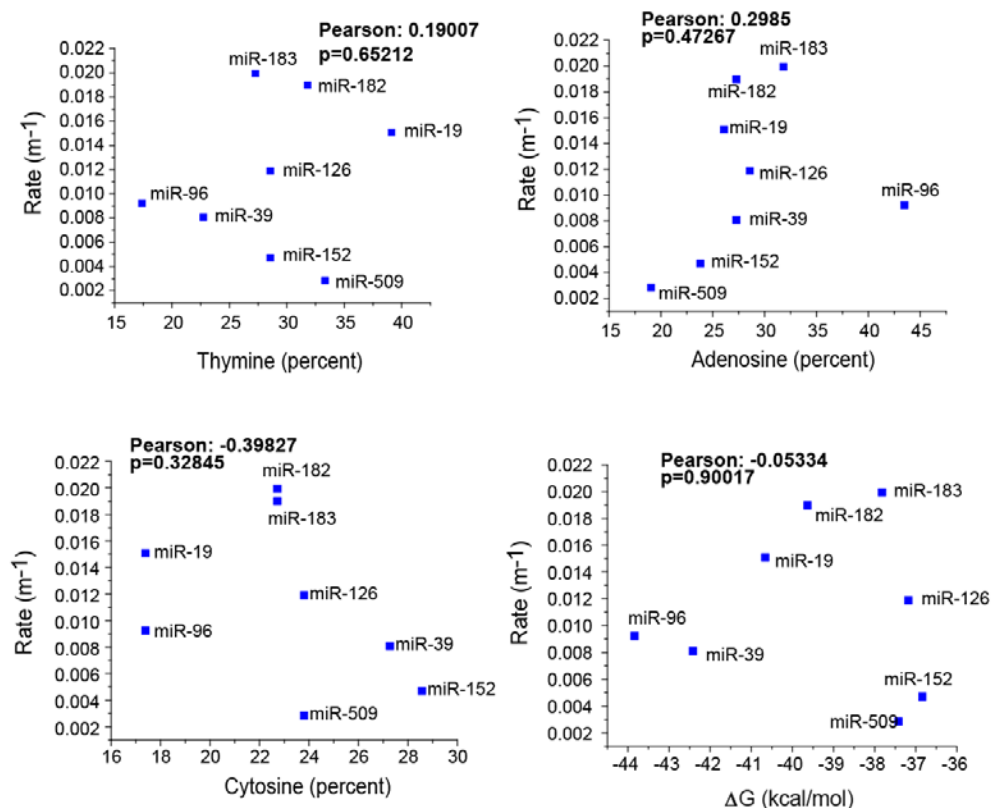
Figure 2.39 GT15mirX sensor response rates of the (9,4) vs. thymine, adenosine, and cytosine content of the miRNA capture sequence, or free energy of hybridization of the miRNA capture sequence. Response of the (9,4) chirality was measured. No statistically significant correlations were found.
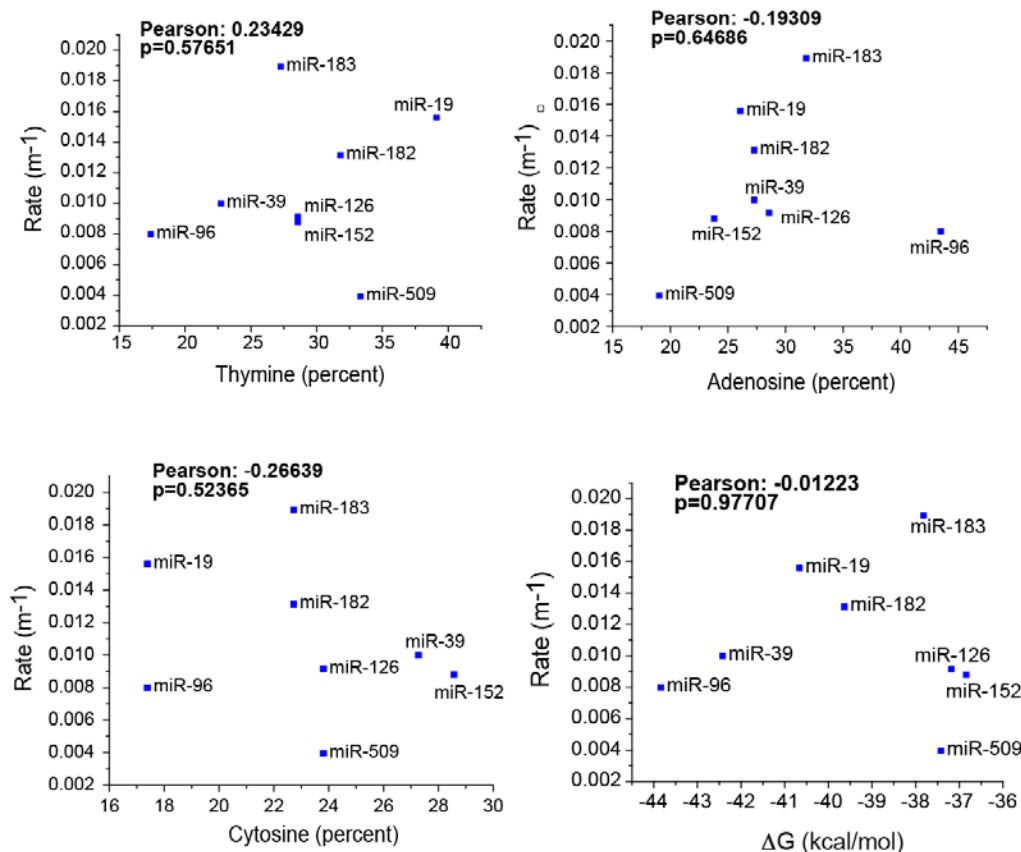
Figure 2.40 GT15mirX sensor response rates of the (8,6) vs. thymine, adenosine, and cytosine content of the miRNA capture sequence, or free energy of hybridization of the miRNA capture sequence. Response of the (8,6) chirality was measured. No statistically significant correlations were found.

To better understand how the length and thermodynamics of hybridization relate to the optical response of the nanotube, we conducted several experiments using modified analyte oligonucleotides. We interrogated the G15mir19 sensor using analyte sequences between 10 and 23 nucleotides long which were complementary to either the 3′ terminal end of the miRNA capture sequence, or the middle of the sequence, as depicted in Figure 2.41. We found that, in general, a shorter analyte sequence resulted in a smaller blue-shifting response of the nanotube, down to approximately 10 nucleotides, where there was virtually no response (Figure 2.42). Additionally, the magnitude of the blue-shifting response was consistently smaller when the analyte sequence was designed to hybridize to the middle of the capture sequence. This difference may be explained by the affinity of the capture sequence to the nanotube, as suggested by the results of the fluorophore quenching experiment, MD simulations, and free energy analyses[48].


```
5'-(GT)15--TCAGTTTTGCATAGATTTGCACA-3'
                      3'-CTAAACGTGT-5'
5'-(GT)15--TCAGTTTTGCATAGATTTGCACA-3'
          3'-AGTCAAAACG-5'
```
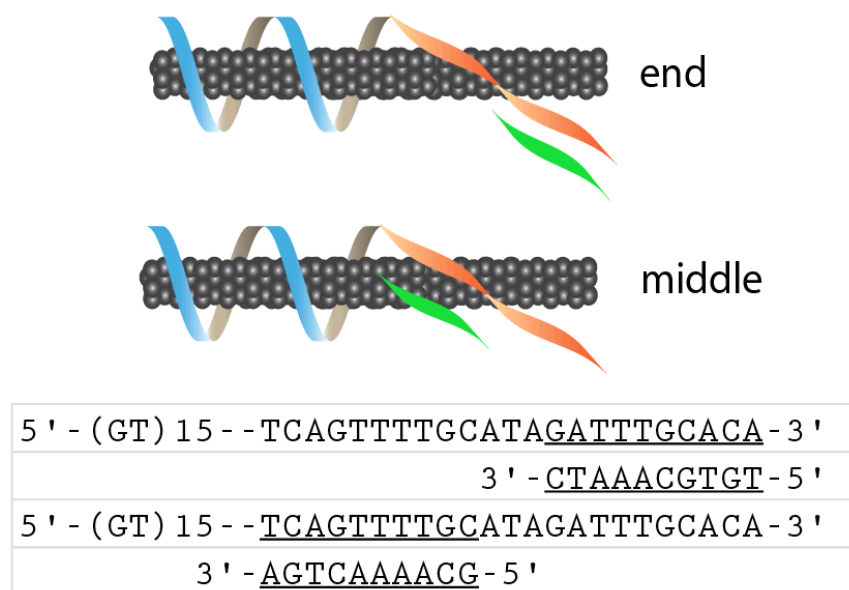
Figure 2.41 Cartoon illustrating truncated analyte sequences complementary to the middle or 3' end of the capture sequence.
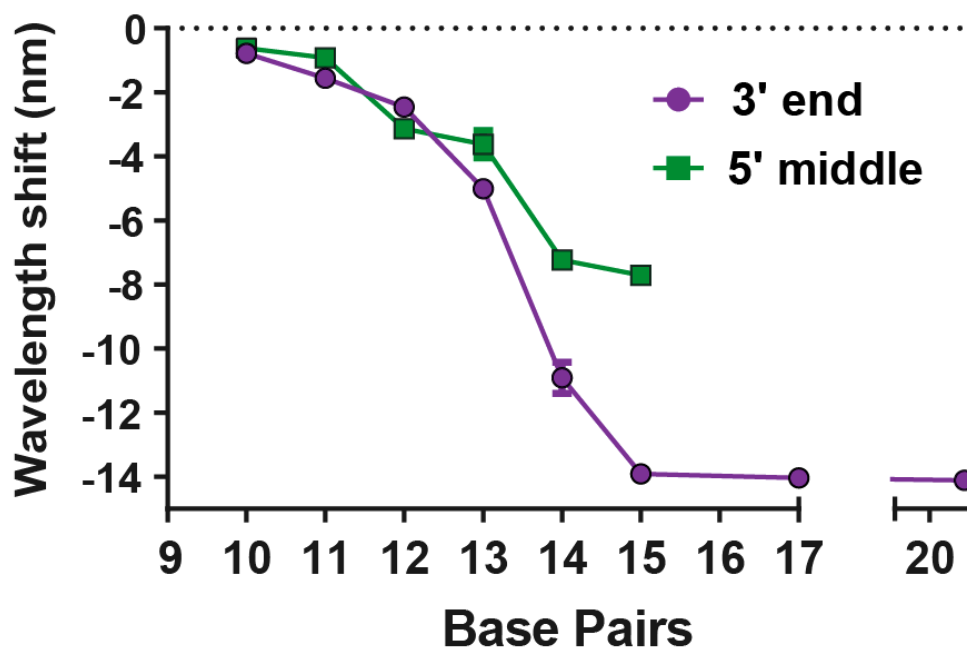
Figure 2.42 Emission response of the sensor to a series of truncated sequences (length specified in the x axis) designed to hybridize to either the middle or 3' end of the capture sequence.

To assess its broad applicability for the detection of different nucleic acid types, we assessed whether the sensor could detect oligonucleotides longer than miRNA sequences. First, we assessed how the GT15mir19 sensor would respond to a long oligonucleotide designed to contain a complementary sequence flanked by non-complementary sequences. On interrogating the sensor with R23-mir19-R23, a 69-bp oligonucleotide with 23 complementary bases in the middle of the sequence, the sensor emission red-shifted—opposite of the expected blue-shifting response—even in the presence of SDBS (Figure 2.43, shown for the (8,6) chirality). We therefore hypothesized that, when R23-mir19-R23 hybridizes to the recognition sequence, the R23 portion at the 5′ end may disrupt the sensor function by increasing the phosphate content near the nanotube surface to cause a red-shift of the nanotube emission. To test this hypothesis, we designed two long oligonucleotide sequences, R23-mir19 and

78

mir19-R23, placing the R23 portion at either the 3′ end or 5′ end. The proposed

orientation upon binding and predicted spectral shifts are shown in Figure 2.44a—the

two sensors were hypothesized to give the opposite spectral responses. Upon

interrogating the sensor, the R23-mir19 oligonucleotide produced a red-shifting

response, and the mir19-R23 oligonucleotide produced a blue-shift, as predicted

(Figure 2.44b). The magnitude of the blue-shift in response to mir19-R23 was smaller

than that produced by the miR-19 control, suggesting that the unhybridized single-

stranded nucleotides may bind to the nanotube surface, diminishing the response. This

hypothesis warrants further study. Regardless, we conclude that sensors based on the

GT15 nanotube binding domain and a general capture sequence can be extended to

detect longer nucleic acid sequences, but the orientation of the oligonucleotide is

critical for eliciting a desired spectral response.
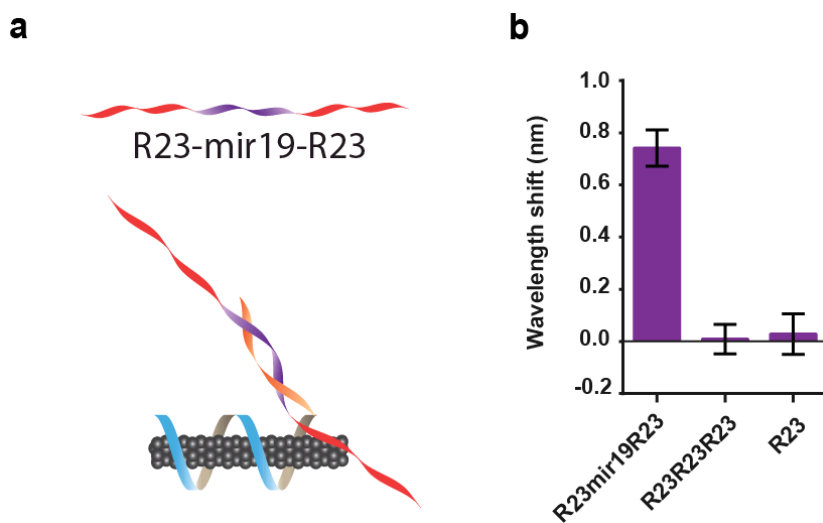
Figure 2.43 Assessing the effect of hybridization location. **a,** Cartoon illustrating a modified analyte sequence and expected configuration upon binding to the GT15mir19 sensor. **b,** Spectral response of the (8,6) nanotube species upon introduction of long analyte sequences to the sensor
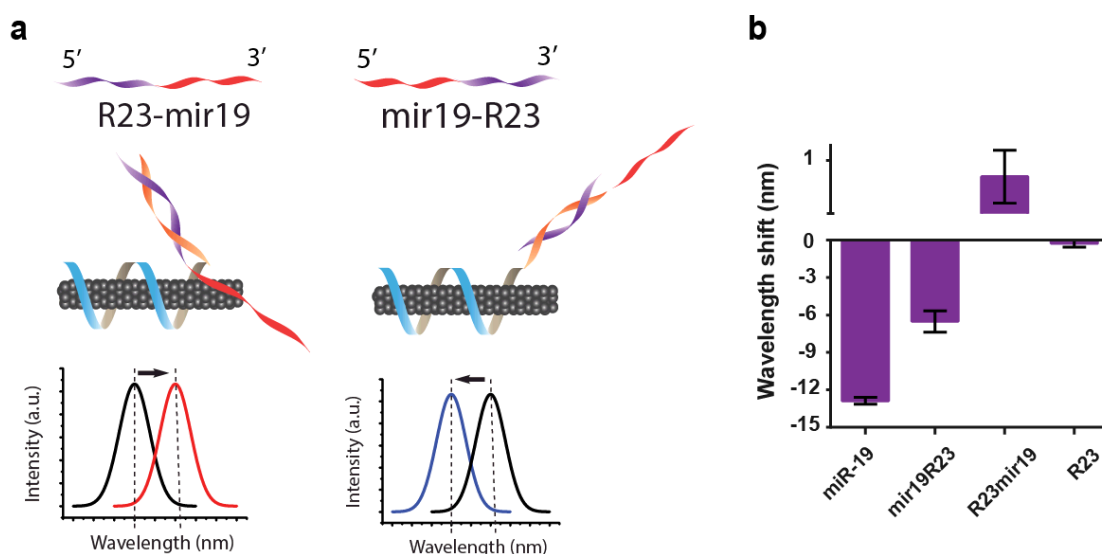
Figure 2.44 Effect of overlap orientation on wavelength shift. **a,** Cartoons depicting experiment designed to assess orientation of partial complementary sequences, as well as predicted sensor responses. **b,** Response of the (8,6) nanotube species upon interrogating the GT15mir19 sensor sensor with the partial complementary oligonucleotides. All error bars represent standard deviation for n = 3 technical replicates.

2.3.5 Measurements of single sensor complexes

We assessed the sensor function on the single-nanotube level via spectral imaging.

The sensor was deposited on a lysine-coated glass surface with sodium dodecyl sulfate

(SDS). We then used hyperspectral microscopy[29] to spectroscopically image the (9,4)

nanotube (Figure 2.45a). The blue-shifting of single nanotubes was apparent upon

interrogating the sensor with miR-19 RNA, but not upon introducing R23 RNA

(Figure 2.45b-d). Using the number of binding sites per nanotube length determined

from AFM measurements (Figure 2.7), we attempted to estimate the number of copies

of miRNA detected per nanotube. Because a diffraction-limited spot could contain a

nanotube up to ~600nm long[49], we estimate a range of detection between 1-60 miRNA

molecules.
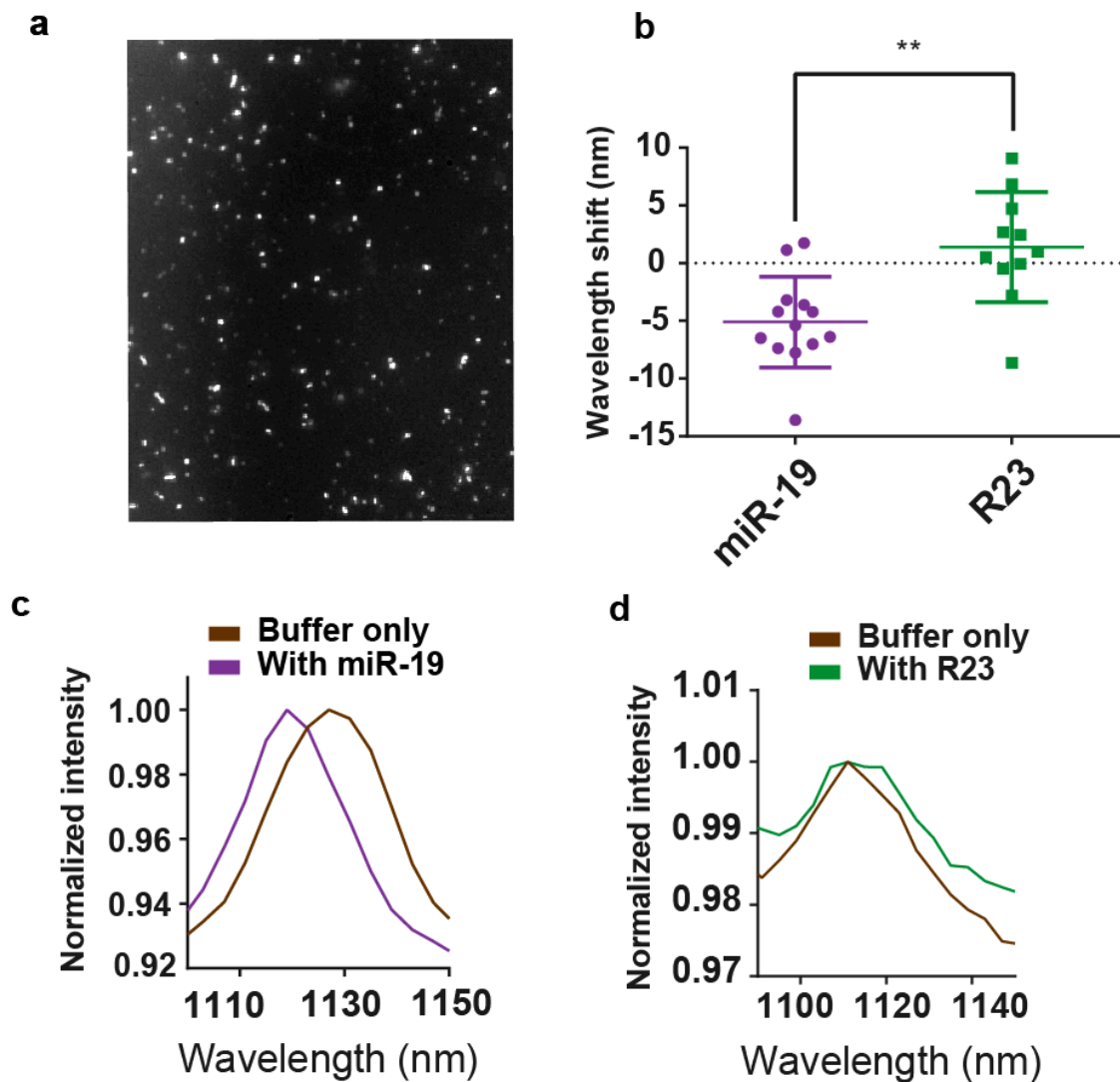
Figure 2.45 Single nanotube response to miRNA hybridization. **a,** Broadband near-infrared image of the GT15mir19 sensor adsorbed to a glass surface. **b,** Change in emission wavelength of individual (9,4) nanotubes after incubation of the surface-bound complexes with miR-19 RNA or R23 RNA at room temperature (unpaired, two-tailed t test, p=0.0014, n = 24). **c,** Representative spectra of the same sensor complex in the buffer-only condition and 50 min after introducing miR-19. **d,** Representative spectra of the same sensor complex in the buffer-only condition and 50 min after introducing the R23 control sequence.

2.3.6 Sensor multiplexing

We assessed the potential for the multiplexed detection of several miRNA sequences via the use of different nanotube chiralities. Two nanotube preparations enriched for different nanotube chiralities were suspended with binding sequences for either miR-19 or miR-509. A preparation enriched in large diameter species, (Nano-C APT-200) was suspended by the GT15mir19 sequence, and a CoMoCAT preparation enriched in small diameter species was suspended using the GT15mir509 sequence. Excitation/emission plots found that the GT15mir19 sensor, encapsulating the APT-200 nanotubes, effectively lacked the (6,5) species (Figure 2.46a), while the GT15mir509 sensor, encapsulating the narrow-diameter enriched CoMoCAT preparation, lacked the (8,6) species (Figure 2.46b). Absorbance spectra verified the differential enrichment of nanotube chiralites between these samples (Figure 2.47). After mixing the two nanotube preparations, each miRNA sequence added individually was recognized by the appropriate nanotube chirality (Figure 2.48). When miR-19 and miR-509 were added together, the spectral shift almost identically recapitulated the shifts seen when either miRNA was added alone.
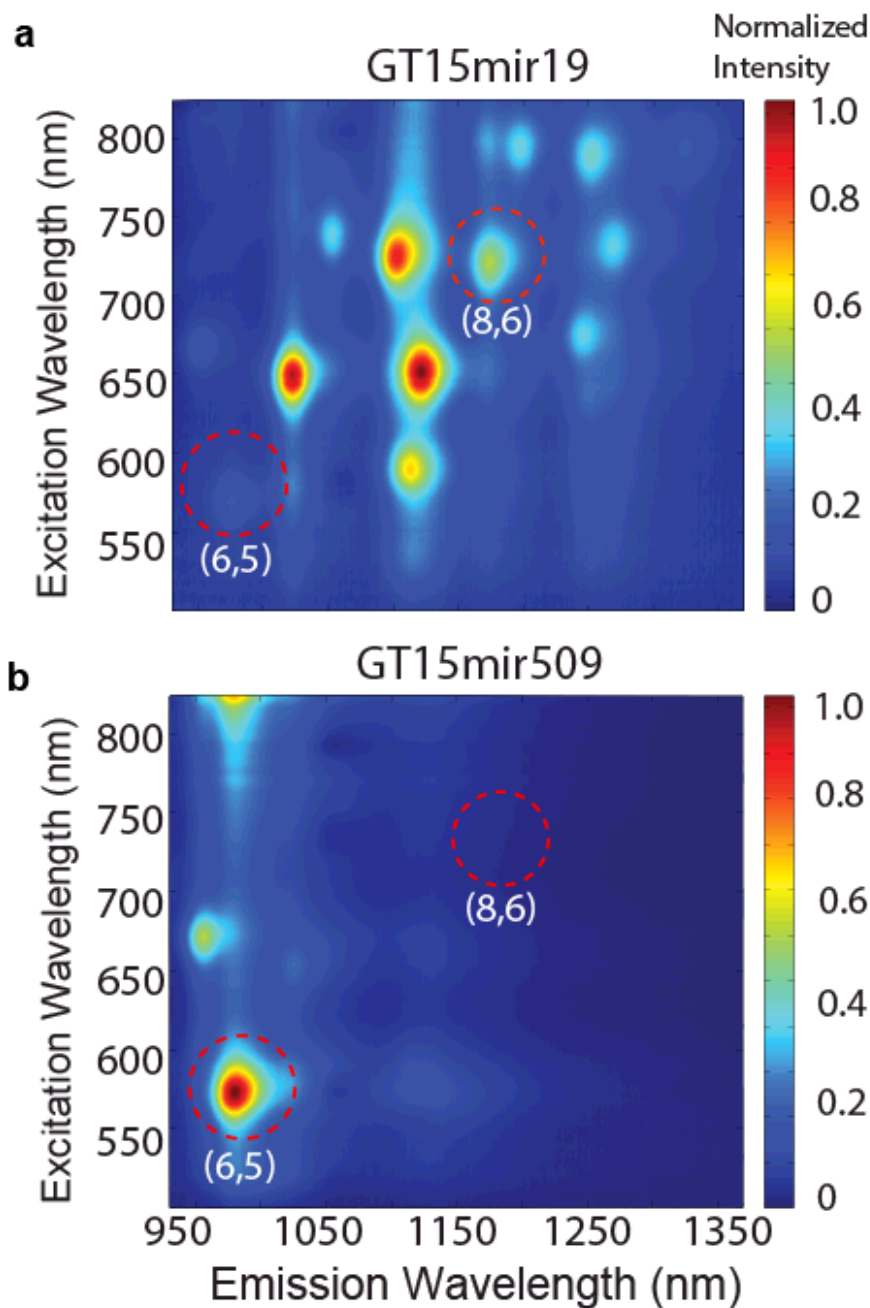
Figure 2.46 Photoluminescence excitation/emission plot of the GT15mir19 sensor synthesized using a large-diameter nanotube preparation. **b,** Photoluminescence excitation/emission plot of the GT15mir509 sensor synthesized using a small-diameter preparation of carbon nanotubes. Red circles highlight the differences in chiralities present.
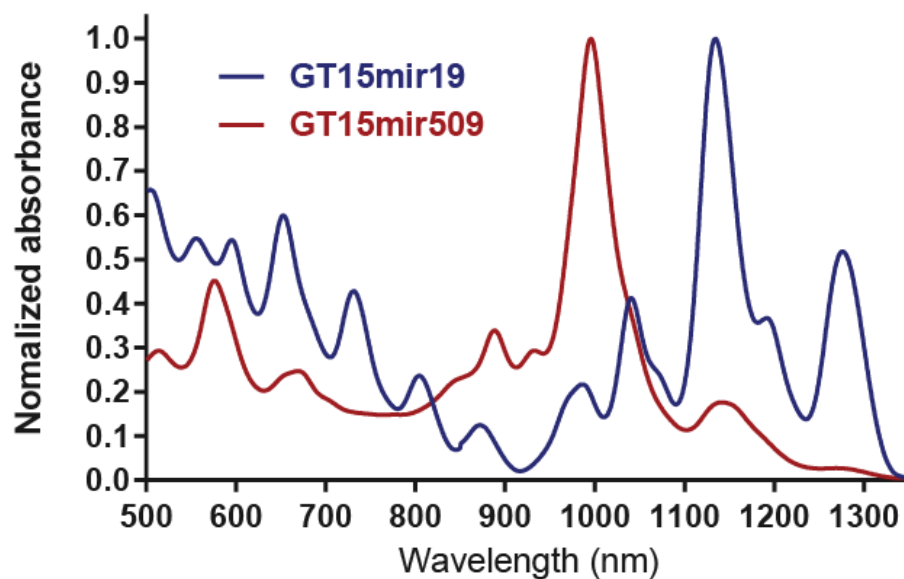
Figure 2.47 Normalized absorbance spectra of GT15mir19 oligonucleotide-suspended APT-200 from Nano-C and GT15mir509 oligonucleotide-suspended CoMoCAT SG65i grade.
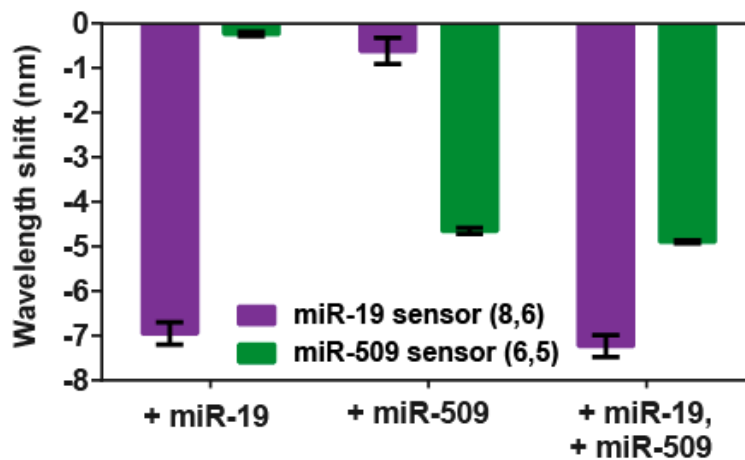
Figure 2.48 Responses of the two sensors mixed together, upon introducing miR-19 alone, miR-509 alone, or both analytes simultaneously. Error bars represent standard deviation for n = 3 technical replicates.

2.3.7 Toehold-mediated strand displacement

We asked whether the spectral response of the sensor could be reversed via toehold-mediated strand displacement. Strand displacement reactions occur through the use of "toeholds," single-strand overhangs on duplexed DNA that facilitate binding of a complementary strand, which is thermodynamically favored due to complete complementarity, and is thus able to displace the shorter bound strand[50]. We truncated the miRNA capture sequence of the GT15mir19 sensor to leave a 6 nucleotide overhang[51] after hybridization with the target strand to test whether the addition of a removing strand (RS) to bind the toehold and displace the target would reverse the spectral shift, according to the proposed scheme in Figure 2.49a. Upon addition of miR-19 to the modified GT15mir19 sensor, the nanotube emission blue-shifted and the intensity increased as expected (Figure 2.49b and 2.49c). After 5 hours, the removing strand was added, at which point the blue-shifting ceased and the emission began to undergo a steady red-shift (Figure 2.49b). The emission intensity exhibited a similar reversal (Figure 2.49c). We note that the signal reversal was slower than detection in the forward direction, which is likely due to the energetic barrier for the truncated capture sequence to displace SDBS from the nanotube surface.
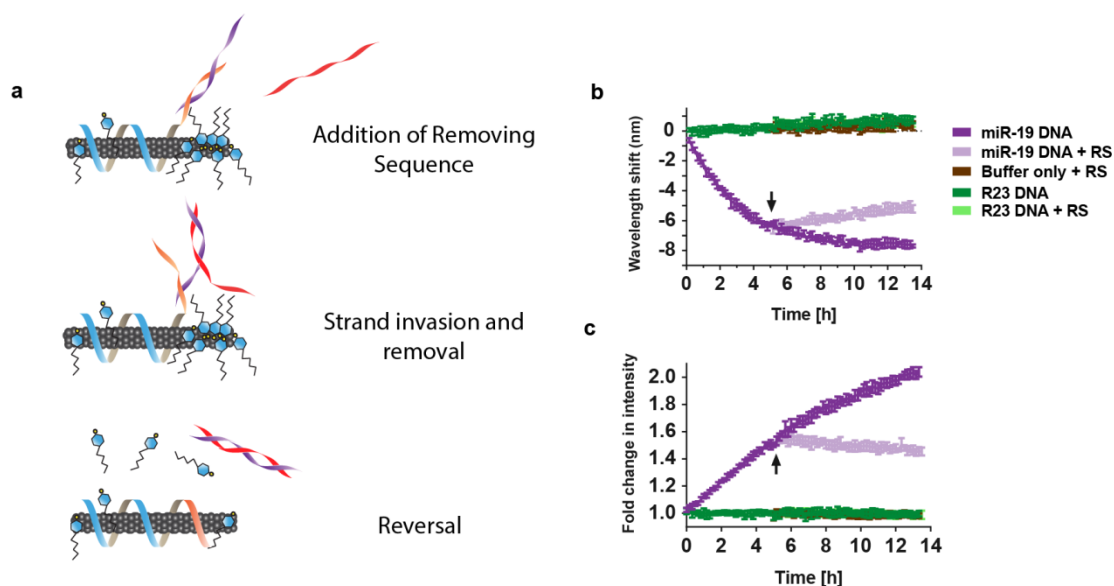
Figure 2.49 Monitoring toehold-mediated strand displacement. a, Cartoon depicting the experiment, wherein the GT15mir19 sensor contains a truncated miRNA-capture sequence (orange domain). Upon hybridization with miR-19, a 6-nucleotide toehold remains on the miRNA sequence (purple strand). The removing strand (red), which is complementary to the entire miRNA sequence, is introduced to remove miR-19. **b,** Kinetic response of the GT15mir19-sensor wavelength upon addition of the target miRNA sequence, and after introducing the removing strand (RS), at the time denoted by the arrow. **c,** Kinetic response of the GT15mir19 sensor intensity, measured during the same experiment. Error bars represent standard deviation for n = 3 technical replicates.

2.3.8 Detection of miRNA in biofluids

We sought to assess the ability of the GT15mir19 sensor to detect miRNA binding events in common biofluids—urine and serum—due to their clinical value as sources of microRNA biomarkers[8]. The GT15mir19 sensor and SDBS were introduced concomitantly to whole urine from 5 healthy donors before interrogating with miR-19 RNA. The wavelength shifting response was clearly detectable against controls down to 1 nM of miRNA, and intensity enhancement gave a similar sensitivity, between 1 and 10 nM (Figure 2.50, Figure 2.51). Variation from sample-to-sample was minimal. In whole serum, we found that target miR-19 DNA was similarly detectable in the

presence of SDBS (Fig 2.52). When target miR-19 RNA was introduced to the sensor, we found only a small response at the highest tested concentration (Fig 2.52). We hypothesized that the RNA detection was complicated by RNases in the serum which might degrade the analyte sequence, as reported elsewhere for synthetic RNA sequences[52]. We therefore introduced proteinase K, a detergent-stable protease used to deactivate RNase, into the serum. Introduction of proteinase K allowed the detection of miR-19 RNA with the same sensitivity as for the DNA analogue (Figure 2.52). When proteinase K was introduced 12 h after mixing miR-19 with serum, the sensitivity of the response to miR-19 RNA was not improved, suggesting that the RNA had been destroyed. To verify broad applicability with this method, we also used miR-21 as a target, due to its significance as a serum colorectal cancer biomarker[53]. We similarly tested GT15mir21 sensor in whole serum treated with proteinase K and found that miR-21 RNA could be detected directly in minimally-treated serum via both blue-shifting and intensity enhancement (Figure 2.53).
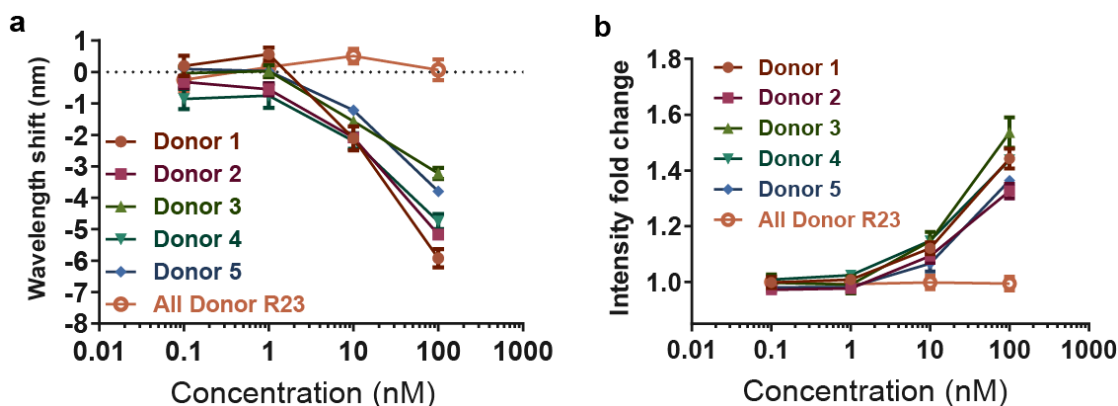
Figure 2.50 Response of the GT15mir19 sensor emission wavelength to miR-19 spiked into urine from 5 healthy donors. The (7,6) nanotube chirality was measured. Error bars represent standard deviation of technical triplicates. **b,** Intensity response of the sensor in urine. Error bars represent standard deviation of technical triplicates.
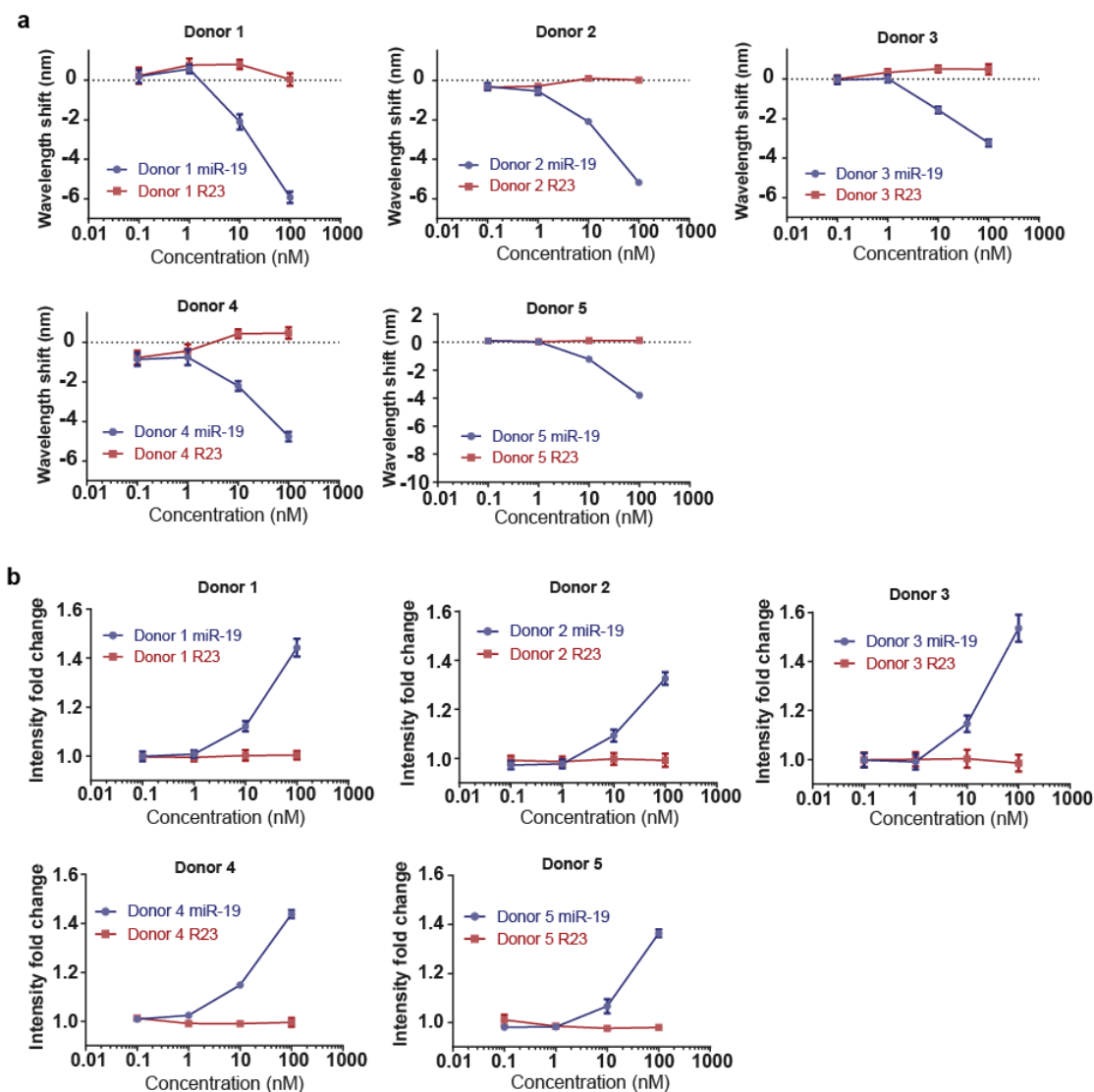
Figure 2.51 Sensor response in urine from individual healthy donors. **a**, Wavelength shift as a function of miR-19 RNA or non-complementary control R23 concentration for each individual donor. **b**, Intensity fold enhancement as a function of added miR-19 RNA or non-complementary control R23 concentration. Error bars represent standard deviation of three technical replicates.
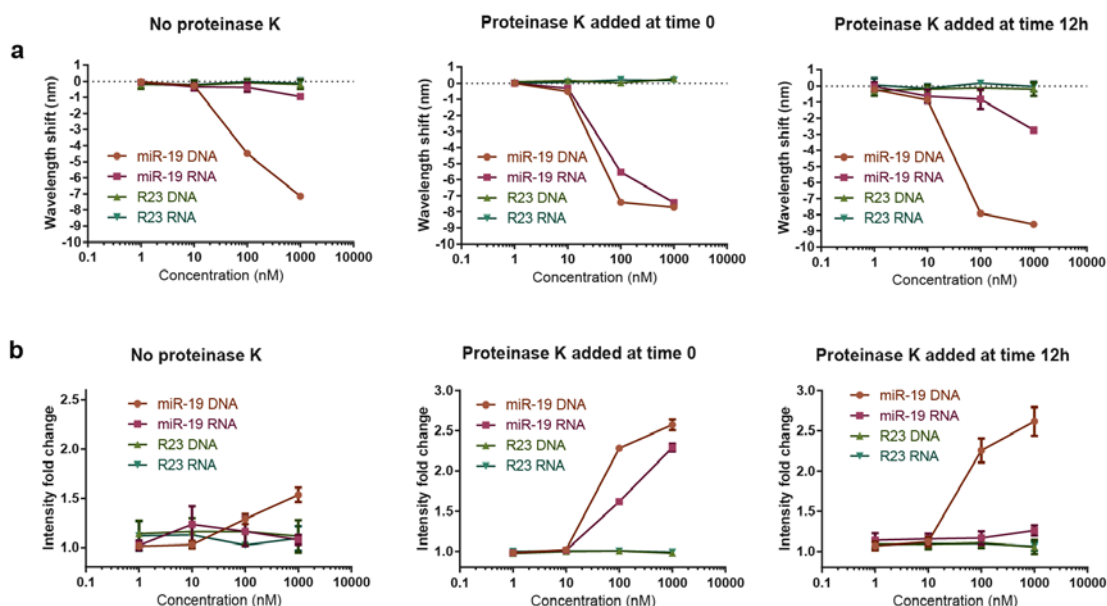
Figure 2.52 Study of the sensor response in serum. **a**, Wavelength shift of the GT15mir19 sensor in whole serum with 0.2% SDBS and upon addition of proteinase K. The response of the (8,6) nanotube is shown. **b**, Intensity change in the same conditions. Error bars represent standard deviation of three technical replicates.
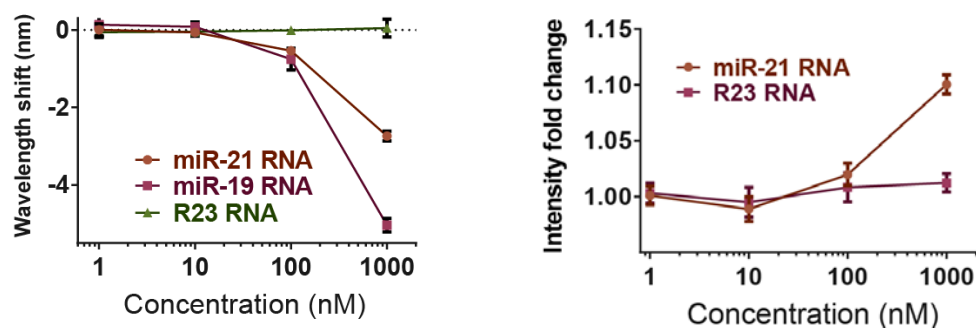
Figure 2.53 Detection of miR-21 in serum. (Left) Wavelength response of the nanotube sensor complex to miR-21 and miR-19 miRNA in fetal bovine serum (FBS). Error bars represent standard deviation of technical triplicates. (Right) Intensity response of the GT15mir21 sensor after introducing the miR-21 RNA oligonucleotide in serum with proteinase K. Error bars represent standard deviation of three technical replicates.

2.3.9 Detection of miRNA detection *in vivo*

We further explored the potential of the sensor to detect miRNA *in vivo* via a minimally-invasive implantable device. We loaded the SDBS-treated GT15mir19 sensor into a semipermeable membrane capillary with a MWCO of 500 kDa (Figure 2.54a). To determine whether this cutoff would to prevent the diffusion of the GT15mir19 sensor complexes outside of the membrane, we calculated the molecular weight of the GT15mir19 sensor. We estimated that the sensor complexes composed of the narrowest diameter (0.8 nm) and average length of 166nm fall within the range of 701 kDa to 839 kDa. The molecular weight of the sensor was estimated using the lower limit of the nanotube diameters to be 0.8 nm, wherein there are 20 carbons around the nanotube circumference. Thus, 80 carbon atoms are present for every 0.283 nm in nanotube length. Taking the average length of the nanotube, as measured via AFM, to be 166 nm, the resulting molecular weight of the nanotube is 564 kDa. The molecular weight of the GT15mir19 DNA sequence is 16.5 kDa. From AFM measurements, we estimated 5-10 copies of DNA per 100 nm, and thus 8.3 to 16.6 copies per 166 nm, adding 137 kDa to 275 kDa to the total complex. Thus, for an average length GT15mir19 sensor with diameter near the lower limit, the molecular weight would be between 701 kDa and 839 kDa.

We surmised that the miR-19 miRNA, with a molecular weight of 7.055 kDa, would pass through the membrane. We also assessed the likelihood that the enhanced signal response provided by SDBS would continue after device implantation. We thus filled the semi-permeable capillary with SDBS-pretreated GT15mir19 sensor and placed it in buffer dialysate for 6 hours. The buffer was changed and the sensor response was assessed with miR-19 every 2 hours (Figure 2.54b and c). We found that the

GT15mir19 sensor exhibited a nearly identical blue-shifting response after 6 hours of dialysis, suggesting that the SDBS remained associated with the sensor even under these conditions.
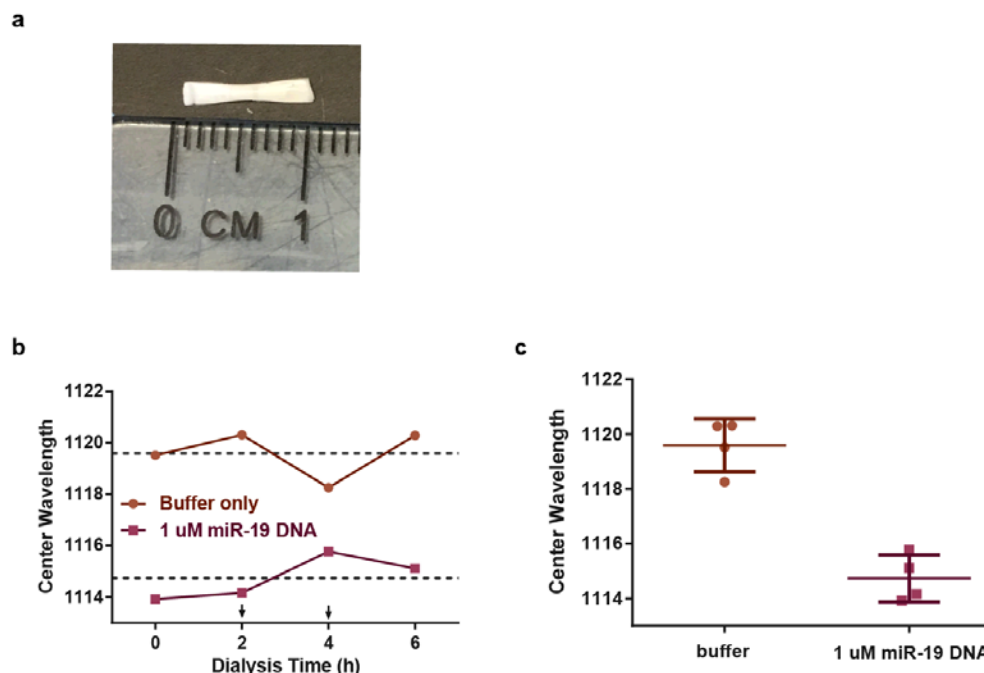
***Figure 2.54 Implantable device testing in vitro*. a,** Semi-permeable membrane encapsulating the GT15mir19 sensor for implantation. **b,** Persistence of wavelength shifting of the GT15mir19 sensor upon dialysis of SDBS. **c,** Emission wavelength response of the sensor, interrogated after the indicated dialysis time. Buffer changes are indicated by the arrows. **c,** Average emission wavelength the sensor in response to miR-19 DNA and buffer control at all time points.

We tested the sensor response *in vivo* after surgically implanting the membrane into the peritoneal cavity of NU/J (nude) mice. The membrane was placed medially over the intestines and sutured to the parietal peritoneum to immobilize the device. We first tested whether DNA could be detected intraperitoneally by injecting 1 nanomole of miR-19 DNA, R23, or the vehicle control. The mice exhibited no obvious adverse effects or changes in behavior following the implantation or injection. After 90m, the mice were anesthetized using isofluorane. A fiber optic-based probe system was

developed to excite an 0.8 cm^2 area with a 730 nm CW laser (Figure 2.55a), collect the emitted near-infrared light through the same fiber bundle, disperse the light with a Czerny-Turner spectrograph, and detect the light via a 1D InGaAs array (Figure 2.55b). Using the nanotube emission signal collected from the mouse, we found that the target miR-19 DNA exhibited a significant blue-shifting response as compared to controls (Figure 2.56a). The experiment was repeated using the RNA version of the analyte, resulting in a similar response (Figure 2.56b). We tested the implantable device in vitro by immersing the filled capillary into buffer containing RNA, finding that the threshold of detection was below 10 pmol (Figure 2.57). To determine the limit of detection *in vivo*, we injected 500 pmol, 100 pmol, or 50 pmol of miR-19 RNA intraperitoneally into mice implanted with the devices. After 120 min, significant wavelength shifting responses were measured down to 100 pmol (Figure 2.58). The devices were removed from the animals and measured ex vivo, resulting in similar results (Figures 2.59). We suspect the higher limit of detection of the device in vivo as compared to in vitro was due to the degradation of microRNA in the peritoneal fluid as well as fluid exchange out of the peritoneal cavity. The measurement of endogenous microRNA targets, which are highly stable due in part to their association with proteins such as Ago2[54, 55], may help improve sensor performance in future investigations.
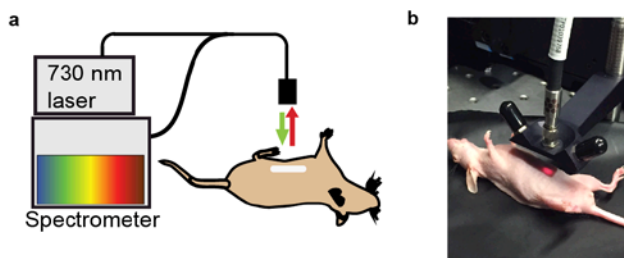
Figure 2.55 Optical probe system for animal studies. a, Diagram of NIR probe apparatus for illuminating and measuring the sensor response *in vivo*. **b,** Image of NIR probe system measuring the nanotube response within a live mouse.
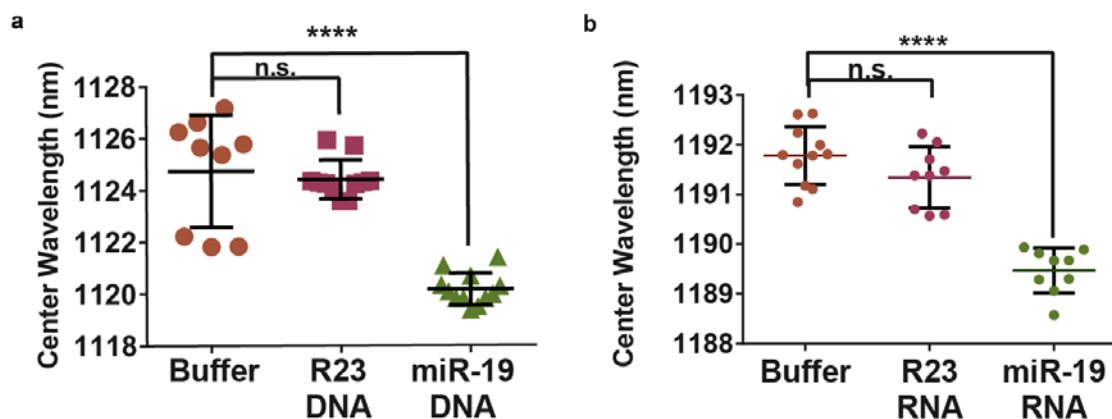
Figure 2.56 Response of the implanted sensor device to miR-19 DNA within the live mouse (3-4 measurements per mouse; 3 mice per group). The (9,4) nanotube species was measured ($p < 0.0001$, Dunnet's multiple comparison test, ordinary one-way ANOVA). Response of the implanted sensor device to 1 nanomole of miR-19 RNA within live mice. The (8,6) nanotube chirality was measured; 3-4 spectra per animal were taken; 3 animals were measured per group ($p < 0.0001$, Dunnet's multiple comparison test, ordinary one-way ANOVA).
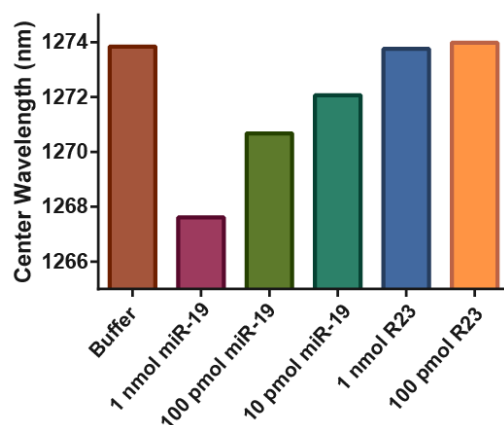
Figure 2.57 Dose-response curve of the GT15mir19 sensor capillary device measured in vitro.
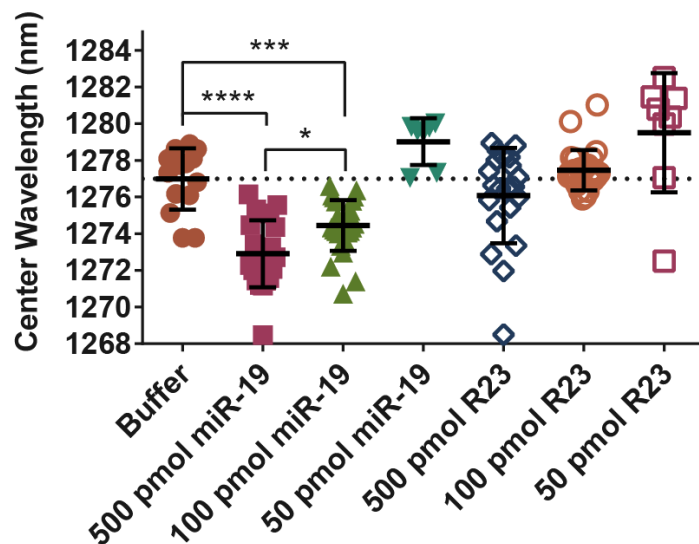
Figure 2.58 Response of the implanted sensor device to 500, 100, and 50 pmol of miR-19 RNA or R23 RNA injected into mice intraperitoneally (3-4 measurements per animal; 3 animals per group), shown for the (8,7) nanotube species. 50 pmol R23 was slightly red-shifted compared to buffer control. Error bars represent standard deviation. Statistical significance was calculated with Dunnet's multiple comparison test. Ordinary ANOVA was used to compare the mean of each group to the mean of the buffer control. Sidak's multiple comparison test with an alpha of 0.05 was used to compare miR-19 groups.
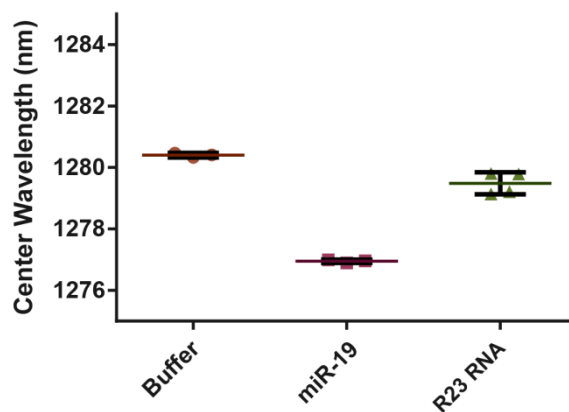
Figure 2.59 Emission from the implantable devices ex vivo. Ex vivo measurements from device removed from one animal in each group after injection of buffer, 500 pmol miR-19 RNA, or 500 pmol R23 RNA. Error bars represent standard error of the mean for 3-4 measurements.

2.4 Outlook

Herein, we engineered a label-free, amplification-free optical sensor for the quantitative detection of oligonucleotide hybridization events in vitro and non-invasively in vivo. The sensor mechanism, resulting from competitive effects of the displacement of both electrostatic charge and water from the carbon nanotube surface, has implications for the improvement of carbon nanotube-based optical and electronic sensors. We also gained a clear understanding over the effects of length, mismatches in sequence, and orientation of longer oligonucleotides on the optical response of the carbon nanotube, providing a basis for continued optimization. The GT15mirX sensor enabled detection via single-molecule sensor elements and multiplexing using multiple nanotube chiralities. The monitoring of toehold-based strand displacement events portends use in nucleic acid-based logic circuits[56] and also allowed the reversal of the sensor response and regeneration of the sensor complex, which may potentially be exploited for continuous use.

Using the current iteration of the sensor, in vitro applications such as point-of-care diagnostics may provide the most immediate route to clinical use. We found that the sensor can directly detect oligonucleotides in heterogeneous biofluids such as urine and serum with minimal pre-treatment, potentially circumventing biases and variability related to typical pre-analytical steps required for RT-qPCR[45]. Regarding sensor parameters pertinent to clinical measurements, Weber et al.[8] surveyed the microRNA content in 12 body fluids, providing useful quantitative information to estimate the physiological range of microRNA. In urine, the median concentration of a microRNA species is on the scale of tens of pM[8], while in plasma and peritoneal fluid it is in the hundreds of pM[8]. Other quantitative sensors[57] found biofluid microRNA

95

concentrations in the high femtomolar range, suggesting that the dynamic range may fall between about 10 fM and 100 pM. The current limit of detection of our sensor in bulk solution is in the picomolar range, although the threshold of detection and dynamic range depends on several factors, including binding site coverage, which have not yet been modulated in the development process. We also demonstrated the ability to measure single-nanotube responses representing 1-60 copies of microRNA binding, suggesting developments that might attain sensitivities down to 10's of copies of microRNA, potentially rivaling the most sensitive techniques[52, 58, 59].

An implantable optical sensor device for the non-invasive detection of biomarkers such as miRNA may potentially be used in conjunction with wearable devices to facilitate the optical readout and data recording. Our sensor implant quantified miRNA down to 100 pmol in vivo, although further optimization of the sensitivity and other parameters is warranted. While in vitro experiments suggest the current version of the sensor to be robust over at least several hours, more testing is needed to determine stability over longer periods. Investigations are also needed to ensure that oligonucleotides can be detected in their physiological states. For example, miRNA is often found associated with the small protein Ago2[54], which makes it physiologically stable. Functionally, Ago2 binds to microRNA in a conformation to favor hybridization with target sequences, especially over an 8 nucleotide section called the seed sequence[60, 61], but steric hindrance or charge interactions of the protein with miRNA could slow access to the protein-bound sections of the strand. Future iterations of a sensor may include locked nucleic acids[62] or peptide nucleic acids[63] to enhance binding affinities to short, unbound sections of miRNA. Future studies are also needed to investigate device form factors for implantation and data collection strategies, such as sensor interrogation using wearable devices.

2.5 Methods

2.5.1 DNA-suspension of carbon nanotubes

Carbon nanotubes produced by the HiPco process (Unidym, Sunnyvale, CA), CoMoCAT process (SG65i grade, Sigma-Aldrich, St. Louis, MO, US), or a combustion process (APT-200, Nano-C,Westwood, MA) were mixed with DNA oligonucleotides (IDT DNA, Coralville, IA) at a 2:1 mass ratio in 1 mL of saline-sodium citrate (SSC) buffer and ultrasonicated for 30 minutes at 40% amplitude (Sonics & Materials, Inc.). The complete list of DNA sequences used for suspension can be found in the Appendix. Following ultrasonication, the dispersions were ultracentrifuged (Sorvall Discovery 90SE) for 30 minutes at 280,000 x g. The top 80% of the supernatant was collected. Absorbance spectra were acquired using a UV/Vis/nIR spectrophotometer (Jasco V-670, Tokyo, Japan). The concentration was calculated using the extinction coefficient $Abs_{910} = 0.02554$ L mg^{-1}cm^{-1}. To remove free DNA, 100 kDa Amicon centrifuge filters (Millipore) were used. The DNA-nanotube complexes were re-suspended in saline-sodium citrate buffer (G Biosciences, St. Louis, MO).

2.5.2 Fluorescence spectroscopy of carbon nanotubes in solution

Fluorescence emission spectra from aqueous nanotube solutions were acquired using a home-built apparatus consisting of a tunable white light laser source, inverted microscope, and InGaAs nIR detector. The SuperK EXTREME supercontinuum white light laser source (NKT Photonics) was used with a VARIA variable bandpass filter accessory capable of tuning the output 500 – 825 nm with a bandwidth of 20 nm. The light path was shaped and fed into the back of an inverted IX-71 microscope (Olympus) where it passed through a 20x nIR objective (Olympus) and illuminated a 50-100 µL nanotube sample in a 96-well plate (Corning). The emission from the

nanotube sample was collected through the 20x objective and passed through a dichroic mirror (875 nm cutoff, Semrock). The light was f/# matched to the spectrometer using several lenses and injected into an Isoplane spectrograph (Princeton Instruments) with a slit width of 410 µm which dispersed the emission using a 86 g/mm grating with 950 nm blaze wavelength. The spectral range was 930 – 1369 nm with a resolution of ~0.7 nm. The light was collected by a PIoNIR InGaAs 640 x 512 pixel array (Princeton Instruments). A HL-3-CAL-EXT halogen calibration light source (Ocean Optics) was used to correct for wavelength-dependent features in the emission intensity arising from the spectrometer, detector, and other optics. A Hg/Ne pencil style calibration lamp (Newport) was used to calibrate the spectrometer wavelength. Background subtraction was conducted using a well in a 96-well plate filled with DI H2O. Following acquisition, the data was processed with custom code written in Matlab which applied the aforementioned spectral corrections, background subtraction, and was used to fit the data with Lorentzian functions.

2.5.3 Atomic force microscopy

The GT15mir19 sensor was incubated overnight at 20 mg/L with 10 uM of the miR-19-hairpin or 10 uM of the R23-hairpin in saline sodium citrate diluted 20x in 20 mM HEPES + 5 mM $MgCl_2$. The sample was plated on a freshly cleaved mica substrate (SPI) for 4 minutes before washing with 10 mL of dH2O and blowing dry with argon gas. An Asylum Research MFP-3D-Bio instrument was used with an Olympus AC240TS AFM probe in AC mode. Data was captured at 2.93 nm/pixel XY resolution and 15.63 pm Z resolution. For AFM under aqueous conditions, 20 mg/L of the GT15mir19 sensor was incubated with 10 uM of the miR-19-hairpin, R23-hairpin, or buffer overnight. All three conditions were spin-filtered 3x with 100 kDa Amicon centrifuge filters, and resuspended with 5 mM $NiCl_2$, 20 mM HEPES pH 6.7 buffer.

The samples were plated onto freshly cleaved mica for 2 minutes before gently washing with the same buffer. Samples were imaged in a droplet of the buffer using an Asylum Research Cypher ES + BlueDrive AFM with an Olympus AC55 probe and imaged using BlueDrive excitation at the ambient temperature of 31°C within the AFM enclosure. All three samples were imaged with the same probe, consecutively, with the same scan settings, starting with the miR-19-hairpin sample, followed by the R23-hairpin control and the buffer control.

2.5.4 Hybridization experiments in buffer conditions and biofluids

Hybridization experiments were conducted with 2 mg/L of the GT15mir19 sensor in saline-sodium citrate buffer at room temperature. Target DNA or RNA was introduced to reach a final concentration of 1 uM. Samples were incubated for 4 hours, unless otherwise noted. Free energy of hybridization was predicted using OligoAnalyzer 3.1 (IDT). Kinetics experiments were measured every 10 minutes using custom LabView code. Hybridization experiments with sodium dodecylbenzenesulfonate (SDBS) were conducted using a final concentration 0.2% wt/v. SDBS was added to the GT15mir19 sensor and allowed to equilibrate overnight at room temperature before target oligonucleotides were added. Toehold-mediated strand displacement experiments were performed with 1 uM of target miR-19 DNA, and 10 uM of the removing strand, composed of an ssDNA oligonucleotide with the complementary sequence to miR-19. Hybridization experiments in urine were conducted in samples from 5 healthy volunteers and stored on ice until the experiment. Concentrated GT15mir19 was added to each sample to final concentration of 0.2 mg/L and SDBS to final concentration of 0.2%. Concentrated DNA and RNA target were added to the indicated concentrations and incubated at room temperature overnight. Serum experiments used fetal bovine serum (Life Sciences) with GT15mir19 added to final concentration 0.2 mg/L and

SDBS at 0.2%. Where indicated, proteinase K (New England Biolabs) was added to a final concentration of 0.5 mg/mL. Spectra was acquired after overnight incubation at room temperature.

2.5.5 Single-nanotube measurements

Single-nanotube measurements were performed by incubating SDS-treated GT15mir19 sensor (0.2% SDS in SSC buffer) on a poly-D-lysine coated glass bottom plate (Mattek, Ashland, MA) for 10 minutes before gently washing with 0.2% SDS in SSC buffer. A final volume of 1 mL SDS-buffer was left in the plate during hyperspectral imaging measurements of the surface-bound nanotubes. A small volume (1 uL) of 1 mM solutions of miR-19 RNA or R23 RNA were then mixed with the buffer. Hyperspectral imaging measurements were repeated after 15 minutes and 50 minutes. Single nanotube emission spectra were collected via a custom near-infrared hyperspectral microscope, as described previously[29]. Data was processed with ImageJ software. Peaks were fit to Voigt functions using custom Matlab code to obtain center wavelength values.

2.5.6 Molecular dynamics simulations

Molecular dynamics (MD) simulations were conducted using the (9,4) nanotube chirality in explicit water. The DNA molecule for GT15mir19 (without complementary strand) was generated as an unstructured single stranded DNA and placed near the (9,4) nanotube, followed by a sufficiently long equilibration MD simulation enhanced with a replica-exchange based method[64, 65] to let the entire strand adsorb on (9,4) nanotube surface. Analysis of an additional 250 ns long MD simulation is presented in the results. The DNA molecule for GT15mir19 hybridized with the complementary strand was created in a partially double stranded form. miR-

19 was generated in the double stranded form using NAB program of AmberTools[66] and was appropriately bonded via phosphodiester bond to the ss(GT)$_{15}$ segment of the GT15mir19 DNA. The ss(GT)15 nanotube binding portion of the first strand was adsorbed to the nanotube. The entire DNA and nanotube construct was solvated in a 10.65 x 10.65 x 14.7179 nm water-box containing approximately 55,000 water molecules and 74 sodium counter-ions, placed randomly, to balance the negative charges from phosphates on the DNA. The total system was approximately 170,000 atoms. The nanotube extended to the edges of the water box and was kept frozen in place during the entire equilibration and simulation time. The nanotube atoms were modeled as sp2 hybridized carbon. All structures were visualized in VMD[67].

The Gromacs 4.6.7 simulation package[68, 69] was used with the Charmm36/TIP3P nucleic acid/water model[70]. Long-range electrostatics were calculated using the particle mesh Ewald method with a 0.9 nm real space cutoff[71]. For van der Waals interactions, a cutoff value of 1.2 nm was used. The energy minimized simulation box was then subjected to 100 ps equilibration in an NVT (T=300 K) ensemble where the number of water molecules were fine-tuned to make average pressure approximately equivalent to atmospheric pressure. Further equilibration runs were performed for 100-200 ns in NVT (T=300 K) ensemble. The movie and analysis used the 250 ns production run, followed by equilibration. Systems were propagated with stochastic Langevin dynamics with a time step of 2 fs. The trajectories were saved every 10 ps, yielding a total of 25,000 snapshots for production analysis. VMD Movie Maker was used to create the movie of the trajectory. Homemade python scripts calling MDAnalysis module[72] were used for all other analysis presented.

2.5.7 Quantification of DNA on the nanotube complex

The GT15mir19 sequence was used to suspend nanotubes as described earlier. After each of 4 centrifugation filter steps using the Amicon centrifuge filter (100 kDa MWCO), the concentration of the filtered DNA was measured using Abs_{260} on a NanoDrop spectrophotometer (ThermoScientific, Waltham, MA). The pellet from centrifugation was also filtered to measure free DNA. The final mass of DNA from the combined values was calculated from the concentration and subtracted from the initial value. From three suspensions, we found that 3.5 (+/-1.8) mg of DNA suspended 1 mg of nanotube, matching previous reports of 2.5 to 5 mg of DNA per 1 mg of nanotube[73].

2.5.8 Device implantation and *in vivo* spectroscopy

All animal experiments were approved by the Institutional Animal Care and Use Committee at Memorial Sloan Kettering Cancer Center. KrosFlo Implant Membranes (500 kD MWCO) were obtained from Spectrum Labs (Rancho Dominguez, CA). The membrane was cut to about 1 cm in length and filled with approximately 15 uL of 2 mg/L GT15mir19-nanotubes. Each end was heat sealed. A total of 36 NU/J (nude) mice (Jackson Labs) were anesthetized with 2% isoflurane and implanted with the membrane. Nine mice were divided into three cohorts of three mice to receive miR-19 DNA, R23 DNA, or buffer vehicle via an intraperitoneal injection of 1 nanomole in 1 mL sodium saline citrate buffer. An identical experiment was performed with miR-19 RNA, R23 RNA, or buffer vehicle at 1 nanomole, 500 picomole, 100 picomole, or 50 picomole in 1 mL sodium saline citrate buffer The mice were removed from anesthesia and allowed to regain consciousness. After 90 or 120 minutes, mice were anesthetized and measured using a custom-built reflectance probe-based spectroscopy system. The system consisted of a continuous wave 1 watt 730 nm diode laser (Frankfurt). The laser light was injected into a bifurcated fiber optic reflection probe

bundle. The sample leg of the bundle included one 200 µm, 0.22 NA fiber optic cable for sample excitation located in the center of six 200 µm, 0.22 NA fiber optic cables for collection of the emitted light. Emission below 1050 nm was filtered using longpass filters, and the light was focused into the slit of a Czerny-Turner spectrograph with 303 mm focal length (Shamrock 303i, Andor). The slit width of the spectrograph was set at 410 µm. The light was dispersed using a 85 g/mm grating with 1350 nm blaze wavelength and collected with an iDus InGaAs camera (Andor). Spectra were fit to Voigt functions using custom Matlab code.

2.6 Acknowledgements

2.7 References

1. Tokuhisa, M., Ichikawa, Y., Kosaka, N. et al. Exosomal miRNAs from Peritoneum Lavage Fluid as Potential Prognostic Biomarkers of Peritoneal Metastasis in Gastric Cancer. *PloS one* **10**, e0130472 (2015).

2. Parrella, P., Zangen, R., Sidransky, D. & Nicol, T. Molecular analysis of peritoneal fluid in ovarian cancer patients. *Modern pathology : an official journal of the United States and Canadian Academy of Pathology, Inc* **16**, 636-640 (2003).

3. Mitchell, P.S., Parkin, R.K., Kroh, E.M. et al. Circulating microRNAs as stable blood-based markers for cancer detection. *Proceedings of the National Academy of Sciences of the United States of America* **105**, 10513-10518 (2008).

4. Dawson, S.J., Tsui, D.W., Murtaza, M. et al. Analysis of circulating tumor DNA to monitor metastatic breast cancer. *The New England journal of medicine* **368**, 1199-1209 (2013).

5. Tomlins, S.A., Aubin, S.M., Siddiqui, J. et al. Urine TMPRSS2:ERG fusion transcript stratifies prostate cancer risk in men with elevated serum PSA. *Science translational medicine* **3**, 94ra72 (2011).

6. Thierry, A.R., Mouliere, F., El Messaoudi, S. et al. Clinical validation of the detection of KRAS and BRAF mutations from circulating tumor DNA. *Nature medicine* **20**, 430-435 (2014).

7. Deras, I.L., Aubin, S.M., Blase, A. et al. PCA3: a molecular urine assay for predicting prostate biopsy outcome. *The Journal of urology* **179**, 1587-1592 (2008).

8. Weber, J.A., Baxter, D.H., Zhang, S. et al. The microRNA spectrum in 12 body fluids. *Clinical chemistry* **56**, 1733-1741 (2010).

9.   Lawrie, C.H., Gal, S., Dunlop, H.M. et al. Detection of elevated levels of tumour-associated microRNAs in serum of patients with diffuse large B-cell lymphoma. *British journal of haematology* **141**, 672-675 (2008).

10.   Yamada, Y., Enokida, H., Kojima, S. et al. MiR-96 and miR-183 detection in urine serve as potential tumor markers of urothelial carcinoma: correlation with stage and grade, and comparison with urinary cytology. *Cancer science* **102**, 522-529 (2011).

11.   Hanke, M., Hoefig, K., Merz, H. et al. A robust methodology to study urine microRNA as tumor marker: microRNA-126 and microRNA-182 are related to urinary bladder cancer. *Urologic oncology* **28**, 655-661 (2010).

12.   Snowdon, J., Boag, S., Feilotter, H., Izard, J. & Siemens, R. A pilot study of urinary microRNA as a biomarker for urothelial cancer. *Cuaj-Can Urol Assoc* **7**, 28-32 (2013).

13.   Lan, Y.F., Chen, H.H., Lai, P.F. et al. MicroRNA-494 Reduces ATF3 Expression and Promotes AKI. *Journal of the American Society of Nephrology* **23**, 2012-2023 (2012).

14.   Chung, Y.W., Bae, H.S., Song, J.Y. et al. Detection of MicroRNA as Novel Biomarkers of Epithelial Ovarian Cancer From the Serum of Ovarian Cancer Patient. *International Journal of Gynecological Cancer* **23**, 673-679 (2013).

15.   Pajek, J., Kveder, R., Gucek, A. et al. Cell-free DNA in the Peritoneal Effluent of Peritoneal Dialysis Solutions. *Ther Apher Dial* **14**, 20-26 (2010).

16.   Johnson, B.N. & Mutharasan, R. Biosensor-based microRNA detection: techniques, design, performance, and challenges. *The Analyst* **139**, 1576-1588 (2014).

17.   Chen, C., Ridzon, D.A., Broomer, A.J. et al. Real-time quantification of microRNAs by stem-loop RT-PCR. *Nucleic acids research* **33**, e179 (2005).

18. Baker, M. MicroRNA profiling: separating signal from noise. *Nature methods* **7**, 687-692 (2010).

19. Hunt, E.A., Broyles, D., Head, T. & Deo, S.K. MicroRNA Detection: Current Technology and Research Strategies. *Annual review of analytical chemistry* **8**, 217-237 (2015).

20. Dong, H., Lei, J., Ding, L. et al. MicroRNA: function, detection, and bioanalysis. *Chemical reviews* **113**, 6207-6233 (2013).

21. Kruss, S., Hilmer, A.J., Zhang, J. et al. Carbon nanotubes as optical biomedical sensors. *Advanced drug delivery reviews* **65**, 1933-1950 (2013).

22. Iverson, N.M., Barone, P.W., Shandell, M. et al. In vivo biosensing via tissue-localizable near-infrared-fluorescent single-walled carbon nanotubes. *Nature nanotechnology* **8**, 873-880 (2013).

23. O'Connell, M.J., Bachilo, S.M., Huffman, C.B. et al. Band gap fluorescence from individual single-walled carbon nanotubes. *Science* **297**, 593-596 (2002).

24. Cheong, W.F., Prahl, S.A. & Welch, A.J. A review of the optical properties of biological tissues. *IEEE Journal of Quantum Electronics* **26**, 2166-2185 (1990).

25. Wang, F., Dukovic, G., Brus, L.E. & Heinz, T.F. The optical resonances in carbon nanotubes arise from excitons. *Science* **308**, 838-841 (2005).

26. Heller, D.A., Jeng, E.S., Yeung, T.K. et al. Optical detection of DNA conformational polymorphism on single-walled carbon nanotubes. *Science* **311**, 508-511 (2006).

27. Barone, P.W., Baik, S., Heller, D.A. & Strano, M.S. Near-infrared optical sensors based on single-walled carbon nanotubes. *Nature materials* **4**, 86-92 (2005).

28.   Cognet, L., Tsyboulski, D.A., Rocha, J.D. et al. Stepwise quenching of exciton fluorescence in carbon nanotubes by single-molecule reactions. *Science* **316**, 1465-1468 (2007).

29.   Roxbury, D., Jena, P.V., Williams, R.M. et al. Hyperspectral Microscopy of Near-Infrared Fluorescence Enables 17-Chirality Carbon Nanotube Imaging. *Scientific reports* **5**, 14167 (2015).

30.   Olive, V., Bennett, M.J., Walker, J.C. et al. miR-19 is a key oncogenic component of mir-17-92. *Genes & development* **23**, 2839-2849 (2009).

31.   Zheng, M., Jagota, A., Strano, M.S. et al. Structure-based carbon nanotube sorting by sequence-dependent DNA assembly. *Science* **302**, 1545-1548 (2003).

32.   Bachilo, S.M., Strano, M.S., Kittrell, C. et al. Structure-assigned optical spectra of single-walled carbon nanotubes. *Science* **298**, 2361-2366 (2002).

33.   Campbell, J.F., Tessmer, I., Thorp, H.H. & Erie, D.A. Atomic force microscopy studies of DNA-wrapped carbon nanotube structure and binding to quantum dots. *Journal of the American Chemical Society* **130**, 10648-10655 (2008).

34.   Roxbury, D., Jena, P.V., Shamay, Y., Horoszko, C.P. & Heller, D.A. Cell Membrane Proteins Modulate the Carbon Nanotube Optical Bandgap via Surface Charge Accumulation. *ACS nano* **10**, 499-506 (2016).

35.   Yang, R., Jin, J., Chen, Y. et al. Carbon Nanotube-Quenched Fluorescent Oligonucleotides: Probes that Fluoresce upon Hybridization. *Journal of the American Chemical Society* **130**, 8351-8358 (2008).

36.   Jung, S., Cha, M., Park, J. et al. Dissociation of single-strand DNA: single-walled carbon nanotube hybrids by Watson-Crick base-pairing. *Journal of the American Chemical Society* **132**, 10964-10966 (2010).

37.   Heller, D.A., Pratt, G.W., Zhang, J.Q. et al. Peptide secondary structure modulates single-walled carbon nanotube fluorescence as a chaperone sensor for nitroaromatics. *Proceedings of the National Academy of Sciences of the United States of America* **108**, 8544-8549 (2011).

38.   Moore, V.C., Strano, M.S., Haroz, E.H. et al. Individually suspended single-walled carbon nanotubes in various surfactants. *Nano letters* **3**, 1379-1382 (2003).

39.   Miyauchi, Y., Saito, R., Sato, K. et al. Dependence of exciton transition energy of single-walled carbon nanotubes on surrounding dielectric materials. *Chemical Physics Letters* **442**, 394-399 (2007).

40.   Haggenmueller, R., Rahatekar, S.S., Fagan, J.A. et al. Comparison of the quality of aqueous dispersions of single wall carbon nanotubes using surfactants and biomolecules. *Langmuir : the ACS journal of surfaces and colloids* **24**, 5070-5078 (2008).

41.   Fantini, C., Cassimiro, J., Peressinotto, V.S.T. et al. Investigation of the light emission efficiency of single-wall carbon nanotubes wrapped with different surfactants. *Chemical Physics Letters* **473**, 96-101 (2009).

42.   Ohno, Y., Iwasaki, S., Murakami, Y. et al. Chirality-dependent environmental effects in photoluminescence of single-walled carbon nanotubes. *Physical Review B* **73** (2006).

43.   Lesnik, E.A. & Freier, S.M. Relative Thermodynamic Stability of DNA, Rna, and DNA-Rna Hybrid Duplexes - Relationship with Base Composition and Structure. *Biochemistry* **34**, 10807-10815 (1995).

44.   Gyi, J.I., Lane, A.N., Conn, G.L. & Brown, T. The orientation and dynamics of the C2 '-OH and hydration of RNA and DNA-RNA hybrids. *Nucleic acids research* **26**, 3104-3110 (1998).

45.   McDonald, J.S., Milosevic, D., Reddi, H.V., Grebe, S.K. & Algeciras-Schimnich, A. Analysis of circulating microRNA: preanalytical and analytical challenges. *Clinical chemistry* **57**, 833-840 (2011).

46.   Gregory, P.A., Bert, A.G., Paterson, E.L. et al. The miR-200 family and miR-205 regulate epithelial to mesenchymal transition by targeting ZEB1 and SIP1. *Nature cell biology* **10**, 593-601 (2008).

47.   Landry, M.P., Vukovic, L., Kruss, S. et al. Comparative Dynamics and Sequence Dependence of DNA and RNA Binding to Single Walled Carbon Nanotubes. *The journal of physical chemistry. C, Nanomaterials and interfaces* **119**, 10048-10058 (2015).

48.   Johnson, R.R., Johnson, A.T. & Klein, M.L. The nature of DNA-base-carbon-nanotube interactions. *Small* **6**, 31-34 (2010).

49.   Cognet, L., Tsyboulski, D.A. & Weisman, R.B. Subdiffraction far-field imaging of luminescent single-walled carbon nanotubes. *Nano letters* **8**, 749-753 (2008).

50.   Machinek, R.R., Ouldridge, T.E., Haley, N.E., Bath, J. & Turberfield, A.J. Programmable energy landscapes for kinetic control of DNA strand displacement. *Nature communications* **5**, 5324 (2014).

51.   Srinivas, N., Ouldridge, T.E., Sulc, P. et al. On the biophysics and kinetics of toehold-mediated DNA strand displacement. *Nucleic acids research* **41**, 10641-10658 (2013).

52.   Johnson-Buck, A., Su, X., Giraldez, M.D. et al. Kinetic fingerprinting to identify and count single nucleic acids. *Nature biotechnology* **33**, 730-732 (2015).

53. Toiyama, Y., Takahashi, M., Hur, K. et al. Serum miR-21 as a diagnostic and prognostic biomarker in colorectal cancer. *Journal of the National Cancer Institute* **105**, 849-859 (2013).

54. Arroyo, J.D., Chevillet, J.R., Kroh, E.M. et al. Argonaute2 complexes carry a population of circulating microRNAs independent of vesicles in human plasma. *Proceedings of the National Academy of Sciences of the United States of America* **108**, 5003-5008 (2011).

55. Turchinovich, A., Weiz, L., Langheinz, A. & Burwinkel, B. Characterization of extracellular circulating microRNA. *Nucleic acids research* **39**, 7223-7233 (2011).

56. Seelig, G., Soloveichik, D., Zhang, D.Y. & Winfree, E. Enzyme-free nucleic acid logic circuits. *Science* **314**, 1585-1588 (2006).

57. Joshi, G.K., Deitz-McElyea, S., Liyanage, T. et al. Label-Free Nanoplasmonic-Based Short Noncoding RNA Sensing at Attomolar Concentrations Allows for Quantitative and Highly Specific Assay of MicroRNA-10b in Biological Fluids and Circulating Exosomes. *ACS nano* **9**, 11075-11089 (2015).

58. Wanunu, M., Dadosh, T., Ray, V. et al. Rapid electronic detection of probe-specific microRNAs using thin nanopore sensors. *Nature nanotechnology* **5**, 807-814 (2010).

59. Gunnarsson, A., Jonsson, P., Marie, R., Tegenfeldt, J.O. & Hook, F. Single-molecule detection and mismatch discrimination of unlabeled DNA targets. *Nano letters* **8**, 183-188 (2008).

60. Schirle, N.T. & MacRae, I.J. The Crystal Structure of Human Argonaute2. *Science* **336**, 1037-1040 (2012).

61. Schirle, N.T., Sheu-Gruttadauria, J. & MacRae, I.J. Structural basis for microRNA targeting. *Science* **346**, 608-613 (2014).

62. Koshkin, A.A., Singh, S.K., Nielsen, P. et al. LNA (Locked Nucleic Acids): Synthesis of the adenine, cytosine, guanine, 5-methylcytosine, thymine and uracil bicyclonucleoside monomers, oligomerisation, and unprecedented nucleic acid recognition. *Tetrahedron* **54**, 3607-3630 (1998).

63. Nielsen, P.E., Egholm, M., Berg, R.H. & Buchardt, O. Sequence-Selective Recognition of DNA by Strand Displacement with a Thymine-Substituted Polyamide. *Science* **254**, 1497-1500 (1991).

64. Sugita, Y. & Okamoto, Y. Replica-exchange molecular dynamics method for protein folding. *Chemical Physics Letters* **314**, 141-151 (1999).

65. Bonomi, M. & Parrinello, M. Enhanced Sampling in the Well-Tempered Ensemble. *Physical review letters* **104** (2010).

66. D.A. Case, R.M.B., W. Botello-Smith, D.S. Cerutti, T.E. Cheatham, III, T.A. Darden, R.E. Duke, T.J. Giese, H. Gohlke, A.W. Goetz, N. Homeyer, S. Izadi, P. Janowski, J. Kaus, A. Kovalenko, T.S. Lee, S. LeGrand, P. Li, C. Lin, T. Luchko, R. Luo, B. Madej, D. Mermelstein, K.M. Merz, G. Monard, H. Nguyen, H.T. Nguyen, I. Omelyan, A. Onufriev, D.R. Roe, A. Roitberg, C. Sagui, C.L. Simmerling, J. Swails, R.C. Walker, J. Wang, R.M. Wolf, X. Wu, L. Xiao, D.M. York and P.A. Kollman AMBER 2016. (2016).

67. Humphrey, W., Dalke, A. & Schulten, K. VMD: Visual molecular dynamics. *J Mol Graph Model* **14**, 33-38 (1996).

68. Berendsen, H.J.C., Vanderspoel, D. & Vandrunen, R. Gromacs - a Message-Passing Parallel Molecular-Dynamics Implementation. *Comput Phys Commun* **91**, 43-56 (1995).

69. Hess, B., Kutzner, C., van der Spoel, D. & Lindahl, E. GROMACS 4: Algorithms for highly efficient, load-balanced, and scalable molecular simulation. *J Chem Theory Comput* **4**, 435-447 (2008).

70. Hart, K., Foloppe, N., Baker, C.M. et al. Optimization of the CHARMM Additive Force Field for DNA: Improved Treatment of the BI/BII Conformational Equilibrium. *J Chem Theory Comput* **8**, 348-362 (2012).

71. Essmann, U., Perera, L., Berkowitz, M.L. et al. A Smooth Particle Mesh Ewald Method. *Journal of Chemical Physics* **103**, 8577-8593 (1995).

72. Michaud-Agrawal, N., Denning, E.J., Woolf, T.B. & Beckstein, O. Software News and Updates MDAnalysis: A Toolkit for the Analysis of Molecular Dynamics Simulations. *Journal of computational chemistry* **32**, 2319-2327 (2011).

73. Zheng, M., Jagota, A., Semke, E.D. et al. DNA-assisted dispersion and separation of carbon nanotubes. *Nature materials* **2**, 338-342 (2003).

CHAPTER 3: CONTROL OF CARBON NANOTUBE SOLVATOCHROMIC RESPONSE TO CHEMOTHERAPEUTIC AGENTS

3.1 Abstract

Alkylating agents such as cisplatin play an essential role in chemotherapy regimens, but initial and acquired resistance in many cancer types often dampen therapeutic response. Poor understanding of the mechanisms of resistance highlight the need for quantitative measurements of alkylating agent distribution at both tissue and sub-cellular levels. Sensors for use in live animals and cells would allow for more effective study of drug action and resistance. Toward this end, single-walled carbon nanotubes suspended with single-strand DNA have suitable optical properties for *in vivo* sensors, such as near-infrared emission and sensitivity to the local environment via solvatochromic responses. Currently, solvatochromic changes of such sensors have been limited by the chemical nature of the analyte, making it impossible to control the direction of energy emission changes. Here, we describe a new approach to control the direction and magnitude of solvatochromic responses of carbon nanotubes. We found that the alkylation of DNA on the nanotube surface can result in small changes in DNA conformation that allow the adsorption of amphiphiles to produce large differences (> 14 nm) in response to different drugs. The technique surprisingly revealed differences among drugs upon alkylation. The ability to control carbon nanotube solvatochromism to desired changes may potentially expand the application of nanotube-based optical sensors for new classes of analytes.

3.2 Introduction

As a class of chemotherapy drugs, alkylating agents have essential roles in many cancer treatment protocols to date due to their cytotoxic effects on dividing cells[1]. The mechanism of action is partly due to alkylation of DNA in the nucleus, which affects replication and induces apoptosis[2]. The platinum analogs, such as cisplatin and carboplatin, are not true alkylating agents but are often grouped with these drugs due to a similar putative mechanism of cytotoxicity[3]. Cisplatin is relatively unreactive in chloride ion-rich environments because a chloride must leave and be replaced by water to produce the reactive intermediate[4]. A lower concentration of chloride in the cytoplasm (~4 mM) facilitates formation of the reactive intermediates[2], where they preferentially react with the nucleophilic N7 position of guanine, producing 1,2-intrastrand GpG crosslinks as the major DNA adduct[5]. Cisplatin has significant antitumor activity in a broad range of solid tumors, and it is curative in the treatment of testicular cancer[3]. However, initial and acquired resistance to cisplatin in some cancer types is a major clinical limitation[6]. The mechanisms that lead to resistance are only partially understood. Attempts to develop improved platinum-based therapies have been met with limited success[7].

Current methods for detecting cisplatin distribution require invasive and destructive measurement of platinum accumulation in tissues *ex vivo*[8-13]. Similar issues exist for other small alkylating agents. An implantable sensor for active alkylating drugs such as cisplatin could be useful in understanding drug reactivity and distribution *in vivo*. Such a sensor could also be used to elucidate mechanisms of acquired resistance and screen reactivity and efficacy of new platinum compounds.

As a nanoscale sensing element, single-walled carbon nanotubes have advantages due to their photostable emission in the near-infrared spectral range[14] that is responsive to

the local environment *via* solvatochromic changes[15-17]. Up to 17 distinct chiralities with unique spectral properties can be measured[18]. Carbon nanotubes non-covalently functionalized with single-stranded DNA have found unique success in applications toward optical biomedical sensors[19] for the measurement of small molecules, proteins, and biological processes[20-23] as well as implantable devices for *in vivo* uses[24, 25]. Previous work has found that alkylating agents can elicit a solvatochromic red-shift upon incubation with DNA-suspended nanotubes[26].

In general, carbon nanotube optical sensors are based on an interaction with the target analyte that leads to modulation of the local dielectric environment, which can elicit a change in emission intensity or a solvatochromic shift in the emission wavelength. The emission can shift towards higher energies (relative blue shift) or towards lower energies (relative red shift). Heretofore, it has not been possible to control the direction of solvatochromic shifting (toward red or blue) to a particular analyte. Exercising control over the direction and magnitude of solvatochromic shifting to a particular analyte is important for expanding the application of nanotube-based sensors where a desired optical output is necessary, such as larger responses to confer greater sensitivities, or as part of a multiplexing scheme that could be used to identify multiple analytes[25, 27].

Herein, we describe a method to control the direction of solvatochromic shifting of carbon nanotube emission in response to a class of analytes, alkylating chemotherapeutic drugs. Using this method, we discovered that it exacerbates the optical response to small chemical differences between drug compounds. While previous work found that the alkylation of DNA on single-walled carbon nanotubes results in a small solvatochromic shift of the nanotubes towards longer wavelengths, we found that the perturbation with a small molecule amphiphile, sodium

dodecylbenzene sulfonate (SDBS) can cause large drug-mediated shifts towards shorter wavelengths. Interestingly, the resulting responses were strikingly different, depending on the alkylating drug. Notably, the responses to platinum compounds, which previously elicited small red-shifting responses, were exacerbated. Also, although cisplatin and transplatin both produced red-shifts in nanotube emission with approximately the same kinetics, the exposure to the amphiphile resulted in transplatin blue shifting the emission to a significantly greater degree. We attribute these phenomena to alkylating agent-induced distortions to the DNA that are drug-dependent, resulting in exposure of the nanotube surface to different degrees. The method produced large differences in drug-induced nanosensor responses.

3.3 Results and discussion

Using single-walled carbon nanotubes (HiPco preparation) suspended with the DNA oligonucleotide with the sequence $(GT)_{15}$, we measured the response of all chiralities to cisplatin. Upon treating the nanotubes with cisplatin (1000 uM) in HEPES (20 mM) buffer for 12 hours, we assayed the sample *via* two-dimensional excitation/emission photoluminescence spectroscopy (PL plots, Figure 3.1)[28] and found that, for all measured chiralities, there was a consistent red-shift in emission ranging from about 2 nm to 4 nm. Some chiralities additionally showed a red-shift in excitation, indicating that for some chiralities, alkylation also induced a change in the ground state absorption energies (Figure 3.2). Because all nanotube chiralities behaved similarly, we moved our focus to a purified chirality, $(GT)_{20}$-suspended (8,4) nanotubes[29]. PL plots of purified $(GT)_{20}$ revealed a high degree of purity, and the emission behaved similarly by red-shifting upon the addition of cisplatin (Figure 3.3.). A dose-response measurement of $(GT)_{20}$-suspended (8,4) nanotubes with cisplatin showed clear cisplatin dose-dependent red-shifting (Figure 3.4). The kinetics were similarly dependent on concentration (Figure 3.5).
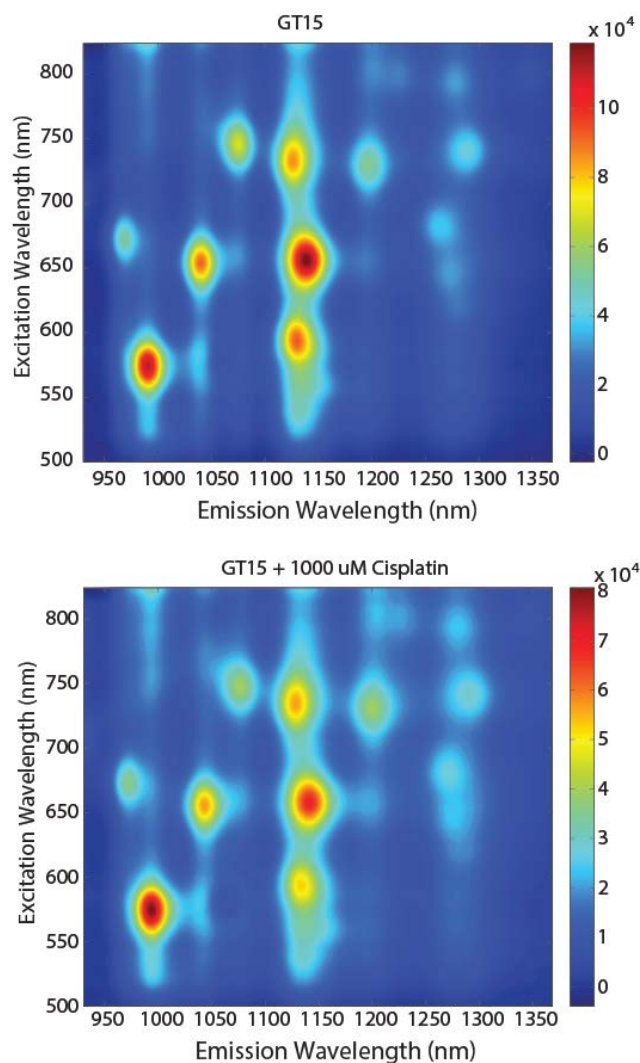
***Figure 3.1 Two-dimensional excitation/emission photoluminescence plots (PL plots)
of (GT)15-suspended HiPCO nanotubes (2 mg/L) in buffer only conditions (top plot)
and after 12h with 1000 uM cisplatin (bottom plot).*** Color bars indicate the emission
intensity in arbitrary units.
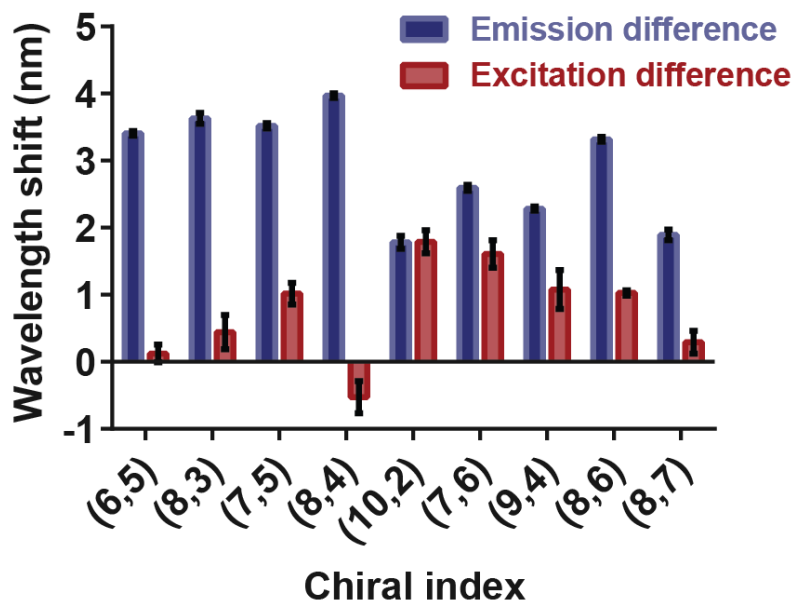
Figure 3.2 Emission and excitation wavelength responses to cisplatin. The emission
wavelengths of the nanotube emission bands from the PL plots in Figure S1 were
subtracted. Peaks were fit to Lorenztian functions. The x-axis lists nanotube species
according to their chiral indices. Error bars represent standard deviation of technical
replicates.
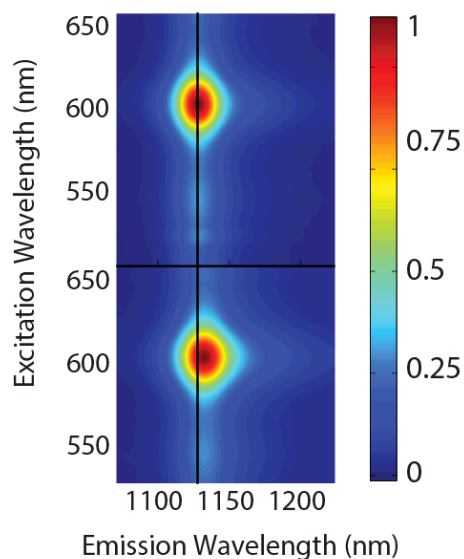
***Figure 3.3 Two-dimensional excitation/emission photoluminescence plot of (top
panel) purified (GT)20-suspended (8,4) nanotubes in buffer and (bottom panel) with
1000 uM cisplatin (bottom plot).*** Vertical black line is a visual reference to compare
center wavelengths.
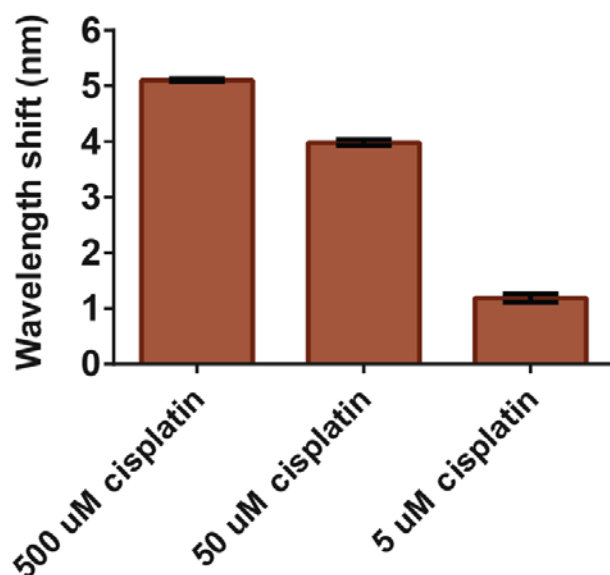
Figure 3.4 Dose-dependent wavelength shifts of (GT)20-suspended (8,4) nanotubes after overnight equilibration with the indicated concentration of cisplatin*.* Differences are based on untreated control samples. Error bars represent standard deviation of technical replicates.
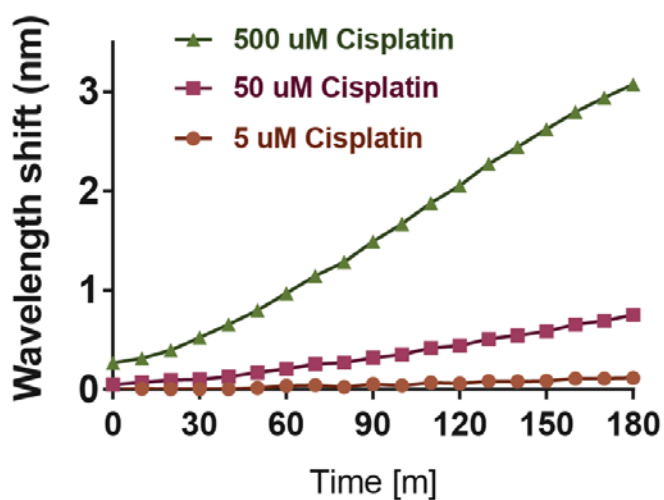
Figure 3.5 Dose-dependent red-shifting kinetics of (GT)20-suspended (8,4) nanotubes during the first three hours after addition of drug*.* Spectra were acquired every 10 minutes following addition of the indicated concentration of cisplatin. Wavelength shifts are presented as difference from buffer treated control sample. Error bars represent standard deviation of technical replicates

121

To determine whether the observed red-shifting of the nanotube from added cisplatin was due to alkylation of the DNA and not due to non-specific interactions, we measured the extent of red-shifting as a function of added sodium chloride. Using $(GT)_{20}$-suspended (8,4) nanotube samples at 2 mg/L, we varied the sodium chloride concentration of the buffer before adding 500 uM cisplatin to each sample. After incubation overnight, we observed a linear decrease in the extent of red-shifting as the concentration of sodium chloride was increased. Above approximately 80 mM NaCl, red-shifting was barely detectable (Figure 3.6). Linear regression applied between 0-80 mM NaCl (R^2 = 0.9885) produced a slope of -0.06177 (Figure 3.7), denoting that, for every 10 mM increase in sodium chloride, the maximal red-shift decreased by about 0.6 nm. This behavior was consistent with the chloride-dependent reactivity of cisplatin, and suggests that a covalent reaction (alkylation) is responsible for the red-shift. Lastly, we investigated whether the red-shift was due to aggregation of nanotubes upon reaction with cisplatin. We immobilized $(GT)_{15}$-suspended nanotubes in 3% agarose gel and found that the addition of cisplatin (500 uM) still resulted in a red-shift (Figure 3.8) with similar kinetics (Figure 3.9), suggesting that aggregation was not a major causative factor of the red-shifting response.
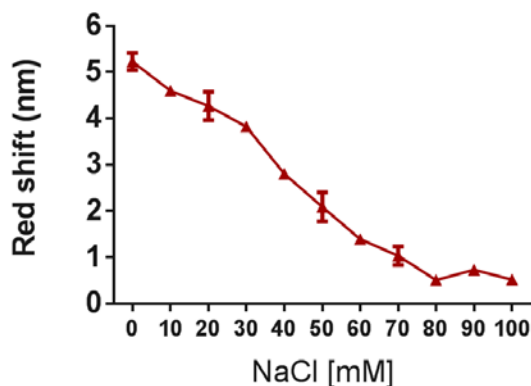
Figure 3.6 Response of the nanotube emission as a function of sodium chloride.
$(GT)_{20}$-suspended (8,4) were incubated with the indicated concentration of sodium chloride overnight and incubated with 500 uM cisplatin or buffer control for an additional 12h. Error bars represent standard deviation of technical replicates.
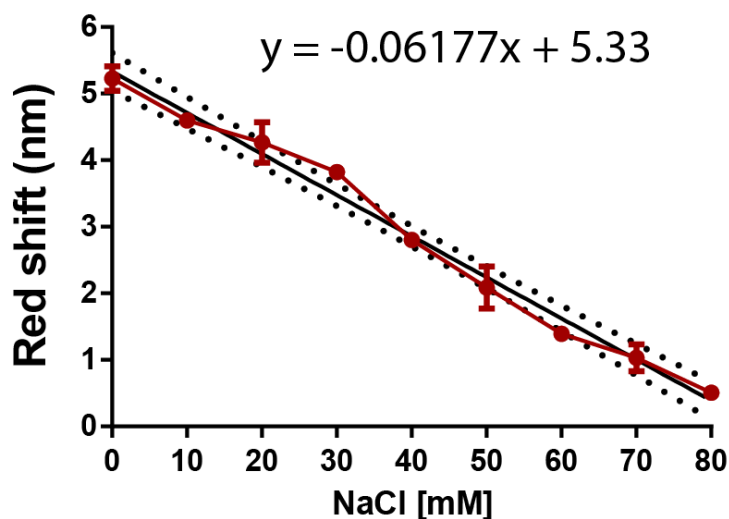
Figure 3.7 Linear regression of nanotube emission red-shifting as a function of sodium chloride from 0 to 80 mM NaCl. Black solid line represents the linear fit with equation y=-0.06177x + 5.33, and dotted black line represents 95% confidence interval of the fit. Error bars represent standard deviation of technical replicates.
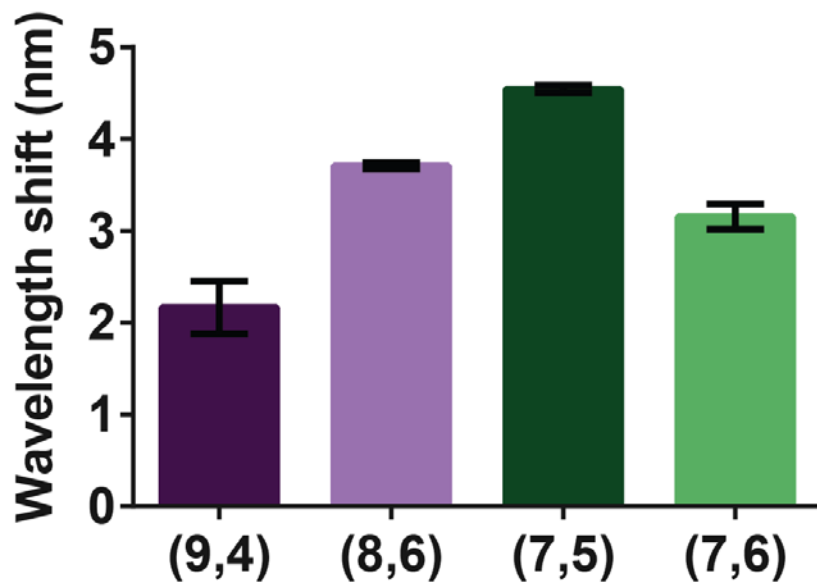
Figure 3.8 Wavelength shifts of (GT)$_{15}$-suspended nanotubes at 2 mg/L immobilized in 3% agarose gel and treated with 100 uM cisplatin overnight. Wavelength shifts relative to buffer treated control are reported for four nanotube chiralities. Error bars represent standard deviation of 3 agarose gel replicates.
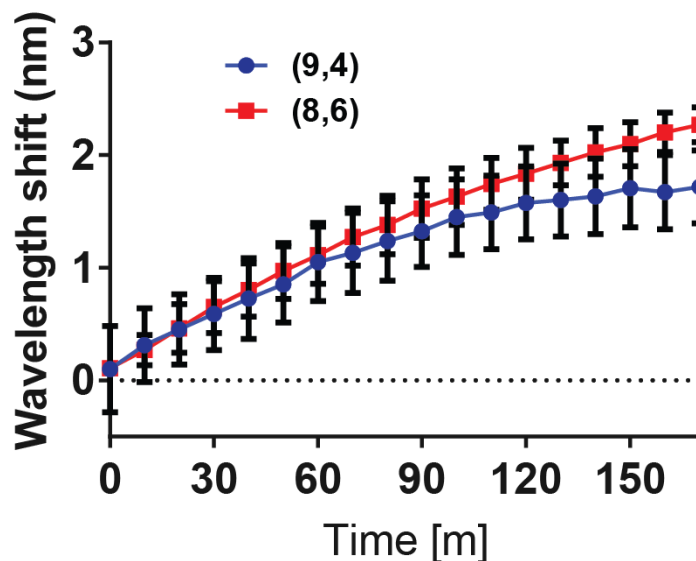
Figure 3. 9 Kinetics of the emission response of (GT)₁₅-suspended nanotubes at 2 mg/L immobilized in 3% agarose gel and treated with 100 uM cisplatin at time 0. Spectra were acquired every 10 m. Two nanotubes chiralities, (9,4) and (8,6), were measured simultaneously under 730 nm excitation. Wavelength shift was computed from buffer only control. Error bars represent standard deviation of 3 gel preparations.

We investigated the effects of amphiphilic molecules on the nanotube response upon alkylation. We hypothesized that the alkylation of cisplatin changes the DNA conformation on the nanotube in a manner that decreases DNA surface coverage. A previous screen of amphiphiles found that SDBS blue-shifts DNA-suspended nanotubes in a manner consistent with nanotube surface accessibility[25]. Thus, we tested if SDBS could modulate the wavelength shifting response of cisplatin. Upon reaction of (GT)₂₀-suspended (8,4) nanotubes with cisplatin in the presence of SDBS, a blue shift was observed, instead of the usual red shift (Figure 3.10a). The spectra were fit to Lorenztian functions to quantify the changes in center wavelength and intensity, showing clear differences (Figure 3.10b). While the wavelength exhibited a clear dependence on SDBS the intensity was largely unaffected. Based on this data, we developed a model of how SDBS allows solvatochromic control of the nanotube

124

(Figure 3.10c). Cisplatin reacts with guanine bases to distort the DNA conformation and expose more of the nanotube surface to water, leading to the observed red-shift in emission[15]. In the presence of SDBS, this same conformational change allows greater exposure of the nanotube surface to the surfactant, which adsorbs to the nanotube surface, producing a blue shift in emission.
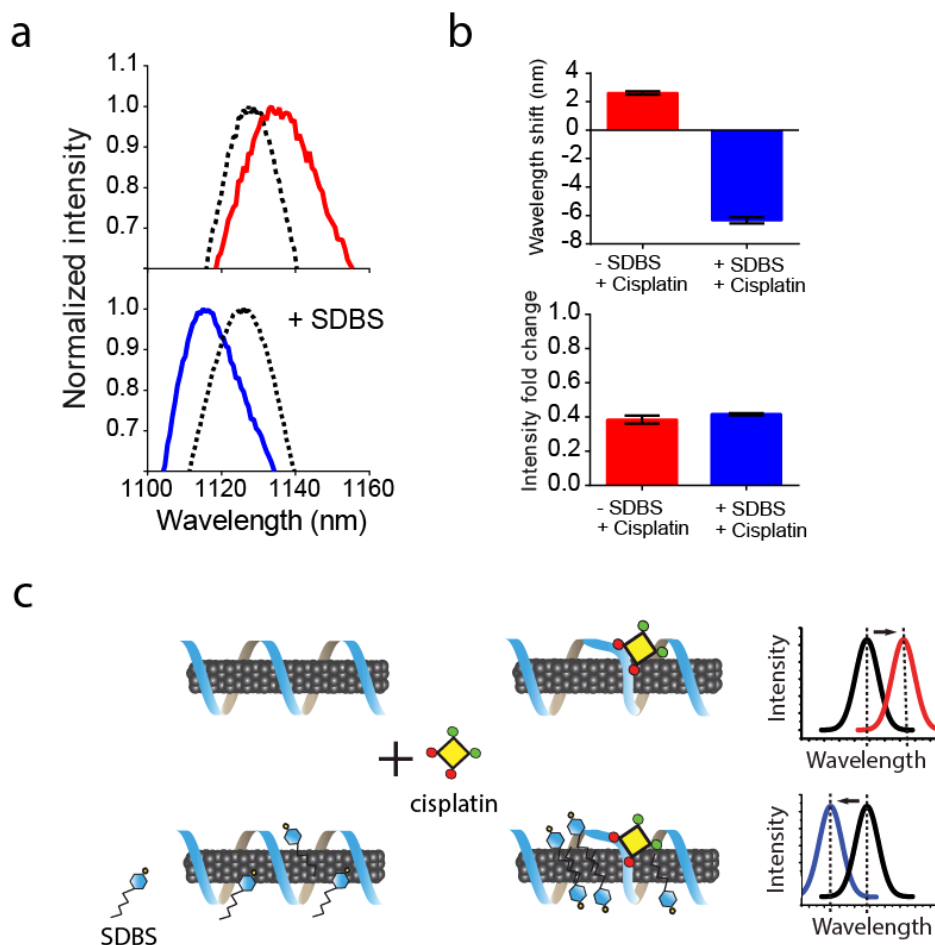
Figure 3.10 Control of solvatochromic shift. **a**, Normalized emission spectra of: (top panel) $(GT)_{20}$-suspended (8,4) nanotubes in buffer (black dotted line) and the nanotubes with 500 uM cisplatin (red line), and (bottom panel) $(GT)_{20}$-suspended (8,4) nanotubes in buffer with 0.2% SDBS (black dotted line), and 0.2% SDBS plus 500 uM cisplatin (blue line). **b)** Change in the (top panel) emission wavelength and (bottom panel) intensity of $(GT)_{20}$-suspended (8,4) nanotube emission after incubation with cisplatin and/or 0.2% SDBS. **c)** Illustration of hypothesized mechanism of solvatochromic shift control. Cisplatin distorts the DNA allowing more water to access the nanotube surface, while SDBS displaces water upon binding to the nanotube.

To better understand the role of SDBS in modulating the solvatochromic response to cisplatin, we devised an additional experiment to remove cisplatin after alkylation. We exposed $(GT)_{15}$-suspended nanotubes to cisplatin (Figure 3.11a, step 1), before dialyzing against a 500 kDa MWCO membrane to remove unbound cisplatin (Figure 3.11a, step 2). After three dialysis steps, (2-3 hours each, with overnight dialysis on the third step), we found that the red-shift persisted relative to a control dialysis experiment without cisplatin (Figure 3.11b). We interpret this result to mean that cisplatin-induced distortion of the DNA persisted throughout the dialysis process. Upon introducing SDBS outside of the dialysis bag (Figure 3.11a, step 3), we observed a blue-shift (Figure 3.11a, step 4). This blue-shift, relative to the cisplatin-free dialysis control, reached a maximum after 90 minutes (Figure 3.11b) and largely recapitulated the shift in the presence of cisplatin (Figure 3.10). We conclude that SDBS does not affect the reactivity of cisplatin with DNA on the nanotube, and that the effect of SDBS is due to the cisplatin-induced modulation of DNA conformation on the nanotube which exposes the nanotube surface.
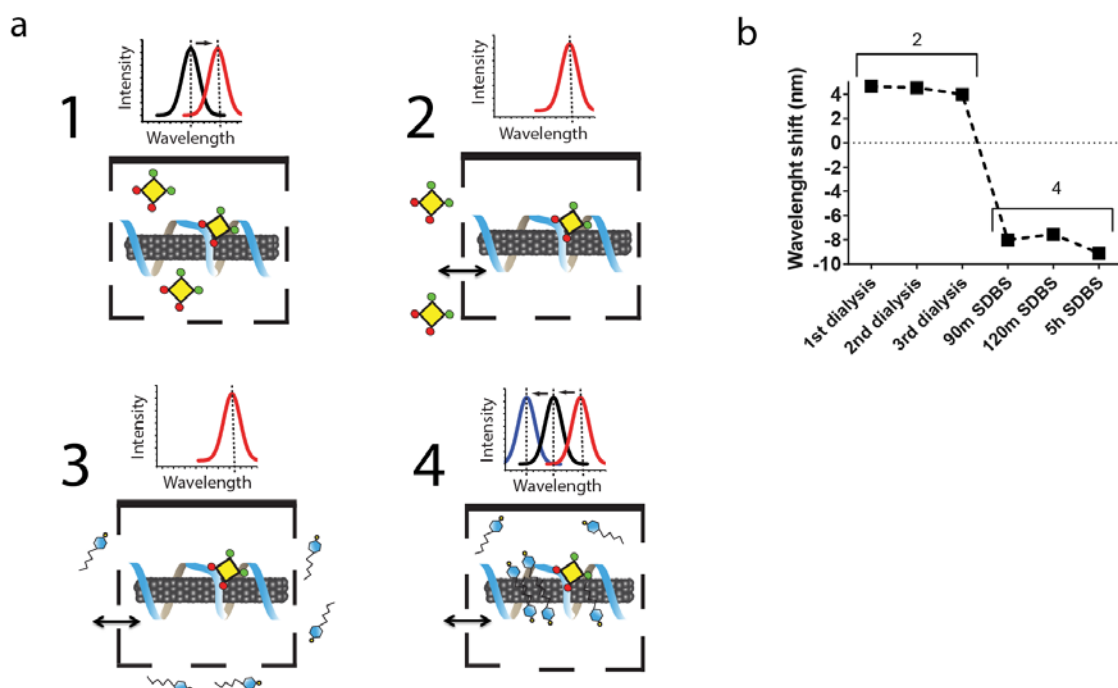
Figure 3.11 Dialysis experiment involving cisplatin and SDBS interactions with the DNA-nanotube complex. **a)** Sequence of experimental steps of dialysis experiment. (1) Cisplatin was introduced to $(GT)_{15}$-encapsulated nanotubes in a dialysis membrane, resulting in a red-shift in emission. (2) The dialysate was changed to remove un-reacted cisplatin, but the red-shift persisted. (3) SDBS was added to the dialysate. (4) The nanotube emission blue-shifted after the addition of SDBS. **b)** Response of the (9,4) nanotube emission, compared to an identically-treated control without cisplatin, corresponding to the experiment outlined in panel **a**. Numbers indicate corresponding step in the experimental outline.

A panel of alkylating agents with applications in chemotherapy was used to assess the generalizability of this phenomenon. Figure 3.12a depicts the chemical structures of the five alkylating agents tested: (1) cisplatin, (2) transplatin, (3) carboplatin, (4) mechlorethamine, and (5) melphalan. When an equimolar (100 uM) amount of each alkylating agent was added to $(GT)_{20}$-suspended (8,4) nanotubes, a consistent red-shift of approximately 2 nm was observed for all alkylating agents except carboplatin (Figure 3.12b). Carboplatin is a second generation platinum analogue that displays less nephrotoxicity than cisplatin, but also significantly less reactivity [30, 31], which may explain the lack of an effect on the nanotubes. When we tested the panel of alkylating agents in the presence of SDBS, all agents that previously red-shifted instead blue-shifted to varying degrees (Figure 3.12b). Carboplatin again showed no change with SDBS, consistent with the hypothesis that a reaction-induced distortion of the DNA is necessary for SDBS to elicit a blue-shift. The other platinum-based drugs exhibited large blue-shifting responses, however. Strikingly, transplatin induced a blue-shifting response of over 14 nm (Figure 3.12b), and it also resulted in a substantial increase in intensity of the nanotube, as compared to the other agents (Figure 3.12c).
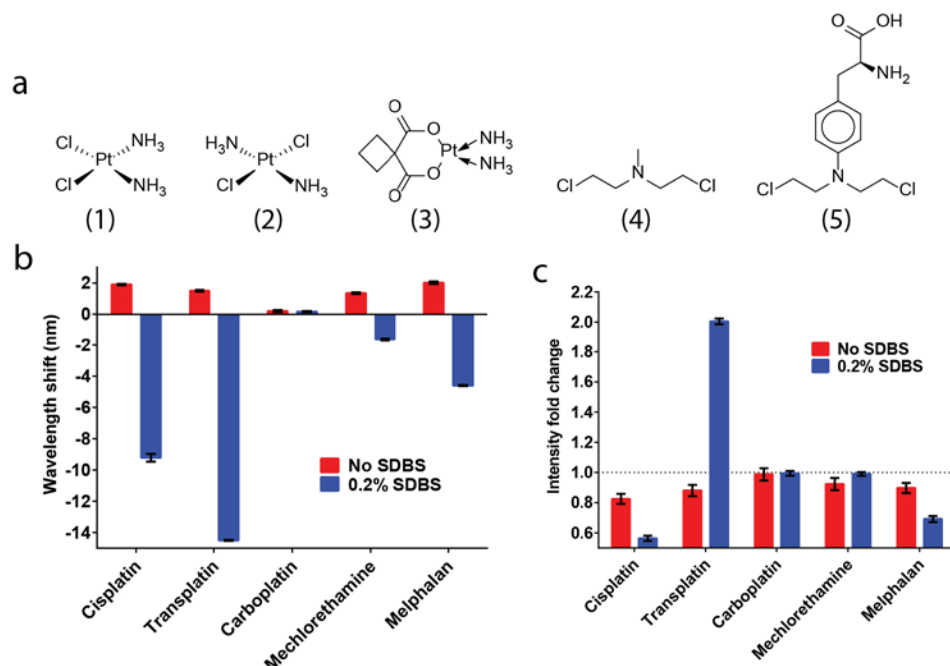
Figure 3.12: Solvatochromic response to a panel of alkylating agents. **a)** Chemical structures of alkylating chemotherapy drugs tested: (1) cisplatin, (2) transplatin, (3) carboplatin, (4) mechlorethamine, (5) melphalan. **b)** Wavelength shifting response of $(GT)_{20}$-suspended (8,4) nanotubes after incubation with the indicated alkylating agent in buffer only (red) and in the presence of 0.2% SDBS. Wavelength shifts are reported relative to nanotubes in buffer only. **c)** Intensity response of the nanotubes under the same conditions. Error bars represent standard deviation of technical triplicates.

The large difference in transplatin activity versus cisplatin warranted further investigation. Transplatin, a stereoisomer of cisplatin, differs only in the spatial relationship of the two chloride leaving groups (Figure 3.13a), but provides no clinical benefit despite its reactivity towards DNA[32, 33]. The type of DNA adduct transplatin forms is thought to be non-toxic to cells compared to that formed by cisplatin[32]. Given the contrast between these two agents, we hypothesized that transplatin was making an adduct that distorted DNA on the nanotube to a greater extent than cisplatin. When tested in buffer-only conditions, we found that the red shifts induced by cisplatin and

transplatin on $(GT)_{20}$-encapsulated nanotubes were similar (Figure 3.13b), and with similar kinetics (Figure 3.13c). This is consistent with previous work showing that cisplatin and transplatin form monofunctional adducts with DNA at approximately the same rate[34]. When the identical kinetics experiment is done in the presence of SDBS, a rapid blue-shift is observed for transplatin compared to cisplatin, which takes several hours and is not apparent on this timescale (Figure 1.13d). In contrast, after two hours, transplatin has almost maximally blue-shifted the nanotube response. Near-infrared PL plots revealed that there was a significant chirality dependence on the rate of blue-shifting, with the two smallest diameter nanotubes ((6,5) and (8,3)) shifting at the fastest rates (Figure 3.14). Although the kinetics and magnitude of red-shifting were nearly identical for cisplatin and transplatin in buffer conditions, the addition of SDBS revealed that transplatin resulted in changes of the DNA conformation of a fundamentally different character that revealed a larger degree of nanotube surface, leading to a greater blue-shifting response. We summarize these findings in an illustration in Figure 3.15. The conformational changes induced by cisplatin and transplatin were optically indistinguishable in normal buffer conditions, but the differences become apparent in the presence of SDBS, revealing that the DNA distortions induced by cisplatin and transplatin were indeed different.
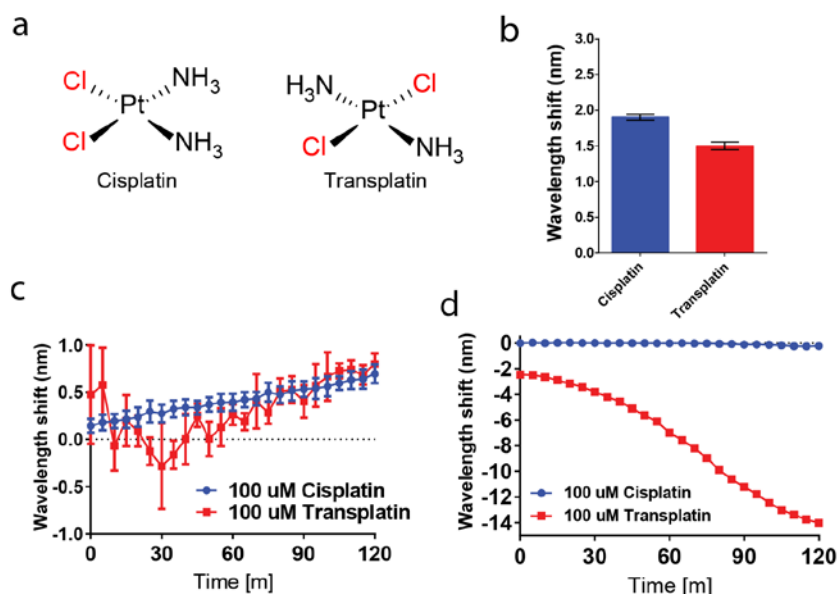
Figure 3.13 Comparison of nanotube response to cisplatin and transplatin. **a)** Chemical structures of cisplatin and transplatin, with the configuration of the chloride leaving groups highlighted in red. **b)** Response of $(GT)_{15}$ encapsulated (9,4) in the presence of 100 uM cisplatin or transplatin in buffer, at 12h. **c)** Kinetic response of the (9,4) nanotube emission wavelength in the presence of cisplatin or transplatin, in buffer-only conditions. **d)** Kinetic responses as in panel **c** but in the presence of 0.2% SDBS. Error bars represent standard deviation.
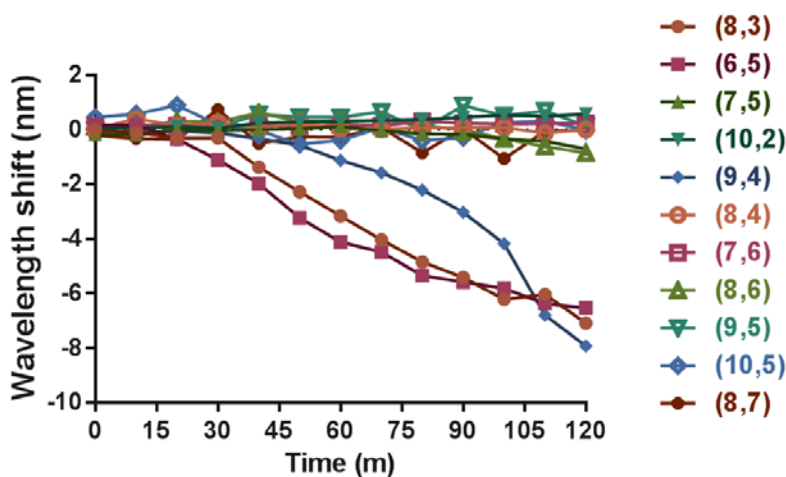
Figure 3.14 Kinetics of emission response of several nanotube chiralities. Two-dimensional excitation/emission photoluminescence spectroscopy (PL) plots were acquired after addition of 100 uM to $(GT)_{15}$-suspended nanotubes in the presence of 0.2% SDBS. The emission wavelength shifts of 11 different nanotube species were calculated as differences from buffer treated controls in 0.2% SDBS.
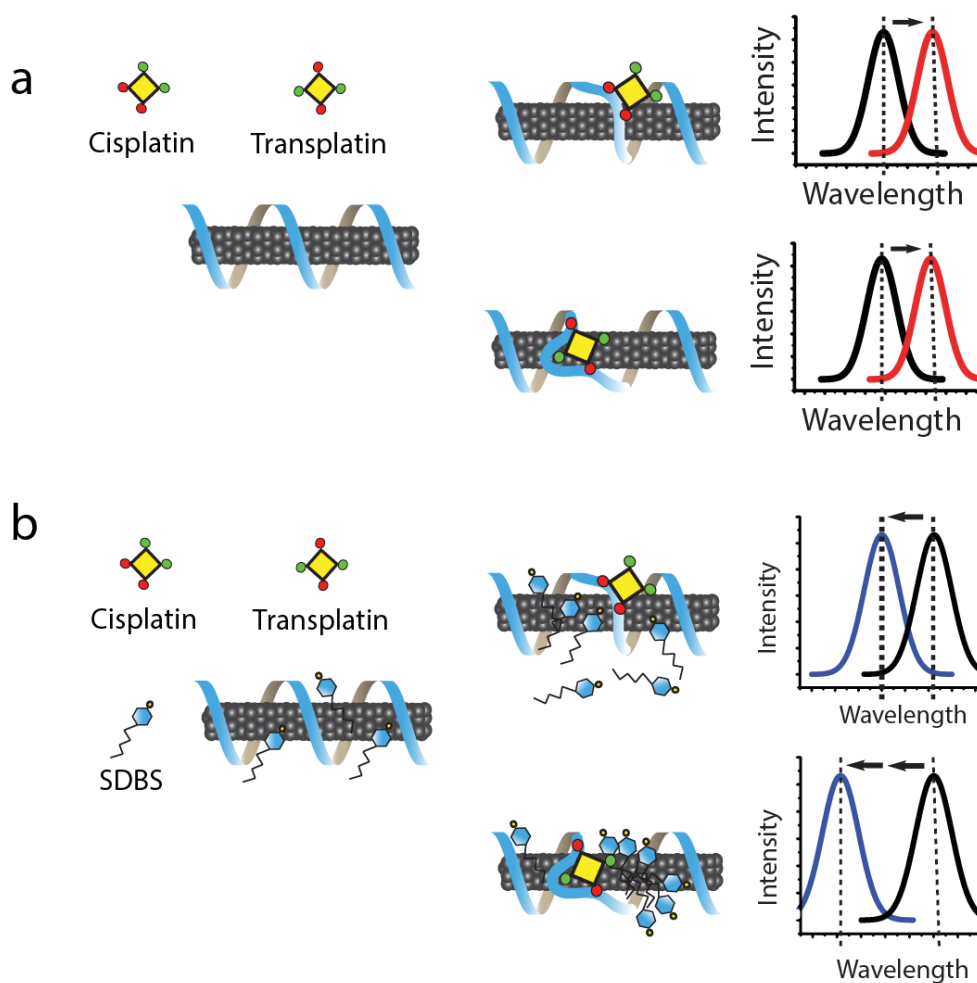
***Figure 3.15 Illustration of the proposed mechanism of the difference in nanotube emission response upon interaction with cisplatin or transplatin*. a)** Cisplatin and transplatin react with DNA on the nanotube to introduce distortions that are different but yield identical optical changes. **b)** The distortion in the transplatin-bound complex allows a greater amount of SDBS to bind to the nanotube surface, producing a larger blue-shift for transplatin-induced distortions.

3.4 Conclusions

We found a method to control the direction of solvatochromic shifting to a class of analytes and probe the structural changes to DNA on the nanotube surface. Alkylating agents such as cisplatin covalently react with DNA on carbon nanotubes to induce conformational changes that increase accessibility of water to the nanotube surface, leading to red-shifting. Based on this mechanism, we found that the addition of SDBS, an amphiphilic surfactant, causes the nanotube to instead blue-shift upon reaction of the drugs to the nanotube-bound DNA. Dialysis experiments suggested that SDBS was a passive reporter of the changes induced by the alkylating agents, providing mechanistic insight into the origin of the solvatochromic changes. To our knowledge, this is the first report describing directional control of carbon nanotube solvatochromic shifts in response to a target analyte. The ability to control the direction of solvatochromic shifts of nanotubes in response to a target analyte has important implications for the future application of sensors where certain output is necessary or desired, such as part of a multiplexed sensing scheme. Finally, we found that cisplatin and transplatin produce different DNA distortions on the nanotube that are optically indistinguishable in buffer only conditions, but apparent only in the presence of SDBS. Such insights will continue to improve application of carbon nanotube sensors for the detection of active chemotherapeutic drugs and other analytes.

3.5 Materials and Methods

3.5.1 DNA-suspension of carbon nanotubes

Carbon nanotubes produced by the HiPco process (Unidym, Sunnyvale, CA) were mixed with DNA oligonucleotides (IDT DNA, Coralville, IA) at a 2:1 mass ratio in 1 mL of HEPES (20 mM) buffer (Thermo Fisher Scientific Waltham, MA) and ultrasonicated for 30 minutes at 40% amplitude (Sonics & Materials, Inc.). The DNA

sequences used for suspension were $(GT)_{15}$, $(AT)_{15,}$ $(TAT)_6$, $(GTT)_3G$, $(CCG)_2CC$, $(TGTT)_2TGT$, $(GGGGT)_6$, all purchased from IDT (Coralville, IA). Following ultrasonication, the dispersions were ultracentrifuged (Sorvall Discovery 90SE) for 30 minutes at 280,000 x g and the top 80% of the supernatant was collected. Absorbance spectra were acquired using a UV/Vis/nIR spectrophotometer (Jasco V-670, Tokyo, Japan). The concentration for HiPco samples was calculated using the extinction coefficient $Abs_{910} = 0.02554$ L $mg^{-1}cm^{-1}$. Excess DNA was removed via 100 kDa Amicon centrifuge filters (Millipore). The DNA-nanotube complexes were re-suspended in HEPES (20 mM) buffer (Thermo Fisher Scientific Waltham, MA). Purified $(GT)_{20}$-suspended (8,4) nanotubes were prepared as described[29].

3.5.2 Fluorescence spectroscopy measurements of carbon nanotubes

Fluorescence emission spectra from aqueous nanotube solutions were acquired with a home-build spectroscopy system as described[25]. Briefly, carbon nanotube samples were assayed in a 96 well plate format on an inverted microscope using a tunable white-light laser (NKT Photonics) coupled to a variable bandpass filter. Emission light was directed into a spectrometer with a focal length of 320 mm and aperture ratio of f/4.6 (Princeton Instruments IsoPlane SCT 320) and InGaAs array camera (Princeton Instruments 640×512 pixel NIRvana). For all experiments, measurements were taken in triplicate across three wells. Concentrated sodium dodecylbenzenesulfonate (Sigma-Aldrich) was prepared in HEPES (20 mM) buffer and added to samples where indicated to a final concentration of 0.2% wt/vol; control samples had an equivalent volume of buffer added. Cisplatin, melphalan, mechlorethamine, carboplatin (all from Sigma-Aldrich) and transplatin (Acros Organics) were all prepared in HEPES (20 mM) buffer, except melphalan which was prepared in DMSO (Acros Organics). Control samples received an equivalent volume of buffer or DMSO. Experiments involving

dialysis used KrosFlo Membranes (500 kD MWCO) from Spectrum Labs (Rancho Dominguez, CA) filled with 15 uL of 2 mg/L sample and dialyzed in 2 mL of HEPES (20 mM) buffer dialysate. Experiments with nanotube immobilized in gels were prepared as described[35] in 3% low melt agarose gels directly into wells of a 96 well plate. Following spectra acquisition, custom code written in Matlab applied spectral corrections and background subtraction as described[25]. Corrected spectra were used to fit the data with Lorentzian functions. Error bars and linear fits were computed with GraphPad Prism 6.

3.6 Acknowledgements

3.7 References

1.   Eastman, A. Activation of Programmed Cell-Death by Anticancer Agents - Cisplatin as a Model System. *Cancer Cell-Mon Rev* **2**, 275-280 (1990).

2.   Siddik, Z.H. Cisplatin: mode of cytotoxic action and molecular basis of resistance. *Oncogene* **22**, 7265-7279 (2003).

3.   Katzung, B.G., Masters, S.B. & Trevor, A.J. Basic & clinical pharmacology, Edn. 11th. (McGraw-Hill Medical ; McGraw-Hill distributor, New York, London; 2009).

4.   Bancroft, D.P., Lepre, C.A. & Lippard, S.J. Pt-195 Nmr Kinetic and Mechanistic Studies of Cis-Diamminedichloroplatinum and Trans-Diamminedichloroplatinum(Ii) Binding to DNA. *Journal of the American Chemical Society* **112**, 6860-6871 (1990).

5.   Pinto, A.L. & Lippard, S.J. Binding of the Antitumor Drug Cis-Diamminedichloroplatinum(Ii) (Cisplatin) to DNA. *Biochimica et biophysica acta* **780**, 167-180 (1984).

6.   Einhorn, L.H. Curing metastatic testicular cancer. *Proceedings of the National Academy of Sciences of the United States of America* **99**, 4592-4595 (2002).

7.   Kelland, L. The resurgence of platinum-based cancer chemotherapy. *Nature reviews. Cancer* **7**, 573-584 (2007).

8.   Chang, Q., Ornatsky, O.I., Siddiqui, I. et al. Biodistribution of cisplatin revealed by imaging mass cytometry identifies extensive collagen binding in tumor and normal tissues. *Scientific reports* **6** (2016).

9.   Fichtingerschepman, A.M.J., Vanoosterom, A.T., Lohman, P.H.M. & Berends, F. Cis-Diamminedichloroplatinum(Ii)-Induced DNA Adducts in Peripheral Leukocytes from 7 Cancer-Patients - Quantitative Immunochemical Detection

of the Adduct Induction and Removal after a Single Dose of Cis-Diamminedichloroplatinum(Ii). *Cancer research* **47**, 3000-3004 (1987).

10. Zenker, A., Galanski, M., Bereuter, T.L., Keppler, B.K. & Lindner, W. Capillary electrophoretic study of cisplatin interaction with nucleoside monophosphates, di- and trinucleotides. *J Chromatogr A* **852**, 337-346 (1999).

11. Reeder, F., Guo, Z.J., Murdoch, P.D. et al. Platination of a GG site on single-stranded and double-stranded forms of a 14-base oligonucleotide with diaqua cisplatin followed by NMR and HPLC - Influence of the platinum ligands and base sequence on 5'-G versus 3'-G platination selectivity. *European Journal of Biochemistry* **249**, 370-382 (1997).

12. Huang, H.F., Zhu, L.M., Reid, B.R., Drobny, G.P. & Hopkins, P.B. Solution Structure of a Cisplatin-Induced DNA Interstrand Cross-Link. *Science* **270**, 1842-1845 (1995).

13. Hah, S.S. & Henderson, P.T. Kinetics of carboplatin-DNA binding in genomic DNA and bladder cancer cells as determined by accelerator mass spectrometry. *Chem Res Toxicol* **19**, 1683-1683 (2006).

14. O'Connell, M.J., Bachilo, S.M., Huffman, C.B. et al. Band gap fluorescence from individual single-walled carbon nanotubes. *Science* **297**, 593-596 (2002).

15. Choi, J.H. & Strano, M.S. Solvatochromism in single-walled carbon nanotubes. *Applied Physics Letters* **90**, 223114 (2007).

16. Gao, J., Gomulya, W. & Loi, M.A. Effect of medium dielectric constant on the physical properties of single-walled carbon nanotubes. *Chemical Physics* **413**, 35-38 (2013).

17. Heller, D.A., Jeng, E.S., Yeung, T.K. et al. Optical detection of DNA conformational polymorphism on single-walled carbon nanotubes. *Science* **311**, 508-511 (2006).

18. Roxbury, D., Jena, P.V., Williams, R.M. et al. Hyperspectral Microscopy of Near-Infrared Fluorescence Enables 17-Chirality Carbon Nanotube Imaging. *Scientific reports* **5**, 14167 (2015).

19. Zheng, M., Jagota, A., Semke, E.D. et al. DNA-assisted dispersion and separation of carbon nanotubes. *Nature materials* **2**, 338-342 (2003).

20. Zhang, J.Q., Kruss, S., Hilmer, A.J. et al. A Rapid, Direct, Quantitative, and Label-Free Detector of Cardiac Biomarker Troponin T Using Near-Infrared Fluorescent Single-Walled Carbon Nanotube Sensors. *Adv Healthc Mater* **3**, 412-423 (2014).

21. Budhathold-Uprety, J., Langenbacher, R.E., Jena, P.V., Roxbury, D. & Heller, D.A. A Carbon Nanotube Optical Sensor Reports Nuclear Entry via a Noncanonical Pathway. *ACS nano* **11**, 3875-3882 (2017).

22. Roxbury, D., Jena, P.V., Shamay, Y., Horoszko, C.P. & Heller, D.A. Cell Membrane Proteins Modulate the Carbon Nanotube Optical Bandgap via Surface Charge Accumulation. *ACS nano* **10**, 499-506 (2016).

23. Zhang, J., Landry, M.P., Barone, P.W. et al. Molecular recognition using corona phase complexes made of synthetic polymers adsorbed on carbon nanotubes. *Nature nanotechnology* **8**, 959-968 (2013).

24. Iverson, N.M., Barone, P.W., Shandell, M. et al. In vivo biosensing via tissue-localizable near-infrared-fluorescent single-walled carbon nanotubes. *Nature nanotechnology* **8**, 873-880 (2013).

25. Harvey, J.D., Jena, P.V., Baker, H.A. et al. A carbon nanotube reporter of microRNA hybridization events in vivo. *Nature Biomedical Engineering* **1**, 0041 (2017).

26.   Heller, D.A., Jin, H., Martinez, B.M. et al. Multimodal optical sensing and analyte specificity using single-walled carbon nanotubes. *Nature nanotechnology* **4**, 114-120 (2009).

27.   Heller, D.A., Pratt, G.W., Zhang, J.Q. et al. Peptide secondary structure modulates single-walled carbon nanotube fluorescence as a chaperone sensor for nitroaromatics. *Proceedings of the National Academy of Sciences of the United States of America* **108**, 8544-8549 (2011).

28.   Bachilo, S.M., Strano, M.S., Kittrell, C. et al. Structure-assigned optical spectra of single-walled carbon nanotubes. *Science* **298**, 2361-2366 (2002).

29.   Ao, G.Y., Khripin, C.Y. & Zheng, M. DNA-Controlled Partition of Carbon Nanotubes in Polymer Aqueous Two-Phase Systems. *Journal of the American Chemical Society* **136**, 10383-10392 (2014).

30.   Knox, R.J., Friedlos, F., Lydall, D.A. & Roberts, J.J. Mechanism of Cytotoxicity of Anticancer Platinum Drugs - Evidence That Cis-Diamminedichloroplatinum(Ii) and Cis-Diammine-(1,1-Cyclobutanedicarboxylato)Platinum(Ii) Differ Only in the Kinetics of Their Interaction with DNA. *Cancer research* **46**, 1972-1979 (1986).

31.   Ho, G.Y., Woodward, N. & Coward, J.I.G. Cisplatin versus carboplatin: comparative review of therapeutic management in solid malignancies. *Crit Rev Oncol Hemat* **102**, 37-46 (2016).

32.   Lippert, B. Trans-diammineplatinum(II): What makes it different from cis-DDP? Coordination chemistry of a neglected relative of cisplatin and its interaction with nucleic acids. *Met Ions Biol Syst* **33**, 105-141 (1996).

33.   Coluccia, M. & Natile, G. Trans-Platinum Complexes in Cancer Therapy. *Anti-Cancer Agent Me* **7**, 111-123 (2007).

34.   Kelland, L.R. & Farrell, N. Platinum-based drugs in cancer therapy. (Humana Press, Totowa, N.J.; 2000).

35.   Galassi, T.V., Jena, P.V., Roxbury, D. & Heller, D.A. Single Nanotube Spectral Imaging To Determine Molar Concentrations of Isolated Carbon Nanotube Species. *Analytical chemistry* **89**, 1073-1077 (2017).

CHAPTER 4: ELECTROSTATIC SCREENING MODULATES ANALYTE BINDING AND EMISSION OF CARBON NANOTUBES

4.1 Abstract

Nanoparticle-based sensing schemes are promising approaches for rapid and selective detection of biomarkers in biological materials. Many nanoparticles have intrinsic charge, and are thus susceptible to electrostatic interactions that can enhance or attenuate sensing. Single-strand DNA suspended carbon nanotubes are advantageous for use in sensing applications, but the polyanionic nature of the DNA backbone suggests that electrostatic interactions could greatly impact sensor performance. Here, using a combination of experimental and computational approaches, we have found and characterized a critical role of the solvent salt conditions in determining the extent of optical changes due to anionic analyte interaction with DNA-suspended nanotubes. Using a well-characterized model anionic analyte, we found that monovalent salts enabled greater optical changes in a highly-dose dependent manner, but not with a neutrally charged analyte. Molecular dynamics simulations were used to derive a quantitative understanding of this mechanism from a free energy standpoint. We also show that salt can be manipulated to enhance the sensitivity of detection for a polyanionic analyte, single-strand DNA, using a DNA-suspended nanotube-based sensor. These results suggest that electrostatic screening is an important parameter for intrinsically charged nanoparticle sensors, and may be tuned with added salt for controlled response to targets.

4.2 Introduction

Early and accurate detection of biomarkers has driven the development of nanoparticle-based biosensors with the goal of providing selective, sensitive, and rapid detection with minimal sample preparation[1]. Nanoparticle-based solutions have several advantages as sensors owing to their high volume to surface ratio, amenability to derivation, multiplexing capacity, and the unique physical properties that emerge at the nanoscale[2]. For cancer, several protein-based biomarkers have been FDA-approved or cleared[3]. Other emerging biomarkers include oligonucleotides such as circulating microRNA[4] and circulating tumor DNA[5]. The variety of different biomarkers has led to a diverse set of recognition moieties and signal transduction elements to be developed[6]. Some recognition moieties are based explicitly on electrostatic attraction[7, 8] to take advantage of the unique charge character of some analytes. Many surface-enhanced Raman scattering based probes and sensors were found to depend on the pH and zeta potential values of the nanoparticle solutions[9], emphasizing the importance in controlling electrostatic interactions in this system. A colorimetric sensor for mercury ions based on different sized silver nanoparticles functionalized with adenine nucleotides showed great variations in detection sensitivity based on electrostatic repulsion between nanoparticles[10].

One promising nanomaterial for sensing, semiconducting single-walled carbon nanotubes, have been pursued as biomedical sensors due to their outstanding optical properties[11]; they fluoresce in the near-infrared spectral range and do not photobleach. Changes in the local dielectric environment around the nanotube surface can elicit a solvatochromic shift[12, 13], forming the theoretical and physical basis for their use as sensors[14, 15]. To make use of their optical properties as sensors, single-walled carbon nanotubes can be made into a colloidal dispersion with single-stranded DNA , where π

stacking enables DNA bases to adsorb to the nanotube surface while the negatively charged phosphate backbone prevents re-aggregation[16]. DNA-suspended nanotubes provide several advantages as sensors, such as biocompatibility[17], stability[18], high yields[16], and relatively facile purification of spectrally distinct chiralities[16, 19] which may enable highly multiplexed sensing schemes.

Recently, the role of the electrostatic charge in DNA-nanotube dispersions has been shown to be important for manipulating nanotube chirality purification[19], optical behavior, and sensing[20]. The negatively charged phosphate backbone prevents re-aggreation of the nanotubes, but may also impact charged analyte detection. Our group has recently shown that hybridization of complementary oligonucleotide sequences with DNA-suspended nanotubes can lead to structural changes that alter the charge distribution on the nanotube surface, and thus the emission character[21]. By combining the anionic amphiphile sodium dodecylbenzenesulfonate (SDBS) with DNA-suspended nanotubes, we found that the emission character provided by both agents is present. Hybridization-induced removal of DNA from the nanotube surface led to greater SDBS emission character, greatly blue-shifting the emission[21]. Furthermore, the magnitude of blue-shifting corresponded with the length of DNA removed from the nanotube surface, with longer sequences leading to greater blue-shifting due to the larger nanotube surface exposed for SDBS binding. Thus, for DNA-suspended nanotubes, SDBS-induced blue-shifting can serve as a quantitative optical assay of accessibility to the nanotube surface.

Using SDBS as a model anionic analyte, we set out to assess the impact of different conditions that could affect SDBS accessibility to the DNA-functionalized nanotube surface. Recent work has shown that monovalent salts such as NaCl are important in

determining DNA-nanotube interactions with each other and thus stability[22-24]. We hypothesized that charge-charge repulsion between the negatively charged DNA phosphate backbone and SDBS is a dominate force controlling accessibility of SDBS to the nanotube surface, despite the significant hydrophobic region of SDBS available to bind the nanotube. The addition of salts to screen this charge should then enable more SDBS binding, and thus greater blue-shifting. However, testing this hypothesis could be complicated by DNA-conformational changes, since the salts may also screen intramolecular repulsion forces along the negatively charged phosphate backbone[12, 25] and in this way change analyte accessibility in a more general way. Herein, using $(GT)_{15}$ DNA suspended nanotubes, we probed the salt-dependent accessibility of SDBS to the nanotube surface by measuring the magnitude of SDBS-induced blue-shifting under different salt conditions. To parse the importance of potential conformational changes of the $(GT)_{15}$ DNA on the nanotube surface in response to added salts, we additionally tested an electrically neutral molecule, PEG-cholesterol, which blue-shifts nanotubes similarly to SDBS. Using molecular dynamics simulations, we were able to quantitatively assess potential DNA-changes due to salt content, as well as the influence of NaCl on the free energy of adsorption of SDBS to DNA-suspended nanotubes. Finally, we extend our study to a polyanionic analyte target, single-strand DNA, using a $(GT)_{15}$-based oligonucleotide sensor as described[21], and found that the threshold of detection could be improved with added salt. From these studies, we conclude that electrostatic screening of the DNA-suspended nanotube by monovalent ions is a primary determinant of interaction with negatively charged analytes, and that the magnitude of nanotube optical response can be tuned depending on the salt concentration. Our findings have implications for the rational design of DNA-suspended carbon nanotube sensors for charged analytes,

where varying the monovalent ion content of the sensing environment can facilitate or abrogate detection of an anionic analyte.

4.3 Results and discussion

We first asked whether the anionic amphiphile SDBS would produce a blue-shift in the emission of carbon nanotubes under different salt conditions. The effect of NaCl alone on nanotube emission, using $(GT)_{15}$-suspended nanotubes in HEPES buffer, was determined by measuring the spectra in 100 mM NaCl. No appreciable shifting in emission wavelength was observed, and intensity changes were insignificant (Figure 4.1a). In SDBS concentrations of 0.2% wt/vol (5.7 mM), we found a large salt-dependent difference in the nanotube emission spectra (Figure 4.1b), including a distinct blue-shifting behavior (Figure 4.1c, d) and intensity increase in the high-salt condition.
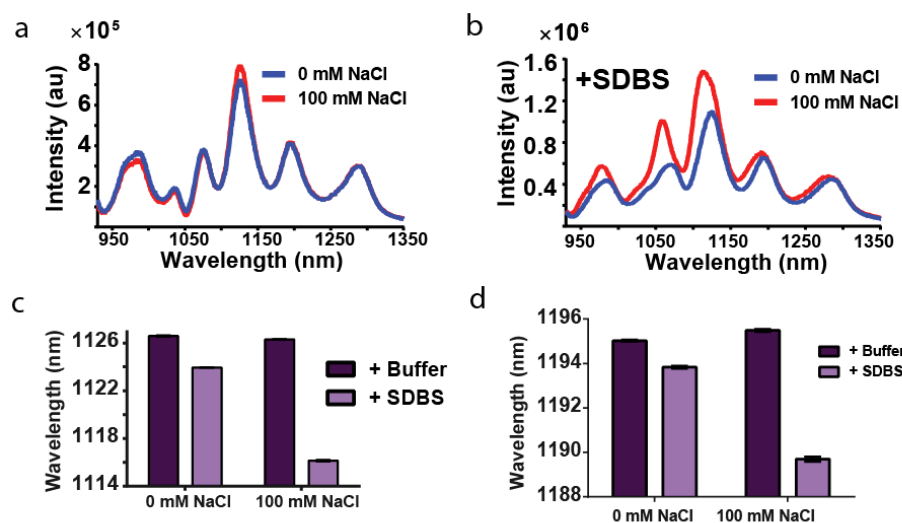
Figure 4.1 Salt dependence on carbon nanotube emission response to anionic amphiphile. **a**, Representative spectra from $(GT)_{15}$-suspended nanotubes in 100 mM sodium chloride (red) or in NaCl-free HEPES buffer (blue).**b**, Representative spectra from $(GT)_{15}$-suspended nanotubes in 0.2% wt/vol sodium dodecylbenzenesulfonate (SDBS) and 100 mM sodium chloride (red) or NaCl-free HEPES buffer (blue). **c**, Center wavelength of the (9,4) nanotube emission in the indicated salt conditions upon addition of 0.2 % wt/vol SDBS or buffer control **d,** Center wavelength values of the (8,6) nanotube emission in the indicated salt conditions after addition of 0.2 % wt/vol SDBS. Error bars represent standard deviation of technical replicates.

We next assessed how the concentration of NaCl affected the magnitude of SDBS-induced blue-shifting behavior of the nanotubes by escalating the NaCl concentration from 0 mM to 100 mM in 10 mM increments, keeping the concentration of SDBS constant at 0.2% wt/vol. After allowing the samples to come to equilibrium (48h incubation), we found that the magnitude of emission wavelength shifting varied nearly linearly with the NaCl concentration, up to approximately 50 or 60 mM NaCl for most measured chiralties (Figure 4.2a). The nanotube emission intensity exhibited a similar dose-dependent increase over the buffer-only control (Figure 4.2b).

147
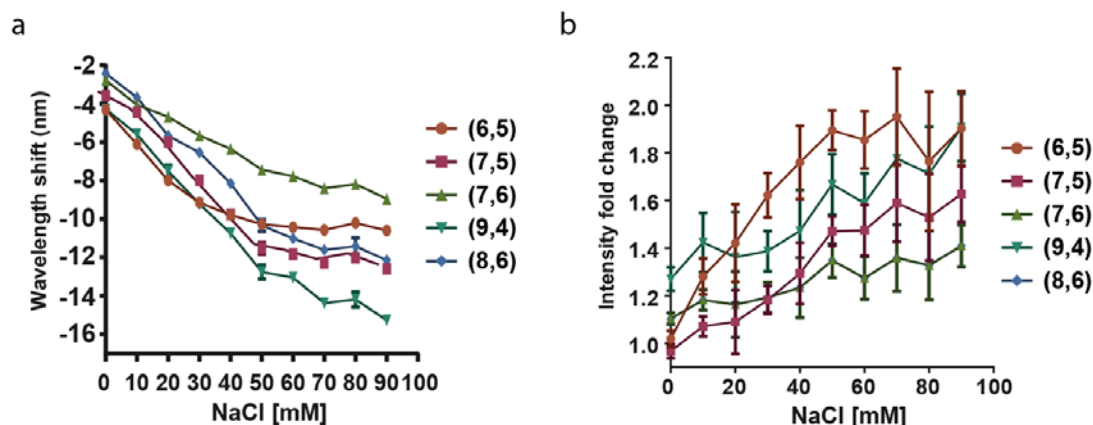
Figure 4.2 NaCl dependent optical effects from SDBS. **a,** Wavelength shifting response of five nanotube chiralities in SDBS as a function of NaCl concentration**. b**, Intensity fold change of five nanotube chiralities in SDBS as a function of NaCl concentration**.** Error bars represent standard deviation of technical replicates.

We then assessed how changes in the salt concentration affected the kinetics of SDBS-induced blue-shifting of the nanotube emission. We measured the emission spectra of the nanotubes every 10 minutes over three hours in escalating salt concentrations. The equilibration time was slow, generally taking several hours. However, over the first three hours, the curves were approximately linear, enabling the use of linear regressions to calculate the slope and estimate the early rate of shifting for three chiralities of nanotubes ($R^2 > 0.9$) (Figure 4.3). Each chirality showed a nearly linear increase in the rate of blue-shifting as the salt concentration was increased (Figure 4.4). We conclude that increasing NaCl concentration increases the rate at which SDBS-mediated blue-shifting occurred.
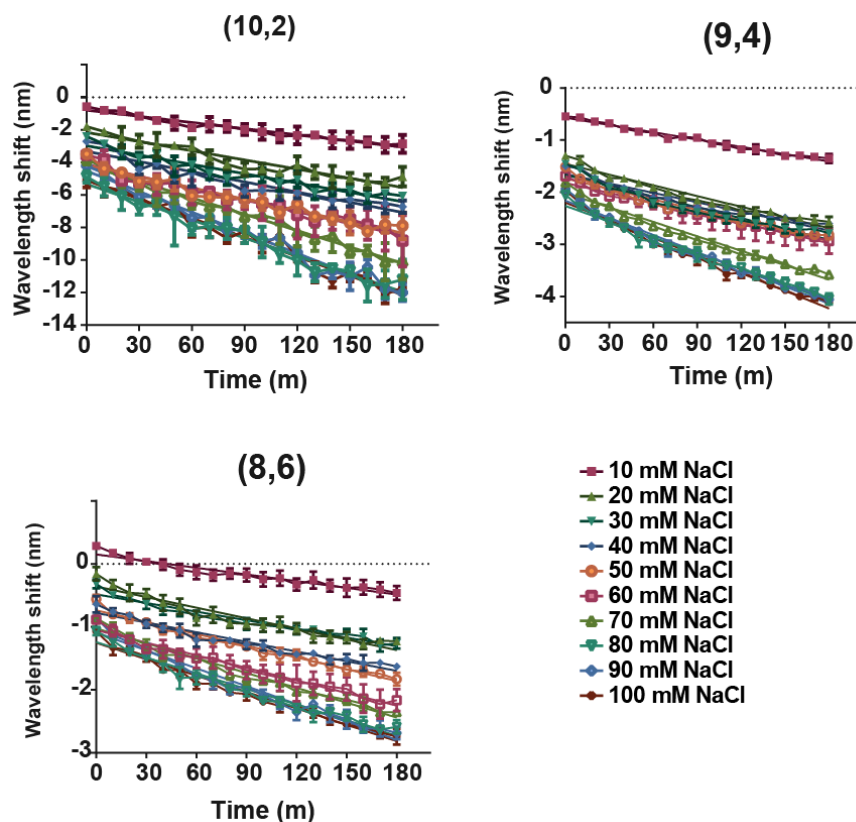
Figure 4.3 Wavelength shift from added SDBS over time for the three indicated nanotube chiralities in the indicated NaCl concentration. Kinetics of SDBS-induced blue-shifting of the (10,2), (9,4) and (8,6) nanotube chiralities with increasing NaCl concentration as indicated by color. Solid lines represent fits from linear regressions, error bars represent standard deviation of technical triplicates.
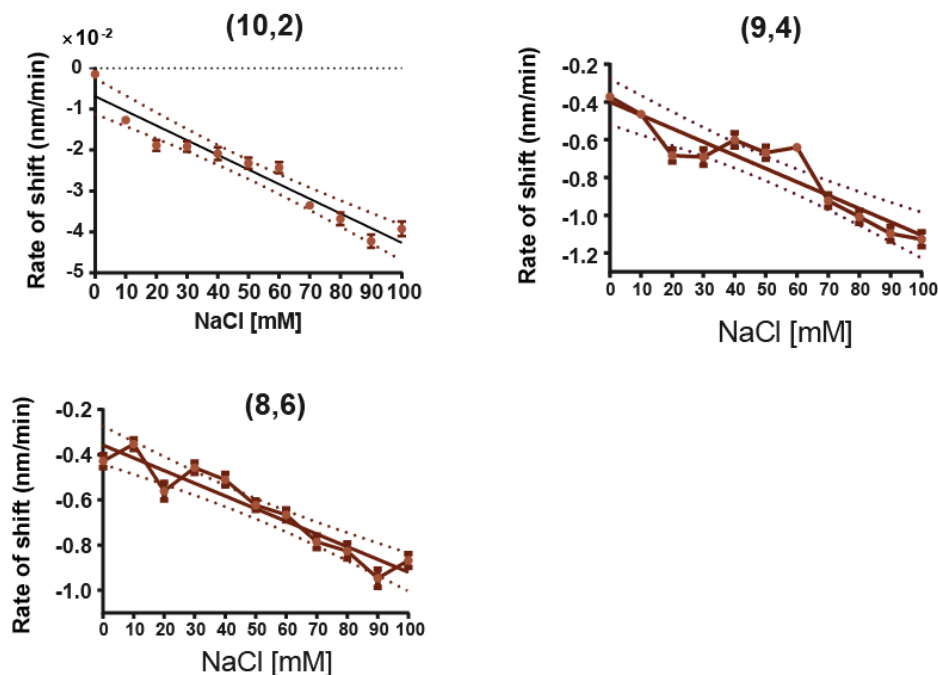
Figure 4.4 Rate of shifting due to SDBS as a function of NaCl concentration for the three indicated chiralities. The rate of SDBS-induced blue-shifting of the (10,2), (9,4), and (8,6) nanotube as a function of NaCl concentration. Solid line represents the fit from a linear regression, and dotted lines represent the 95% confidence interval. Error bars in all instances represent the standard deviation of technical triplicates.

To test if the NaCl-dependent effects on SDBS-induced blue-shifting could be extended to divalent ions, we repeated the kinetics experiment with $MgCl_2$. To match the total salt charge, $MgCl_2$ was added at half the molar concentration used for NaCl. By itself, $MgCl_2$ red-shifted the nanotubes and partially quenched the fluorescence (Figure 4.5). Kinetics of the SDBS-mediated blue-shifting were measured in 0, 12.5, 25, and 50 mM $MgCl_2$; however, $MgCl_2$ appeared to prevent any significant SDBS-induced blue-shifting (Figure 4.6). The effect of divalent ions on SDBS accessibility may have been complicated by the previously reported de-stabilizing effects of divalent ions on the DNA-suspended nanotubes[25].
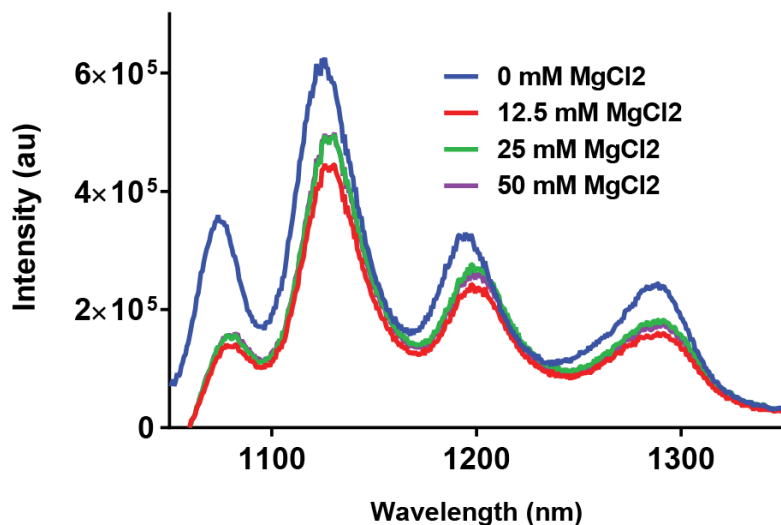
Figure 4.5 Effect of divalent ions on the nanotube spectra. Emission spectra of $(GT)_{15}$ DNA-suspended nanotubes after introducing 0, 12.5, 25, and 50 mM $MgCl_2$.
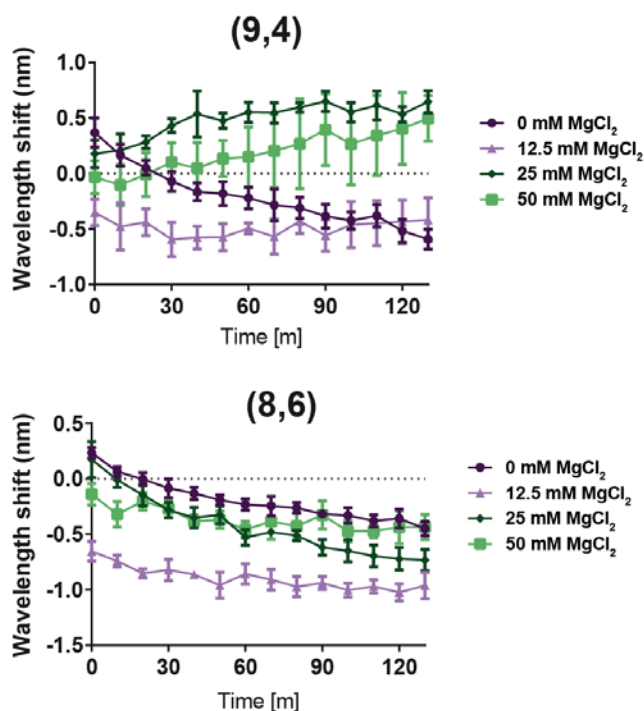
Figure 4.6 SDBS-induced shifting over time with MgCl2. Emission wavelength shift from control of DNA-encapsulated nanotubes after addition of SDBS in the indicated $MgCl_2$ condition over time. Data from the (9,4) and (8,6) nanotube chiralities are shown. Error bars represent standard deviation of technical replicates.

Because the data implicates electrostatic screening effects from monovalent ions as a possible determinant of SDBS-induced blue-shifting, we next tested if KCl, which is often used to improve charge screening in DNA-related assessments such as PCR[26], would also enhance SDBS-induced blue-shifting on an equi-molar basis. Indeed, at both 50 mM and 100 mM KCl, we observed SDBS-induced blue-shifting, often with a greater magnitude as compared to NaCl (Figure 4.7). The greater magnitude of blue-shifting suggests that potassium may interact with DNA on the carbon nanotube to screen charges better than sodium, allowing more SDBS to access the nanotube surface.
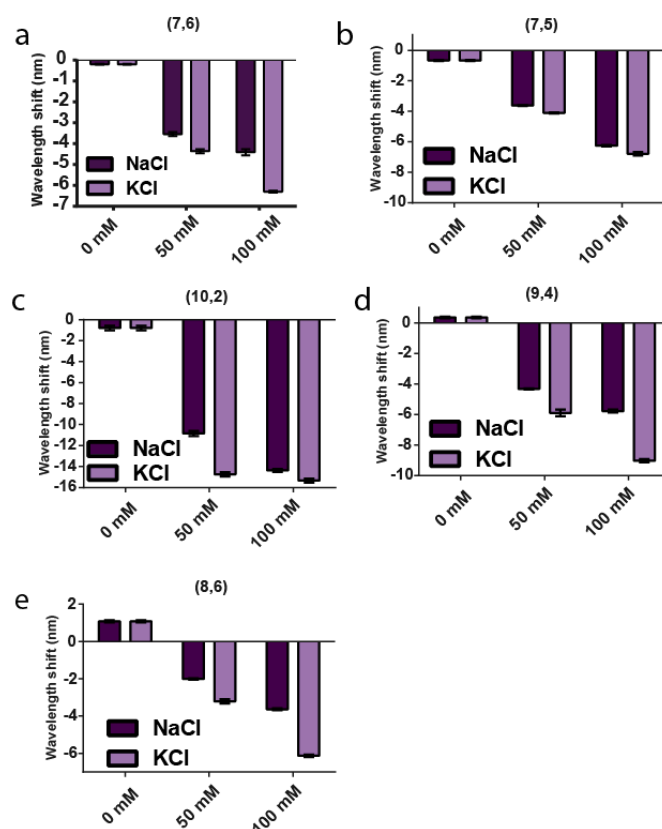
Figure 4.7 Comparison of NaCl and KCl for five chiralities. Emission wavelength changes of the (7,6) nanotube chirality after equilibration with 0.2% SDBS in the indicated concentration of NaCl or KCl. Error bars represent standard deviation of technical triplicates.

Although the enhancement effect of monovalent ions appears to be due to electrostatic screening between the negatively charged DNA phosphate backbone and the negatively charged SDBS, we hypothesized that monovalent ions could also affect the conformation of $(GT)_{15}$ on the nanotube. Intramolecular electrostatic screening among adjacent phosphates could be responsible for changes in DNA conformation that leads to greater SDBS accessibility. To test this, we used a neutral molecule, polyethylene glycol (PEG)-modified cholesterol, that also blue-shifts the nanotube emission upon interaction with the surface. We reasoned that, if charge screening affected the DNA conformation to expose the nanotube surface to enhance analyte binding, then PEG-cholesterol-dependent blue-shifting should exhibit sensitivity to NaCl. Two concentrations of PEG-cholesterol were introduced to $(GT)_{15}$-suspended nanotubes in either buffer alone or with 100 mM NaCl. For both concentrations of PEG-cholesterol tested, the presence of NaCl did not affect the magnitude of blue-shifting for nearly all nanotube chiralities measured (Figure 4.8). Intensity enhancement was also not affected (Figure 4.9). These data suggest that monovalent ions do not change intrinisc sensitivity to analytes via DNA rearrangment but act extrinsically by a screening effect between the DNA and the charged analyte. We present our model of salt-dependent accesibility in Figure 4.10. In the absence of salt, the electrostatic repulsion between the negatively charged phosphate backbone of the DNA and the anionic sulfate group limits the amount of SDBS that can adsorb to the nanotube, resultuing in only a minor blueshift. In the presence of monovalent ions, charge screening enables greater SDBS access, leading to a larger blue-shift.

153
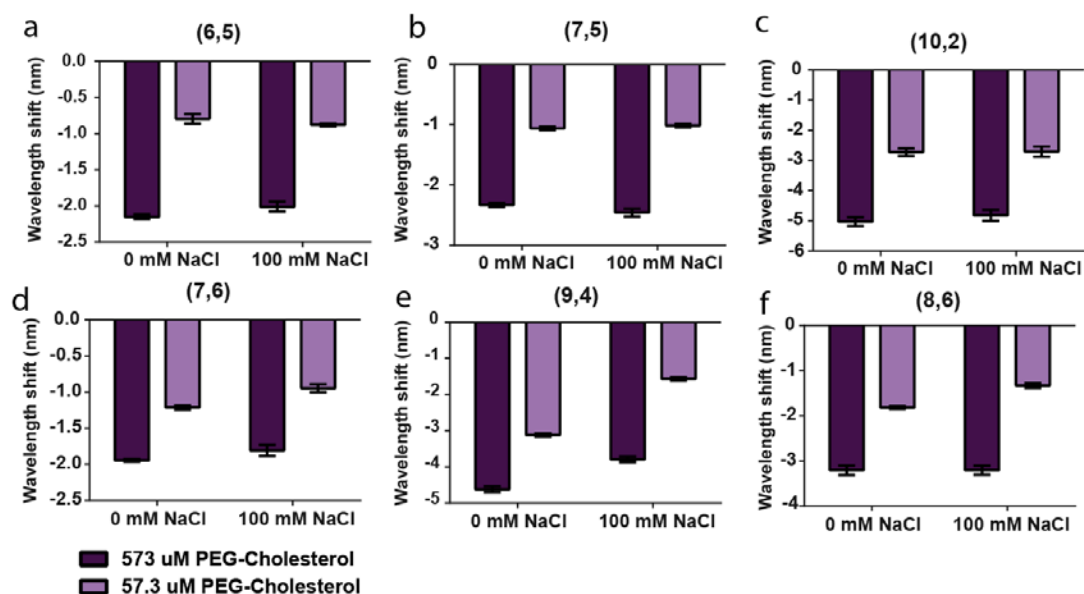
Figure 4.8 Neutral analyte effect on wavelength in salt. Emission wavelength changes of DNA-encapsulated nanotubes after addition of the indicated concentration of polyethylene glycol (PEG)-modified cholesterol and incubation overnight in 0 mM or 100 mM NaCl solvent conditions. The (6,5), (7,5) (10,2), (7,6), (9,4), and (8,6) nanotube chiralities are shown. Error bars represent standard deviation of technical triplicates.

(6,5)

(7,5)

(10,2)

(7,6)

(9,4)

(8,6)

■ 573 uM PEG-Cholesterol
■ 57.3 uM PEG-Cholesterol
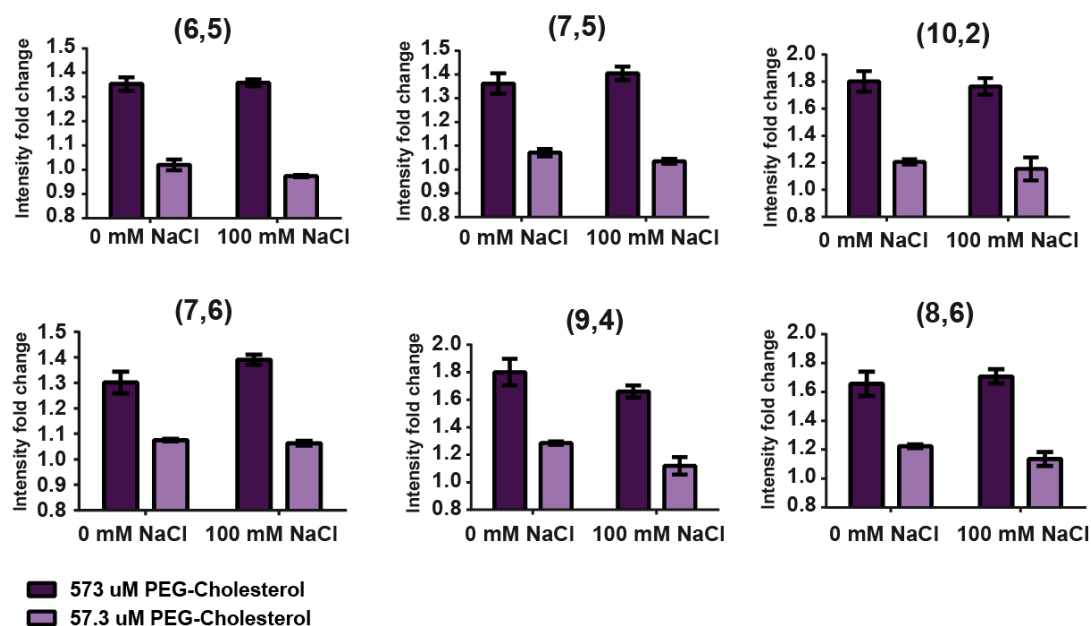
Figure 4.9 Neutral analyte effect on intensity in salt. Intensity fold change of DNA-wrapped nanotubes after addition of the indicated concentration of polyethylene glycol (PEG)-modified cholesterol and incubation overnight in 0 mM or 100 mM NaCl solvent conditions. The (6,5), (7,5), (10,2), (7,6), (9,4), and (8,6) nanotube chiralities are shown. Error bars represent standard deviation of technical triplicates.
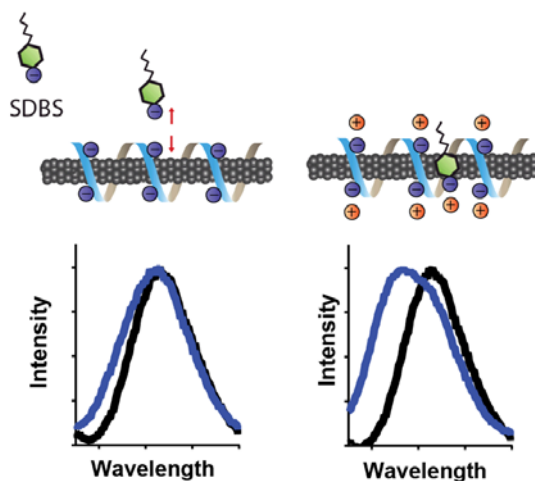
Figure 4.10 Model depiciting the hypothesized mechanism for monovalent salt-dependent anionic analyte binding to (GT)₁₅ DNA-suspended nanotubes. Example spectra corresponding to the hypothesized structures in each condition of baseline nanotube emission (black) and emission after treatment with SDBS (blue).

155

We ran serial molecular dynamics simulations to investigate our proposed model. We first quantitatively assessed the effect of salt on the DNA encapsulating the nanotube by introducing a $(GT)_{15}$-suspended (9,4) nanotube to three different salt concentrations, 0 mM, 100 mM, and 500 mM, in a in a 8.0 nm x 8.0 nm x 9.8119 nm cubic box solvated in explicit water (approximately 20,000 molecules, see Methods). We ran the simulation for 200 ns, after which we assessed ion and water densities on the nanotube surface under each condition (Figure 4.11). We reasoned that changes in phosphate and water densities would indicate a major disturbance to the DNA on the nanotube. In all cases, no differences in these parameters were observed, agreeing with experimental data showing no optical changes due to NaCl alone (Figure 4.1). A concentration-dependent increase in sodium density around the DNA phosphate groups was observed in the simulations, consistent with our proposed screening model in Figure 4.10.
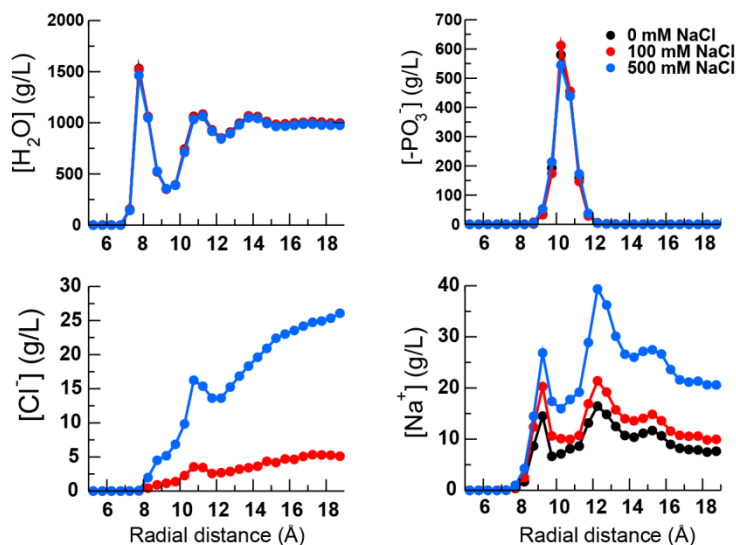
Figure 4.11 Molecular dynamics of DNA-suspened nanotubes in salt.Water, phosphate, chloride, and sodium density at different distances from the DNA-suspended (9,4) nanotube surface calculated from molecular dynamics simulations performed with 0 mM NaCl (black), 100 mM NaCl (red), and 500 mM NaCl (blue) in a 8.0 nm x 8.0 nm x 9.8119 nm cubic box solvated in explicit water (approximately 20,000 molecules) for 200 ns. Six simulations were performed at each salt concentration.

We next conducted molecular dynamics simulations to assess the effects of SDBS on the DNA-wrapped nanotube in the absence of salt. The surfactant was introduced to the vicinity of the (9,4) (GT)$_{15}$ DNA-encapsulated nanotube. After 200 ns of simulation time, we observed SDBS adsorbing to the bare surface of the nanotube without apparent displacement of the DNA (snapshot in Figure 4.12). From the simulation, we quantified phosphate, sulfate, sodium, and chloride ion density as well as water density (Figure 4.12). Notably, the density of phosphate at all radial distances showed no change versus the SDBS-free control, indicating that DNA remained bound to the surface and was not displaced by SDBS, despite the increase in sulfate concentration near the surface. We also found that the water density near the nanotube surface decreased when SDBS was added. We therefore conclude that the expulsion of water by SDBS, and the resulting decrease in the local dielectric constant, most likely explains how SDBS experimentally elicits a blue-shift. This result agrees nicely with the experimental findings of the emission response of DNA-suspended nanotubes to SDBS, which show broadened spectral peaks which seem to retain the characteristics of both DNA-suspended nanotubes and SDBS-suspended nanotubes[21]. Sodium accumulation near the surface of the nanotube was largely unaffected by SDBS adsorption.
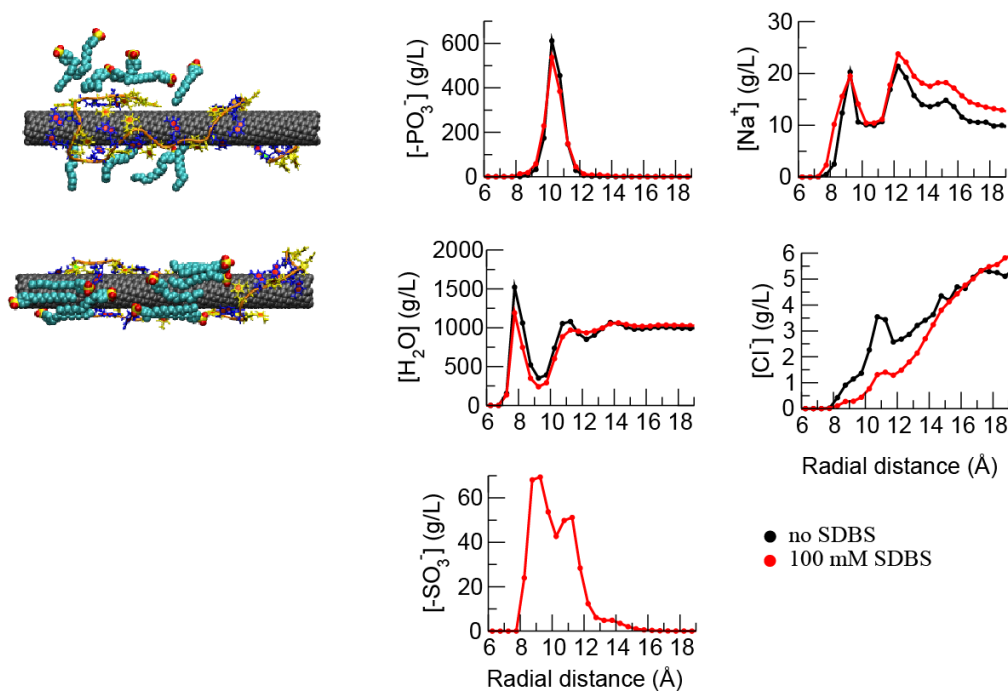
Figure 4.12 Molecular dynamics of DNA-suspened nanotubes with SDBS.
Trajectory snapshots and density concentrations of selected parameters from
molecular dynamics simulations of a $(GT)_{15}$ DNA suspended nanotube with 100 mM
SDBS. Snapshots depict SDBS adsorption to the bare nanotube surface of a $(GT)_{15}$
DNA suspended nanotube. Phosphate, sodium, water, chloride, and sulfate densities
are quantified as a function of radial distance with no SDBS (black) and 100 mM
SDBS (red).

We aimed to quantitatively examine SDBS interactions with the DNA-wrapped

nanotube under different salt conditions. We used molecular dynamics simulations to

calculate changes in the free energy of adsorption of SDBS to the $(GT)_{15}$-suspended

(9,4) nanotube. We first placed a single SDBS molecule in the vicinity of the DNA-

suspended nanotube at various salt concentrations (Figure 4.13). In this case, we found

that there was no salt-dependent change in the free energy of SDBS adsorption (Figure

4.13a and c, single SDBS). Based on the trajectory snapshot, there appeared to be a

large area of bare-nanotube surface accessible to SDBS, which we conclude may have

allowed for adsorption with minimal electrostatic interactions with the DNA. In a simulation with excess SDBS, which better represents the experimental conditions, increasing salt concentration resulted in a lower free energy of adsorption (Figure 4.13b and c, excess SDBS). In this simulation, SDBS exhibited greater coverage of the DNA-suspended nanotube. This increased coverage may have induced greater electrostatic barriers between the SDBS and the DNA-encapsulated nanotube, potentially explaining the effect of salt on SDBS adsorption in this case.
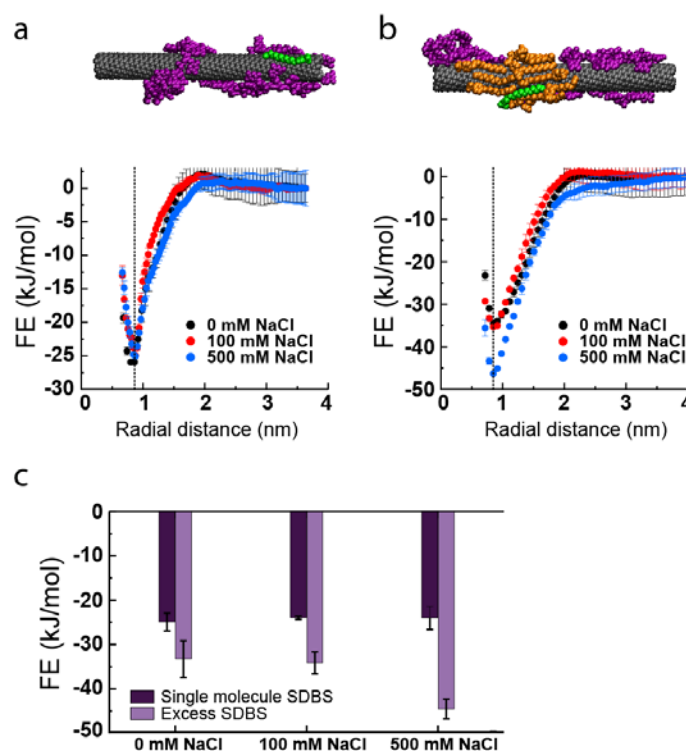
Figure 4.13 Molecular dynamics simulations of anionic amphiphile adsoprtion to DNA-encapsulated nanotubes. **a**, Simulation snapshot and corresponding plot of free energy (FE) of adsorption of a single molecule of SDBS (green) on the (9,4) nanotube species bound by the $(GT)_{15}$ DNA sequence (purple) in the three indicated salt conditions. Vertical dotted line indicates the radial distance with the most negative FE. **b**, Simulation snapshot and FE of adsorption of SDBS (green and orange) added in excess, in the indicated salt conditions. The green SDBS indicates the molecule used to calculate the free energy of adsorption. **c**, Adsorption free energies calculated for dilute and concentrated SDBS at radial distances corresponding with the vertical dotted lines in parts **a** and **b**. Error bars represent standard deviation of the mean from three simulations.

The simulation results and experimental data suggest that charge-charge repulsion between the DNA on the nanotubes and the SDBS is a primary factor affecting the accessibility of the amphiphile. The simulation and cholesterol data suggest that NaCl does not significantly alter the DNA conformation, but it allows sodium ions to effectively screen the charges to lessen repulsion and allow SDBS to access the nanotube surface. The simulations also suggest that salt may screen charges from SDBS already adsorbed to the nanotube, which may become significant as more SDBS adsorbs. No clear secondary surfactant structures, such as hemi-micelles[27], were observed to form on the nanotube surface, consistent with studies describing random adsorption of other surfactants to nanotubes[28].

To investigate whether charge screening would affect the detection of other analytes, we tested how salt would affect detection of nucleic acid hybridization. We previously developed a complex consisting of a nanotube encapsulated by a single-stranded DNA oligonucleotide consisting of a "nanotube-binding" $(GT)_{15}$ domain and an "analyte-binding" domain of 23 nucleotides complementary to a target oligonucleotide[21]. The hybridization results in a partial desorption of the pair from the nanotube that causes a blue-shifting of the nanotube emission wavelength. For the analyte, we used a DNA analogue of a microRNA (miR-19) and chose the suitable complementary sequence as the "analyte-binding" domain on the nanotube. Focusing on the (9,4) chirality, we introduced several concentrations of miR-19 in the presence of 0 mM NaCl or 150 mM NaCl and assessed emission wavelength (Figure 4.14a). In the no-salt condition, miR-19 DNA did not elicit a response. In the presence of 150 mM NaCl, we observed a blue shift down to a concentration of 100 nM miR-19 DNA, suggesting that hybridization did not occur in the absence of NaCl. We next tested if NaCl can be adjusted to improve the detection of low concentration targets. We hypothesized that

hybridization, and thus the magnitude of blue-shifting, could be enhanced by further increasing the NaCl concentration to overcome electrostatic repulsion. Using the (7,5) chirality, which only slightly blue-shifts upon addition of 100 nM miR-19 DNA in 150 mM NaCl, we repeated the hybridization experiment in escalating salt conditions. We found an enhancement of the blue-shifting response up to about 750 mM NaCl, after which the sensor function started to become adversely affected (Figure 4.14b). A non-complementary, length matched oligonucleotide control, R23, did not produce a blue-shifting response at any NaCl concentration. Our results are in agreement with other work that showed DNA hybridization of 24 base-pair sequences in solution is optimally enhanced at 800 mM NaCl[29]. We present a model of charge screening leading to enhanced hybridization in Figure 4.14c.
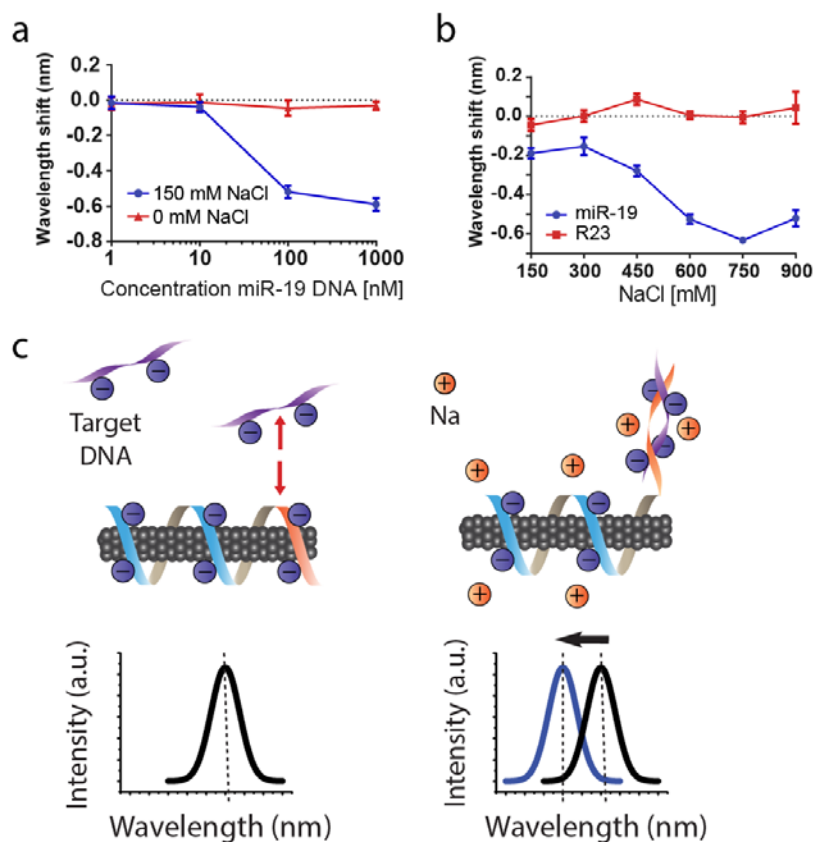
Figure 4.14 Salt-dependent optical detection of a polyanionic analyte, single stranded DNA. **a**, Wavelength shift of an oligonucleotide sensor, GT15mir19, as a function of target oligonucleotide (miR-19 DNA) concentration in 0 mM NaCl or 150 mM NaCl. **b**, Wavelength shift of GT15mir19 with 10 nM miR-19 or 10 nM non-complementary control (R23) with escaltating NaCl concentration. **c**, Model of hyopthesized mechanism for target oligonucleotide interaction with DNA-suspended nanotube sensor (GT15mir19) under zero salt conditions (left) and with salt (right). Observed spectral shifts in each condition are represented by generic spectra where black represents the baseline spectra and blue represents spectra after hybridization.

4.4 Conclusion

The impact of electrostatic interactions between nanoparticles and analytes can play a critical role in the success[30] or failure[31] of a nanoparticle sensor. Nanoparticles with intrinsic surface charge, such as gold nanoparticles functionalized with oligonucleotides, are especially sensitive to the solvent salt conditions[32]. Many biomarkers have multivalent charges, such as oligonucleotides, making electrostatic interactions of nanoparticles and analytes an integral part of successful sensing schemes. Carbon nanotubes functionalized with DNA have an intrinsic negative charge, but the impact of electrostatic repulsion with potential analytes has not been well addressed. Using an experimental and computational approach, we have found an important role for NaCl in determining the sensitivity of DNA-suspended nanotubes to anionic analytes. The role of NaCl in enabling SDBS-dependent blueshifting, for example, was striking; the magnitude of SDBS-induced blue-shifting for the (9,4) nanotube chirality was nearly quadrupled by the addition of NaCl. From an applications standpoint, controlling the salt content of the sensing environment could provide a simple route to tune the magnitude and kinetics of an optical response to anionic analytes.

Because the DNA is non-covalently associated with the carbon nanotube, there is a certain degree of freedom in conformations that the DNA can take on the surface. As a polyanionic molecule, we reasoned that electrostatic screening from added salts could change intrinsic sensitivity to analytes *via* a DNA conformation change, complicating experimental system. This does not appear to be the case, as a neutrally charged analyte interacted with the nanotube independent of the salt concentration. Molecular dynamics simulations strengthened this view, as no major DNA rearrangement was observed in our simulations. The effect of salt on the free energy of absorption of

SDBS in the simulations provide quantitative insight in how analyte binding may be controlled by changing the salt concentration of the sensing environment. This strong control of analyte binding through changes in the salt concentration may have important consequences for other intrinsically charged nanoparticles, and represents an important parameter that must be considered in future point-of-care applications.

4.5 Materials and Methods

4.5.1 DNA-suspension of carbon nanotubes

Carbon nanotubes produced by the HiPco process (Unidym, Sunnyvale, CA) were mixed with $(GT)_{15}$ or $(GT)_{15}$-TCAGTTTTGCATAGATTTGCACADNA oligonucleotides (IDT DNA, Coralville, IA) at a 2:1 mass ratio in 1 mL of 20 mM 4-(2-hydroxyethyl)-1-piperazineethanesulfonic acid) (HEPES, Thermo Fisher Scientific) buffer or deionized water for hybridization experiments and ultrasonicated for 30 minutes at 40% amplitude (Sonics & Materials, Inc.). Following ultrasonication, the dispersions were ultracentrifuged (Sorvall Discovery 90SE) for 30 minutes at 280,000 x g. The top 80% of the supernatant was collected. Absorbance spectra were acquired using a UV/Vis/nIR spectrophotometer (Jasco V-670, Tokyo, Japan), and the concentration was calculated using the extinction coefficient $Abs_{910} = 0.02554$ L mg^{-1}cm^{-1}. To remove free DNA, 100 kDa Amicon centrifuge filters (Millipore) were used. The DNA-nanotube complexes were re-suspended in 20 mM HEPES buffer or deionized water.

4.5.1 Salt-dependent effects on analyte accessibility

For all experiments, DNA-suspended nanotubes were used at a final concentration of 0.2 mg/L diluted from a stock solution in either 20 mM HEPES or deionized water. Concentrated stock solutions of sodium chloride, potassium chloride, and magnesium chloride (Thermo Fisher Scientific) were prepared in 20 mM HEPES and diluted to the indicated concentration in the figures. A stock solution of sodium dodecylbenzenesulfonate (SDBS) in 20 mM HEPES buffer was used to produce a final concentration of 0.2% wt/vol where indicated. Cholesterol-PEG 600 (Sigma-Aldrich) was reconstituted to a stock of 5.73 mM in phosphate buffered saline. Hybridization experiments were performed in deionized water or PBS, with additional NaCl spiked in to indicated final concentration using a concentrated stock solution. The target sequence, miR-19, is TGTGCAAATCTATGCAAAACTGA and non-complementary control strand, R23, is TCGGTCAGTGGGTCATTGCTAGT.

4.5.2 Fluorescence spectroscopy of carbon nanotubes in solution

Fluorescence emission spectra from aqueous nanotube solutions were acquired using a home-built apparatus consisting of a tunable white light laser source, inverted microscope, and InGaAs nIR detector. The SuperK EXTREME supercontinuum white light laser source (NKT Photonics) was used with a VARIA variable bandpass filter accessory capable of tuning the output 500 – 825 nm with a bandwidth of 20 nm. The light path was shaped and fed into the back of an inverted IX-71 microscope (Olympus) where it passed through a 20x nIR objective (Olympus) and illuminated a 50-100 µL nanotube sample in a 96-well plate (Corning). The emission from the nanotube sample was collected through the 20x objective and passed through a dichroic mirror (875 nm cutoff, Semrock). The light was f/# matched to the spectrometer using several lenses and injected into an Isoplane spectrograph

(Princeton Instruments) with a slit width of 410 µm which dispersed the emission

using a 86 g/mm grating with 950 nm blaze wavelength. The spectral range was 930 –

1369 nm with a resolution of ~0.7 nm. The light was collected by a PIoNIR InGaAs

640 x 512 pixel array (Princeton Instruments). A HL-3-CAL-EXT halogen calibration

light source (Ocean Optics) was used to correct for wavelength-dependent features in

the emission intensity arising from the spectrometer, detector, and other optics. A

Hg/Ne pencil style calibration lamp (Newport) was used to calibrate the spectrometer

wavelength. Background subtraction was conducted using a well in a 96-well plate

filled with DI H2O. Following acquisition, the data was processed with custom code

written in Matlab which applied the aforementioned spectral corrections, background

subtraction, and was used to fit the data with Lorentzian functions. Graphs and linear

fits were performed in GraphPad Prism 6.

4.5.3 Molecular dynamics simulations

We first performed 200 ns serial molecular dynamics (MD) simulations of a $(GT)_{15}$

suspended, (9,4) nanotube to determine unbiased density distributions of unbiased salt

and other molecule concentrations. A total of six simulations were performed at three

different salt concentrations (0, 100, and 500 mM) and two different SDBS

concentrations (0 and 100 mM). Simulation boxes contained a (9,4) chirality carbon

nanotube in a 8.0 nm x 8.0 nm x 9.8119 nm cubic box solvated in explicit water

(approximately 20,000 molecules). The exact number of water molecules in each case

was fine-tuned to adjust the average pressure to approximately atmospheric pressure.

The nanotube extended to the edges of the water box and was kept frozen in place

during the course of the simulation. The DNA molecule was initially generated using

the NAB program of AmberTools[33]. After placing the DNA near the nanotube,

sufficiently long equilibrations were performed until the distance between nanotube

and DNA remained constant. The nanotube atoms were modelled as sp^2 hybridized carbon. DNA/water is represented with CHARMM36/TIP3P force field[34]. Parameters for linear non-branched SDBS was obtained from a study by MacKerell and co-workers (He et al., 2010), which follows general parameterization strategy for CHARMM force field[35]. The systems were propagated using stochastic Langevin dynamics with a friction coefficient of 1 ps^{-1} and time step of 2 fs using GROMACS 4.6.7 simulation package[36, 37]. Long-range electrostatics were treated with particle mesh Ewald method with a 0.9 nm real space cut-off distance and van der Waals interactions were calculated following a 1.2 nm cut-off distance[38]. Each simulation box was pre-equilibrated with 10-20 ns NVT (T=300K simulations). Further production simulations were run for 200 ns for each case, where we collected the density profiles afterwards using custom python scripts calling the MDAnalysis module[39]. All visualizations were performed using VMD program[40].

We next performed enhanced sampling simulations to quantify the adsorption free energy of SDBS using two different SDBS concentration conditions. In one case the simulation box contained the addition of a single SDBS molecule to the (GT)$_{15}$ suspended nanotube; the other case contained addition of excess SDBS to the (GT)$_{15}$ suspended nanotube. For each SDBS concentration, three different salt conditions were simulated using an umbrella sampling technique[41] where we defined the adsorption with a reaction coordinate of the radial distance between the center of mass of SDBS and the nanotube. In the excess SDBS case, a single SDBS molecule is pulled along the radial direction as well. A total of 16 umbrella windows at radial distances of 0.65, 0.85, 1.10, 1.25, 1.45, 1.65, 1.85, 2.05, 2.25, 2.45, 2.65, 2.85, 3.05, 3.25, 3.45, 3.65 nm were used with a spring constant of 400 kJ/mol/nm. Each umbrella is simulated for 30 ns in parallel, allowing an exchange between adjacent replicas[42] to

further enhance the sampling. Initial 10 ns is discarded as equilibration from each window. The WHAM code by Grossfield[43] was used to compute resultant free energies. Errors are the standard blocked errors using 2 equal non-overlapping blocks.

4.6 Acknowledgements

4.7 References

1. Holzinger, M., Le Goff, A. & Cosnier, S. Nanomaterials for biosensing applications: a review. *Front Chem* **2** (2014).

2. Chi, X.Q., Huang, D.T., Zhao, Z.H. et al. Nanoprobes for in vitro diagnostics of cancer and infectious diseases. *Biomaterials* **33**, 189-206 (2012).

3. Chinen, A.B., Guan, C.M., Ferrer, J.R. et al. Nanoparticle Probes for the Detection of Cancer Biomarkers, Cells, and Tissues by Fluorescence. *Chemical reviews* **115**, 10530-10574 (2015).

4. Kosaka, N., Iguchi, H. & Ochiya, T. Circulating microRNA in body fluid: a new potential biomarker for cancer diagnosis and prognosis. *Cancer science* **101**, 2087-2092 (2010).

5. Diaz, L.A. & Bardelli, A. Liquid Biopsies: Genotyping Circulating Tumor DNA. *Journal of Clinical Oncology* **32**, 579-+ (2014).

6. Huang, X., Liu, Y.Y., B., Xiong, Y. & Chen, X. Nanotechnology-Enhanced No-Wash Biosensors for in Vitro Diagnostics of Cancer. *ACS nano* **11**, 5238-5292 (2017).

7. Li, H.X. & Rothberg, L. Colorimetric detection of DNA sequences based on electrostatic interactions with unmodified gold nanoparticles. *Proceedings of the National Academy of Sciences of the United States of America* **101**, 14036-14039 (2004).

8. Appel, E.A., Tibbitt, M.W., Greer, J.M. et al. Exploiting Electrostatic Interactions in Polymer-Nanoparticle Hydrogels. *Acs Macro Lett* **4**, 848-852 (2015).

9.   Alvarez-Puebla, R.A., Arceo, E., Goulet, P.J.G., Garrido, J.J. & Aroca, R.F. Role of nanoparticle surface charge in surface-enhanced Raman scattering. *Journal of Physical Chemistry B* **109**, 3787-3792 (2005).

10.   Tan, H.L., Liu, B.X. & Chen, Y. Effects of the Electrostatic Repulsion Between Nanoparticles on Colorimetric Sensing: An Investigation of Determination of Hg2+ with Silver Nanoparticles. *Plasmonics* **8**, 705-713 (2013).

11.   Boghossian, A.A., Zhang, J., Barone, P.W. et al. Near-infrared fluorescent sensors based on single-walled carbon nanotubes for life sciences applications. *ChemSusChem* **4**, 848-863 (2011).

12.   Heller, D.A., Jeng, E.S., Yeung, T.K. et al. Optical detection of DNA conformational polymorphism on single-walled carbon nanotubes. *Science* **311**, 508-511 (2006).

13.   Heller, D.A., Pratt, G.W., Zhang, J.Q. et al. Peptide secondary structure modulates single-walled carbon nanotube fluorescence as a chaperone sensor for nitroaromatics. *Proceedings of the National Academy of Sciences of the United States of America* **108**, 8544-8549 (2011).

14.   Choi, J.H. & Strano, M.S. Solvatochromism in single-walled carbon nanotubes. *Applied Physics Letters* **90**, 223114 (2007).

15.   Gao, J., Gomulya, W. & Loi, M.A. Effect of medium dielectric constant on the physical properties of single-walled carbon nanotubes. *Chemical Physics* **413**, 35-38 (2013).

16.   Zheng, M., Jagota, A., Semke, E.D. et al. DNA-assisted dispersion and separation of carbon nanotubes. *Nature materials* **2**, 338-342 (2003).

17.   Dong, L., Joseph, K.L., Witkowski, C.M. & Craig, M.M. Cytotoxicity of single-walled carbon nanotubes suspended in various surfactants. *Nanotechnology* **19**, 255702 (2008).

18.   Vogel, S.R., Kappes, M.M., Hennrich, F. & Richert, C. An unexpected new optimum in the structure space of DNA solubilizing single-walled carbon nanotubes. *Chemistry* **13**, 1815-1820 (2007).

19.   Ao, G.Y., Khripin, C.Y. & Zheng, M. DNA-Controlled Partition of Carbon Nanotubes in Polymer Aqueous Two-Phase Systems. *Journal of the American Chemical Society* **136**, 10383-10392 (2014).

20.   Roxbury, D., Jena, P.V., Shamay, Y., Horoszko, C.P. & Heller, D.A. Cell Membrane Proteins Modulate the Carbon Nanotube Optical Bandgap via Surface Charge Accumulation. *ACS nano* **10**, 499-506 (2016).

21.   Harvey, J.D., Jena, P.V., Baker, H.A. et al. A carbon nanotube reporter of microRNA hybridization events in vivo. *Nature Biomedical Engineering* **1**, 0041 (2017).

22.   Qiu, X.Y., Ke, F.Y., Timsina, R., Khripin, C.Y. & Zheng, M. Attractive Interactions between DNA-Carbon Nanotube Hybrids in Monovalent Salts. *J Phys Chem C* **120**, 13831-13835 (2016).

23.   Qiu, X., Khripin, C.Y., Ke, F., Howell, S.C. & Zheng, M. Electrostatically driven interactions between hybrid DNA-carbon nanotubes. *Physical review letters* **111**, 048301 (2013).

24.   Ke, F.Y. & Qiu, X.Y. Nanoscale Structure and Interaction of Condensed Phases of DNA-Carbon Nanotube Hybrids. *J Phys Chem C* **119**, 15763-15769 (2015).

25.   Jin, H., Jeng, E.S., Heller, D.A. et al. Divalent ion and thermally induced DNA conformational polymorphism on single-walled carbon nanotubes. *Macromolecules* **40**, 6731-6739 (2007).

26.   McPherson, M.J. & Møller, S.G. PCR, Edn. 2nd. (Taylor & Francis, New York; 2006).

27.   Islam, M.F., Rojas, E., Bergey, D.M., Johnson, A.T. & Yodh, A.G. High weight fraction surfactant solubilization of single-wall carbon nanotubes in water. *Nano letters* **3**, 269-273 (2003).

28.   Yurekli, K., Mitchell, C.A. & Krishnamoorti, R. Small-angle neutron scattering from surfactant-assisted aqueous dispersions of carbon nanotubes. *Journal of the American Chemical Society* **126**, 9902-9903 (2004).

29.   Tsuruoka, M. & Karube, I. Rapid hybridization at high salt concentration and detection of bacterial DNA using fluorescence polarization. *Comb Chem High T Scr* **6**, 225-234 (2003).

30.   Hu, J., Zheng, P.C., Jiang, J.H. et al. Electrostatic Interaction Based Approach to Thrombin Detection by Surface-Enhanced Raman Spectroscopy. *Analytical chemistry* **81**, 87-93 (2009).

31.   Burns, C., Spendel, W.U., Puckett, S. & Pacey, G.E. Solution ionic strength effect on gold nanoparticle solution color transition. *Talanta* **69**, 873-876 (2006).

32.   Hurst, S.J., Lytton-Jean, A.K.R. & Mirkin, C.A. Maximizing DNA loading on a range of gold nanoparticle sizes. *Abstr Pap Am Chem S* **233** (2007).

33.   D.A. Case, R.M.B., W. Botello-Smith, D.S. Cerutti, T.E. Cheatham, III, T.A. Darden, R.E. Duke, T.J. Giese, H. Gohlke, A.W. Goetz, N. Homeyer, S. Izadi, P. Janowski, J. Kaus, A. Kovalenko, T.S. Lee, S. LeGrand, P. Li, C. Lin, T. Luchko, R. Luo, B. Madej, D. Mermelstein, K.M. Merz, G. Monard, H.

Nguyen, H.T. Nguyen, I. Omelyan, A. Onufriev, D.R. Roe, A. Roitberg, C.

Sagui, C.L. Simmerling, J. Swails, R.C. Walker, J. Wang, R.M. Wolf, X. Wu,

L. Xiao, D.M. York and P.A. Kollman AMBER 2016. (2016).

34.   Hart, K., Foloppe, N., Baker, C.M. et al. Optimization of the CHARMM

Additive Force Field for DNA: Improved Treatment of the BI/BII

Conformational Equilibrium. *J Chem Theory Comput* **8**, 348-362 (2012).

35.   He, X.B., Guvench, O., MacKerell, A.D. & Klein, M.L. Atomistic Simulation

Study of Linear Alkylbenzene Sulfonates at the Water/Air Interface. *Journal of*

Physical Chemistry B **114**, 9787-9794 (2010).

36.   Berendsen, H.J.C., Vanderspoel, D. & Vandrunen, R. Gromacs - a Message-

Passing Parallel Molecular-Dynamics Implementation. *Comput Phys Commun*

91, 43-56 (1995).

37.   Hess, B., Kutzner, C., van der Spoel, D. & Lindahl, E. GROMACS 4:

Algorithms for highly efficient, load-balanced, and scalable molecular

simulation. *J Chem Theory Comput* **4**, 435-447 (2008).

38.   Essmann, U., Perera, L., Berkowitz, M.L. et al. A Smooth Particle Mesh Ewald

Method. *Journal of Chemical Physics* **103**, 8577-8593 (1995).

39.   Michaud-Agrawal, N., Denning, E.J., Woolf, T.B. & Beckstein, O. Software

News and Updates MDAnalysis: A Toolkit for the Analysis of Molecular

Dynamics Simulations. *Journal of computational chemistry* **32**, 2319-2327

(2011).

40.   Humphrey, W., Dalke, A. & Schulten, K. VMD: Visual molecular dynamics. *J*

Mol Graph Model **14**, 33-38 (1996).

41.   Torrie, G.M. & Valleau, J.P. Monte-Carlo Study of a Phase-Separating Liquid-

Mixture by Umbrella Sampling. *Journal of Chemical Physics* **66**, 1402-1408

(1977).

42.   Sugita, Y., Kitao, A. & Okamoto, Y. Multidimensional replica-exchange
        method for free-energy calculations. *Journal of Chemical Physics* **113**, 6042-
        6051 (2000).

43.   Grossfield, A. WHAM: the weighted histogram analysis method. *Version 2(9)*
        (2012).

CHAPTER 5: DETECTION OF VIRAL RNA BASED ON DENATURED-PROTEIN ENHANCED OPTICAL SENSING

5.1 Abstract

Direct optical detection of virus or virus-associated components directly in patient serum could facilitate diagnostics and guide clinicians to selecting optimal treatment. Detection of viral RNA is one option, but the RNA is contained within a protein capsid and occasionally lipid bilayer, requiring a lysis step to liberate the RNA. Single-walled carbon nanotubes have recently been shown to be a viable option for the detection of small oligonucleotides such as microRNA in biofluids like urine and serum. Here we have found that the optical changes of the nanotube due to hybridization can be enhanced by protein denatured with a common surfactant, sodium dodecyl sulfate (SDS). While SDS alone does very little to the nanotube, and protein rich solutions like serum ruined the functionality of the sensor, the combination produced an unexpected enhancement in solvatochromism upon hybridization with target oligonucleotide. We found the mechanism to be due to hydrophobic patches of the denatured protein chain interacting with the nanotube surface after hybridization. Because the sensor works best in protein denaturing conditions, we demonstrate potential clinical use by treating an intact lentivirus model with SDS and a nanotube sensor for a region of the viral genome and showing specific hybridization.

5.2 Introduction

As biomarkers, cell-free oligonucleotides in biofluids such as serum offer the potential to diagnose, monitor, and stratify disease states based on specific expression patterns, changes, or mutations[1-3]. Indeed, realizing such potential has been the subject of recent work focusing on "liquid biopsies[4]," which aims to use such accessible biomarkers to complement or even obviate the need for an invasive, traditional biopsy. In particular, circulating microRNA has been identified as a promising target[2], but circulating tumor DNA[5] and other cell-free DNA[6] fragments are also of great interest. While the focus of cell-free oligonucleotide detection has been for cancer, many other diseases of interest also show specific expression patterns of oligonucleotides[7]. In additionally, detection of exogenous DNA and RNA strands such as those found in viruses is also highly desirable[8]. Rapid, quantitative detection of viral oligonucleotides without the need for purification, amplification, or labeling of the oligonucleotide could help diagnose infectious disease before symptoms appear, monitor the course of the disease, and also characterize viral subtypes and clades[9]. A simple point-of-care option such as this would be especially valuable in developing countries prone to infectious disease outbreak[9], such as Ebola[10]. Because the viral genome is typically sequestered inside a protein capsid and in some cases an additional lipid bilayer, a point-of-care sensor would have to be compatible with lysing conditions to liberate the viral oligonucleotides. In addressing the need for such point-of-care options, diverse solutions based on nanomaterials are being developed, which have recently been reviewed elsewhere[11].

Single-strand DNA-suspended single-walled carbon nanotubes represent one such class of nanomaterials being pursued as an optical sensor[12], and have recently been shown to be able to detect biomarker oligonucleotides such as microRNA directly in biological fluids such as serum and urine[13]. Carbon nanotube-based sensors are

fluorescent in the near-infrared range[14] and do not photobleach[15], with many chiralities present defined in part by unique excitation and emission spectra[16]. Changes in the local dielectric environment, such as upon interaction with an analyte[17], leads to solvatochromic changes (relative blue- or red-shifting of the emission wavelength) in the nanotube emission[18], forming the basis for their use as optical sensors[19]. While such carbon nanotube sensors were shown to detect target oligonucleotides in simple buffer conditions with a modest shift in emission wavelength, the optical change upon detection could be greatly enhanced by the presence of sodium dodecylbenzenesulfonate (SDBS). This was found to be due to changes in the nanotube surface area after hybridization that allows for SDBS to bind to the nanotube and induce changes in its optical emission. The enhancement from SDBS was found to persist in biofluids such as serum and urine and enabled detection of short DNA oligonucleotides and microRNA[13].

Herein, we describe another means for hybridization enhancement that only occurs in protein-rich biological solutions. By itself, protein-rich solutions such as serum prevent detection of target oligoncleotide. We found that the addition of a different surfactant, sodium dodecylsulfate (SDS), which does little on its own to enhance the solvatochromic change after hybridization with target oligonucleotide, provides greatly enhanced solvatochromism when combined with serum. To deduce the mechanism of this enhancement, purified proteins of different molecular weight and character, such as bovine serum albumin, γ-globulins, casein, and hydrolyzed casein peptides, were tested with and without SDS. From these studies we conclude that hydrophobic pockets of the SDS-denatured protein interact with the nanotube upon hybridization, leading to a greatly enhanced blue-shift. Finally, we demonstrate the potential for clinical application by detecting single-strand viral RNA from an intact

178

lentivirus model using a nanotube-sensor for a specific for a region of the lentiviral RNA and lysing the virus with SDS.

5.3 Results and discussion

Using a carbon nanotube-based sensor for miR-19 microRNA sequence as previously described (GT15mir19)[13], we characterized the effect of serum proteins on detection using a single-stranded DNA target strand. In buffer only conditions, the detection of target DNA produces a blue-shift in nanotube emission for most chiralities. However, the addition of a small amount of fetal bovine serum (10%), abrogated any wavelength changes in response to target oligonucleotide (Figure 5.1a). Two-dimensional excitation/emission photoluminescence spectroscopy (PL plot) was used to assay optical changes for 11 different nanotube chiralities incubated with FBS after addition of target oligonucleotide or a non-complementary control strand. For every chirality measured, FBS ablated any optical changes in response to target oligonucleotide (Figure 5.1b). To better understand the effect of FBS on the sensor's baseline fluorescence, we measured the optical changes of the sensor as a dose-response to dilutions of FBS in the absence of any hybridization. Increasing concentrations of FBS induced steady red-shifting, as well as a concurrent increase in intensity (Figure 5.2). Because nanotube solvatochromism occurs in response to changes in the local dielectric environment of the nanotube, we interpret this red-shift and intensity increase to mean that material from the serum is either closely associating with the bare-regions of the DNA coated nanotubes, electrostatically interacting with the phosphate backbone to induce DNA conformation changes, or some combination thereof.
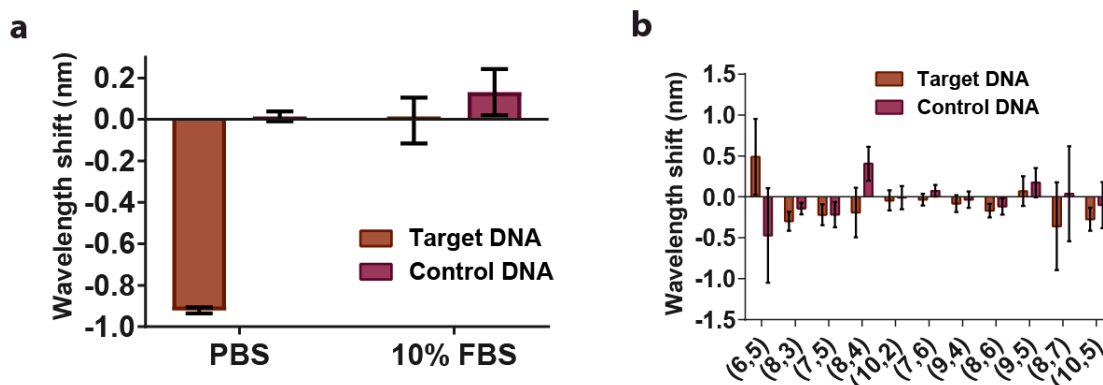
***Figure 5.1 Impact of serum on carbon nanotube oligonucleotide sensor function.* a**,
Wavelength shift of GT15mir19 nanotube sensor after overnight incubation with 1 uM
target DNA (orange) or control DNA (purple) in either PBS or 10% FBS. **b**,
Wavelength shift after overnight incubation with 1 uM target DNA (orange) or control
DNA (purple) for the indicated nanotube chiralities in fetal bovine serum (FBS).
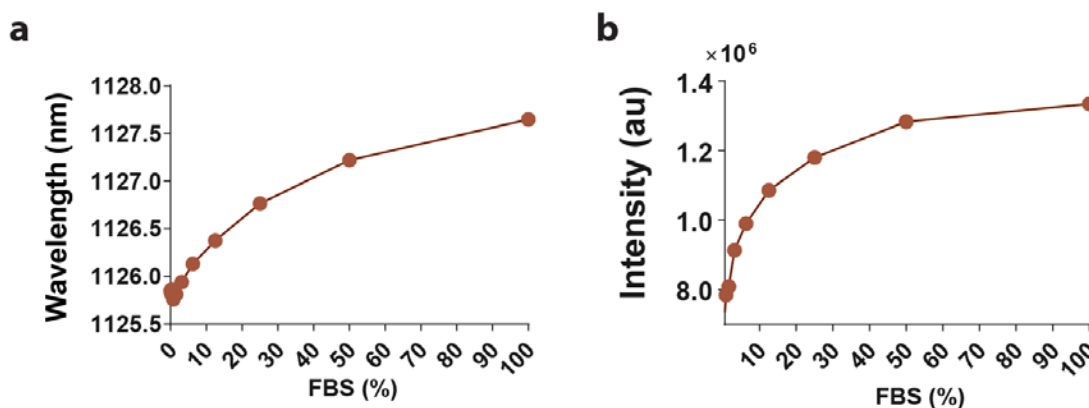
***Figure 5.2 Dose-dependent effects of serum on nanotube sensor baseline
fluorescence.* a**, Center wavelength of the (9,4) chirality as a function of added fetal
bovine serum (FBS) incubated overnight. **b,** Intensity of the (9,4) chirality as a
function of added fetal bovine serum (FBS) incubated overnight

In an attempt to reduce this apparent FBS-induced fouling of the sensor, we hypothesized that an anionic detergent, sodium dodecyl sulfate (SDS) may associate with bare-regions of the nanotube and block non-specific binding of serum components. SDS can be used to suspend carbon nanotubes[14], due to hydrophobic interactions between the nanotube surface and the 12-carbon long alkyl chain[20]. We first tested whether addition of SDS would change the baseline fluorescence of the GT15mir19 sensor. Dilutions ranging from 0.1% to 1% wt/vol SDS showed no significant changes in emission wavelength (Figure 5.3a) or intensity (Figure 5.3b). When hybridization of target DNA was measured in the presence of SDS via PL plots, only slight enhancement was observed for some chiralities compared to the buffer only condition (Figure 5.4). Although SDS seemed to have little effect on the DNA-wrapped nanotube baseline fluorescence and changes during hybridization, we hypothesized that SDS may at least preserve hybridization detection under serum conditions. GT15mir19 sensor was added to whole FBS with target or control oligonucleotide, followed by addition of concentrated SDS to a final concentration of 1%. After 4h, PL plots were acquired to measure the nanotube optical response. Surprisingly, every nanotube showed a greatly enhanced solvatochromic response to target oligonucleotide, with emission blue-shifting from 3 to 9 nanometers depending on chirality (Figure 5.5a) as well as an increase in emission intensity (Figure 5.5b). Excitation wavelengths also shifted, indicating change in the ground state-absorption (Figure 5.6). When the concentration of target oligonucleotide was varied, the sensor retained dose-dependent blue-shifting behavior for quantitative detection of target oligonucleotide (Figure 5.7).
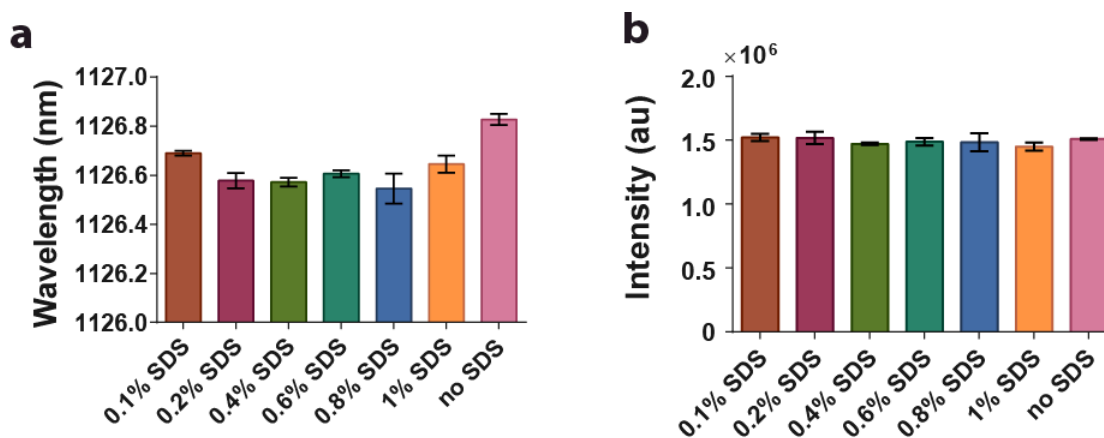
Figure 5.3 Baseline effects of SDS. **a**, Center wavelength of GT15mir19 nanotube sensor after overnight incubation with the indicated concentration of SDS, shown for the (9,4) nanotube chirality. Intensity of GT15mir19 nanotube sensor after overnight incubation with the indicated concentration of SDS, shown for the (9,4) nanotube chirality. Error bars represent standard deviation of technical triplicates
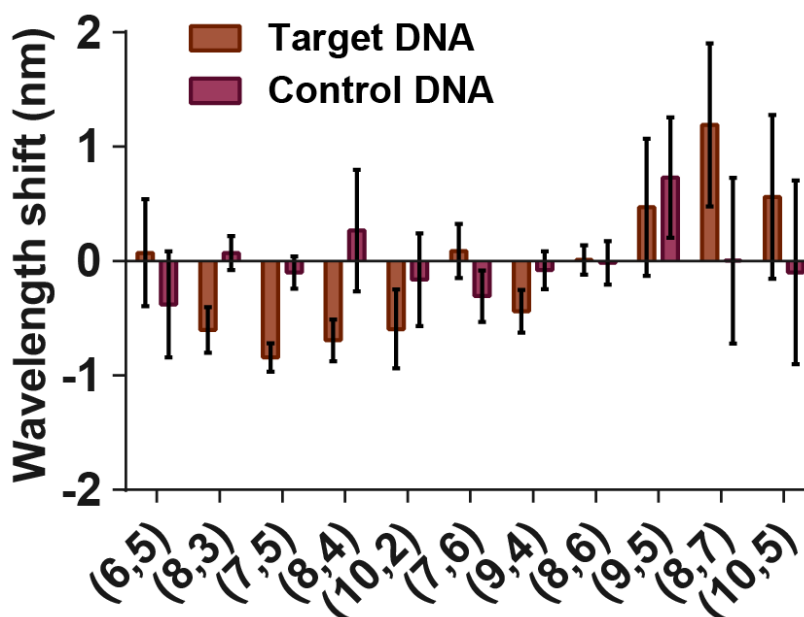
Figure 5.4 Effect of SDS on hybridization. Wavelength shift after overnight incubation with 1 uM target DNA (orange) or control DNA (purple) for the indicated nanotube chiralities in 1% SDS.
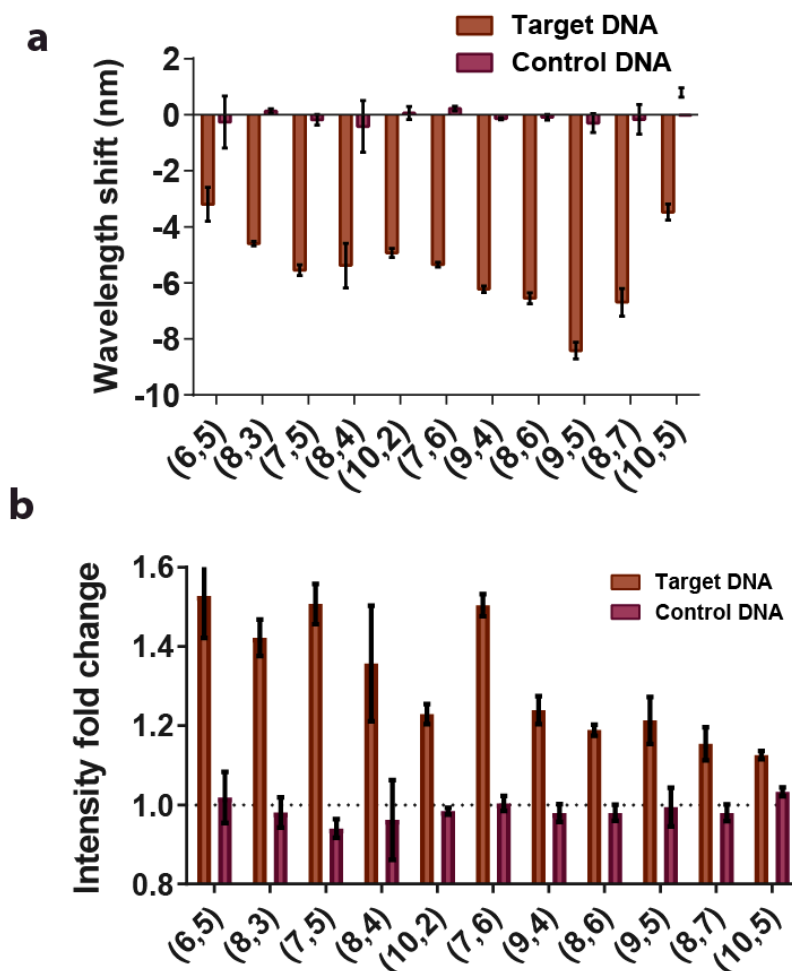
Figure 5.5Effect of serum with SDS on wavelength and intensity after hybridization
a, Wavelength shift of GT15mir19 nanotube sensor after overnight incubation with 1 uM target DNA (orange) or control DNA (purple) for the indicated nanotube chiralities in FBS treated with 1% SDS. **b**, Intensity fold change of GT15mir19 nanotube sensor after overnight incubation with 1 uM target DNA (orange) or control DNA (purple) for the indicated nanotube chiralities in FBS treated with 1% SDS
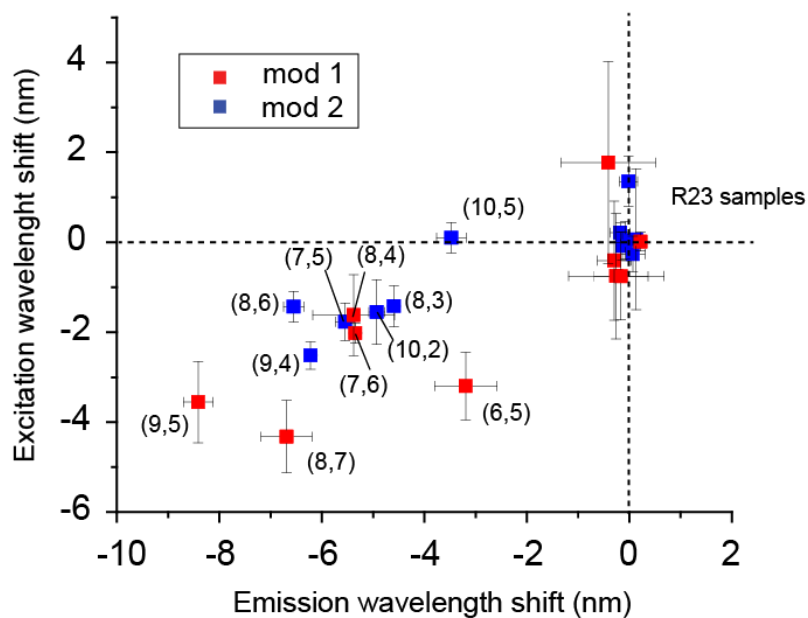
Figure 5.6 Changes in excitation and emission after hybridization in serum with SDS. Plots of excitation and emission wavelength shifts in response to target DNA and control (R23) in serum treated with 1% SDS. Nanotubes treated with target DNA are labeled by chirality, while the nanotubes treated with R23 control DNA have labels omitted for clarity. Colors indicate mod type of the nanotube. Error bars represent standard deviation of technical triplicates.
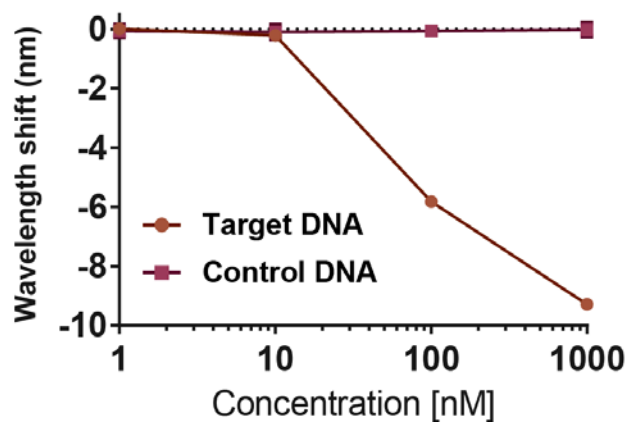
Figure 5.7 Dose-response behavior of target oligonucleotide in serum with SDS. Wavelength shift of GT15mir19 nanotube sensor after overnight incubation with indicated concentrations of target DNA (orange) or control DNA (purple) in FBS treated with 1% SDS. In all cases 2 mg/L GT15mir19 was used. Error bars represent standard deviation of technical replicates.

We next measured the kinetics of wavelength shifting for the (8,6) nanotube after addition of target DNA and non-complementary control DNA in both PBS buffer and serum, with and without SDS (Figure 5.8). Addition of SDS to buffer only conditions had little effect compared to the buffer control, and there was no detection of target in untreated serum. The combination of serum and SDS produced a greatly enhanced blue-shift that became apparent after about 30m. Compared to the buffer conditions, the shape of the kinetic trace was sigmoidal with an inflection point around 2h that reached a minimum by 3h.
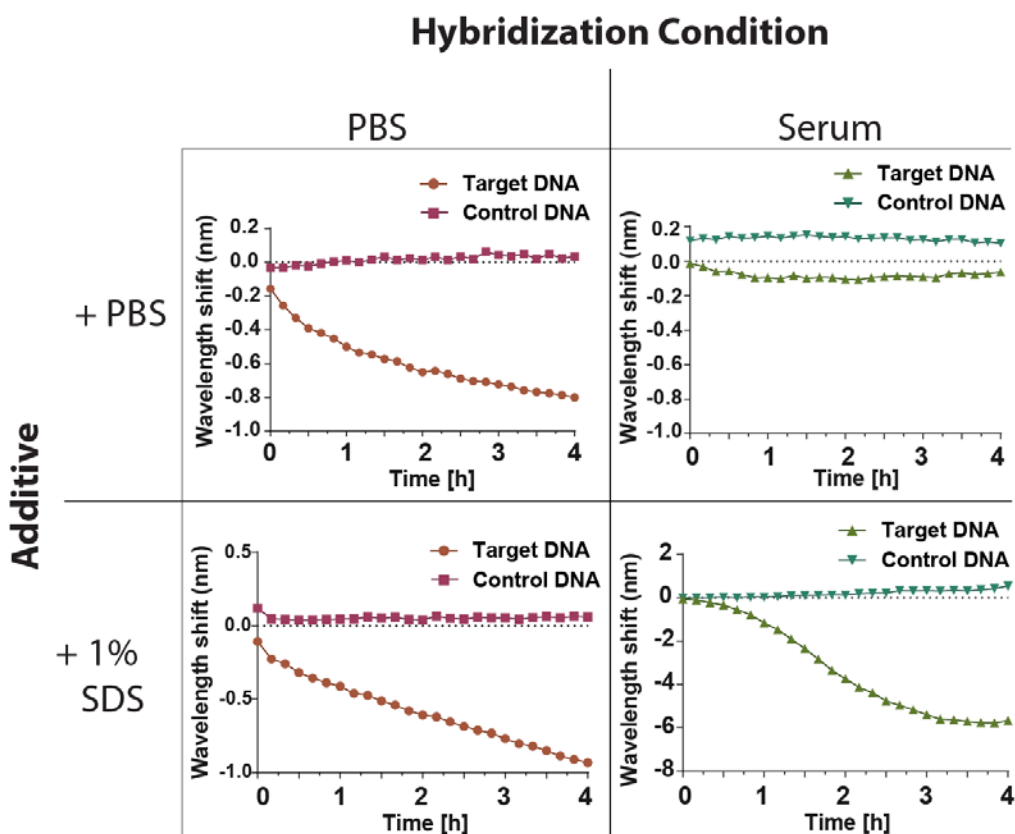
Figure 5.8 Dynamics of the carbon nanotube oligonucleotide sensor under different hybridization conditions with different additives. Each condition depicts 2 mg/L GT15mir19 nanotube sensor treated with 1 uM target DNA (orange in PBS, light green in serum) or control DNA (purple in PBS, dark green in serum) added at time 0 and measured every 10m for 4h.

185

We have previously reported hybridization-induced enhancement of solvatochromic changes using sodium dodecylbenzene sulfonate (SDBS), which also enabled detection in serum conditions[13]. We compared the kinetics of SDS + serum to the enhancement provided by SDBS in both buffer and serum upon hybridization with target DNA. SDBS-enhanced blue-shifting kinetics upon hybridization produced a similar line shape regardless of buffer or serum conditions, characterized by a blue-shift that approaches a maximum overtime with pseudo-first order kinetics (Figure 5.9a). This similarity in kinetics suggests a similar mechanism in both conditions, which we have previously reported to be due to SDBS interacting with newly exposed regions of the nanotube after hybridization. When the kinetics of hybridization-induced enhancement in SDS + serum is compared to SDBS, there is a long lag period followed by a gentler slope (Figure 5.9b). Although slower than SDBS, the SDS + serum combination produces a final blue-shifted value of greater magnitude (Figure 5.9c and d). The kinetics of emission intensity displays a more complicated pattern, with initial quenching, a short period of apparent stabilization, and then steady intensity increase that extends beyond baseline. When the kinetics of intensity change is plotted on the same graph as wavelength shift, it appears that the inflection point for the wavelength shifting is also where the intensity begins to increase (Figure 5.10). Because SDS only provides enhancement in the presence of serum, and because of the relatively complex kinetics of SDS + serum enhancement compared to SDBS, we hypothesized that SDS-denatures a component of the serum that binds to the newly exposed regions upon hybridization to provide an enhanced blue-shift.
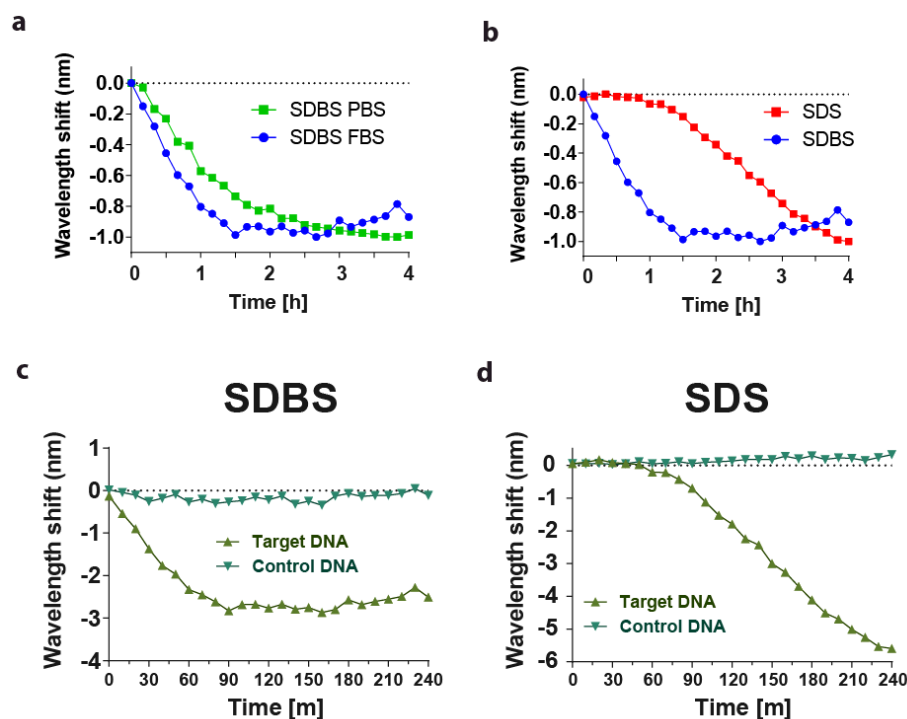
***Figure 5.9 Comparison of hybridization-induced enhancement dynamics* a**,
Normalized (0 to -1, with -1 being most blue-shifted) wavelength shift of GT15mir19
nanotube sensor over time with 1 uM target DNA in 0.2% sodium
dodecylbenzenesulfonate (SDBS) in PBS (green) or FBS (blue). **b**, Wavelength shift
of GT15mir19 nanotube sensor over time with 1 uM target DNA in serum with 0.2%
SDBS (blue) or serum with 1% SDS (red). c and d, Dynamics of wavelength shift for
GT15mir19 in serum with 0.2% SDBS or 1% SDS treated with 1 uM target or control
DNA.
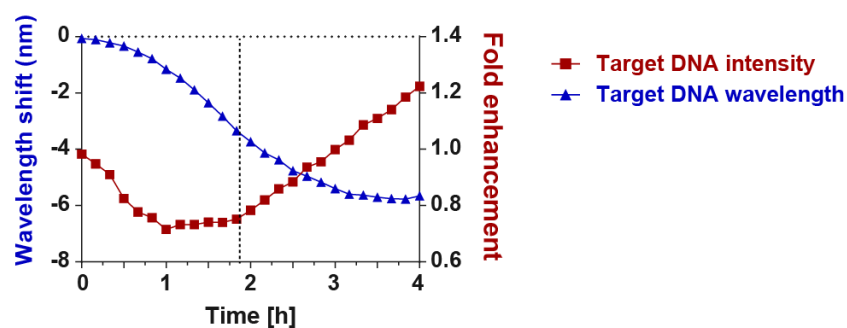
Figure 5.10 Overlay of wavelength shifting and intensity dynamics. Overlay of
wavelength shift (blue, left axis) and intensity fold enhancement (red, right axis)
overtime after addition of 1 uM target DNA in serum treated with 1% SDS. Vertical
dotted line indicates approximate time where intensity beings to increase

Serum is a complex biological fluid with many protein and non-protein components[21]. Because non-polar compounds tend to blue-shift nanotubes[22, 23], we hypothesized that lipoproteins, which transport non-polar fats[24], may be the component of serum responsible for SDS-induced hybridization enhancement. GT15mir19 sensor was spiked into human lipoprotein-deficient serum (LPDS) or standard FBS with different concentrations of target DNA, followed by addition of concentrated SDS to a final concentration of 1% wt/vol. The dose-response behavior and magnitude of blue-shift upon hybridization with target oligonucleotide was largely indistinguishable between the two serum conditions (Figure 5.11), suggesting that lipoproteins only play a minor role.
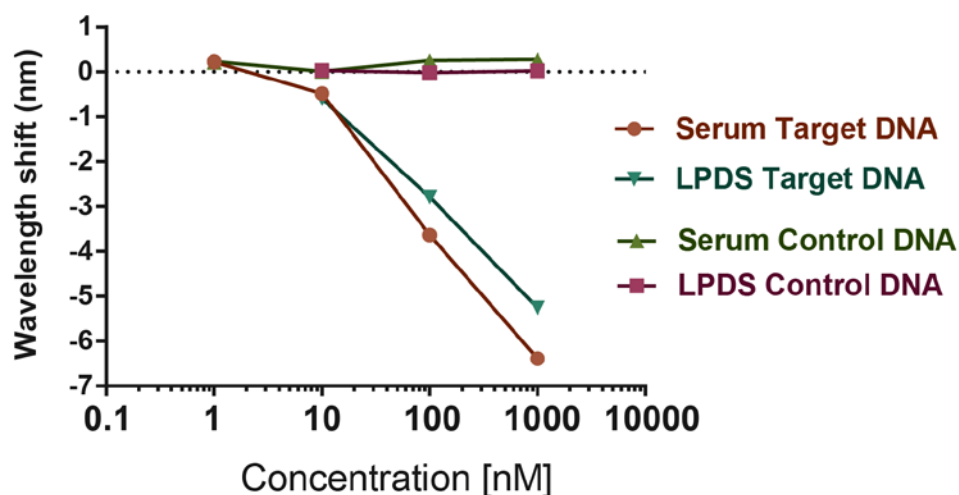
Figure 5.11 Wavelength shift response of GT15mir19 to dilutions of target DNA or control DNA in fetal bovine serum (FBS) treated with 1% SDS or human lipoprotein-deficient serum treated with 1% SDS after incubation overnight.

The most abundant macromolecule component of serum is albumin, which ranges from 35 mg/mL to 50 mg/mL in healthy individuals[25]. Using purified bovine serum albumin (BSA), we tested the high end of the normal range, 50 mg/mL, with SDS to see if this purified component of serum would enhance hybridization in the absence of other serum components. A serial dilution of target DNA produced dose-dependent enhanced blue-shifting, indicating that BSA + SDS provided enhancement of blue-shifting in a hybridization dependent manner (Figure 5.12). We next kept the concentration of target DNA and SDS constant at 1 uM and varied the concentration of BSA. For most chiralities, there was a highly dose-dependent pattern in blue-shifting and intensity enhancement (Figure 5.13), although some chiralities displayed less shifting at the highest protein concentration (Figure 5.14). Interestingly, even in these cases, the intensity enhancement was still dose-dependent. Finally, we kept the concentration of BSA and target oligonucleotide constant and varied the SDS concentration. We escalated the concentration from 0 to 6% in 1% increments, but observed no additional enhancement above 2% SDS (Figure 5.15). Narrowing the tested percentages between 0 and 1% in 0.1% increments however revealed that blue-shifting was dose-dependent in this range. The critical micelle concentration (CMC) of SDS is approximately 0.23 % wt/vol; just below the CMC, at 0.2% wt/vol, SDS did not have any enhancement effect. These data support our hypothesis that SDS-denatured protein is a major causative agent in serum for the observed hybridization-induced blue-shift enhancement.
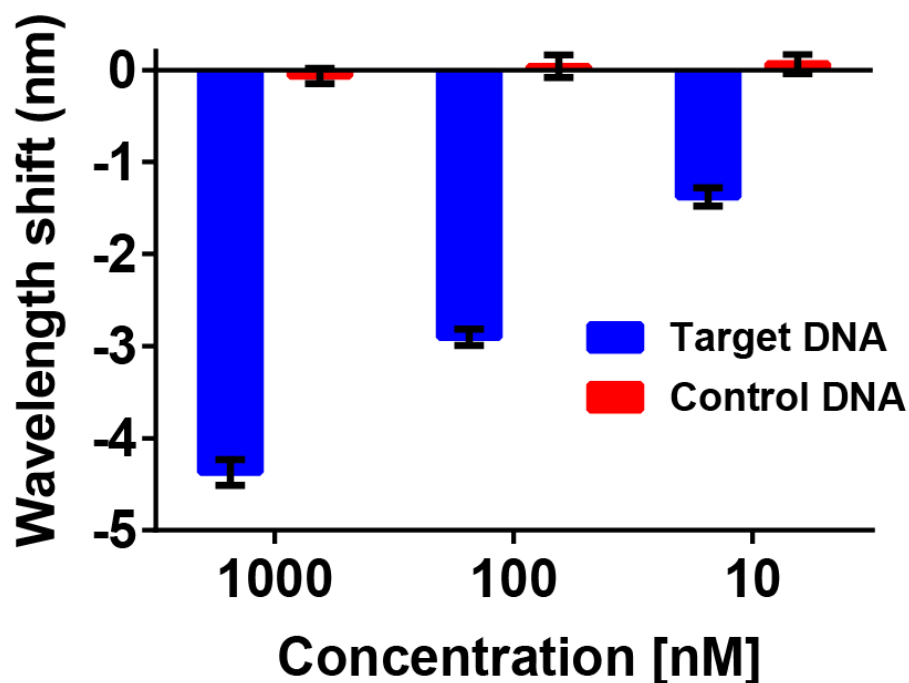
***Figure 5.12 Dose-response in BSA with serum*.** Wavelength shift of the (9,4) nanotube after treatment with the indicated concentration of target or control DNA in 50 mg/mL BSA treated with 1% SDS. Incubation proceeded for 4h. Error bars represent standard deviation.
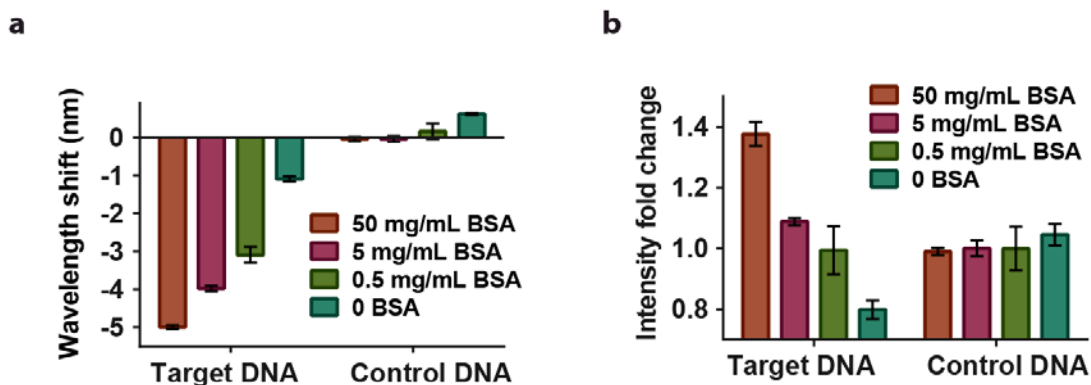
***Figure 5.13 Assessment of albumin and SDS contribution to hybridization-induced blue-shifting* a**, Wavelength shift of GT15mir19 nanotube sensor after treatment with 1 uM target DNA or control DNA in PBS with 1% SDS and the indicated concentration of bovine serum albumin (BSA). **b**, Intensity fold-change of GT15mir19 nanotube sensor after treatment with 1 uM target DNA or control DNA in PBS with 1% SDS and the indicated concentration of BSA
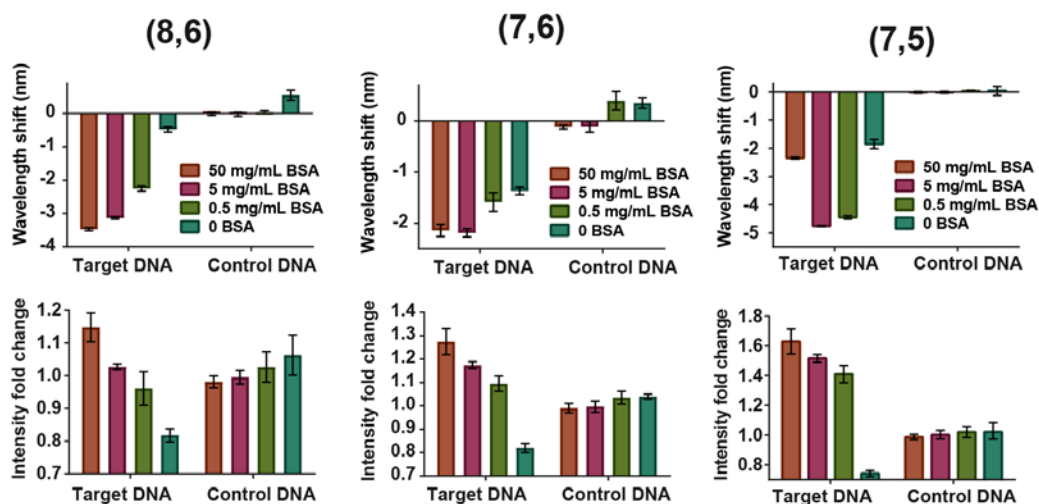
Figure 5.14 Chirality specific behavior from BSA + SDS enhanced hybridization.
Wavelength shift (top) and intensity fold change (bottom) of GT15mir19 nanotube
sensor for three additional chiralities after treatment with 1 uM target DNA or control
DNA in PBS with 1% SDS and the indicated concentration of bovine serum albumin
(BSA).
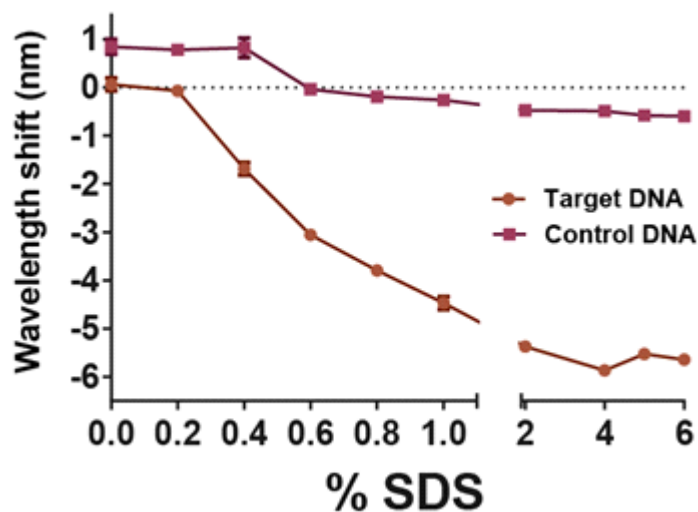
Figure 5.15 Role of SDS in BSA + SDS enhanced hybridization. Wavelength shift of
GT15mir19 nanotube sensor after overnight incubation with 50 mg/mL BSA and 1
uM of target (orange) or control (purple) DNA and escalating concentrations of SDS .

Considerable effort has been put forth in understanding the microstructure and mechanism of SDS denaturation of proteins, including the relative contribution of hydrophobic interactions versus ionic interactions[26-28]. The currently accepted view is that below the critical micelle concentration of SDS, there is protein tertiary structure unfolding to a protein chain[29], and at micellular concentrations chain expansion drives complete denaturation. The interaction is predominantly hydrophobic at submicellular concentrations, and exclusively hydrophobic at micellar concentrations. In this model, the chain expansion is driven by micelle nucleation on hydrophobic patches of the protein chain[30]. Based on our experimental observations and this model, we propose the following mechanism for SDS-denatured protein enhancement of hybridization-induced blue-shifting: hybridization with target oligonucleotide leads to partial desorption of DNA from the nanotube, exposing the hydrophobic surface to the solvent conditions[13]. SDS-driven loss of tertiary structure and exposure of hydrophobic patches on the protein chain, which would typically be coated by an SDS micelle[31], have a stronger affinity for the newly-exposed nanotube surface than with SDS, leading to preferential binding of the hydrophobic patch to the nanotube surface. The competition between SDS and the bare nanotube surface for the hydrophobic patch may explain the relatively slow kinetics and complicated shape compared to SDBS (Figure 5.9). The binding of the peptide chain hydrophobic patch decreases the local dielectric environment around the nanotube, producing the observed blue-shift in emission. The rest of the DNA-coated nanotube is protected due to charge-charge repulsion between the negatively charged SDS-denatured protein chain and the negatively charged DNA phosphate backbone. Because SDS does not change baseline fluorescence (Figure 5.3) and produces almost no enhancement of blue-shifting after hybridization with the target (Figure 5.4), we conclude that free SDS itself makes little contribution to the observed blue-shift. Protein by itself red-shifts the nanotube and

largely prevents hybridization (Figure 5.1), possibly due to electrostatic interactions with the DNA-suspended nanotube[32] that are eliminated by SDS coating the protein chain. The hybridization conditions and resulting optical outputs are summarized in Figure 5.16.
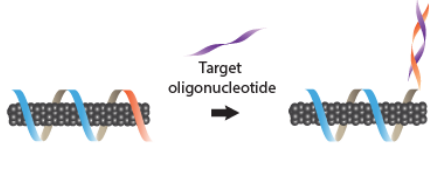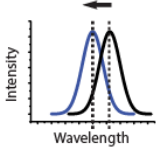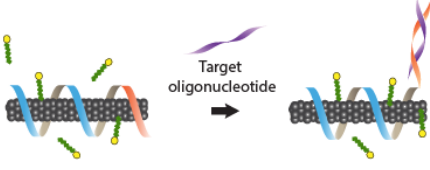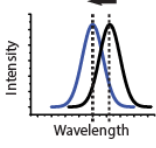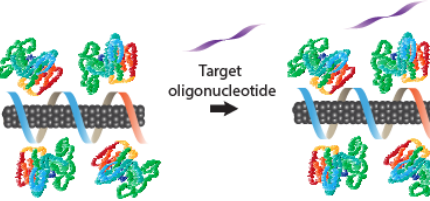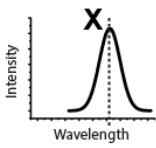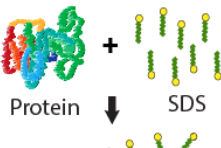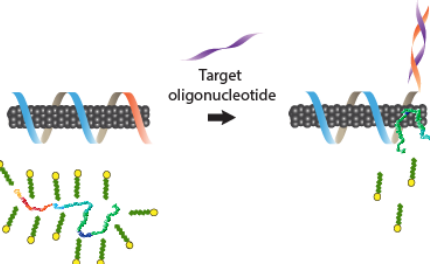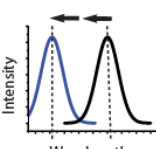
Figure 5.16 Summary of components added to GT15mir19 nanotube sensor, the observed optical effects, and models of hypothesized structures. Grey cylinders represent the carbon nanotube, and suspending DNA is represented by blue (GT15 portion) and orange (complementary region to target oligonucleotide) ribbon.

We next tried to understand the impact of the protein size and tertiary character on SDS-denatured protein enhancement of hybridization-induced blue-shifting. Using the relatively large γ-globulins (1200 kDa compared to albumin, 66.5 kDa), a subset of the second most abundant protein class in serum after albumin, we tested if SDS denaturation would lead to enhanced blue-shifting upon hybridization. A solution of γ-globulins at 35 mg/mL was tested with 2% wt/vol SDS with target or control DNA. In this case, although we found that SDS-denatured γ-globulins were relatively slow, there was a similar equilibrium blue-shift compared to BSA (Figure 5.17a). Unlike BSA, SDS-denatured γ-globulins did not lead to increased intensity upon hybridization (Figure 5.17b). Another protein, casein, the main protein component of milk, is not found in serum but has a micellular tertiary structure as a distinguishing characteristic[33]. Hydrolyzed casein, which is casein that has been digested into smaller peptide and protein fragments, was also tested to compare the effect of protein fragmentation. We tested whether SDS + casein would recapitulate the results seen for BSA and immunoglobulins, and whether SDS + hydrolyzed casein would produce any enhancement due to the fragmentation from partial digestion. Casein and hydrolyzed casein were prepared at 35 mg/mL and SDS was added to 2% wt/vol, followed by target or control DNA. For most chiralities, SDS + casein enhanced hybridization induced blue-shifting and intensity increase, while hydrolyzed casein provided only modest benefit over controls (Figure 5.17c, d). This is consistent with work showing that the degree of hydrolysis of casein is correlated with loss of hydrophobicity[34]. However, we noted that some chiralities showed significant hybridization-induced blue-shift enhancement with SDS + hydrolyzed casein, sometimes exceeding the enhancement produced by SDS + casein (Figure 5.18). These results suggest that most proteins, independent of their tertiary structure, combined with SDS will lead to hybridization-induced enhancement with a similar magnitude at equilibrium. A

194

relatively long protein chain appears to be important, as most chiralities did not respond well to SDS + hydrolyzed casein as an enhancing agent. Two chiralities were notable exceptions, where SDS + hydrolyzed casein performed better than full length casein. Chirality-dependent selectivity to analytes has been reported[13, 35, 36], but the mechanism for chirality selectivity observed here requires further study.
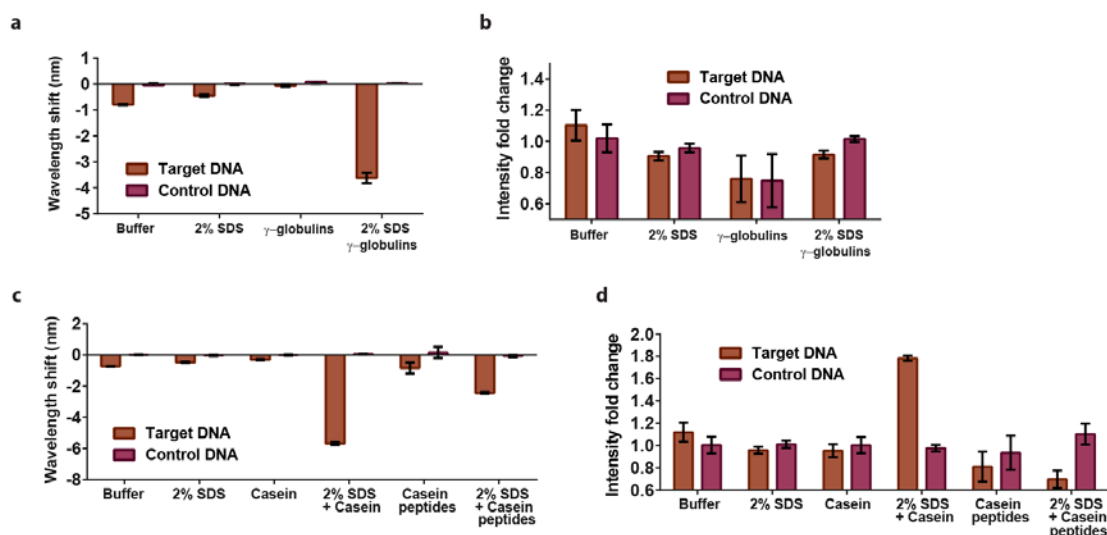
Figure 5.17 Effect of tertiary character and integrity of protein as part of hybridization conditions **a**, Wavelength shift of GT15mir19 nanotube sensor after treatment with 1 uM target DNA or control DNA in PBS buffer, 2% SDS, 35mg/mL γ-globulins**,** and 2% SDS with 35 mg/mL overnight. **b**, Intensity fold change corresponding to experiment in part a. **c**, Wavelength shift of GT15mir19 nanotube sensor after treatment with 1 uM target DNA or control DNA in PBS, 2% SDS, 35mg/mL casein**,** 2% SDS with 35 mg/mL casein, 35 mg/mL hydrolyzed casein peptides, and 2% SDS with 35 mg/mL hydrolyzed casein peptides overnight. **d,** Intensity fold change corresponding to experiment in part c.
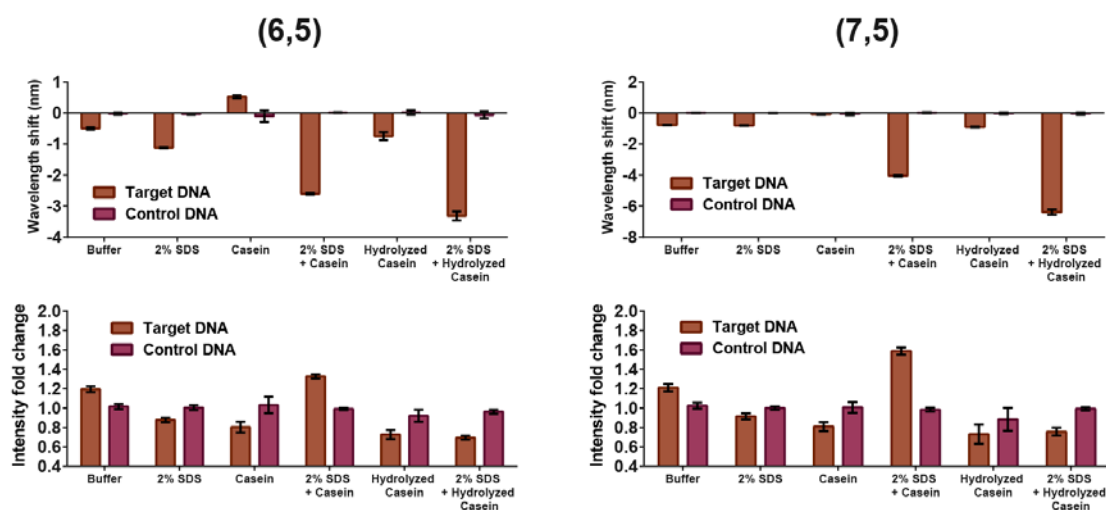
Figure 5.18 Chirality differences in response to peptide length. Wavelength shift (top) and intensity fold change (bottom) of GT15mir19 nanotube sensor for two additional chiralities after overnight incubation with 1 uM target DNA or control DNA in PBS, 2% SDS, 35 mg/mL casein, 2% SDS plus 35 mg/mL casein, 35 mg/mL hydrolyzed casein, or 2% SDS plus 35 mg/mL hydrolyzed casein.

Finally we tested whether the single-strand RNA genome[37] of intact lentivirus could be detected using SDS to both liberate the genome and denature proteins for hybridization-induced enhancement of a nanotube sensor. A sensor was constructed for the poly A tail of the virus genome by using (GT)15-(T)15 DNA to suspend carbon nanotubes. As a control, a sensor for a poly-T sequence, which does not exist in the virus genome, was similarly constructed with (GT)15-(A)15 DNA. The functionality of both sensors was first assessed with short strands of DNA target and 0.2% SDBS. The sensor for poly-A sequences, (GT)15-(T)15, showed a rapid (complete in 90m) and robust blue-shift when treated with (A)15, but no change was observed after treatment with (T)15, which served as a control for non-specific oligonucleotide binding (Figure 5.19a). To test the sensor with intact virus, we synthesized lentivirus according to molecular biology protocols intended for gene transduction. A lentiviral vector was chosen as a model virus due to its similar structure and function to wildtype lentivirus, but such vectors can be produced in high-yield and have been

engineered to be replication incompetent for safety[38]. Concentrated viral stocks were treated with 1% SDS and (GT)15(T)15, the sensor for the poly A tail, or with (GT)15(A)15, to serve as a control for non-specific interactions. The center wavelength of the (8,6) nanotube was measured every 10m over 180m. The sensor for poly-A sequences, (GT)15(T)15, began to blue-shift within 20m, and by 180m had shifted about 3 nm. The kinetics displayed a sigmoidal shape, suggesting enhancement from denatured viral proteins. The control sensor, (GT)15(A)15, blue-shifted by about 0.5 nm over 180m, indicating some non-specific interactions (Figure 5.19b). We present a model for such detection in Figure 5.19c; here, intact lentivirus is treated with SDS and a carbon nanotube sensor. The SDS denatures the lentivirus envelope and protein structure, releasing the single-strand RNA genome. Hybridization with the poly A tail enables binding by the detergent-denatured protein, leading to a blue-shift of the nanotube emission.
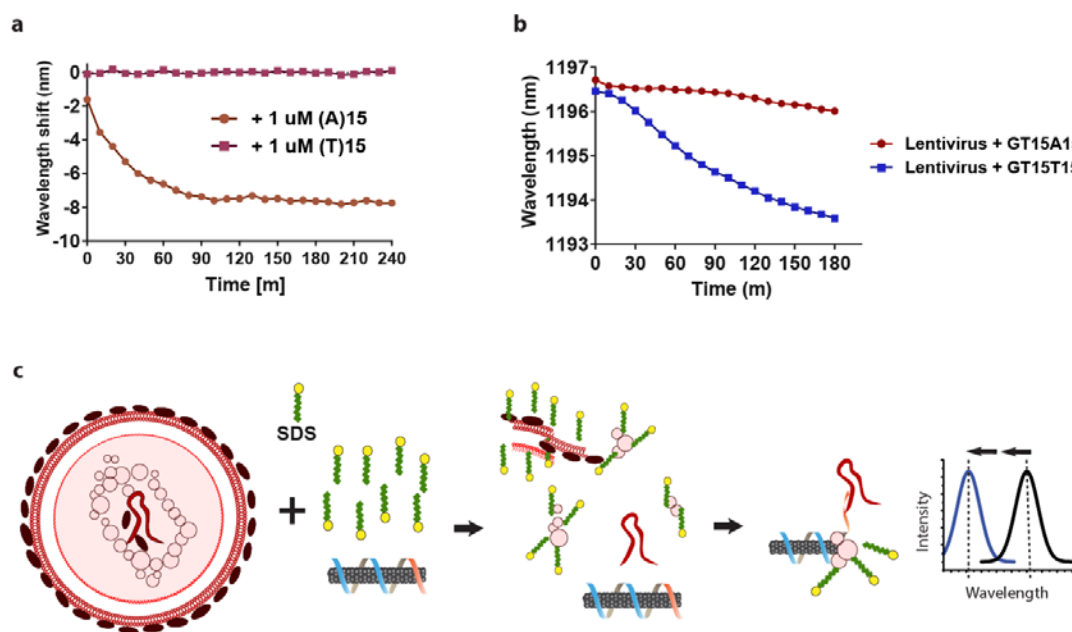
Figure 5.19 Detection of viral RNA using a lentivirus model. a, Kinetics of
wavelength shift for (GT)15-T(15) suspended (8,6) with 1 uM of target
oligonucleotide, (A)15, or non-target control, (T)15, using 0.2% SDBS and blue-shift
enhancing agent. b, Kinetics of the (8,6) center wavelength for (GT)15-T(15)
suspended nanotubes or (GT)15-A(15) suspended nanotubes with concentrated
lentivirus and 2% SDS. c, model depicting how lentivirus RNA can be detected with a
carbon nanotube sensor and SDS. The virus is ruptured and denatured by SDS,
liberating the RNA genome, which hybridizes to the sensor. Denatured viral proteins
provide enhanced blue-shifting upon hybridization.

5.4 Conclusions

Here, we have shown how SDS-treated serum can interact with carbon nanotubes to enhance blue-shifting due to hybridization induced removal of DNA from the nanotube surface. In understanding why SDS-treated serum provided such enhancement, we tested lipoprotein deficient serum as well as purified serum proteins to identify the causative agent. Lipoprotein depleted serum behaved nearly identically as untreated serum, suggesting that lipoproteins play little role. Purified protein treated with SDS could largely recapitulate the enhancement seen with serum, but not with the same magnitude of blue-shift. This may be due to a combinatorial effect of several proteins present in serum, or a non-protein factor that we could not identify. Serum is a complex biological fluid, containing all the proteins not involved in clotting as well as electrolytes, lipids, vitamins and minerals, and hormones[21]. The enhancement to hybridization-induced blue-shifting by SDS-treated protein was quite unexpected due to the fact that SDS alone does very little to DNA-suspended nanotubes, and protein alone red-shifts DNA-suspended nanotubes. Based on the current understanding of SDS-induced protein denaturation and the mechanism of the DNA-carbon nanotube sensor, we propose a model where hydrophobic patches from the SDS-denatured protein bind to newly exposed nanotube surface after hybridization, leading to the enhancement in blue-shifting.

For clinical applications, we believe that in vitro diagnostics based on detection of short oligonucleotides in protein rich environments such as serum could benefit from the use of carbon nanotube-based sensors with SDS. We have previously reported the use of another detergent, SDBS, to enhance detection of oligonucleotides in serum. In serum, we believe that SDBS and SDS operate with two distinct mechanisms, where SDBS interacts with the nanotube directly after hybridization while SDS only

functions to expose hydrophobic centers in denatured proteins, which then interacts with the nanotube. Although SDBS produces a faster response in serum, SDS produces a shift with a greater magnitude, and thus may be better suited for in vitro applications. SDS is also a standard molecular biology agent with wide availability and well-understood properties and applications. As a proof-of-principle for direct optical detection of virus, we have shown here how SDS can be combined with a DNA-nanotube sensor to liberate lentiviral RNA from a complete virus structure, and provide enhanced blue-shifting from SDS-denatured viral proteins detection after hybridization. Such detection could take place directly in serum samples where point of care detection is desirable. The DNA-nanotube sensor solution and SDS are both highly stable and can be stored at room temperature. While we have used laser excitation and an InGaAs array camera for detection, cheaper LEDs could also be used for excitation and some nanotubes, such as the (8,4) and (6,5), can be detected by standard CCD cameras. An LED/CCD camera detection apparatus could be a relatively simple, affordable, and portable device for deployment in regions lacking critical biomedical infrastructure. For example, Ebola is a virus with a single-strand RNA genome that may be amenable to detection with our method; direct optical detection without the need for purification, amplification, labeling, or the use of perishable reagents such as antibodies could be beneficial for controlling future outbreaks. While we have shown here an application with a lentivirus model, we believe that SDS could also be applied to detection of single-strand oligonucleotides in other viruses and pathogen types, as well as in circulating cancer cells.

5.5 Materials and Methods

5.5.1 DNA-suspension of carbon nanotubes

Carbon nanotubes produced by the HiPco process (Unidym, Sunnyvale, CA) were mixed with DNA oligonucleotides (IDT DNA, Coralville, IA) at a 2:1 mass ratio in 1 mL of PBS buffer (Thermo Fisher Scientific Waltham, MA) and ultrasonicated for 30 minutes at 40% amplitude (Sonics & Materials, Inc.). The DNA sequences used for suspension were

GTGTGTGTGTGTGTGTGTGTGTGTGTGTGTTCAGTTTTGCATAGATTTGCACA (GT15mir19)[13],

GTGTGTGTGTGTGTGTGTGTGTGTGTGTGTTTTTTTTTTTTTTTTT ((GT)15-T(15)), and

GTGTGTGTGTGTGTGTGTGTGTGTGTGTGTAAAAAAAAAAAAAAAA ((GT)15-A(15)) all purchased from IDT (Coralville, IA). Following ultrasonication, the dispersions were ultracentrifuged (Sorvall Discovery 90SE) for 30 minutes at 280,000 x g and the top 80% of the supernatant was collected. Absorbance spectra were acquired using a UV/Vis/nIR spectrophotometer (Jasco V-670, Tokyo, Japan). The concentration for HiPco samples was calculated using the extinction coefficient Abs_{910} = 0.02554 L $mg^{-1}cm^{-1}$. Excess DNA was removed via 100 kDa Amicon centrifuge filters (Millipore). The DNA-nanotube complexes were re-suspended in PBS (Thermo Fisher Scientific Waltham, MA).

5.5.2 Fluorescence spectroscopy measurements of carbon nanotubes

Fluorescence emission spectra from aqueous nanotube solutions were acquired with a home-build spectroscopy system as described[13]. Briefly, carbon nanotube samples were assayed in a 96 well plate format on an inverted microscope using a tunable white-light laser (NKT Photonics) coupled to a variable bandpass filter. Emission light

was directed into a spectrometer with a focal length of 320 mm and aperture ratio of f/4.6 (Princeton Instruments IsoPlane SCT 320) and InGaAs array camera (Princeton Instruments 640 × 512 pixel NIRvana). For all experiments, measurements were taken in triplicate across three wells. Following spectra acquisition, custom code written in Matlab applied spectral corrections and background subtraction as described[13]. Corrected spectra were used to fit the data with Voigt functions. Error bars and linear fits were computed with GraphPad Prism 6.

5.5.3 Hybridization conditions

Concentrated sodium dodecyl sulfate (Sigma-Aldrich) was prepared in PBS buffer and added to samples to the final concentration indicated, or 1% wt/vol where not indicated; control samples had an equivalent volume of PBS added. Carbon nanotubes were used at a final concentration of 2 mg/L for all experiments. Fetal bovine serum (FBS) (Life Technologies) and human lipoprotein deficient serum (LPDS) (J65516 Lipoprotein Deficient Serum, human, BT-931 from Alfa Aesar) were used for serum-based experiments, and had concentrated nanotubes or SDS added directly to the whole serum. Bovine serum albumin, bovine γ-globulins, casein, and hydrolyzed casein (all from Sigma-Aldrich) were resuspended in PBS to the indicated concentrations. Concentrated target DNA (TGTGCAAATCTATGCAAAACTGA) complementary to the DNA-nanotube sensor or non-complementary control DNA (TCGGTCAGTGGGTCATTGCTAGT) (both from IDT DNA, Coralville, IA) was added to the indicated final concentration. Non-treated controls received an equivalent volume of PBS. Hybridization was allowed to proceed overnight for equilibrium measurements. Kinetics were measured immediately after addition of target. Assessment of (GT)15-T(15) and (GT)15-A(15) used 0.2% SDBS (Sigma-Aldrich) as

202

described[13] to verify expected behavior with AAAAAAAAAAAAAAA or TTTTTTTTTTTTTTT (IDT DNA, Coralville, IA).

5.5.4 Lentivirus production

Lentivirus was produced from transfected packaging cells (293T) using 100 ng pLX304 plasmid[39], 100 ng of packaging plasmid (psPAX2) and 10 ng of envelope plasmid (VSV-G). Virus was collected 48 and 70 h after transfection and concentrated 10-fold.

5.6 Acknowledgements

5.7 References

1.   Schwarzenbach, H., Hoon, D.S. & Pantel, K. Cell-free nucleic acids as biomarkers in cancer patients. *Nature reviews. Cancer* **11**, 426-437 (2011).

2.   Mitchell, P.S., Parkin, R.K., Kroh, E.M. et al. Circulating microRNAs as stable blood-based markers for cancer detection. *Proceedings of the National Academy of Sciences of the United States of America* **105**, 10513-10518 (2008).

3.   Zen, K. & Zhang, C.Y. Circulating microRNAs: a novel class of biomarkers to diagnose and monitor human cancers. *Medicinal research reviews* **32**, 326-348 (2012).

4.   Crowley, E., Di Nicolantonio, F., Loupakis, F. & Bardelli, A. Liquid biopsy: monitoring cancer-genetics in the blood. *Nature reviews. Clinical oncology* **10**, 472-484 (2013).

5.   Wan, J.C.M., Massie, C., Garcia-Corbacho, J. et al. Liquid biopsies come of age: towards implementation of circulating tumour DNA. *Nature Reviews Cancer* **17**, 223-238 (2017).

6.   Pantel, K. Blood-Based Analysis of Circulating Cell-Free DNA and Tumor Cells for Early Cancer Detection. *Plos Med* **13** (2016).

7.   Corsten, M.F., Dennert, R., Jochems, S. et al. Circulating MicroRNA-208b and MicroRNA-499 Reflect Myocardial Damage in Cardiovascular Disease. *Circ-Cardiovasc Gene* **3**, 499-506 (2010).

8.   Elnifro, E.M., Ashshi, A.M., Cooper, R.J. & Klapper, P.E. Multiplex PCR: Optimization and application in diagnostic virology. *Clin Microbiol Rev* **13**, 559-+ (2000).

9.   Niemz, A., Ferguson, T.M. & Boyle, D.S. Point-of-care nucleic acid testing for infectious diseases. *Trends in biotechnology* **29**, 240-250 (2011).

10. Broadhurst, M.J., Brooks, T.J.G. & Pollock, N.R. Diagnosis of Ebola Virus Disease: Past, Present, and Future. *Clin Microbiol Rev* **29**, 773-793 (2016).

11. Huang, X., Liu, Y.Y., B., Xiong, Y. & Chen, X. Nanotechnology-Enhanced No-Wash Biosensors for in Vitro Diagnostics of Cancer. *ACS nano* **11**, 5238-5292 (2017).

12. Kruss, S., Hilmer, A.J., Zhang, J. et al. Carbon nanotubes as optical biomedical sensors. *Advanced drug delivery reviews* **65**, 1933-1950 (2013).

13. Harvey, J.D., Jena, P.V., Baker, H.A. et al. A carbon nanotube reporter of microRNA hybridization events in vivo. *Nature Biomedical Engineering* **1**, 0041 (2017).

14. O'Connell, M.J., Bachilo, S.M., Huffman, C.B. et al. Band gap fluorescence from individual single-walled carbon nanotubes. *Science* **297**, 593-596 (2002).

15. Wang, F., Dukovic, G., Brus, L.E. & Heinz, T.F. The optical resonances in carbon nanotubes arise from excitons. *Science* **308**, 838-841 (2005).

16. Roxbury, D., Jena, P.V., Williams, R.M. et al. Hyperspectral Microscopy of Near-Infrared Fluorescence Enables 17-Chirality Carbon Nanotube Imaging. *Scientific reports* **5**, 14167 (2015).

17. Heller, D.A., Pratt, G.W., Zhang, J.Q. et al. Peptide secondary structure modulates single-walled carbon nanotube fluorescence as a chaperone sensor for nitroaromatics. *Proceedings of the National Academy of Sciences of the United States of America* **108**, 8544-8549 (2011).

18. Heller, D.A., Jeng, E.S., Yeung, T.K. et al. Optical detection of DNA conformational polymorphism on single-walled carbon nanotubes. *Science* **311**, 508-511 (2006).

19.   Barone, P.W., Baik, S., Heller, D.A. & Strano, M.S. Near-infrared optical sensors based on single-walled carbon nanotubes. *Nature materials* **4**, 86-92 (2005).

20.   Xu, J., Mueller, R., Hazelbaker, E. et al. Strongly Bound Sodium Dodecyl Sulfate Surrounding Single-Wall Carbon Nanotubes. *Langmuir : the ACS journal of surfaces and colloids* **33**, 5006-5014 (2017).

21.   Adkins, J.N., Varnum, S.M., Auberry, K.J. et al. Toward a human blood serum proteome - Analysis by multidimensional separation coupled with mass spectrometry. *Mol Cell Proteomics* **1**, 947-955 (2002).

22.   Choi, J.H. & Strano, M.S. Solvatochromism in single-walled carbon nanotubes. *Applied Physics Letters* **90**, 223114 (2007).

23.   Gao, J., Gomulya, W. & Loi, M.A. Effect of medium dielectric constant on the physical properties of single-walled carbon nanotubes. *Chemical Physics* **413**, 35-38 (2013).

24.   Scanu, A.M. & Wisdom, C. Serum-Lipoproteins Structure and Function. *Annual review of biochemistry* **41**, 703-& (1972).

25.   Tietz, N.W., Burtis, C.A., Ashwood, E.R. & Bruns, D.E. Tietz textbook of clinical chemistry and molecular diagnostics, Edn. 4th. (Elsevier Saunders, St. Louis, Mo.; 2006).

26.   Chen, S.H. & Teixeira, J. Structure and fractal dimension of protein-detergent complexes. *Physical review letters* **57**, 2583-2586 (1986).

27.   Guo, X.H., Zhao, N.M., Chen, S.H. & Teixeira, J. Small-angle neutron scattering study of the structure of protein/detergent complexes. *Biopolymers* **29**, 335-346 (1990).

28.   Turro, N.J., Lei, X.G., Ananthapadmanabhan, K.P. & Aronson, M. Spectroscopic Probe Analysis of Protein-Surfactant Interactions - the Bsa/Sds

System. *Langmuir : the ACS journal of surfaces and colloids* **11**, 2525-2533 (1995).

29.   Ibel, K., May, R.P., Sandberg, M. et al. Structure of Dodecyl-Sulfate Protein Complexes at Subsaturating Concentrations of Free Detergent. *Biophys Chem* **53**, 77-83 (1994).

30.   Bhuyan, A.K. On the Mechanism of SDS-Induced Protein Denaturation. *Biopolymers* **93**, 186-199 (2010).

31.   Shirahama, K., Tsujii, K. & Takagi, T. Free-Boundary Electrophoresis of Sodium Dodecyl Sulfate-Protein Polypeptide Complexes with Special Reference to Sds-Polyacrylamide Gel-Electrophoresis. *Journal of biochemistry* **75**, 309-319 (1974).

32.   Roxbury, D., Jena, P.V., Shamay, Y., Horoszko, C.P. & Heller, D.A. Cell Membrane Proteins Modulate the Carbon Nanotube Optical Bandgap via Surface Charge Accumulation. *ACS nano* **10**, 499-506 (2016).

33.   Swaisgood, H.E. Review and Update of Casein Chemistry. *J Dairy Sci* **76**, 3054-3061 (1993).

34.   Mahmoud, M.I., Malone, W.T. & Cordle, C.T. Enzymatic-Hydrolysis of Casein - Effect of Degree of Hydrolysis on Antigenicity and Physical-Properties. *J Food Sci* **57**, 1223-1229 (1992).

35.   MJ, O.C., Eibergen, E.E. & Doorn, S.K. Chiral selectivity in the charge-transfer bleaching of single-walled carbon-nanotube spectra. *Nature materials* **4**, 412-418 (2005).

36.   Salem, D.P., Landry, M.P., Bisker, G. et al. Chirality dependent corona phase molecular recognition of DNA-wrapped carbon nanotubes. *Carbon* **97**, 147-153 (2016).

37.   Tang, H.L., Kuhen, K.L. & Wong-Staal, F. Lentivirus replication and regulation. *Annual review of genetics* **33**, 133-170 (1999).

38.   Sakuma, T., Barry, M.A. & Ikeda, Y. Lentiviral vectors: basic to translational. *Biochemical Journal* **443**, 603-618 (2012).

39.   Yang, X.P., Boehm, J.S., Yang, X.P. et al. A public genome-scale lentiviral expression library of human ORFs. *Nature methods* **8**, 659-U680 (2011).

CHAPTER 6 A CUMULATIVE SENSOR FOR *IN VIVO* DOXORUBICIN EXPOSURE

6.1 Abstract

Doxorubicin is a highly successful chemotherapy drug with indications for many cancers, but cumulative dose-toxicity leads to cardiomyopathy. Experimentally, doxorubicin is also being applied as part of intraperitoneal delivery methods. For monitoring doxorubicin exposure, an implantable, optically-based cumulative sensor could help provide personalized care and improve experimental therapies. Using DNA-suspended carbon nanotubes, we have discovered that the polycyclic aromatic hydrocarbon pyrene, when derivatized to be soluble, induces a large and uniform red-shift in carbon nanotube emission. We have ascribed this to be a property of DNA-intercalating agents, including doxorubicin. Sensing of doxorubicin was obtained in buffer, serum, intracellularly, and from single nanotubes on a surface covered with buffer or serum. Doxorubicin adsorption to the DNA-suspended nanotubes did not displace DNA and could not be reversed, and we calculate approximately 180 molecules bound to a typical 166nm long nanotube as we have prepared. Several implantable devices were tested, and doxorubicin was found to be detectable in a cumulative way. Real time, *in vivo* detection of doxorubicin injected into the peritoneum was obtained, as well as compartment specific measurements. The robust and cumulative sensing of doxorubicin suggests suitability for clinical and experimental applications.

6.2 Introduction

Many clinically useful drugs for chemotherapy are based on interactions with DNA, which can be covalent, electrostatic, or intercalating interactions[1]. DNA intercalation is a non-covalent interaction driven by hydrophobic and π- π interactions between a planar, aromatic polycyclic compound that is approximately the size of two DNA bases[2]. Intercalation often distorts the DNA[3] to prevent replication or other essential cell functions[4], which is therapeutically useful for halting cell-division in cancer cells[5] but can also be highly toxic to normally dividing cells[6]. DNA intercalating agents have additionally found wide-spread use in molecular biology to visualize DNA. Some intercalating agents undergo a solvatochromic change in the DNA microenvironment that enables fluorescence[7]. Ethidium bromide is the most common and well-studied of such dyes[8], with safer alternatives also on the market[7]. Other compounds, such as Hoechst stains, are used in live cells to visual DNA in real-time[9]. Although several intercalating drugs have proven clinically useful in cancer chemotherapy, some pollutants are also recognized to be intercalating agents with carcinogenic potential. Polycyclic aromatic hydrocarbons result from incomplete combustion of organic material and form a class of mutagenic and carcinogenic pollutants due in part to their DNA intercalating ability[10]. The first experimentally induced cancers were driven by benz[a]anthracene, a PAH found in soot[11]. Rapid optical detection of PAH could be beneficial for environmental monitoring[12, 13] or other toxicology applications.

Drugs based on DNA intercalating agents include the anthracyclines, a powerful class of drugs that are used for a variety of solid and blood based malignancies. Major drugs in this class include daunorubicin, doxorubicin, epirubicin, idarubicin, and valrubicin[14]. Doxorubicin in particular has become one of the most widely used chemotherapy drugs, often in combination with other drugs. Doxorubicin has indications for breast cancer, acute lymphoblastic leukemia, bladder cancer, Ewing sarcoma, Hodgkin

lymphoma, non-Hodgkin lymphoma, osteosarcoma, recurrent small cell lung cancer, and soft tissue sarcomas. Doxorubicin also has off-label uses for advanced endometrial carcinoma, multiple myeloma, thymomas, uterine sarcoma, and Waldenstrom macroglobulinemia[15]. Despite the broad efficacy of doxorubicin, its administration must be closely monitored due to dose-limiting cardiotoxicity, which limits both acute and lifetime dosing. The cardiotoxicity is cumulative and irreversible. Based on retrospective analyses of clinical events, the incidence of cardiotoxicity is about 7.5% at a lifetime dose of 550 mg/m^2,[16] which has become the recommended upper-limit. While the exact mechanism of cardiotoxicity is still controversial[17], most hypotheses are related to an increase in reactive oxygen species[18, 19]. Establishment of 550 mg/m^2 as an upper limit for a lifetime dose is pragmatic from an epidemiological perspective; because the mechanism is not completely understood, it is not yet possible to predict patient specific life-time dose limits. Doxorubicin is typically administered intravenously, but is also used as part of hyperthermic intraperitoneal chemotherapy (HIPEC) for certain cancers restricted to the peritoneum[20, 21]. An ongoing clinical trial is assessing the highest tolerable dose of heated doxorubicin for unresectable or refractory pelvic and abdominal rhabdomyosarcoma and undifferentiated sarcomas in children (NCT03111069). For both traditional IV administration and administration as part of HIPEC, an implantable optical sensor could be useful for assessing drug distribution in particular anatomic sites in real time. A cumulative sensor near the heart or within cardiac tissue could also provide precise information on patient-specific exposure to doxorubicin, and eventually enable better control of life-time exposure to doxorubicin and prevention of cardiomyopathy.

Like DNA intercalating drugs, single-walled carbon nanotubes also strongly interact with single-stranded DNA[22]. Single-walled carbon nanotubes are composed entirely of

sp^2 hybridized carbon, and can be qualitatively thought of as a polycyclic aromatic carbon sheet like graphene rolled into a cylinder with a diameter between about 0.8 nm to 1.2 nm[23], depending on preparation. Because the surface of the carbon nanotube is composed entirely of π electrons, DNA bases are driven to interact with the surface based on the many of the same forces as DNA intercalating agents. π-π stacking between the bases and the nanotube surface drives adsorption, and flexibility in the single-strand DNA backbone enables wrapping around the nanotube so that all bases can bind, providing a high avidity interaction[22, 24]. The negatively charged phosphate backbone then serves to prevent re-aggregation through electrostatic repulsion[25], making single-strand DNA an effective dispersant for preparing colloidal solutions of carbon nanotubes. Also like some DNA intercalating agents, single-walled carbon nanotubes are fluorescent[26], but do not photobleach[27]. The fluorescence is in the near-infrared range, which is highly penetrant to tissue[28]. Single-walled carbon nanotubes undergo solvatochromic changes depending on their local dielectric environment[29, 30], which can be utilized for selective sensing of chemical and biological analytes[31, 32]. Stable fluorescence in the tissue-penetrating near-infrared range and sensitivity to analytes make carbon nanotube based sensors outstanding candidates for implantable optical sensors. Sensors based on DNA-suspended nanotubes have been shown to be feasible for *in vivo* detection of some analytes[33, 34].

Previous reports show that some polycyclic aromatic hydrocarbons, such as pyrene, have strong affinity for nanotubes[35] and can utilized as part of a non-covalent functionalization scheme[36]. Other work has shown that doxorubicin also has affinity for carbon nanotubes that have been non-covalently functionalized with lipid-PEG[37]. This was later demonstrated to be a viable method of drug delivery[38]. However, the impact of these molecules on the photoluminescence of the nanotubes was not

213

assessed. We have shown that DNA-suspended nanotubes can be combined with some amphiphilic molecules in a way where the optical character from both the DNA and amphiphilic molecule can be discerned in the spectrum, and found that the amphiphile binds to the free space on the nanotube[34]. Given the strong affinity of polycyclic aromatic hydrocarbons and doxorubicin for carbon nanotubes, we hypothesized that DNA-suspended nanotubes may be made into a sensor for these agents that might have utility as an implantable device.

Herein, we have explored the impact of a soluble pyrene derivative and DNA intercalating agents on the optical properties of DNA-suspended carbon nanotubes. We found that a soluble pyrene derivative greatly red-shifted the emission and excitation of DNA-suspended nanotubes, but not surfactant suspended nanotubes. This red-shift was unexpected, as molecules that bind to the nanotube and displace water tend to blue-shift nanotubes. In testing a panel of DNA-intercalating agents, we found that these agents also red-shifted DNA-suspended nanotubes, and often quenched the emission intensity to varying degrees. One such agent, doxorubicin, was selected as a target analyte due to the utility of a carbon nanotube-based sensor. Doxorubicin was found to elicit dose-dependent red-shifting and intensity quenching in both buffer and serum conditions with rapid kinetics. Like pyrene, doxorubicin did not affect surfactant suspended nanotubes. In exploring the mechanism we found that the suspending DNA is not displaced, and calculated about 180 molecules of doxorubicin bind strongly to a DNA wrapped nanotube of average length (166nm), and could not be reversed by washing or dialysis. We also found that single nanotubes on a surface can detect doxorubicin in both buffer and serum conditions, and when averaged largely recapitulate the shifts seen in solution. Three modalities of implantable devices were tested *in vitro*; two hydrogels, agarose and alginate, and a heat-sealable

214

semipermeable membrane. Using the semipermeable membrane based device, we show that *in vitro* sensing is cumulative. Implantation into the mouse peritoneum allowed for detection of injected doxorubicin, and kinetics measurements show this detection to be rapid. Finally two devices were surgically implanted in anatomically distinct sites separated by a thin layer of fascia. After injection with doxorubicin, we found that it did not appreciably pass through the fascia, giving us anatomically specific sensing.

6.3 Results and Discussion

Recent work has shown that some amphiphilic molecules with affinity for carbon nanotubes can be combined with DNA-suspended nanotubes to form a stable "co-surfactant" system and impart new or enhanced functionality to DNA-suspended nanotube-based sensors[34]. We hypothesized that pyrene may be an effective agent in binding free sites on DNA-suspended nanotubes. To make a soluble form of pyrene, 1-pyrenebutyric acid was activated with N-Hydroxysuccinimide (NHS) and combined with excess polyethylene glycol 100 with a terminal primary amine. The resulting solution was water soluble, producing a dark yellow-brown solution. A fluorescence scan between 350nm and 650nm showed sharp peaks between 350nm and 400nm, characteristic of pyrene monomers, and a large peak centered at approximately 480 nm, indicative of excimer formation [39] (Figure 6.1a), suggesting that the PEG reaction with NHS-activated 1-pyrenebutyric acid produced a water soluble product (Pyrene-PEG). Pyrene-PEG was added to a DNA-suspended nanotube-based sensor for short oligonucleotides[34] and compared to other amphiphilic molecules, sodium dodecylbenzene sulfonate (SDBS) and sodium deoxycholate (SDC). SDBS is known to associate with the nanotube tube surface without displacement of the suspending DNA producing a moderately blue-shifted emission. SDC also has high affinity for the

215

nanotube surface, but is known to displace the suspending DNA, producing a greater blue-shift in emission[40]. The blue-shift from both of these agents is understood to be due to the exclusion of water from the nanotube surface, and the resulting decrease in the local dielectric environment[29, 30, 34]. Based on this mechanism, we hypothesized that pyrene-PEG would also produce a blue-shift in the nanotube emission. To our surprise, the addition of pyrene-PEG greatly red-shifted the DNA-suspended nanotubes, while SDBS blue-shifted a modest degree and SDC greatly blue-shifted the nanotube emission (Figure 6.1b). The speed at which these red-shifts occurred was remarkable; within approximately 5 minutes, the nanotubes were nearly maximally-red-shifted (Figure 6.1c). The red-shift induced by pyrene-PEG was universal across all measured nanotube chiralities (Figure 6.1d), and produced a consistent red-shift between of about 12-16 nm with no apparent dependence on chirality (Figure 6.1e). There was additionally a consistent red-shift in the excitation wavelength of about 5 and 7 nm, also apparently independent of chirality (Figure 6.1f). This pyrene-PEG induced red-shift is unique to DNA-suspended nanotubes, as addition to SDC-suspended nanotubes did not produce any change (Figure 6.1g).
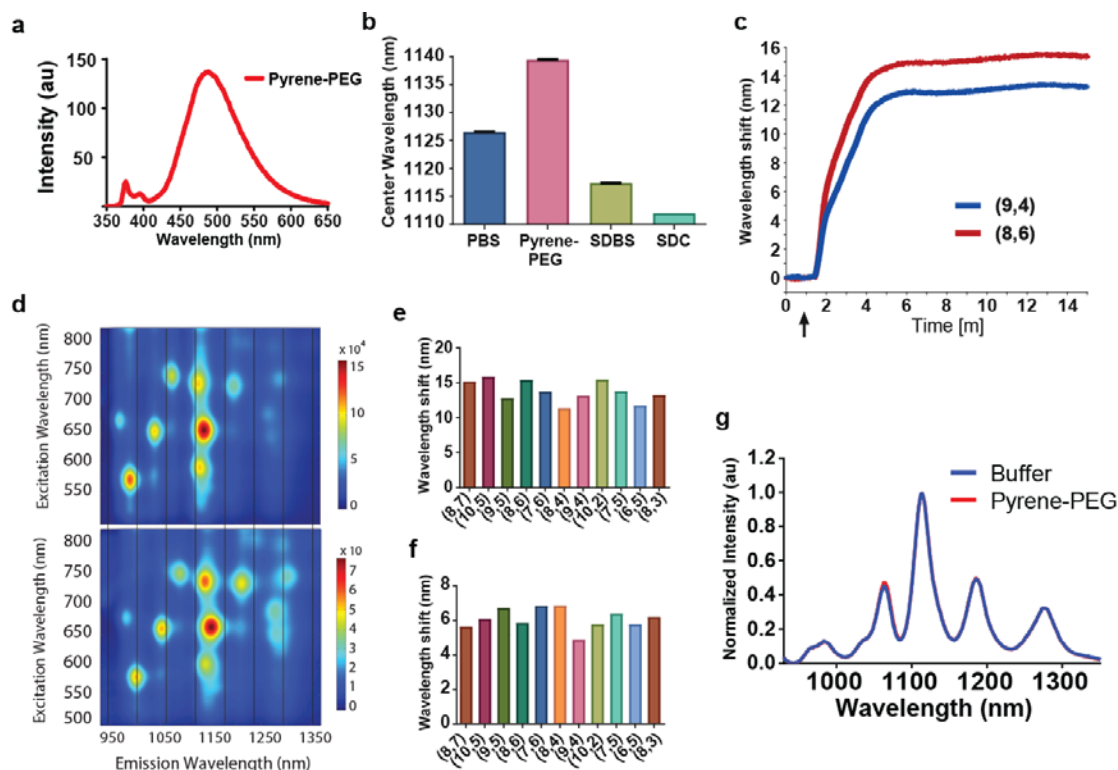
Figure 6.1 Optical effects of Pyrene-PEG on DNA-suspended nanotubes. a,
Polyethylene glycol solubilized pyrene-derivative (pyrene-PEG) fluorescence scan
between 350nm and 650nm with 317 nm excitation. b, Quantified center wavelengths
of DNA-suspended nanotubes treated with buffer control (PBS), pyrene-PEG, sodium
dodecylbenzenesulfonate (0.2% wt/vol), and sodium deoxycholate (0.2% wt/vol) after
overnight incubation. c, Quantified center wavelength overtime for two DNA-
suspended nanotube chiralities, (9,4) and (8,6), after addition of pyrene-PEG
(indicated by arrow). d, PL plots depicting buffer treated DNA-suspended nanotubes
(top) and pyrene-PEG treated nanotubes (bottom). Colors indicate intensity (arbitrary
units). Black vertical lines drawn to aid comparison. e, quantified emission
wavelength shift for 11 chiralities after treatment with pyrene-PEG. f, quantified
excitation wavelength shift for 11 chiralities after treatment with pyrene-PEG. g,
Intensity normalized emission spectra of SDC-suspended nanotubes excited with
730nm laser after treatment with buffer or pyrene-PEG. Error bars represent standard
deviation of technical replicates.

The functionality of the DNA-suspended nanotube-based sensor was assessed in buffer or serum conditions with the addition of pyrene-PEG. The nanotube sensor is based on hybridization with target oligonucleotides and partial desorption from the nanotube surface[34], so we hypothesized that pyrene-PEG may enhance optical changes due to hybridization with target. In both buffer and serum, with all tested conditions, pyrene-PEG greatly red-shifted the nanotubes and prevented any further optical changes from the target oligonucleotide, control non-complementary oligonucleotides, or proteins in the serum (Figure 6.2). The relative affinity of pyrene-PEG for the nanotube surface was tested by pre-treating DNA-suspended nanotubes with SDBS, which produces a distinct blue-shifted shoulder in the emission spectra, followed by addition of pyrene-PEG. The presence of SDBS did not impact the red-shift due to pyrene-PEG (Figure 6.3a), producing similar final emissions as the buffer treated control. There again was no apparent dependence on nanotube chirality (Figure 6.3 b-d).
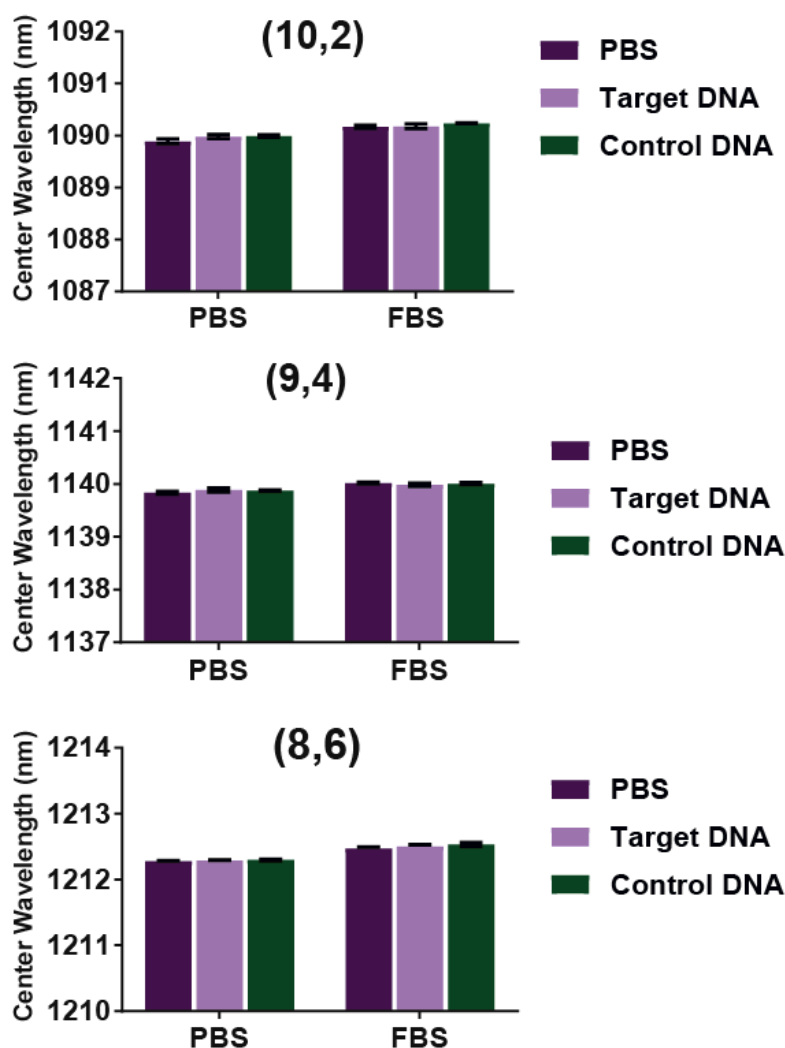
Figure 6.2 Impact of Pyrene-PEG on a DNA-suspended nanotube sensor for a specific oligonucleotide. Quantified center wavelength for the three indicated chiralities of a DNA-suspended nanotube sensor for a specific oligonucleotide sequence treated with target DNA, a non-complementary control sequence, or buffer only vehicle in buffer conditions or whole serum after addition of pyrene-PEG. Error bars represent standard deviation of technical replicates.
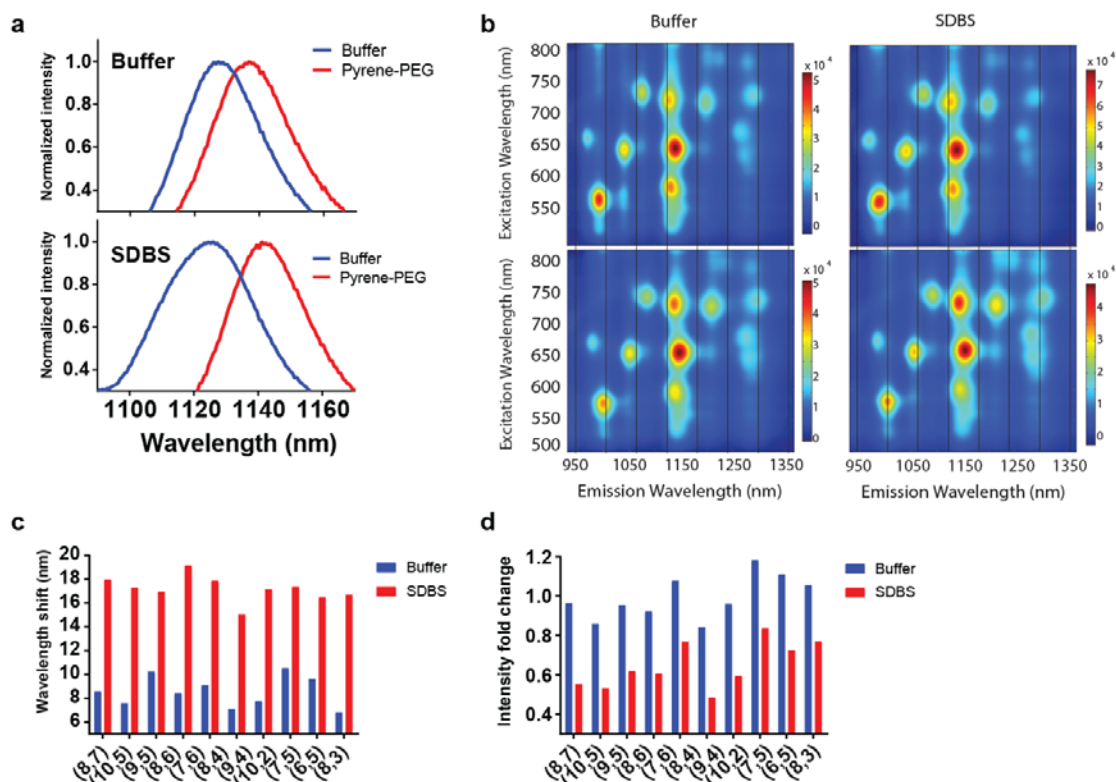
Figure 6.3 Relative affinity of Pyrene-PEG and SDBS. a, Spectra of the (9,4) chirality after treatment with buffer overnight followed by addition of pyrene-PEG (top) or treatment with 0.2% SDBS overnight followed by pyrene-PEG (bottom). Intensity is normalized. b, PL plots of buffer or 0.2% SDBS pre-treatment overnight followed by addition buffer control (top panels) or pyrene-PEG (bottom panels). Colors indicate intensity (arbitrary units). Black vertical lines drawn to aid comparison. c, quantified wavelength shift after pyrene-PEG addition to buffer or 0.2% SDBS pre-treated nanotubes for 10 chiralities. d, intensity fold change after pyrene-PEG addition to buffer or 0.2% SDBS pre-treated nanotubes.

Pyrene is a common by-product of partial combustion of organic material, but does not have the same carcinogenicity as closely related compounds such as benzo[a]pyrene. Benzo[a]pyrene, with one additional fused benzene ring, is metabolized to diol epoxide that intercalates in DNA and covalently binds nucleophilic guanine bases[41]. Pyrene is also observed to be an intercalating agent when made to be water soluble[42]. Because of the strong and rapid affinity of pyrene-PEG for DNA-suspended nanotubes, but not for SDC-suspended nanotubes, we hypothesized that the observed red-shifting from pyrene-PEG may be due to its intercalating properties. To test this, a panel of other known DNA intercalating agents was tested in equi-molar amounts with DNA-suspended nanotubes (Figure 6.4a). Three of the compounds, ethidium bromide, SYBR green, and Hoechst 33258 are used to measure DNA content by fluorescent changes after intercalating. Doxorubicin, a chemotherapy drug, is an effective agent against rapidly dividing cells due in part to its affinity for DNA. Pyrene-PEG was included as reference. Each agent produced greatly red-shifted emission similar to pyrene-PEG, except for Hoechst 33258 which was slightly less effective (Figure 6.4b). The emission intensity for most agents was reduced to varying degrees, with doxorubicin and ethidium bromide producing the greatest loss of intensity (Figure 6.4c).

Because of the potential clinical utility of an optical sensor for doxorubicin, we focused on doxorubicin to further characterize its interaction. We tested whether DNA-suspension is necessary for detection by adding doxorubicin to SDC-suspended nanotubes. Like pyrene-PEG, there was no change (Figure 6.4d). We next tested the relative affinity by again pre-treating DNA-suspended nanotubes with SDBS and adding doxorubicin. The SDBS effectively prevented red-shifting by doxorubicin, and

the spectral emission character from bound SDBS persisted (Figure 6.4e). We

conclude that compared to pyrene-PEG, the affinity of doxorubicin is not as strong.
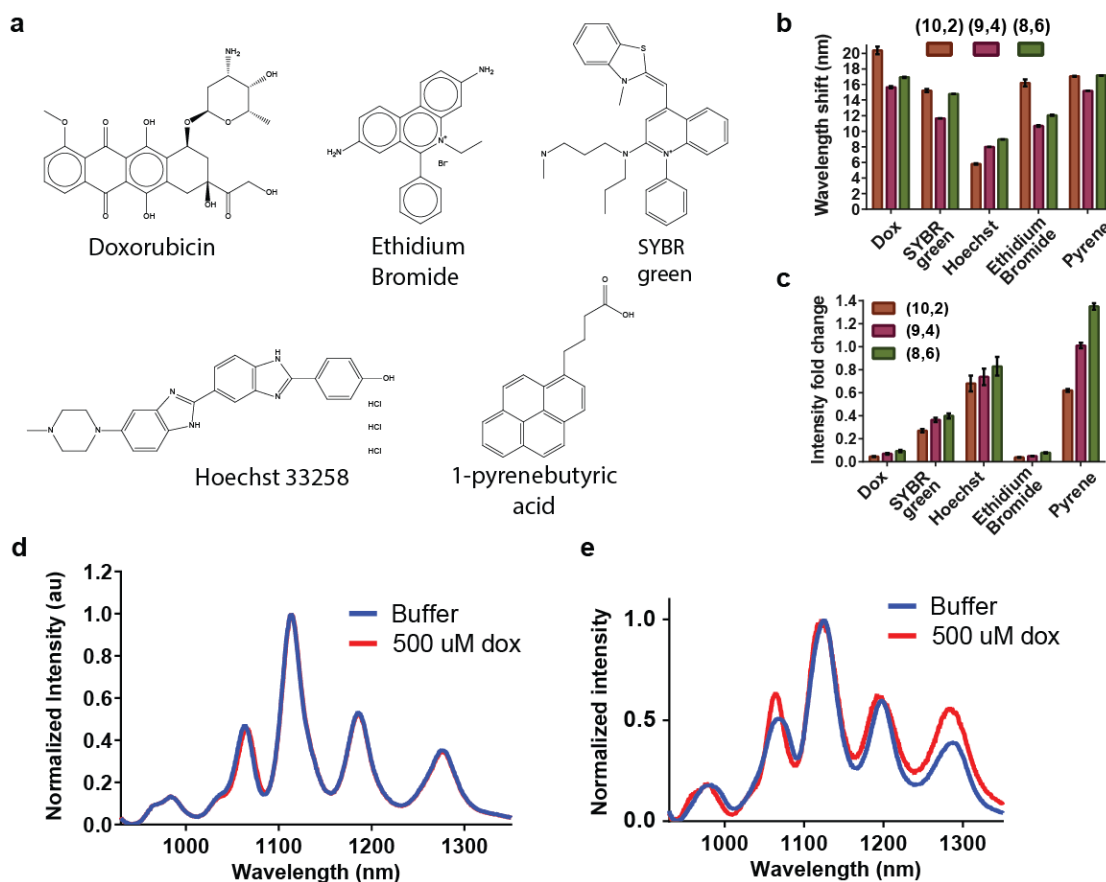
Figure 6.4 Interaction of DNA intercalating agents with DNA-suspended nanotubes.
a, structures of the five DNA-intercalating agents tested. b, wavelength shift relative to
a buffer treated control for three chiralities after addition of 1 uM of the indicated
compound. c, corresponding intensity fold change relative to buffer treated control for
three chiralities after addition of 1 uM of the indicated compound. d, Intensity
normalized emission spectra of SDC-suspended nanotubes excited with 730nm laser
after treatment with buffer or doxorubicin. e, Intensity normalized emission spectra of
0.2% SDBS pre-treated DNA-suspended nanotubes after treatment with buffer or
doxorubicin. Error bars represent standard deviation of technical triplicates.

Quantitative sensing behavior was assessed by measuring DNA-suspended nanotube emission changes from a serial dilution of doxorubicin. For most chiralities, there was dose-dependent red-shifting from 500 nM to 50 uM, after which there was no additional red-shift (Figure 6.5a). Intensity quenching closely matched the wavelength shifting behavior, but for most chiralities quenching was detectable before any major red-shifting (Figure 6.5b). The kinetics of wavelength shifting and intensity change was measured for three nanotube chiralities after addition of doxorubicin at time 0m (Figure 6.5c). The kinetics of wavelength shifting was relatively rapid, with the majority of the changes taking place before the spectra could be acquired. Intensity changes were almost immediate, with most of the dynamics unable to be captured. We next tested if quantitative sensing of doxorubicin was possible in complex biological solutions such as serum. We have previously reported that serum non-specifically red-shifts nanotubes and prevents functionality of a DNA-suspended nanotube sensor, due to electrostatic interactions with serum proteins. Using serum, we repeated the dose-response experiment to see if doxorubicin could still be detected. For the measured chiralities, dose-dependent red-shifting (Figure 6.5d) and intensity quenching (Figure 6.5e) were observed, although with less sensitivity compared to buffer only conditions. This may be due to doxorubicin binding serum proteins [43].
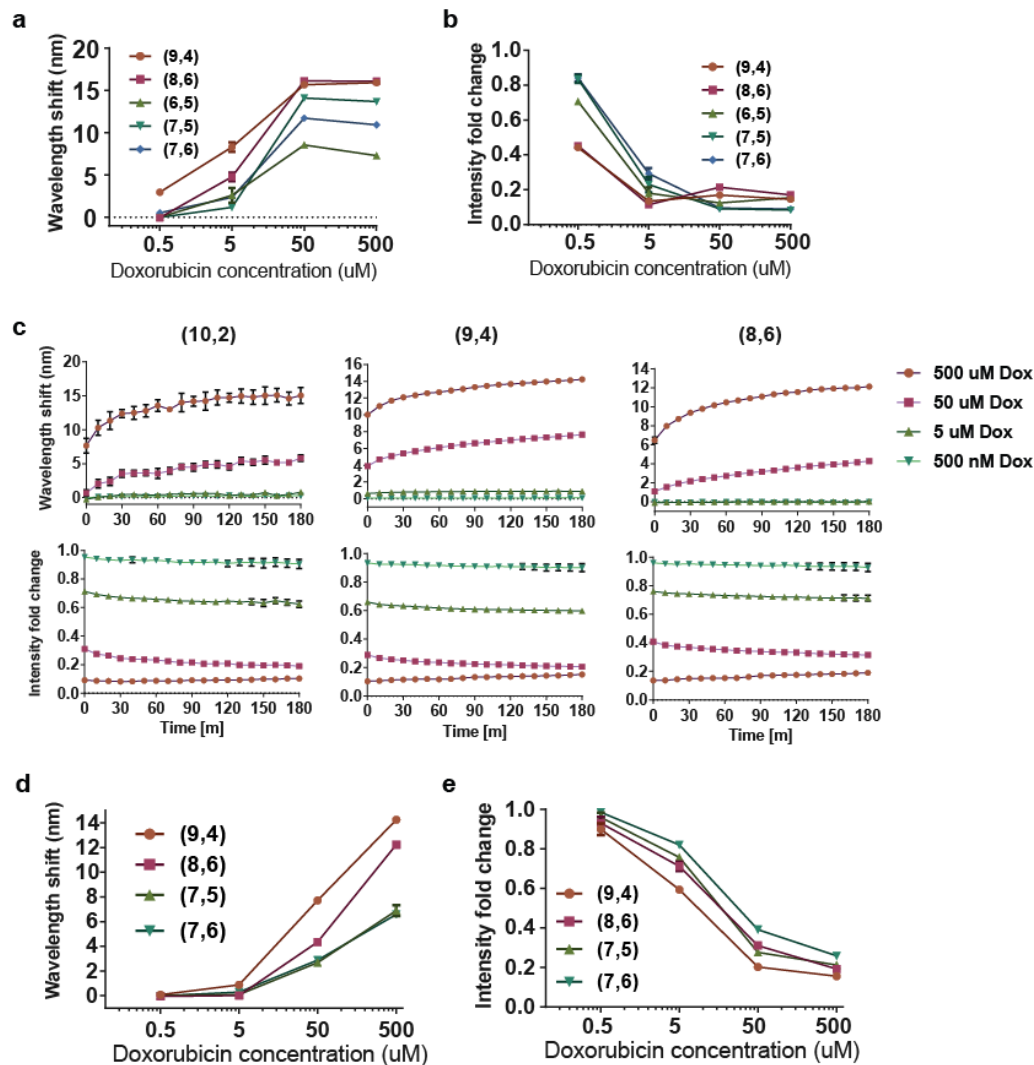
Figure 6.5 Sensitivity and kinetics of doxorubicin-induced optical changes. **a**, Quantified center wavelength shift of 5 nanotube chiralities as a function of doxorubicin concentration in buffer conditions. **b**, intensity fold change relative to buffer treated control for 5 nanotube chiralities as a function of doxorubicin concentration in buffer conditions. **c**, Kinetics of wavelength shifting (top panels) and intensity changes (bottom panels) for the three indicated nanotube chiralities after addition of the four indicated concentrations of doxorubicin at time 0 minutes. **d**, Quantified center wavelength shift of 5 nanotube chiralities as a function of doxorubicin concentration in whole serum. **e**, Intensity fold change relative to buffer treated control for 5 nanotube chiralities as a function of doxorubicin concentration in whole serum. Error bars represent standard deviation of technical triplicates.

Mechanistic studies were undertaken to better understand how doxorubicin may be eliciting the observed optical changes. In buffer conditions, added doxorubicin produces visible flocculation. Dynamic light scattering of the DNA-suspended nanotubes in buffer alone or with doxorubicin show that with doxorubicin, the correlation of signal takes a longer time to decay. By the time the correlation coefficient decays to 0 for the buffer treated control, the correlation coefficient for the doxorubicin treated sample is just beginning to change, consistent with the presence of large aggregates (Figure 6.6a). We hypothesized that the quenching of intensity may be due to aggregation with metallic nanotubes, which can provide a non-radiative decay pathway excited nanotubes[26]. Using (8,4) chirally pure, $(GT)_{20}$ suspended nanotubes[44], which do not contain metallic nanotubes, we measured the optical response after addition of doxorubicin. Severe quenching was observed, making background fluorescence from doxorubicin prominent in the spectra (Figure 6.6b, left); however, enough nanotube emission was collected to reveal a red-shift of approximately 8 nm (Figure 6.6c). Reducing agents such as the soluble vitamin E analog Trolox have been reported to increase the fluorescent intensity of DNA-suspended single-walled carbon nanotubes[45]. Using a concentrated solution of Trolox, we spiked some into the doxorubicin treated sample. After allowing 15 minutes of equilibration, spectra was again acquired revealing modest intensity restoration from the doxorubicin quenched nanotubes (Figure 6.6b, right). Trolox had negligible effect on the center wavelength (Figure 6.6c). An absorbance spectrum from 400 nm to 1350 nm was measured for the buffer treated control and the doxorubicin treated sample (Figure 6.6d). Doxorubicin absorbs strongly at 500 nm, complicating analysis of the E_{22} transition. The peak corresponding to E_{11} showed red-shifting and bleaching[46] after treatment with doxorubicin. We conclude that metallic nanotubes are not a likely source of quenching, even though doxorubicin causes flocculation.
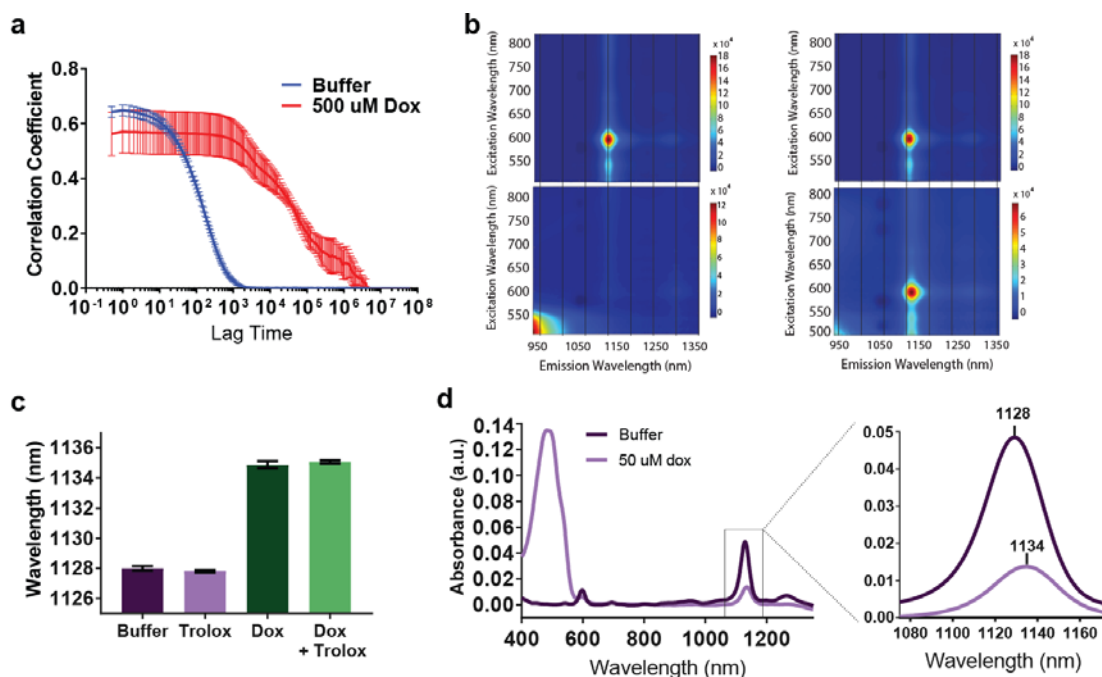
Figure 6.6 Assessment of the role of flocculation and purity of nanotube preparations on optical changes. a, Correlation coefficient overtime as calculated from dynamic light scattering for three trials of buffer treated and doxorubicin treated DNA-suspended nanotubes. b, GT20 suspended, (8,4) purified chirality after treatment with buffer (top panels) or 50 uM doxorubicin without the reducing agent Trolox (bottom left) or addition of Trolox (0.2 mg/mL) (bottom right). Colors indicate intensity (arbitrary units). Black vertical lines drawn to aid comparison. c, quantified wavelength of GT20 suspended purified (8,4) after treatment with buffer, 0.2 mg/mL Trolox, 50 uM doxorubicin, or 50 uM doxorubicin with 0.2 mg/mL Trolox. d, Absorbance scan of buffer or 50 uM doxorubicin treated GT20 suspended purified (8,4), with inset depicting the center wavelength of the absorbance peak. Error bars represent standard deviation

226

We hypothesized that DNA intercalating agents such as doxorubicin displace the DNA suspending the nanotube by competing for interaction with the adsorbing nucleotide bases. To measure DNA displacement, we treated DNA-suspended nanotubes with buffer, doxorubicin, or SDC, followed by spin filtration through 100 kDa membranes to allow flow through of displaced DNA but not of nanotubes. The flow through was then measured for absorbance at 260 nm to quantify the amount of DNA present (Figure 6.7a). The sample treated with buffer produced no signal with the absorbance spectrometer. SDC, which is known to displace DNA[40], was included as a positive control and produced detectable levels of DNA. Doxorubicin also produced some signal, but comparison of the complete absorbance spectra revealed a large degree of noise. To overcome the difficulty in measuring the intrinsic absorbance of DNA, we suspended carbon nanotubes with Cy5-labeled DNA. Cy5 is a fluorophore that absorbs strongly at 650nm and appears blue to the naked eye. After suspending nanotubes with the Cy5-conjugated DNA, we added doxorubicin and measured nanotube emission to verify that Cy5 did not impact nanotube sensitivity to doxorubicin. As expected, the nanotubes red-shifted with doxorubicin (Figure 6.7b), up to 17 nm in some cases (Figure 6.7c). We subjected the Cy5-DNA suspended nanotubes to buffer, doxorubicin, or SDC treatment followed by spin filtration. The sample treated with SDC resulted in a flow through that had a blue-appearance, while the buffer treated sample was clear (Figure 6.7d). The doxorubicin treated sample had a slight red tint, likely from unbound doxorubicin. Absorbance scans were taken to measure Cy5 absorbance from the flow through in all three conditions (Figure 6.7e). The SDC treated sample produced a strongly absorbing peak centered at 650nm. The buffer and doxorubicin treated samples did not produce any peak. Finally we treated Cy5-DNA suspended nanotubes with doxorubicin, and measured the flow through. We then added SDC directly to the doxorubicin treated nanotubes, and again measured

227

the flow through (Figure 6.7f). We again observed that only after treatment with SDC did the flow through produce the characteristic Cy5 absorbance peak. Control experiments were run to assess the effect of SDC and doxorubicin on Cy5 absorbance by using a pure sample of Cy5-conjugated DNA mixed with each component. Both SDC (Figure 6.7g) and doxorubicin (Figure 6.7h) had only a minor effect on the absorbance, validating our approach. We conclude that doxorubicin does not displace the DNA suspending the nanotube to a significant degree.
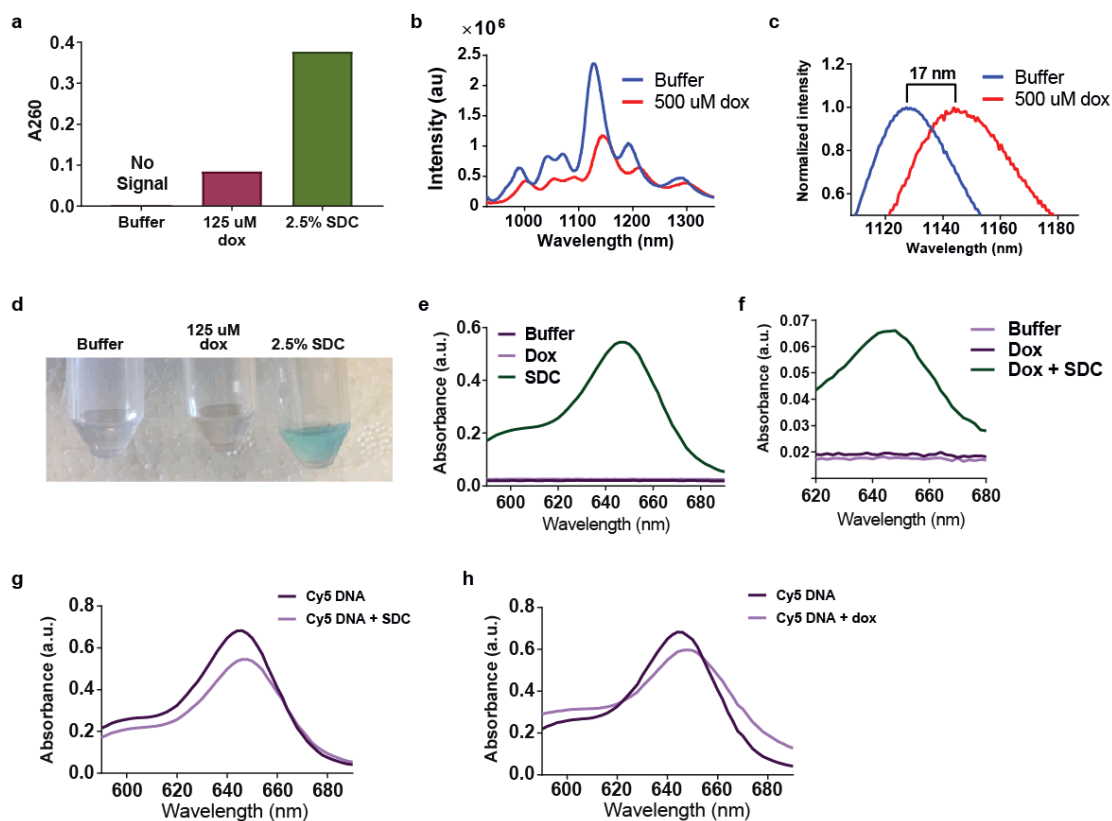
Figure 6.7 Stability studies of DNA suspended nanotubes treated with doxorubicin.
a, Absorbance measurements at 260 nm for flow through after treatment of DNA-suspended nanotubes with buffer, 125 uM doxorubicin, or 2.5% SDC. Buffer treated sample flow through could not be quantified. b, Emission spectra of Cy5- DNA suspended nanotubes after treatment with buffer or treatment with 500 uM doxorubicin. c, Normalized intensity and wavelength shift of buffer treated sample versus 500 uM doxorubicin treated sample. Different (17nm) is indicated between the peaks. d, Appearance of flow through after treatment of Cy5-DNA-suspended nanotubes with buffer, 125 uM doxorubicin, or 2.5% SDC. e, Absorbance scan of flow through depicted in panel d. f, Absorbance of flow through from same sample treated first with buffer, then with 125 uM doxorubicin, then with 2.5% SDC. g, absorbance scan of pure Cy5-DNA and Cy5-DNA with 2.5% SDC. h, absorbance scan of pure Cy5-DNA and Cy5-DNA with 500 uM doxorubicin.

We next attempted to measure the quantity of doxorubicin that binds to DNA-suspended nanotubes. A known mass of $(GT)_{15}$ suspended nanotubes was added to 500 uM doxorubicin, and an equal volume of buffer was added to a control. After incubation, the samples were centrifuged to pellet the flocculated nanotubes (Figure 6.8a), and a sample of the supernatant was assayed for doxorubicin using an absorbance scan (Figure 6.8b). The difference in absorbance was compared to a doxorubicin standard curve (Figure 6.8c), and used to estimate the mass of doxorubicin lost from solution due to binding the nanotubes. From this data we estimate that 1 ug of $(GT)_{15}$ suspended nanotubes binds to 0.95 ug of doxorubicin. This is less than previous reports of doxorubicin loading on phospholipid-PEG suspended nanotubes, which calculated a 4:1 ratio of doxorubicin to carbon nanotube by mass[37]. Here, they estimated the phospholipid-PEG coating to cover only 10% of the nanotube surface, which may explain the difference we observed with DNA. We next attempted to wash away the bound doxorubicin by pelleting the sample, aspirating the supernatant, and adding 100 uL of buffer and vortexing. This was performed three times, with the supernatant extracted for absorbance measurements after each wash (Figure 6.9a). The first wash released some doxorubicin from the nanotubes, giving the supernatant a red hue. The following washes did not change color, but the nanotube pellet appeared to have a red tint. Based on comparing the absorbance of the supernatant from each wash (Figure 6.9b) to the standard curve, we calculated that about 0.35 ug of doxorubicin was returned to solution by washing. We conclude that 0.6 ug of doxorubicin binds to 1 ug of $(GT)_{15}$ suspended nanotubes strongly enough to resist desorption from pelleting and washing. The average length of carbon nanotubes that results from our suspension process is 166 nm[47]. The mass of nanotube this length (estimated using the (6,5)) is 3×10^{-19} g[48]. Thus, for one nanotube, we calculate that approximately 180 molecules of doxorubicin bind strongly. The

emission spectra from the nanotubes after treatment with buffer, 500 uM dox, or 500 uM dox followed by three washes was acquired to assess the impact of washing on the nanotube optical response to doxorubicin (Figure 6.9c). We observed that the emission spectrum was largely unaltered by washing as compared to the sample that received 500 uM dox without pelleting and washing (Figure 6.9d). We conclude that 0.6 ug of dox binds nearly irreversibly to 1 ug of $(GT)_{15}$ suspended nanotubes, and is responsible for the observed nanotube emission changes. Additional doxorubicin that is less strongly bound does not appear to contribute further to the optical changes, as removal of the less strongly bound doxorubicin had little impact on the nanotube emission.
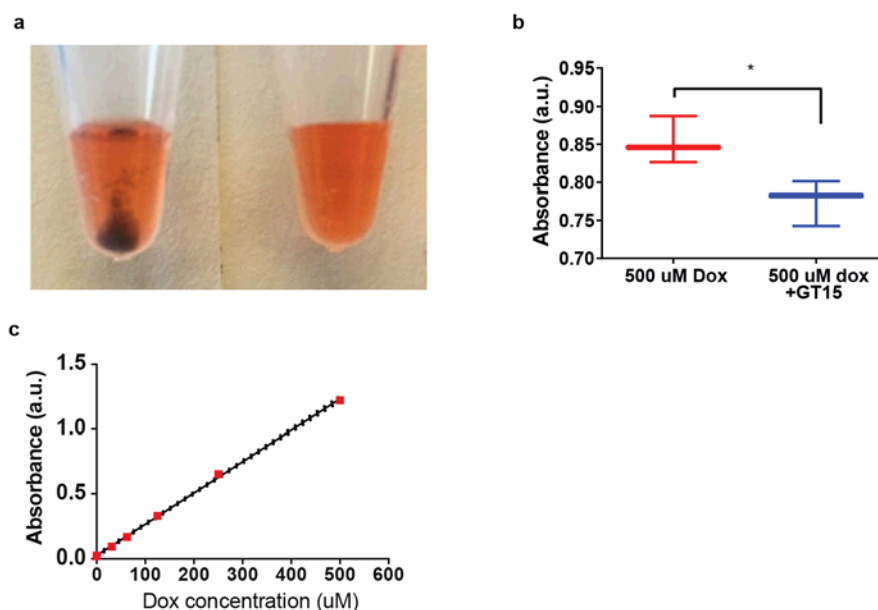
Figure 6.8 Quantitative measurements of doxorubicin affinity for DNA-suspended nanotubes. Image of 500 uM doxorubicin with DNA-suspended nanotubes or buffer vehicle after centrifugation. b, Absorbance of supernatant from buffer treated doxorubicin sample and nanotube-treated doxorubicin sample for three independent measurements. Error bars represent standard deviation. Significance determined with t-test; p = 0.0354 c, Standard curve of doxorubicin absorbance as a function of concentration. Measurements taken in triplicate. Black solid line represents fit to linear regression Y = 0.002424*X + 0.0212. Error bars representing standard deviation were too small to render.
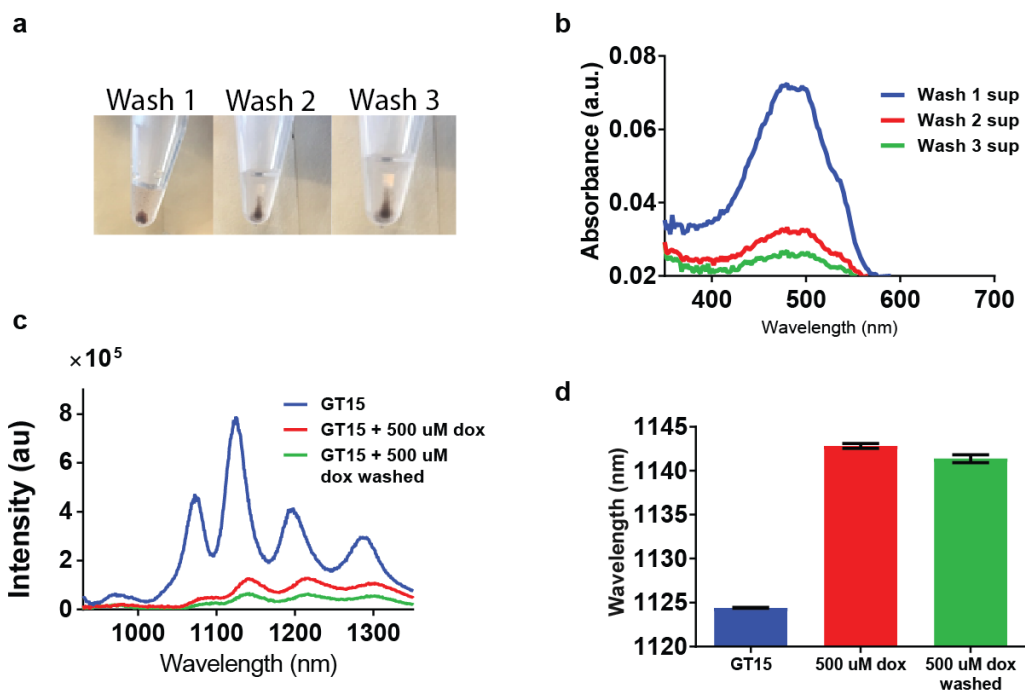
Figure 6.9 Persistence of spectral changes after washing. a, images of supernatant of doxorubicin treated DNA-suspended nanotubes after centrifugation and washing with 100 uL of buffer. b, absorbance scan of the wash supernatant corresponding to the image in panel a. c, Emission spectra of DNA-suspended nanotubes with buffer treatment (blue), 500 uM doxorubicin (red), or 500 uM doxorubicin after three washes (green). d, Quantified center wavelength of the (9,4) chirality after treatment with buffer (blue), 500 uM doxorubicin (red) or 500 uM doxorubicin followed by three washes (green). Error bars represent standard deviation.

Single-nanotube responses to doxorubicin were assessed in buffer conditions and in serum conditions. DNA-suspended nanotubes were added to a lysine-coated glass bottom plate and allowed to incubate for 10m before washing and replacing the buffer. Single-nanotubes were apparent on the surface according to broadband image acquisition (as diffraction limited dots) and hyperspectral measurements (Figure 6.10a). Spectra of the (9,4) nanotubes were acquired before and after addition of a buffer vehicle control or concentrated doxorubicin to a final concentration of 50 uM. After 10m of incubation the spectra were acquired again and the shift of each individual nanotube calculated. Treatment with doxorubicin produced a significant (****) wavelength shift of 11.6 nm ± 1.5 nm (Figure 6.10b). The spectra from buffer treated and doxorubicin treated single nanotubes were averaged together into a composite spectrum (Figure 6.10c, d). The average spectra of the single nanotubes largely recapitulated the spectra seen in solution phase, with a magnitude of shift approaching that seen in solution (15.6 nm in solution compared to 11.6 nm when single nanotubes are averaged). We next measured the before and after spectra of single (9,4) nanotubes after treatment with buffer or doxorubicin in whole serum. The shift of each measured nanotube was calculated before and after treatment with buffer or doxorubicin. A significant (****) shift compared to buffer was again observed, with an average red-shift magnitude of 7.7 ± 0.9 nm (Figure 6.10e). The averaged shift from single nanotubes closely recapitulates the shift seen in solution phase with serum of 7.8 nm.
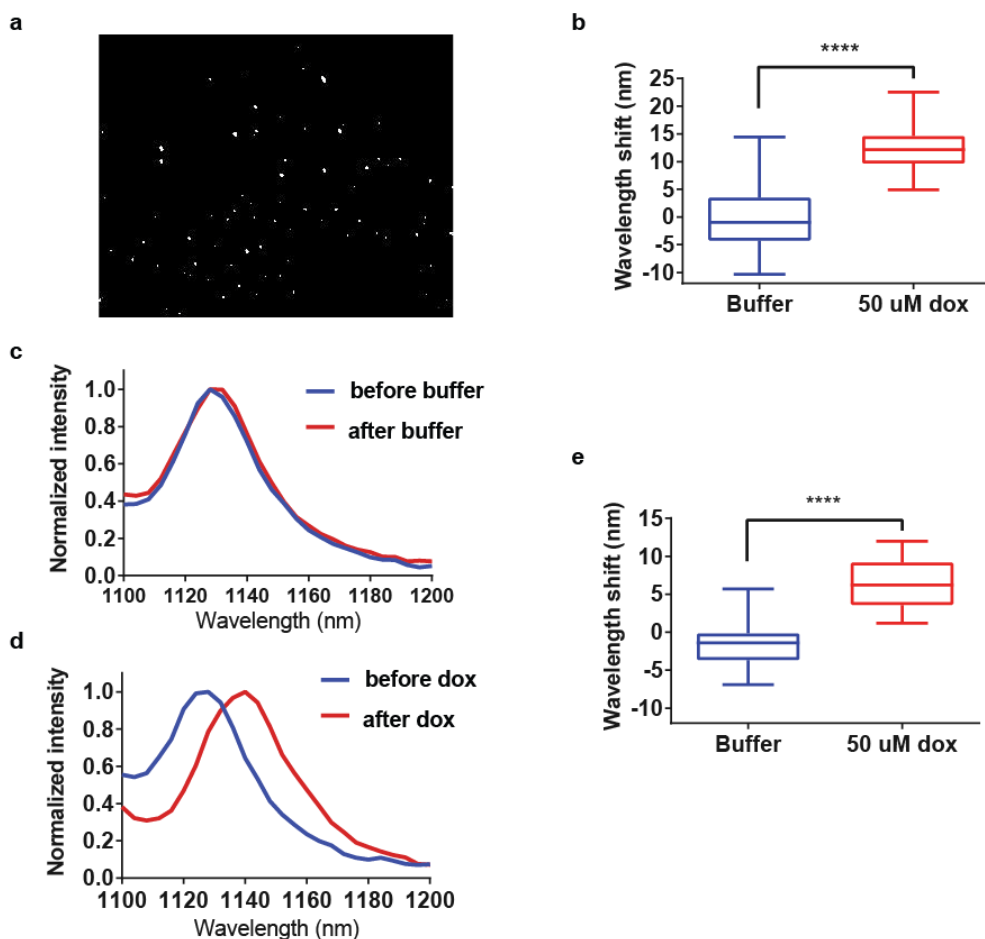
Figure 6.10 Single-nanotube measurements after doxorubicin treatment in buffer and whole serum. a, representative image of carbon nanotubes on the surface of a lysine-coated glass bottom plate in buffer before any treatment. b, Wavelength shift of single nanotubes in buffer treated with buffer or 50 uM doxorubicin. Differences were pooled for each condition in the box and whisker plot. Statistical significance calculated with unpaired t-test. Buffer n=36, 50 uM dox treatment n=19. c, composite spectra of all single nanotube spectra before and after buffer. d, composite spectra of all single nanotube spectra before and after 50 uM dox. E, Wavelength shift of single nanotubes in whole serum treated with buffer or 50 uM doxorubicin. Differences were pooled for each condition in the box and whisker plot. Statistical significance calculated with unpaired t-test. Buffer n= 18, 50 uM doxorubicin n = 28.

Because doxorubicin is able to elicit an optical response in complex protein environments, we tested whether doxorubicin could be detected by nanotubes inside of cells. (GT)$_{15}$ suspended nanotubes were incubated with the RAW 264.7 murine macrophage cell line overnight. Nanotubes are internalized via phagocytosis[49], and the nanotubes remain localized in phagocytic vesicle in the cell. Cell viability is unaffected by this treatment[50, 51]. White light images showed normal cell morphology (Figure 6.11a), and broadband images revealed punctate spots of nanotube filled vesicles inside most of the cells (Figure 6.11b). Three cohorts of cells were treated with 500 uM doxorubicin or buffer control and incubated 1h, after which the nanotubes were measured via hyperspectral cubes, focusing on the (9,4) chirality. Spectra from the three cohorts in each condition were averaged and quantified. Treatment with 500 uM dox elicited a red-shift of approximately 7.9nm (Figure 6.11c). This is less than what would be expected in solution phase in serum (~14nm), and may be due to sequestration of doxorubicin to other cell material.
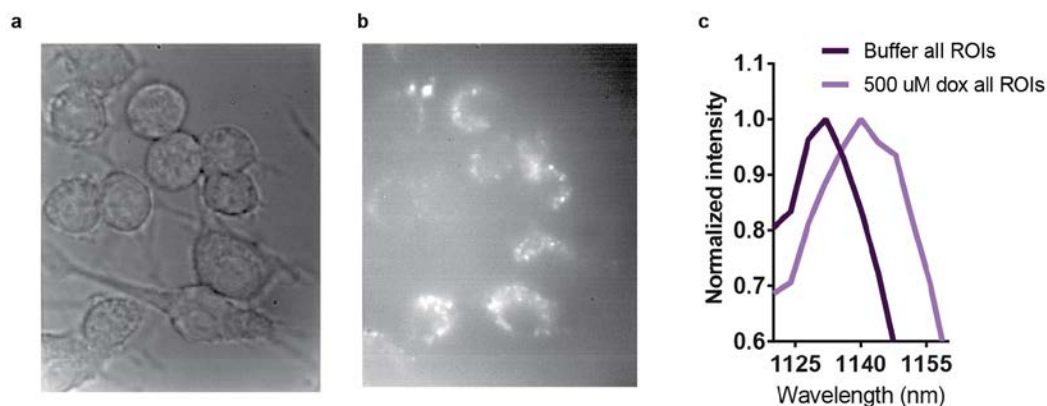
Figure 6.11 Response of internalized nanotubes after treatment with doxorubicin. a, White light image of macrophage cell line on glass surface. b, broadband nanotube emission under 730 nm excitation corresponding to the region of interest depicted in panel a. c, Averaged spectra after selecting nanotube emissive spots in cells treated with buffer or treated with 500 uM doxorubicin. Each condition represents three separate runs and approximately 50 cells.

To make an implantable sensor for doxorubicin, three different materials with precedent for use were tested. We first tested a suspension of DNA-suspended nanotubes in an agarose gel. Testing *in vitro* showed that the kinetics were unaffected by gel encapsulation, with maximal red-shifting and intensity quenching by 10 minutes. Agarose gel is known to prevent nanotubes from aggregating[52], providing additional evidence that aggregation is not the source of the quenching. The doxorubicin treated agarose gel (about 20 uL volume) was dialyzed in 50 mL of DI water with three changes, where the last change was allowed to proceed overnight. The red-shift was not reversed by the dialysis, consistent with the inability to wash away doxorubicin in previous experiments (Figure 6.12a). Another hydrogel, alginate, was tested due to its ease of use and precedent for use *in vivo* with suspended nanotubes for sensing applications[33]. Again, we observed red-shifting and quenching in response to doxorubicin, making this hydrogel a potential implantation material (Figure 6.12b). Lastly, we tested an implantable membrane where a nanotube solution can be heat-sealed inside as we have previously reported[34]. An in vitro dose-response assessment produced a surprising pattern, where concentrations above 5 uM doxorubicin red-shifted and recovered some of the intensity loss, even to levels brighter than baseline for some chiralities (Figure 6.12c). When the dialysis membranes were tested *again in vitro* in whole serum, we noted a similar phenomenon, but with the maximal quenching taking place at 50 uM rather than 5 uM, consistent with the penalty in sensitivity from detection in solution phase in serum (Figure 6.12d). To better understand the surprising restoration of intensity with higher concentrations of doxorubicin using the dialysis membrane, more concentrations were tested closer to 5 uM and more dilute than 5 uM. We observed that the wavelength did not shift at concentrations less than 1 uM. However, before the red-shift could be detected, the intensity begins to drop. Beyond about 5 uM, the intensity begins to restore to levels

236

comparable to untreated controls (Figure 6.13a). While analyzing the wavelength shift of carbon nanotubes has several advantages as a sensor output for an implantable sensor, it is also possible to make use of ratiometric intensity changes to control for factors that could change absolute intensity, such as tissue irregularities. Thus, we measured the intensity ratio of two nanotubes, the (9,4) and the (8,7), to test if ratiometric quenching could be measured in concentration regimes below 5 uM. Indeed, we found that ratiometric sensing could improve our threshold of detection to between 50 and 500 nM (Figure 6.13b).
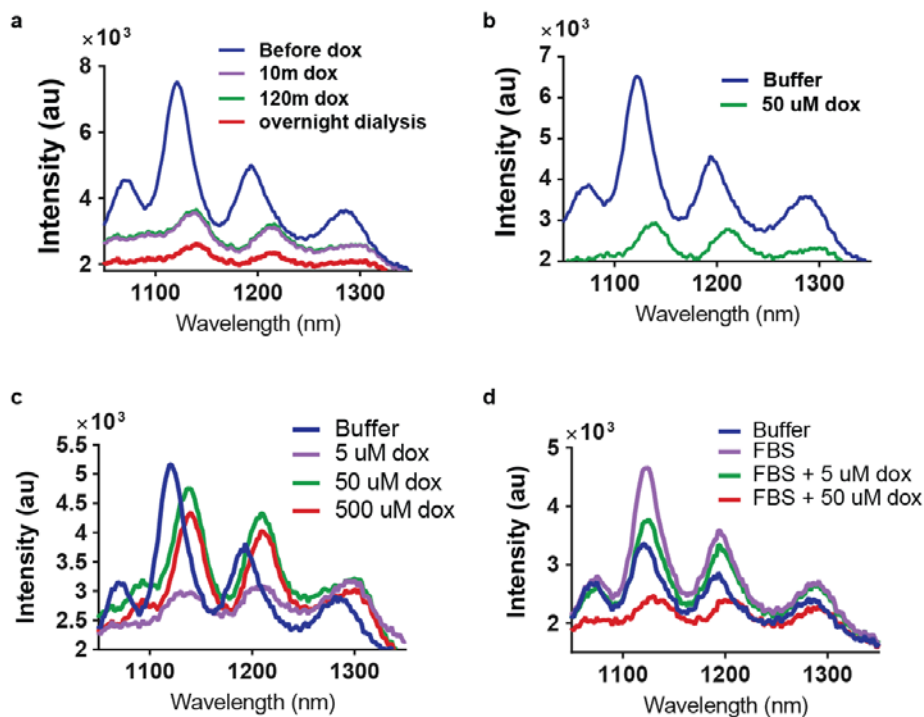
Figure 6.12 Hydrogel and dialysis based device responsivity in vitro. a, DNA-suspended nanotubes cast in 4% wt/vol agarose gel before treatment with doxorubicin, 10 minutes after treatment with 50 uM doxorubicin, and 120 minutes after treatment with 50 uM doxorubicin. Red line represents spectra after dialysis overnight with three dialysate changes. b, Alginate spheres (6% wt/vol) with DNA-suspended nanotubes after overnight treatment with buffer or 50 uM doxorubicin. c, Emission spectra from DNA-suspended nanotubes in a heat sealed implantable semi-permeable membrane after overnight incubation with escalating doses of doxorubicin in buffer. d, Emission spectra from DNA-suspended nanotubes in a heat sealed implantable semi-permeable membrane after overnight incubation with escalating does of doxorubicin in whole serum (FBS). A control sample was incubated in buffer only (blue).
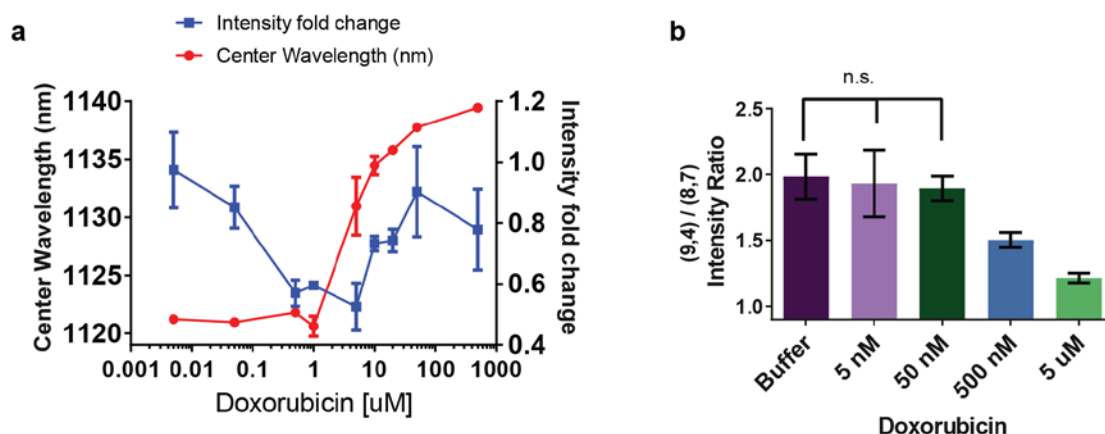
Figure 6.13 Wavelength shifting and intensity changes of DNA-suspended nanotubes as part of an implantable membrane tested in vitro. Center wavelength (red line, left y-axis) and intensity fold change (blue, right y-axis) of the (9,4) nanotube in a heat sealed implantable semi-permeable membrane after overnight incubation with the indicated concentration of doxorubicin. b, Intensity ratio of the (9,4) and (8,7) nanotube in a heat sealed implantable semi-permeable membrane for concentrations less than 5 uM doxorubicin. All error bars represent standard deviation of three implants tested *in vitro*. Test of significance was done using t-test. Only non-statistically significance differences are labeled in b; 500 nM and 5 uM are significantly different than the buffer treated control.

Because earlier experiments suggest that doxorubicin binding is largely irreversible, an implantable carbon nanotube-based sensor may be useful for cumulative sensing. We hypothesized that the optical changes from overnight incubation in 10 mL of 5 uM will be equivalent to overnight incubation in 1 mL of 50 uM, since in both cases the total mass of doxorubicin is 29 ug. We prepared DNA-suspended nanotubes in implantable devices and incubated them overnight in 1 mL of buffer, 1 mL of 5 uM doxorubicin, or 1 uL of 50 uM doxorubicin to serve as controls. Concurrently, we incubated devices overnight in 1 mL of 5 uM doxorubicin and 10 mL of 5 uM for an experimental group. The controls behaved as expected, where 5 uM doxorubicin

238

treatment induced red-shifting and maximal quenching while 50 uM dox further red-shifted the nanotubes and restored intensity (Figure 6.14a). In the experimental group, 5 uM dox in 1 mL again induced red-shifting and maximal quenching; however, 5 uM in 10 mL produced a spectrum that was nearly identical to incubation in 1 mL of 50 uM doxorubicin (Figure 6.14b). We quantified the center wavelength (Figure 6.14c) and intensity (Figure 6.14d) for the (9,4) nanotube and found that the values were not different in a statistically significant way.
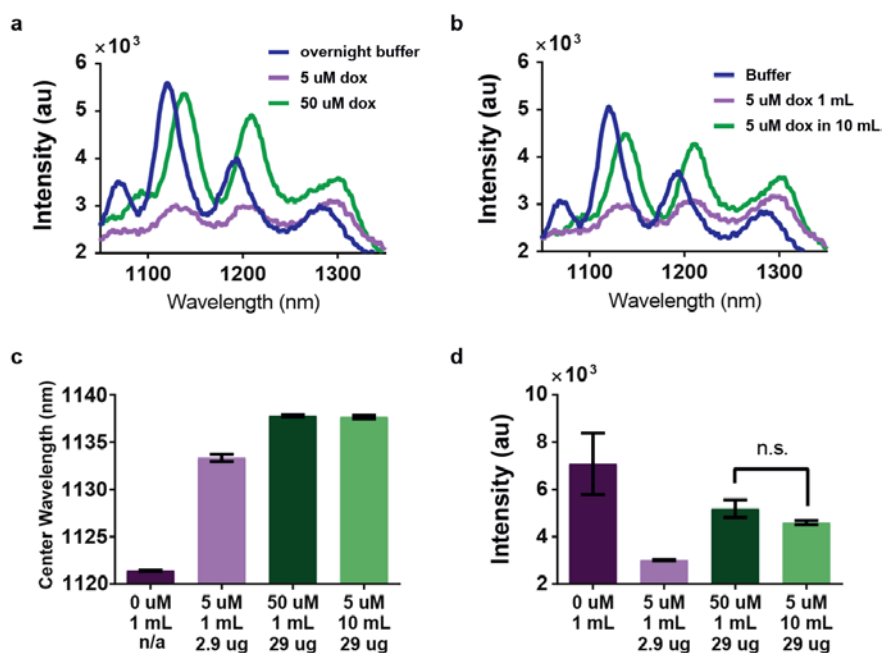
Figure 6.14 Test of cumulative sensing in vitro. A, emission spectra of DNA-suspended nanotubes in implantable membrane device after incubation in 1 mL of buffer, 5 uM doxorubicin, or 50 uM doxorubicin. b, Emission spectra of DNA-suspended nanotubes in implantable membrane device after overnight incubation in 1 mL of buffer, 1 mL of 5 uM doxorubicin, or 10 mL of 5 uM doxorubicin. c, Quantification of the (9,4) center wavelength from spectra in panels a and b with doxorubicin concentration, volume, and total mass doxorubicin listed below. d, Intensity corresponding to the data in panel c. No significant difference in intensity between incubation in 1 mL of 50 uM doxorubicin or 10 mL of 5 uM doxorubicin. Error bars represent standard deviation of three measurements.

Using the dialysis membrane device for implantation, we surgically placed the device into the peritoneum of mice as previously described[34]. After allowing the animals to awaken and become ambulatory for an hour, they were again anaesthetized with isoflurane and fluorescence measurements of the implanted carbon nanotubes were taken through the skin with a laser probe apparatus as previously described[34]. Following measurement, an intraperitoneal injection of 1 mL of doxorubicin was administered, and the mice were again allowed to awaken and become ambulatory. After 30m, the mice were again anaesthetized and the nanotube implant was measured. Injected doxorubicin produced the expected red-shift and intensity quenching (Figure 6.15a, representative spectra).

We next repeated the experiment, but measured the carbon nanotube implant continuously (with 0.5s exposures) to measure the kinetics of doxorubicin binding immediately after injection. Initial spectra were acquired, followed by injection of doxorubicin into peritoneum. The (8,6) nanotube was monitored over the course of the experiment. Initial quenching was observed (Figure 6.15b), followed by red-shifting (Figure 6.15c) at approximately 4 minutes. The mouse was periodically monitored (gaps in data) for any laser induced damage to the skin, but none was noted. The threshold of detection *in vivo* was measured by surgically implanting the nanotube sensor device into four mice, and injecting either buffer, 5 uM dox, 50 uM dox, or 500 uM dox. For both the (9,4) and (8,6) nanotube, significant red-shifting was observed for both the 50 uM and 500 uM doxorubicin injection, but not for 5 uM (Figure 6.16a, b). An examination of the implantable devices *ex vivo* corroborates the *in vivo* data (Figure 6.16c, d). Detection of 50 uM doxorubicin, but not 5 uM doxorubicin, is consistent with the dose response data taken in whole serum.
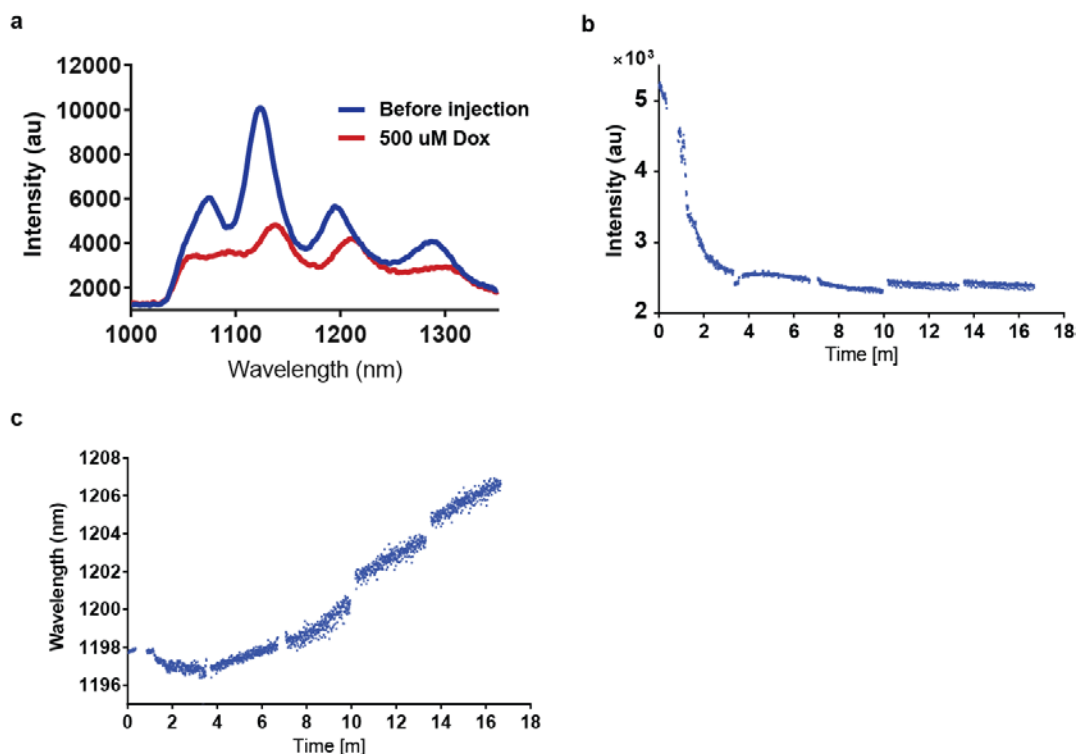
Figure 6.15 Implanted sensor response and kinetics to injected doxorubicin.
Emission spectrum of implanted membrane device before injection of doxorubicin and
30m after intraperitoneal injection of 1 uL uM doxorubicin. b, Intensity of implanted
nanotube device measured for the (8,6) in real-time after intraperitoneal injection of 1
mL doxorubicin at time 0 minutes. c, center wavelength of the (8,6) nanotube device
measured in real-time after intraperitoneal injection. Kinetics data was taken every 0.5
second for the duration of the experiment. Gaps in data are from periodic monitoring
of the mouse.
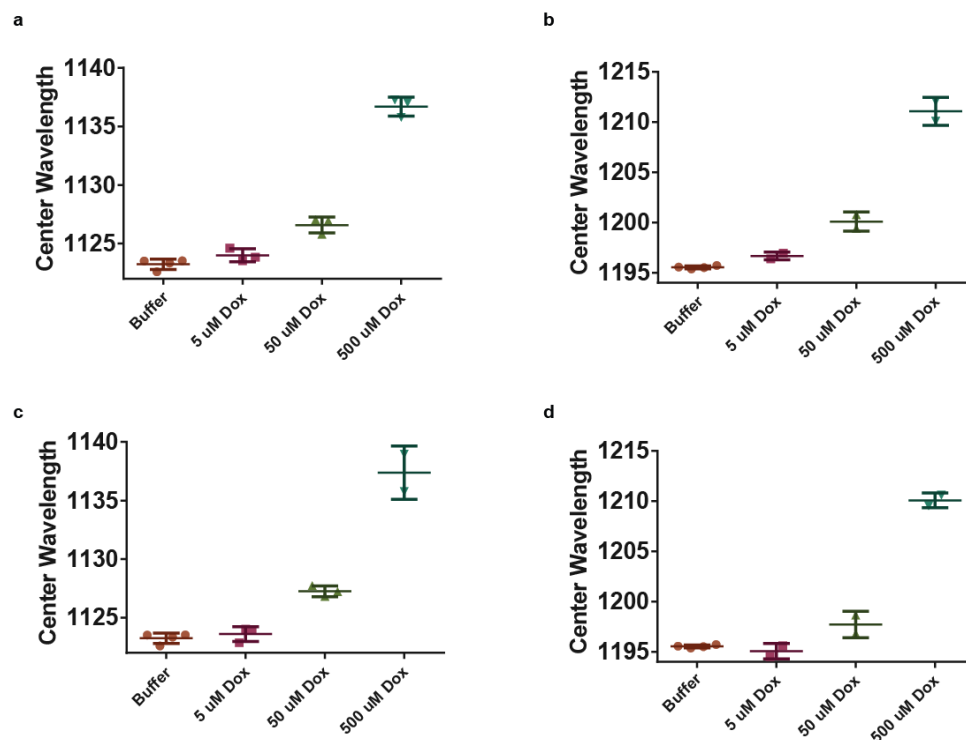
Figure 6.16 Dose-escalation of doxorubicin in vivo. a, Center wavelength of the (9,4) nanotube from implanted membrane devices after injection with 1 mL of buffer, 5 uM dox, 50 uM dox, or 500 uM dox. b, Center wavelength of the (8,6) nanotube from implanted membrane devices after injection with 1 mL of buffer, 5 uM dox, 50 uM dox, or 500 uM dox. c, Center wavelength of the (9,4) from membrane devices *ex vivo* after removal from the mouse. d, Center wavelength of the (8,6) from membrane devices *ex vivo* after removal from the mouse. Error bars represent standard deviation from 3 measurements per mouse per condition.

Finally we tested whether implanted carbon nanotube sensor devices could be used to obtain anatomic compartment specific measurement of doxorubicin. We surgically implanted two carbon nanotube devices separated by the peritoneal membrane. The peritoneal membrane defines the peritoneal cavity, and separates it from the skin. One device was placed in the peritoneum, while the other device was implanted under the skin but over the peritoneal membrane. Whole mouse imaging in the custom built hyperspectral imager modeled after an IVIS system was used to assess implant placement. Two white light images show the mouse before surgery and after, with one of the implantable devices visible protruding under the skin. Broadband imaging with 730 nm illumination show the nanotube emission from the two implanted devices. The suture is also slightly auto fluorescent and apparent near the incision (Figure 6.17a). Doxorubicin was injected in the peritoneum, and intensity of the nanotube fluorescence from the implanted devices monitored (Figure 6.17b). The mouse imager showed quenching of the device in the peritoneum, but not of the device under the skin (Figure 6.17c). Hyperspectral imaging was attempted; the implant under the skin however showed no wavelength changes (Figure 6.17d, e) but the emission was too quenched to collect spectral data from the peritoneal implant (Figure 6.17f). The mouse was then imaged under the probe, where each of the devices was measured. Compared to the device implanted outside the peritoneum, the device inside red-shifted and quenched a large degree (Figure 6.17g). Measurement of the devices *ex vivo* confirmed the red-shift observed *in vivo* (Figure 6.17h). Using two implantable devices, we found that doxorubicin was restricted to the inside of the peritoneum for the course of this experiment, giving us anatomic location specific sensing of the drug.
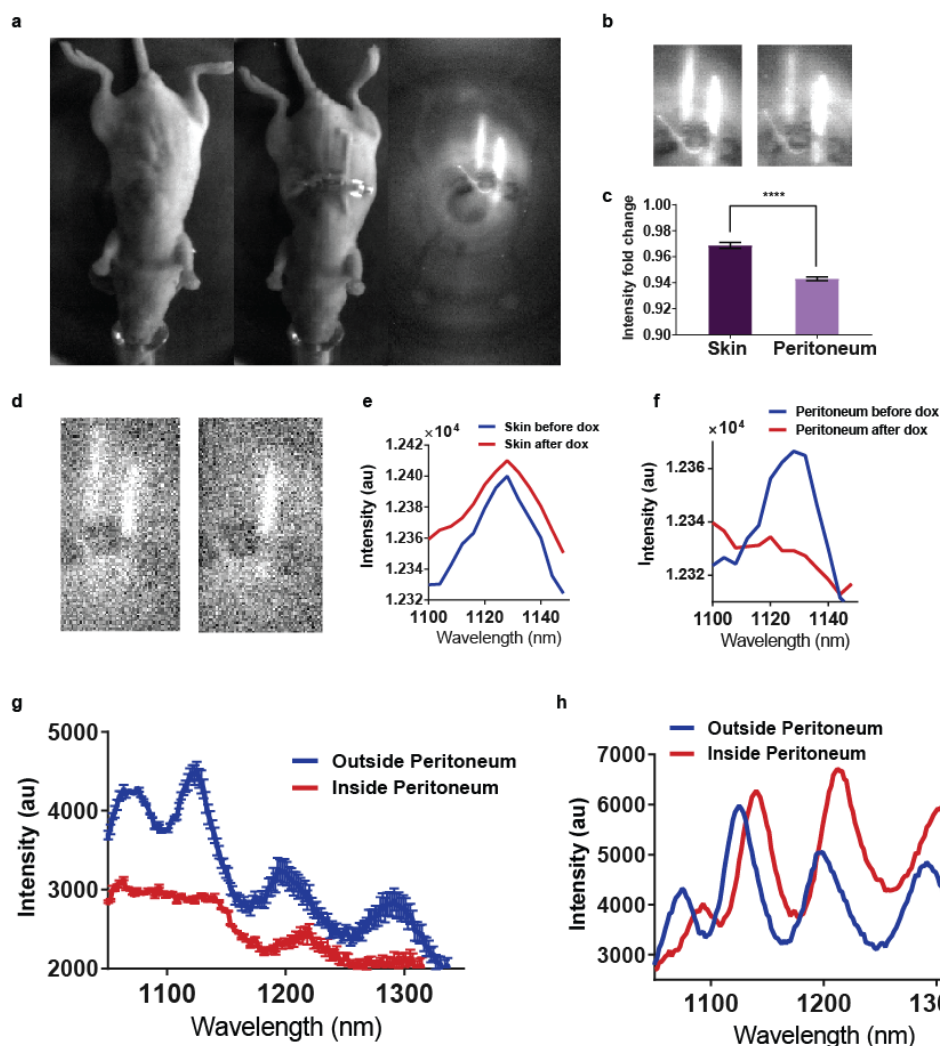
Figure 6.17 Differential response of implanted sensors in anatomically distinct locations. a, Image of the mouse before surgery (left), after implantation of devices in peritoneum and under skin (center), and broadband emission under 730nm illumination (right). b, Broadband emission of implanted devices in peritoneum (device on left) and under skin (device on right) before injection (left image) and 20m after injection (right image). c, quantification of intensity from the images in b. d, Section of hyperspectral cube corresponding to intensity at 1124 nm before injection (left image) and after injection (right image). e, spectral data of the implant under the skin before and after injection of doxorubicin. f, Spectral data of the implant in the peritoneum before and after injection of doxorubicin. g, Emission spectra from the device under the skin (blue, outside peritoneum) and inside the peritoneum (red) as measured with probe apparatus. h, emission spectra of the device under the skin (blue, outside peritoneum) and inside the peritoneum (red) taken *ex vivo* after the experiment.

6.4 Conclusions and outlook

Although pyrene-derivatives have been previously reported to be effective agents in non-covalently modifying carbon nanotubes, their interaction has been henceforth restricted to structural applications[36]. Some reports have looked at fluorescence changes of the pyrene derivative itself upon adsorption to the nanotube[53], but the impact of pyrene-derivatives on the intrinsic fluorescence of carbon nanotubes has not been addressed. Pyrene is a convenient molecule to study as it is one of the simplest polycyclic aromatic hydrocarbons, and derivatives such as 1-pyrenebutyric acid are readily available for functionalization. Polycyclic aromatic hydrocarbons as a whole are often carcinogenic pollutants formed from incomplete combustion of organic material. Part of their carcinogenicity is related to their planar, aromatic structure that is conducive to DNA intercalation. Using methoxypolyethylene glycol, a common material for imparting hydrophilicity to insoluble compounds, we were able to solubilize pyrene to test its effect on DNA-suspended nanotubes. We found a surprising effect—a large and rapid red-shift in carbon nanotube emission. Generally speaking, amphiphilic molecules that bind strongly to carbon nanotubes and provide a hydrophobic environment protected from water blue-shift the emission of nanotubes[54-56]. Compared to other surfactants, DNA-suspended nanotubes are typically relatively red-shifted due to incomplete coverage of the surface[56]. This feature has been useful for many sensing applications using DNA-suspended nanotubes[34]. We had hypothesized that pyrene-PEG would strongly adsorb to free surface area on DNA-suspended carbon nanotubes and exclude more water, leading to a blue-shift like the surfactants SDBS and SDC. Instead, pyrene-PEG red-shifted nearly 15 nm in some cases, matching the magnitude with which SDC blue-shifts DNA-wrapped nanotubes. Theoretical ab initio calculations predict that pyrene should have little impact on the electronic structure of nanotubes[57]. The apparent independence of chiral identity was

also surprising, as the environmental effects on nanotube optical properties are usually sensitive to chirality and mod type of the nanotube[58]. The strength with which pyrene-PEG associates with DNA-suspended nanotubes was also unexpected, blocking the interaction of SDBS and serum with the nanotube. However, the lack of effect of pyrene-PEG on SDC-suspended nanotubes suggests that the DNA-suspension is critical to sensitivity. It is still unknown if this is because of the sparse coverage provided by DNA, or a DNA-specific interaction with pyrene-PEG. Because of the large and rapid effect on DNA-suspended nanotube fluorescence, we believe that DNA-suspended nanotubes may be useful as sensors for other polycyclic aromatic hydrocarbons[59] in the environment as part of monitoring efforts.

The unexpected optical effects of pyrene-PEG led us to discover that other DNA-intercalating agents also largely recapitulate the impact on DNA-suspended nanotube fluorescence. Importantly, the ability to detect doxorubicin in this case could help address the issue of dose-monitoring for cumulative toxicity in patients by incorporating DNA-suspended nanotubes into an implantable device. One unfortunate effect doxorubicin had on DNA-suspended nanotubes was intensity quenching. Compared to other materials, the quantum yield of DNA-suspended nanotubes is already quite poor[60], making intensity quenching potentially problematic. Although other nanotube sensors have been reported based on quenching upon contact with an analyte[61], this mode of sensing is not ideal for *in vivo* applications, where a strong signal is required. Indeed, in the current study the quenching was below the threshold of detection for one mode of detection, although with a probe-based measurement the red-shift and intensity quenching was clearly detectable. We were able to rule out DNA-displacement and flocculation (with or without metallic nanotubes present) as the origin of this intensity loss from doxorubicin, and found that reducing agents were moderately useful in restoring some loss of intensity. At physiological pH,

doxorubicin is positively charged; it is possible that the electron-withdrawing character creates non-radiative decay sites on the nanotube sidewall, leading the observed intensity loss[62, 63]. This is supported by the partial intensity restoration by the reducing agent Trolox. For reasons that are still not clear, incorporation of the nanotubes into the implantable dialysis membrane enables high doses of doxorubicin to restore some intensity. This was repeated several times *in vitro*, and observed *ex vivo* after removal of the implant after several hours post doxorubicin exposure. The hydrogels displayed a similar effect, suggesting some kind of doxorubicin-mediated interaction with the implant substrate. Further work to reveal the exact mechanism for this may enable future implantable sensors for doxorubicin to be brightly fluorescent.

As an applied sensor material for doxorubicin, DNA-suspended nanotubes displayed several qualities that make them outstanding candidates. The optical response to doxorubicin was quite robust, even in the complex protein environment of whole serum and within cells. We have also shown that doxorubicin-responsive DNA-suspended nanotubes can be incorporated in hydrogels and semipermeable membranes for implantation without losing responsiveness to doxorubicin. The inability to reverse doxorubicin-induced red-shifting and the cumulative sensing behavior could make this particularly useful for human clinical applications, where dose-related toxicity of doxorubicin to patients is cumulative. We envision a possible sensing device to part of a small stent that could be placed near the heart in a minimally invasive manner through arteries. For research purposes, an implantable sensor could also be useful for doxorubicin as part of hyperthermic intraperitoneal chemotherapy (HIPEC) procedures, where site-specific measurement of doxorubicin can take place in live animals or patients[64]. This could help provide more precise therapy by accounting for patient-to-patient variation in doxorubicin distribution. In experimental model systems,

it may also be possible to introduce DNA-suspended nanotubes into specific cells of target organs to study doxorubicin accessibility in live organisms. This may be especially helpful in understanding cancer resistance to doxorubicin as cell intrinsic processes or extrinsic processes in the context of the live animal.

6.5 Materials and methods

6.5.1 Preparation of PEGylated pyrene derivative

Excess N-Hydroxysuccinimide (NHS) active 1-pyrenebutyric acid (1-Pyrenebutyric acid N-hydroxysuccinimide ester, Sigma Aldrich) was incubated with methoxypolyethylene glycol amine, M.W. 1,000 (PEG 1000, Alfa Aesar) in DMSO at room temperature overnight while vortexing. A centrifugal vacuum evaporator was used to remove DMSO, and the pellet was resuspended in deionized water. The sample was again centrifuged to pellet non-soluble 1-pyrenebutryic acid that did not conjugate to PEG. A fluorescence scan from 350 nm to 650 nm using 317 nm excitation was taken of the soluble Pyrene-PEG using the Tecan Infinite M1000 plate reader (Tecan Group Ltd, Switzerland).. The spectra contained evidence of excimer formation consistent with other reports of solubilized pyrene derivatives[65].

6.5.2 Suspension of carbon nanotubes

For DNA suspension, carbon nanotubes produced by the HiPco process (Unidym, Sunnyvale, CA) were mixed with DNA oligonucleotides (IDT DNA, Coralville, IA) at a 2:1 mass ratio in 1 mL of saline-sodium citrate (SSC) buffer and ultrasonicated for 30 minutes at 40% amplitude (Sonics & Materials, Inc.). For sodium deoxycholate (SDC) suspension, 1 mg of HiPco nanotubes were similarly sonicated in 2% wt/vol SDC prepared in water. Following ultrasonication, the dispersions were

ultracentrifuged (Sorvall Discovery 90SE) for 30 minutes at 280,000 x g. To remove

free DNA, 100 kDa Amicon centrifuge filters (Millipore) were used. The DNA-

nanotube complexes were re-suspended in saline-sodium citrate buffer (G Biosciences,

St. Louis, MO). The top 80% of the supernatant was collected. Absorbance spectra for

all dispersions were acquired using a UV/Vis/nIR spectrophotometer (Jasco V-670,

Tokyo, Japan). The concentration was calculated using the extinction coefficient

$Abs_{910} = 0.02554$ L mg^{-1}cm^{-1}.

The DNA sequences used for suspension were:

GTGTGTGTGTGTGTGTGTGTGTGTGTGTTCAGTTTTGCATAGATTTGCAC

A

GTGTGTGTGTGTGTGTGTGTGTGTGTGT

GTGTGTGTGTGTGTGTGTGTGTGTGTGTGTGTGTGTGT

CTTCCCTTC-Cy5

all purchased from IDT (Coralville, IA). Purification of the (8,4) nanotube chirality

suspended in (GT)20 was performed as previously described[44].

6.5.3 Fluorescence spectroscopy of carbon nanotubes in solution

Fluorescence emission spectra from aqueous nanotube solutions were acquired using a

home-built apparatus consisting of a tunable white light laser source, inverted

microscope, and InGaAs nIR detector. The SuperK EXTREME supercontinuum white

light laser source (NKT Photonics) was used with a VARIA variable bandpass filter

accessory capable of tuning the output 500 – 825 nm with a bandwidth of 20 nm. The

light path was shaped and fed into the back of an inverted IX-71 microscope

(Olympus) where it passed through a 20x nIR objective (Olympus) and illuminated a

50-100 µL nanotube sample in a 96-well plate (Corning). The emission from the

nanotube sample was collected through the 20x objective and passed through a dichroic mirror (875 nm cutoff, Semrock). The light was f/# matched to the spectrometer using several lenses and injected into an Isoplane spectrograph (Princeton Instruments) with a slit width of 410 µm which dispersed the emission using an 86 g/mm grating with 950 nm blaze wavelength. The spectral range was 930 – 1369 nm with a resolution of ~0.7 nm. The light was collected by a PIoNIR InGaAs 640 x 512 pixel array (Princeton Instruments). A HL-3-CAL-EXT halogen calibration light source (Ocean Optics) was used to correct for wavelength-dependent features in the emission intensity arising from the spectrometer, detector, and other optics. A Hg/Ne pencil style calibration lamp (Newport) was used to calibrate the spectrometer wavelength. Background subtraction was conducted using a well in a 96-well plate filled with DI H2O. Following acquisition, the data was processed with custom code written in Matlab which applied the aforementioned spectral corrections, background subtraction, and was used to fit the data with Lorentzian functions.

6.5.4 Solution phase experimental conditions

Unless otherwise noted, the concentration of nanotubes used for all experiments was 1 mg/L. Doxorubicin hydrochloride salt (LC labs) was prepared in a concentrated stock solution of 5 mM in deionized water and added to samples to the indicated final concentrations. Control sample received a volume-matched addition of water. Ethidium bromide, SYBR green, and Hoechst 33258 (all from ThermoFisher) were added to a final concentration of 1 uM. Experiments in serum used fetal bovine serum (ThermoFisher) with concentrated nanotubes added for a negligible increase in volume. Sodium dodecylbenzenesulfonate (Sigma Aldrich) was used at a final concentration of 0.2% wt/vol, prepared from a stock solution at 4% wt/vol. Hybridization experiments were conducted with 1 mg/L of the GT15mir19 sensor in

saline-sodium citrate buffer at room temperature. Concentrated target DNA was introduced to reach a final concentration of 1 uM target DNA (TGTGCAAATCTATGCAAAACTGA) complementary to the DNA-nanotube sensor or non-complementary control DNA (TCGGTCAGTGGGTCATTGCTAGT) (both from IDT DNA, Coralville, IA). Samples were incubated for 4 hours.

6.5.5 DNA-displacement, flocculation, and doxorubicin accumulation measurements

Measurement of DNA-displacement used 100 kDa Amicon centrifuge filters (Millipore) to separate displaced DNA. Absorbance of unmodified DNA was measured using the NanoDrop 2000 spectrophotometer (Thermo Fisher Scientific). DNA modified with Cy5 was measured using the Tecan Infinite M1000 plate reader (Tecan Group Ltd, Switzerland) taking absorbance scans with 2nm steps. Experiments measuring the loss of doxorubicin in 100 uL of 500 uM doxorubicin after incubation with 20 mg/L GT15 nanotubes were performed by centrifugation at maximum speed (21130 RCF) for 5 minutes, then extraction of the supernatant. The supernatant was subjected to absorbance scans from 350 nm to 700 nm using 2 nm steps, and compared to an identically treated control sample without addition of nanotubes. A standard curve was constructed with known concentrations of doxorubicin to calculate mass of doxorubicin that was lost due to the presence of nanotubes. The pellet of nanotubes was then washed in an attempt to liberate bound doxorubicin, which was again assessed by an absorbance scan of the supernatant and comparison to the standard curve. Quantification of flocculation was done using dynamic light scattering (Zetasizer Nano ZS, Malvern Instruments) for three independent runs.

6.5.6 Single-nanotube measurements

Single-nanotube measurements were performed by incubating GT15 suspended nanotubes on a poly-D-lysine coated glass bottom plate (Mattek, Ashland, MA) for 10 minutes before washing with 20 mM HEPES buffer three times and adding 1 mL of 20mM HEPES buffer containing ($\pm$)-6-Hydroxy-2,5,7,8-tetramethylchromane-2-carboxylic acid (Trolox) at 2 mg/mL. Hyperspectral cubes were obtained as described before and after addition of 50 uM doxorubicin. Three independent runs were performed. Data was processed with ImageJ software. Peaks were fit to Voigt functions using custom Matlab code to obtain center wavelength values, and the differences of each nanotube from each condition was pooled to make an average spectra and construct box and whisker plots.

6.5.7 Measurement of nanotube response to doxorubicin in cells

A murine macrophage cell line (RAW 264.7, TIB-71 obtained from ATCC) was propagated at 37°C and 5% CO_2 in DMEM with 10% heat-inactivated FBS, 2.5% HEPES, 1% glutamine, and 1% penicillin/streptomycin (all from Gibco). Cells were plated on glass bottom petri-dishes (Mattek) and treated with 1mg/mL GT15 nanotubes added directly to the medium overnight. Cells were washed in warm PBS three times before hyperspectral measurements. For both the buffer treated and doxorubicin treated cells, regions of interest (ROIs) were selected using ImageJ software over approximately 50 cells in each condition. Reported spectra are based on the average of all ROIs.

6.5.8 Hyperspectral microscopy

Hyperspectral microscopy was performed by illuminating the sample with a continuous wave 730 nm diode laser (output power = 2 W) via a multimode fiber. A

custom beam shaping module was used to produce a top hat intensity profile with a maximum of 20% variation at the sample surface. Shaped laser emission was reflected into an Olympus IX-71 inverted microscope modified for near infrared transmission and focused onto the sample with a 100X (UAPON100XOTIRF, NA=1.49) oil objective (Olympus, USA) via a longpass dichroic mirror with a cut-on wavelength of 880 nm. Spatially resolved, near-infrared emission from the sample was fed into a volume Bragg grating (VBG) where specific wavelength components of the polychromatic light was diffracted and passed again through the VBG resulting in a monochromatic beam, which was collected by a 256 x 320 pixel InGaAs array (Photon Etc.). Data was compiled as a continuous stack of images for the indicated wavelength ranges (hyperspectral cubes) wherein every pixel of a near-infrared image was spectrally resolved.

6.5.9 Device implantation and *in vivo* spectroscopy

All animal experiments were approved by the Institutional Animal Care and Use Committee at Memorial Sloan Kettering Cancer Center. KrosFlo Implant Membranes (500 kD MWCO) were obtained from Spectrum Labs (Rancho Dominguez, CA). The membrane was cut to about 1 cm in length and filled with approximately 15 uL of 1 mg/L GT15 nanotubes. Each end was heat sealed. All mice used were NU/J (nude) from Jackson Labs, and anesthetized with 2% isoflurane for surgeries and spectra acquisition. Initial assessment or responsivity *in vivo* used three mice with 1 mL injection of 500 uM doxorubicin. Dose-escalation studies used one mouse per condition. Kinetics of after injection of doxorubicin and whole mouse hyperspectral imaging of anatomic compartment specific sensing is reported for one mouse each. Probe-based measurements were taken using a custom-built reflectance probe-based spectroscopy system. The system consisted of a continuous wave 1 watt 730 nm diode

laser (Frankfurt). The laser light was injected into a bifurcated fiber optic reflection probe bundle. The sample leg of the bundle included one 200 µm, 0.22 NA fiber optic cable for sample excitation located in the center of six 200 µm, 0.22 NA fiber optic cables for collection of the emitted light. Emission below 1050 nm was filtered using longpass filters, and the light was focused into the slit of a Czerny-Turner spectrograph with 303 mm focal length (Shamrock 303i, Andor). The slit width of the spectrograph was set at 410 µm. The light was dispersed using an 85 g/mm grating with 1350 nm blaze wavelength and collected with an iDus InGaAs camera (Andor). Spectra were fit to Voigt functions using custom Matlab code. Whole mouse hyperspectral imaging of nanotubes *in vivo* was performed using a preclinical hyperspectral mouse imaging system (Photon Etc., Montreal). Two continuous wave 730 nm diode lasers each with an output power of 2 W were reflected off optical mirrors and distributed over the entire mouse, resulting in a maximum power density of 340 mW/cm^2. Emission light was filtered through an 1100 nm longpass filter to reduce autofluorescence. Intensity from broadband imaging was quantified with custom software (PhySpec, Photon Etc.). Hyperspectral cubes were obtained via a volume Bragg grating (VBG) analogous to the system used for hyperspectral microscopy of cells and single nanotubes.

6.6 Acknowledgements

6.7 References

1. Cheung-Ong, K., Giaever, G. & Nislow, C. DNA-Damaging Agents in Cancer Chemotherapy: Serendipity and Chemical Biology. *Chemistry & biology* **20**, 648-659 (2013).

2. Ren, J., Jenkins, T.C. & Chaires, J.B. Energetics of DNA intercalation reactions. *Biochemistry* **39**, 8439-8447 (2000).

3. Smith, S.B., Finzi, L. & Bustamante, C. Direct Mechanical Measurements of the Elasticity of Single DNA-Molecules by Using Magnetic Beads. *Science* **258**, 1122-1126 (1992).

4. Koster, D.A., Palle, K., Bot, E.S.M., Bjornsti, M.A. & Dekker, N.H. Antitumour drugs impede DNA uncoiling by topoisomerase I. *Nature* **448**, 213-217 (2007).

5. Hurley, L.H. DNA and its associated processes as targets for cancer therapy. *Nature Reviews Cancer* **2**, 188-200 (2002).

6. Harvey, R.G. & Geacintov, N.E. Intercalation and Binding of Carcinogenic Hydrocarbon Metabolites to Nucleic-Acids. *Accounts of Chemical Research* **21**, 66-73 (1988).

7. Spence, M.T.Z. & Johnson, I.D. The molecular probes handbook : a guide to fluorescent probes and labeling technologies, Edn. 11th. (Live Technologies Corporation, Carlsbad, CA; 2010).

8. Lepecq, J.B. & Paoletti, C. A Fluorescent Complex between Ethidium Bromide and Nucleic Acids - Physical-Chemical Characterization. *Journal of molecular biology* **27**, 87-& (1967).

9.   Martin, R.M., Leonhardt, H. & Cardoso, M.C. DNA labeling in living cells. *Cytom Part A* **67A**, 45-52 (2005).

10.   Straif, K., Baan, R., Grosse, Y. et al. Carcinogenicity of polycyclic aromatic hydrocarbons. *The Lancet. Oncology* **6**, 931-932 (2005).

11.   Fujiki, H. Gist of Dr. Katsusaburo Yamagiwa's papers entitled "Experimental study on the pathogenesis of epithelial tumors" (I to VI reports). *Cancer science* **105**, 143-149 (2014).

12.   Miguel, A.H., Kirchstetter, T.W., Harley, R.A. & Hering, S.V. On-road emissions of particulate polycyclic aromatic hydrocarbons and black carbon from gasoline and diesel vehicles. *Environ Sci Technol* **32**, 450-455 (1998).

13.   Kumke, M.U., Lohmannsroben, H.G. & Roch, T. Fluorescence spectroscopy of polynuclear aromatic compounds in environmental monitoring. *Journal of fluorescence* **5**, 139-152 (1995).

14.   Katzung, B.G., Masters, S.B. & Trevor, A.J. Basic & clinical pharmacology, Edn. 11th. (McGraw-Hill Medical ; McGraw-Hill distributor, New York, London; 2009).

15.   in UpToDate (Waltham, MA.

16.   Vonhoff, D.D., Layard, M.W., Basa, P. et al. Risk-Factors for Doxorubicin-Induced Congestive Heart-Failure. *Ann Intern Med* **91**, 710-717 (1979).

17.   Thorn, C.F., Oshiro, C., Marsh, S. et al. Doxorubicin pathways: pharmacodynamics and adverse effects. *Pharmacogenet Genom* **21**, 440-446 (2011).

18.   Minotti, G., Recalcati, S., Menna, P. et al. Doxorubicin cardiotoxicity and the control of iron metabolism: Quinone-dependent and independent mechanisms. *Method Enzymol* **378**, 340-+ (2004).

19.   Wallace, K.B. Adriamycin-induced interference with cardiac mitochondrial calcium homeostasis. *Cardiovasc Toxicol* **7**, 101-107 (2007).

20.   Goodman, M.D., McPartland, S., Detelich, D. & Saif, M.W. Chemotherapy for intraperitoneal use: a review of hyperthermic intraperitoneal chemotherapy and early post-operative intraperitoneal chemotherapy. *J Gastrointest Oncol* **7**, 45-57 (2016).

21.   Rossi, C.R., Foletto, M., Mocellin, S. et al. Hyperthermic Intraoperative intraperitoneal chemotherapy with cisplatin and doxorubicin in patients who undergo cytoreductive surgery for peritoneal carcinomatosis and sarcomatosis - Phase I study. *Cancer* **94**, 492-499 (2002).

22.   Zheng, M., Jagota, A., Semke, E.D. et al. DNA-assisted dispersion and separation of carbon nanotubes. *Nature materials* **2**, 338-342 (2003).

23.   Baughman, R.H., Zakhidov, A.A. & de Heer, W.A. Carbon nanotubes - the route toward applications. *Science* **297**, 787-792 (2002).

24.   Roxbury, D., Tu, X., Zheng, M. & Jagota, A. Recognition ability of DNA for carbon nanotubes correlates with their binding affinity. *Langmuir : the ACS journal of surfaces and colloids* **27**, 8282-8293 (2011).

25.   Manohar, S., Tang, T. & Jagota, A. Structure of homopolymer DNA-CNT hybrids. *J Phys Chem C* **111**, 17835-17845 (2007).

26.   O'Connell, M.J., Bachilo, S.M., Huffman, C.B. et al. Band gap fluorescence from individual single-walled carbon nanotubes. *Science* **297**, 593-596 (2002).

27.   Wang, F., Dukovic, G., Brus, L.E. & Heinz, T.F. The optical resonances in carbon nanotubes arise from excitons. *Science* **308**, 838-841 (2005).

28.   Cheong, W.F., Prahl, S.A. & Welch, A.J. A review of the optical properties of biological tissues. *IEEE Journal of Quantum Electronics* **26**, 2166-2185 (1990).

29.   Gao, J., Gomulya, W. & Loi, M.A. Effect of medium dielectric constant on the physical properties of single-walled carbon nanotubes. *Chemical Physics* **413**, 35-38 (2013).

30.   Choi, J.H. & Strano, M.S. Solvatochromism in single-walled carbon nanotubes. *Applied Physics Letters* **90**, 223114 (2007).

31.   Heller, D.A., Jeng, E.S., Yeung, T.K. et al. Optical detection of DNA conformational polymorphism on single-walled carbon nanotubes. *Science* **311**, 508-511 (2006).

32.   Barone, P.W., Baik, S., Heller, D.A. & Strano, M.S. Near-infrared optical sensors based on single-walled carbon nanotubes. *Nature materials* **4**, 86-92 (2005).

33.   Iverson, N.M., Barone, P.W., Shandell, M. et al. *In vivo* biosensing via tissue-localizable near-infrared-fluorescent single-walled carbon nanotubes. *Nature nanotechnology* **8**, 873-880 (2013).

34.   Harvey, J.D., Jena, P.V., Baker, H.A. et al. A carbon nanotube reporter of microRNA hybridization events *in vivo*. *Nature Biomedical Engineering* **1**, 0041 (2017).

35.   Zhang, J., Lee, J.K., Wu, Y. & Murray, R.W. Photoluminescence and electronic interaction of anthracene derivatives adsorbed on sidewalls of single-walled carbon nanotubes. *Nano letters* **3**, 403-407 (2003).

36.   Chen, R.J., Zhang, Y.G., Wang, D.W. & Dai, H.J. Noncovalent sidewall functionalization of single-walled carbon nanotubes for protein immobilization. *Journal of the American Chemical Society* **123**, 3838-3839 (2001).

37.   Liu, Z., Sun, X.M., Nakayama-Ratchford, N. & Dai, H.J. Supramolecular chemistry on water-soluble carbon nanotubes for drug loading and delivery. *ACS nano* **1**, 50-56 (2007).

38. Liu, Z., Fan, A.C., Rakhra, K. et al. Supramolecular Stacking of Doxorubicin on Carbon Nanotubes for *In vivo* Cancer Therapy. *Angew Chem Int Edit* **48**, 7668-7672 (2009).

39. Winnik, F.M. Photophysics of Preassociated Pyrenes in Aqueous Polymer-Solutions and in Other Organized Media. *Chemical reviews* **93**, 587-614 (1993).

40. Jena, P.V., Safaee, M.M., Heller, D.A. & Roxbury, D. DNA-Carbon Nanotube Complexation Affinity and Photoluminescence Modulation Are Independent. *ACS applied materials & interfaces* **9**, 21397-21405 (2017).

41. Weinstein, I.B., Jeffrey, A.M., Jennette, K.W. et al. Benzo[a]Pyrene Diol Epoxides as Intermediates in Nucleic-Acid Binding Invitro and Invivo. *Science* **193**, 592-595 (1976).

42. Laib, S., Krieg, A., Hafliger, P. & Agorastos, N. DNA-intercalation on pyrene modified surface coatings. *Chemical communications*, 5566-5568 (2005).

43. Agudelo, D., Bourassa, P., Bruneau, J. et al. Probing the Binding Sites of Antibiotic Drugs Doxorubicin and N-(trifluoroacetyl) Doxorubicin with Human and Bovine Serum Albumins. *PloS one* **7** (2012).

44. Ao, G.Y., Khripin, C.Y. & Zheng, M. DNA-Controlled Partition of Carbon Nanotubes in Polymer Aqueous Two-Phase Systems. *Journal of the American Chemical Society* **136**, 10383-10392 (2014).

45. Lee, A.J., Wang, X., Carlson, L.J. et al. Bright fluorescence from individual single-walled carbon nanotubes. *Nano letters* **11**, 1636-1640 (2011).

46. MJ, O.C., Eibergen, E.E. & Doorn, S.K. Chiral selectivity in the charge-transfer bleaching of single-walled carbon-nanotube spectra. *Nature materials* **4**, 412-418 (2005).

47.   Roxbury, D., Jena, P.V., Shamay, Y., Horoszko, C.P. & Heller, D.A. Cell Membrane Proteins Modulate the Carbon Nanotube Optical Bandgap via Surface Charge Accumulation. *ACS nano* **10**, 499-506 (2016).

48.   Ignatova, T., Chandrasekar, S., Pirbhai, M., Jedlicka, S.S. & Rotkin, S.V. Micro-Raman spectroscopy as an enabling tool for long-term intracellular studies of nanomaterials at nanomolar concentration levels. *Journal of Materials Chemistry B* (2017).

49.   Cui, X., Wan, B., Yang, Y., Ren, X. & Guo, L.H. Length effects on the dynamic process of cellular uptake and exocytosis of single-walled carbon nanotubes in murine macrophage cells. *Scientific reports* **7**, 1518 (2017).

50.   Heller, D.A., Baik, S., Eurell, T.E. & Strano, M.S. Single-Walled Carbon Nanotube Spectroscopy in Live Cells: Towards Long-Term Labels and Optical Sensors. *Advanced materials* **17**, 2793-2799 (2005).

51.   Jena, P.V., Roxbury, D., Galassi, T.V. et al. A Carbon Nanotube Optical Reporter Maps Endolysosomal Lipid Flux. *bioRxiv* (2017).

52.   Galassi, T.V., Jena, P.V., Roxbury, D. & Heller, D.A. Single Nanotube Spectral Imaging To Determine Molar Concentrations of Isolated Carbon Nanotube Species. *Analytical chemistry* **89**, 1073-1077 (2017).

53.   Salice, P., Gambarin, A., Daldosso, N., Mancin, F. & Menna, E. Noncovalent Interaction between Single-Walled Carbon Nanotubes and Pyrene-Functionalized Gold Nanoparticles in Water-Soluble Nanohybrids. *J Phys Chem C* **118**, 27028-27038 (2014).

54.   Miyauchi, Y., Saito, R., Sato, K. et al. Dependence of exciton transition energy of single-walled carbon nanotubes on surrounding dielectric materials. *Chemical Physics Letters* **442**, 394-399 (2007).

55. Haggenmueller, R., Rahatekar, S.S., Fagan, J.A. et al. Comparison of the quality of aqueous dispersions of single wall carbon nanotubes using surfactants and biomolecules. *Langmuir : the ACS journal of surfaces and colloids* **24**, 5070-5078 (2008).

56. Fantini, C., Cassimiro, J., Peressinotto, V.S.T. et al. Investigation of the light emission efficiency of single-wall carbon nanotubes wrapped with different surfactants. *Chemical Physics Letters* **473**, 96-101 (2009).

57. Tournus, F., Latil, S., Heggie, M.I. & Charlier, J.C. pi-stacking interaction between carbon nanotubes and organic molecules. *Physical Review B* **72** (2005).

58. Ohno, Y., Iwasaki, S., Murakami, Y. et al. Chirality-dependent environmental effects in photoluminescence of single-walled carbon nanotubes. *Physical Review B* **73** (2006).

59. Xu, J.W., Du, J.J., Jing, C.Y., Zhang, Y.L. & Cui, J.L. Facile Detection of Polycyclic Aromatic Hydrocarbons by a Surface-Enhanced Raman Scattering Sensor Based on the Au Coffee Ring Effect. *ACS applied materials & interfaces* **6**, 6891-6897 (2014).

60. Carlson, L.J., Maccagnano, S.E., Zheng, M., Silcox, J. & Krauss, T.D. Fluorescence efficiency of individual carbon nanotubes. *Nano letters* **7**, 3698-3703 (2007).

61. Bisker, G., Dong, J., Park, H.D. et al. Protein-targeted corona phase molecular recognition. *Nature communications* **7**, 10241 (2016).

62. Wang, F., Dukovic, G., Knoesel, E., Brus, L.E. & Heinz, T.F. Observation of rapid Auger recombination in optically excited semiconducting carbon nanotubes. *Physical Review B* **70** (2004).

63. Larsen, B.A., Deria, P., Holt, J.M. et al. Effect of solvent polarity and electrophilicity on quantum yields and solvatochromic shifts of single-walled carbon nanotube photoluminescence. *Journal of the American Chemical Society* **134**, 12485-12491 (2012).

64. Harrison, L.E., Bryan, M., Pliner, L. & Saunders, T. Phase i trial of pegylated liposomal doxorubicin with hyperthermic intraperitoneal chemotherapy in patients undergoing cytoreduction for advanced intra-abdominal malignancy. *Annals of surgical oncology* **15**, 1407-1413 (2008).

65. Chen, S.H., Duhamel, J., Peng, B.L., Zaman, M. & Tam, K.C. Interactions between a Series of Pyrene End-Labeled Poly(ethylene oxide)s and Sodium Dodecyl Sulfate in Aqueous Solution Probed by Fluorescence. *Langmuir : the ACS journal of surfaces and colloids* **30**, 13164-13175 (2014).

APPENDIX

Supplementary Tables for Chapter 2

Table S1: List of amphipathic molecules used to study the enhancement of the sensor response.

Name	Abbreviation	Class of amphipathic molecule
Sodium deoxycholate	SDC	ionic surfactant
Sodium dodecyl sulfate	SDS	ionic surfactant
Sodium dodecylbenenesulfonate	SDBS	ionic surfactant
Pluronic F-68	Pluronic	non-ionic triblock copolymers
Triton X-100	n/a	non-ionic surfactant
IGEPAL CO-530	IGEPAL	non-ionic surfactant
Span 80	n/a	non-ionic surfactant
Brij 52	n/a	non-ionic surfactant
D-α-Tocopherol polyethylene glycol 1000 succinate	TPGS	non-ionic surfactant (vitamin E)
1,2-distearoyl-sn-glycero-3-phosphoethanolamine-N-[methoxy(polyethylene glycol)-1000] (ammonium salt))	Lipid-PEG	PEGylated lipid
Bovine serum albumin	BSA	protein

Table S2. GT15mirX sequences used in this work.

Name	Sequence (5' to 3')
GT15mir19	GTGTGTGTGTGTGTGTGTGTGTGTGTGTGTTCAGTTTTGCATAGATTTGCACA
GT15mir126	GTGTGTGTGTGTGTGTGTGTGTGTGTGTGTGCATTATTACTCACGGTACGA
GT15mir182	GTGTGTGTGTGTGTGTGTGTGTGTGTGTGTTGTGAGTTCTACCATTGCCAAA
GT15mir152	GTGTGTGTGTGTGTGTGTGTGTGTGTGTGTCCAAGTTCTGTCATGCACTGA
GT15mir509	GTGTGTGTGTGTGTGTGTGTGTGTGTGTGTTGATTGCCACTGTCTGCAGTA
GT15mir96	GTGTGTGTGTGTGTGTGTGTGTGTGTGTGTAGCAAAAATGTGCTAGTGCCAAA
GT15mir183	GTGTGTGTGTGTGTGTGTGTGTGTGTGTGTAGTGAATTCTACCAGTGCCATA
GT15mir494	GTGTGTGTGTGTGTGTGTGTGTGTGTGTGTGAGGTTTCCCGTGTATGTTTCA
GT15mir39	GTGTGTGTGTGTGTGTGTGTGTGTGTGTGTCAAGCTGATTTACACCGGTGA
GT15mir21	GTGTGTGTGTGTGTGTGTGTGTGTGTGTGTTCAACATCAGTCTGATAAGCTA
GT15mir141	GTGTGTGTGTGTGTGTGTGTGTGTGTGTGTCCATCTTTACCAGACAGTGTTA
GT15mir429	GTGTGTGTGTGTGTGTGTGTGTGTGTGTGTACGGTTTTACCAGACAGTATTA
GT15mir200b	GTGTGTGTGTGTGTGTGTGTGTGTGTGTGTTCATCATTACCAGGCAGTATTA
GT15mir19-minus6	GTGTGTGTGTGTGTGTGTGTGTGTGTGTGTTCAGTTTTGCATAGATT
GT6mir19-Cy5	GTGTGTGTGTGTTCAGTTTTGCATAGATTTGCACA-Cy5

Table S3. Analyte/target sequences used in this work.

Name	Sequence (5' to 3')
miR-19 DNA	TGTGCAAATCTATGCAAAACTGA
miR-19 RNA	UGUGCAAAUCUAUGCAAAACUGA
miR-21 DNA	TAGCTTATCAGACTGATGTTG
miR-21 RNA	UAGCUUAUCAGACUGAUGUUG
R23 DNA	TCGGTCAGTGGGTCATTGCTAGT
R23 RNA	UCGGUCAGUGGGUCAUUGCUAGU
miR-126	TCGTACCGTGAGTAATAATGC
miR-182	TTTGGCAATGGTAGAACTCACA
miR-152	TCAGTGCATGACAGAACTTGG
miR-509	TACTGCAGACAGTGGCAATCA
miR-96	TTTGGCACTAGCACATTTTTGCT
miR-183	TATGGCACTGGTAGAATTCACT
miR-494	TGAAACATACACGGGAAACCTC
miR-39	TCACCGGGTGTAAATCAGCTTG
miR-141	TAACACTGTCTGGTAAAGATGG
miR-200b	TAATACTGCCTGGTAATGATGA
miR-429	TAATACTGTCTGGTAAAACCGT
Removing Seq.	TCAGTTTTGCATAGATTTGCACA

Table S4. Truncated miR analyte sequences designed to hybridize to the middle of miRNA capture sequence.

Name	Sequence
GT15mir19	5'-GTGTGTGTGTGTGTGTGTGTGTGTGTGTGT<u>TCAGTTTTGCATAGATTTGCACA</u>-3'
mir19-10	3'-AGTCAAAACG-5'
mir19-11	3'-AGTCAAAACGT-5'
mir19-12	3'-AGTCAAAACGTA-5'
mir19-13	3'-AGTCAAAACGTAT-5'
mir19-14	3'-AGTCAAAACGTATC-5'
mir19-15	3'-AGTCAAAACGTATCT-5'

Table S5. Truncated miR analyte sequences designed to hybridize to the 5' end of miRNA capture sequence.

Name	Sequence
GT15mir19	5'-GTGTGTGTGTGTGTGTGTGTGTGTGTGTGT<u>TCAGTTTTGCATAGATTTGCACA</u>-3'
mir19-10	3'-CTAAACGTGT-5'
mir19-11	3'-TCTAAACGTGT-5'
mir19-12	3'-ATCTAAACGTGT-5'
mir19-13	3'-TATCTAAACGTGT-5'
mir19-14	3'-GTATCTAAACGTGT-5'
mir19-15	3'-CGTATCTAAACGTGT-5'
mir19-17	3'-AACGTATCTAAACGTGT-5'

Table S6. Elongated analyte sequences used in this work.

Name	Sequence (5' to 3')
R23mir19R23	TCGGTCAGTGGGTCATTGCTAGT<u>TGTGCAAATCTATGCAAAACTGA</u>TCGGTCAGTGGGTCATTGCTAGT
mir19R23	TCGGTCAGTGGGTCATTGCTAGT<u>TGTGCAAATCTATGCAAAACTGA</u>
R23mir19	<u>TGTGCAAATCTATGCAAAACTGA</u>TCGGTCAGTGGGTCATTGCTAGT
R23R23R23	TCGGTCAGTGGGTCATTGCTAGTCGGTCAGTGGGTCATTGCTAGTTCGGTCAGTGGGTCATTGCTAGT